ISAS - INTERNATIONAL SCHOOL
FOR ADVANCED STUDIES

The EXOSAT Spectral Survey of Blazars

Magister Philosophiæ

CANDIDATE

Rita Maria Sambruna

SUPERVISOR

Prof. A. Treves

Academic year 1991-1992
Astrophysics Sector

TRIESTE

SISSA - SCUOLA
INTERNAZIONALE
SUPERIORE
DI STUDI AVANZATI
TRIESTE
Strada Costiera 11

Acknowledgements

I am grateful to Paul Barr for providing me with most of the EXOSAT data used in the present work. The Astrophysical Department of the European Space Agency at ESTEC, Noordwjick, is acknowledged for giving me the access to the software and hardware facilities I needed. In particular, I thank Gianpiero Tagliaferri for his hospitality during my stay at ESTEC and for his continuous advise. Profs. Laura Maraschi and Aldo Treves are warmly thanked for the many useful discussions and encouragements. I want to acknowledge Prof. Sciama and SISSA for the financial support. A very special thanks to Joe for all his help.

CONTENTS

TABLES

FIGURES

CHAPTER I

Introduction

BL Lacertae (BL Lac) objects are extragalactic sources characterized by a high degree ($> 3\%$) of linear polarization in the optical light, dramatic variability at almost all frequencies, and weak or absent emission lines (see Angel & Stockmann 1980 for a review). Together with the Highly Polarized Quasars (HPQ) and Optically Violent Variables (OVV), for which strong emission lines are usually found, they form the blazar class.

BL Lac objects are well known X-ray emitters (Schwartz *et al.* 1979; Piccinotti *et al.* 1982). A number of them have been discovered in X-ray surveys (Maccacaro *et al.* 1982; Stocke *et al.* 1991; Giommi *et al.* 1991). X-ray selected BL Lacs (XBL) seem to differ from the radio selected BL Lacs (RBL) in many properties (Stocke *et al.* 1985; Ledden & O'Dell 1985; Stocke *et al.* 1990), although in X-ray they have the same luminosity distributions (Maraschi *et al.* 1986; Padovani & Urry 1990; Morris *et al.* 1991). The distinction between the two classes appear sometimes controversial (see, *e.g.*, Schwartz *et al.* 1989). However, this is not the proper place to enter into details; in this thesis we have followed the accepted classification found in the literature.

Our knowledge of the X-ray spectral distributions of BL Lac objects is still rather limited, unlike that for other classes of Active Galactic Nuclei (AGN). In fact, it is commonly found that the X-ray spectra of AGN are adequately represented at higher energies by a single power law (Williams *et al.* 1992; Lawson *et al.* 1992), while at lower energies a "soft excess" is often found

(Turner & Pounds 1989; Turner *et al.* 1990). In addition, the values of the X-ray slopes are tightly defined for the some classes of objects (Turner & Pounds 1989; Canizares & White 1989; Wilkes & Elvis 1987; Worrall & Wilkes 1990).

For BL Lac objects, the situation is less clear. From a sample of 13 objects, observed with the *Einstein* IPC, Madejski & Schwartz (1989) found an average (photon) index of $\sim$ 2.1 in the energy range 0.2 – 4 keV. The GINGA observations of 3 XBL gave an average slope $\geq$ 2.7 in the 2 – 35 keV range (Ohashi 1989), while for 2 RBL a mean of $\sim$ 1.8 was found. In a review of the results obtained for some individual objects with the EXOSAT data, Maraschi & Maccagni (1988) gave a mean value of $\sim$ 2.5 in 0.1 – 10 keV.

There seems to be a difference in X-ray spectral shape between the class of BL Lac objects and that of other AGN. For example, an interesting comparison has been done for a sample of BL Lac objects (6 XBL and 24 RBL), Highly Polarized Quasars (12), and flat radio spectrum quasars (19) by Worrall & Wilkes (1990), on the basis of the *Einstein* IPC spectra. The result of their analysis is that the BL Lac objects are, on average, steeper in slopes than the latter two groups.

In early reports for some individual, bright objects, for which data coverage of more than one decade in energy was available, a flattening of the spectrum above 10 keV (hard tail) was detected (see Urry 1986 and references therein), but not confirmed later (Ohashi *et al.* 1989). An independent result was obtained by Madejski & Schwartz (1989). Fitting the simultaneous *Einstein* IPC and MPC data for a sample of six objects, they found a systematic steepening in 1 – 3 keV, *i.e.* a downward curvature of the spectra. Convex spectra were also seen in the EXOSAT observations of PKS 0548-322 (Barr *et al.* 1988), and of the BL Lac objects as a class in a preliminary report by Barr *et al.* (1989), based on 17 objects.

In the *Einstein* OGS spectrum of the bright object PKS 2155-304, Canizares & Kruper (1984) found an absorption feature at $\sim$ 0.6 keV which they attribute to highly ionized oxygen. There is increasing evidence that this feature is characteristic of the BL Lac class (Madejski *et al.* 1991, 1992).

To summarize, it is not clear if the X-ray spectral distribution of BL Lac objects can be represented with a unique model. However, it must be stressed that the majority of the previous works have considered a restricted number of objects, in limited energy bands. The European X-ray Observatory Satellite (EXOSAT) database provides the opportunity to study in a systematic way spectral data obtained over a larger energy band (0.1 – 10 keV).

Here we present a study in the 0.1 – 10 keV of the energy distributions of 8 RBL and 19 XBL, using data retrieved from the EXOSAT archive at ESTEC, Noordwijk. This work was done in collaboration with other groups. Some spectra were re-extracted from the original tapes (by P.Barr) to further improve their quality. The spectra were analyzed with the XSPEC fitting program implemented at ESTEC. The EXOSAT data for some objects have been previously published. The results of the analysis for four individual objects, for which the EXOSAT data were still unpublished, have been submitted for publication (Sambruna *et al.* 1992).

In addition, the possibility to compare the spectral properties of the BL Lac objects with those of other blazars, namely the HPQ and OVV, has been considered. For only few of these objects the archive could provide good data, which were retrieved and studied as a separate group. However, due to the paucity of the objects found only a tentative comparison could be performed between the various classes.

CHAPTER II

The EXOSAT archival data

2.1 The ME data

The Medium Energy (ME; Turner *et al.* 1981) of EXOSAT is a passively collimated instrument, consisting of eight Argon filled proportional counters, sensitive in the 1 – 20 keV energy range, with a resolution of 21 % at 6 keV. Xenon filled proportional counters (1 – 50 keV), will not be considered here. The detectors were grouped to form two panels ("halves"). During the observations, one half was pointing toward the source ("aligned half"), while the other monitored the sky ("offset half"), giving an independent estimate of the background (particle induced background and, as a minor component, the extragalactic X-ray background). Because the two halves have not the same background level, for weak sources they were interchanged during the observation ("array swap"), in order the background be monitored by the same detectors which provide the source data.

The ME database provides:

- a background subtracted on-source spectrum integrated over the entire observing period;
- on-source background subtracted light curves in the range 1 – 8 keV,

with 30 s time resolution;

• high time resolution (1 – 10 s) on-source background subtracted light curves in the ranges 1 – 3.8, 3.8 – 8, and 1 – 8 keV;

• background light curves in the range 1 – 8 keV (30 s resolution).

The archival ME data were originally reduced by the automatic analysis described in the "The EXOSAT Database System: Available Databases" manual (1991). The quality of the products relies in a critical way on the background subtraction method. The automatic procedure can select, in a "hierarchical manner", among different subtraction methods, depending on whether the background was acquired during array swaps or with a slew manoeuvre. In general, the best results are obtained in the case of the array swaps because the background is estimated by the same detectors at different times.

As a measure of the reliability of the background subtraction, the extracted spectra were subsequently flagged with a number ranging from 0 to 5 (quality factor QF; 0 = unusable, 5 = excellent). The QFs, together with the source count rates and associated errors in the energy ranges 1 – 8 keV, and other relevant parameters (see the example in Appendix A), were written in the database.

In general, only spectra flagged 3-5 can be used for spectral analysis purposes. In some cases, however, it is possible to improve the quality of a spectrum with flag < 3 by going back to the original tape and performing a more complex re-extraction analysis. It is important to note that, for sources as faint as BL Lac objects, the QF shall not be the only selection criterion. In fact, the QFs rely *only* on the background subtraction, and tell us only how satisfactorily it was done. One should take into account also the significance of the signal after the background subtraction. An example is shown in Figure 2.1, where one of the available database spectra of the RBL B2 1308+32 is plotted.

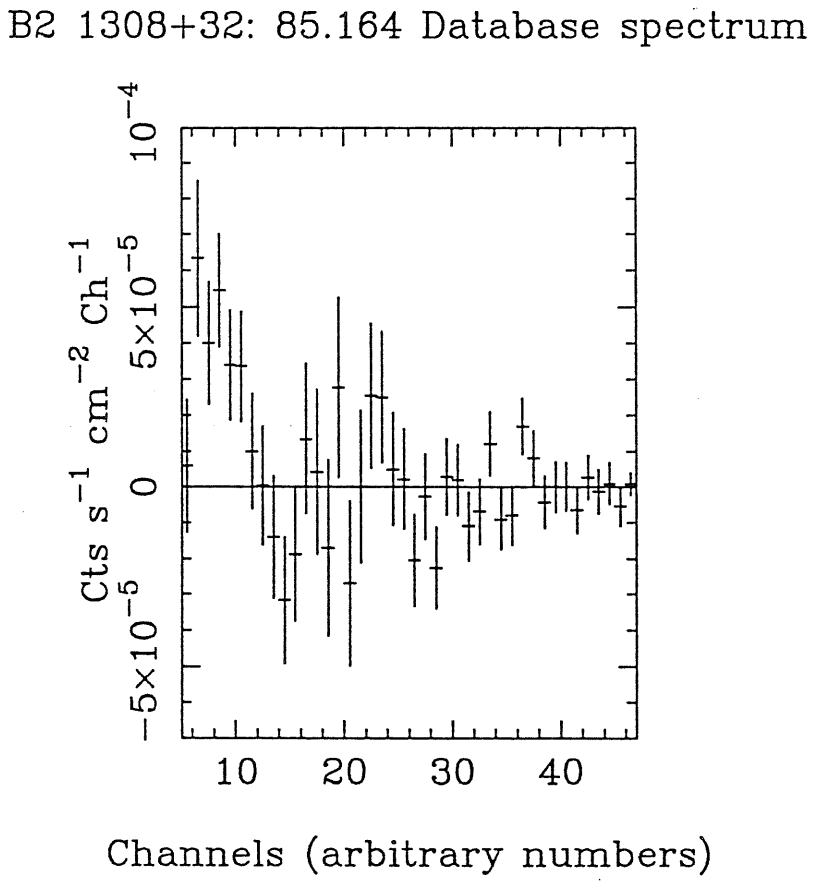

Figure 2.1: Database spectrum, rebinned at 3σ, for which QF = 3 but not suitable for spectral analysis (see text).

In the Figure, the spectrum has been rebinned, for clarity, in such a way that each new bin contains a 3σ signal. This spectrum has an acceptable QF, but it is not suitable for spectral analysis, because no significant signal is left (the count rate is 0.19 ± 0.04 cts s^{-1}; see below). Only five points significantly above zero are found in Figure 2.1, and of them only two at 3σ level. In Figure 2.2.a the 85.055 spectrum of the XBL H1426+428 (see below), having QF = 2 and signal significant at $> 5\sigma$ level, is shown. For comparison, the re-extracted spectrum is plotted in Figure 2.2.b. Only data from the detectors in which the highest signal to noise (s/n) ratio was found, have been used. The better quality of the product, which has a greater amount of signal, is evident.

In addition, a number of other elements should be carefully considered before using a spectrum, even of good quality. For example, the automatic procedure is insensitive to the presence of other (bright) sources in the field of view, which therefore can affect the target intensity, or of weak X-ray contaminating sources in the offset detectors, which result in an overestimation of the background, or of other spurious events (as the 'hot-spots'). One can infer the presence of possible contaminating sources by looking at the LE image (see below) and at the ME background light curve.

In general, to select the data we followed this procedure. For a given object and for each observing epoch, the ME count rates provided by the automatic analysis in the 1 – 8 keV energy range were considered. We discarded the observations for which the significance at which the signal was detected was less than a given threshold, which we fixed at 5σ. At first only the observations flagged ≥ 3 were taken into account. Before retrieving the spectrum from the database, a number of visual inspections has been performed. We plotted the spectrum in counts per channel to check the quality of the extracted signal, and, keeping in mind the above problems, we looked at the corresponding background

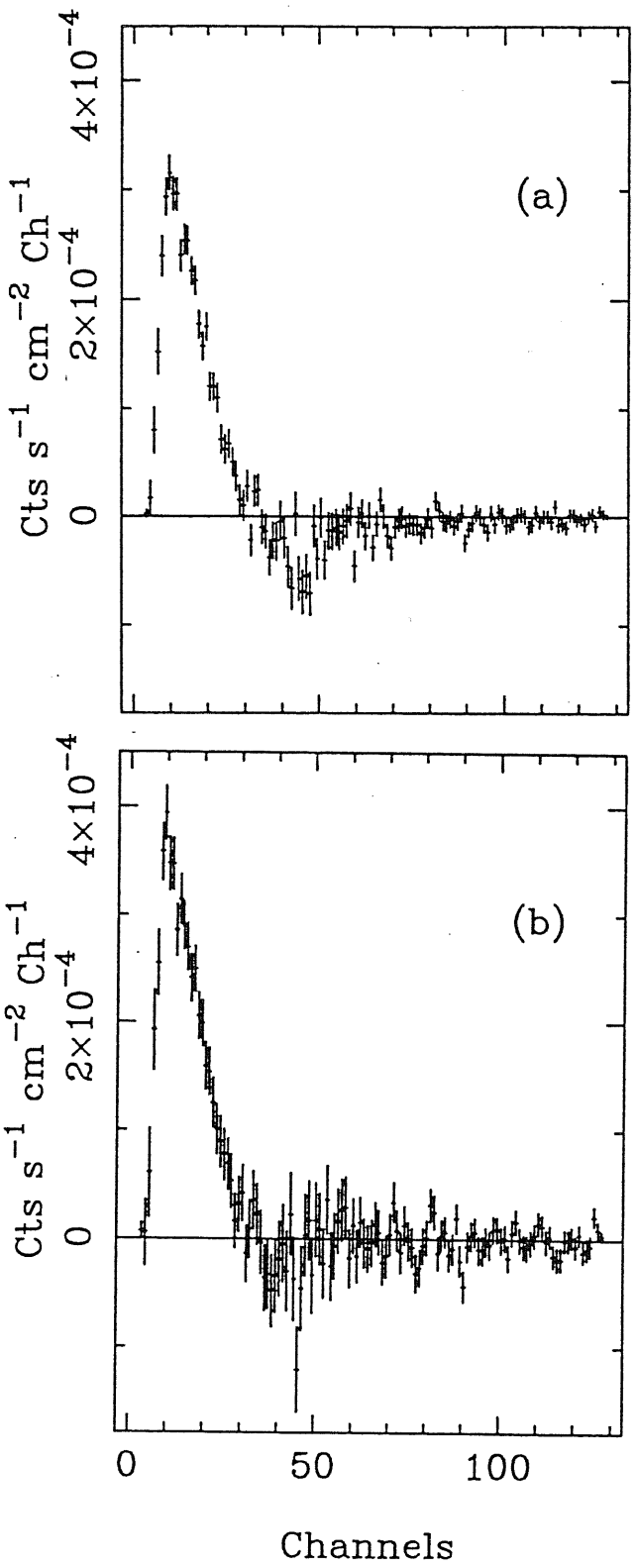

Figure 2.2: Database (a) and re-extracted (b) spectrum. The database spectrum has QF = 2. The re-extraction yielded a greater amount of signal, as is apparent comparing the two panels.

light curve and at the LE images. The observations with significance at 5σ but flagged < 3 were re-extracted, obtaining improved results. The re-extraction was performed by P. Barr using the VAX-HP software implemented at ESTEC. We are provided with a final set of data which were treated in a uniform way.

2.2 The LE data

The Low Energy (LE; de Korte *et al.* 1981) imaging telescope operated in the soft X-ray band (0.02 – 2.5 keV). A photon counting Channel Multiplier Array (CMA), without intrinsic energy resolution, was located in the focal plane. Of the five available filters interposed in the beam (offering broad-band spectral resolution), only thin Lexan (Lexan 3000Å, 3LX), Aluminum-Parylene (AP), and Boron (BO) were used for the observations reported here. The average source detection threshold is 0.002 counts s^{-1} (for a typical 10,000 s exposure and 3LX filter), corresponding to a flux of 7 $\times 10^{-13}$ ergs cm^{-2} s^{-1}.

The CMA database contains:

- images accumulated in each filter used during the observation;
- background subtracted light curves.

In the present work, only images were studied. After being accumulated, images were processed by the automatic procedure to search for point-like sources, using a sliding cell method (program DETECT; see the XIMAGE manual [Giommi & Tagliaferri 1992] for details). When a source is detected, its equatorial coordinates, count rate (in cts s^{-1}), count rate error (at 1σ), and detection probability are calculated and written in the database. An example is reported in Appendix A. In Figure 2.3 we plot the image of the LE field of view, taken with the CMA

and the 3LX filter. The target source (the X-ray selected BL Lac 1218+304) is indicated close to the center. The square box close to it indicates a CMA 'hot-spot'. Two additional serendipitous sources (Mrk 766 and ON 325) are also apparent.

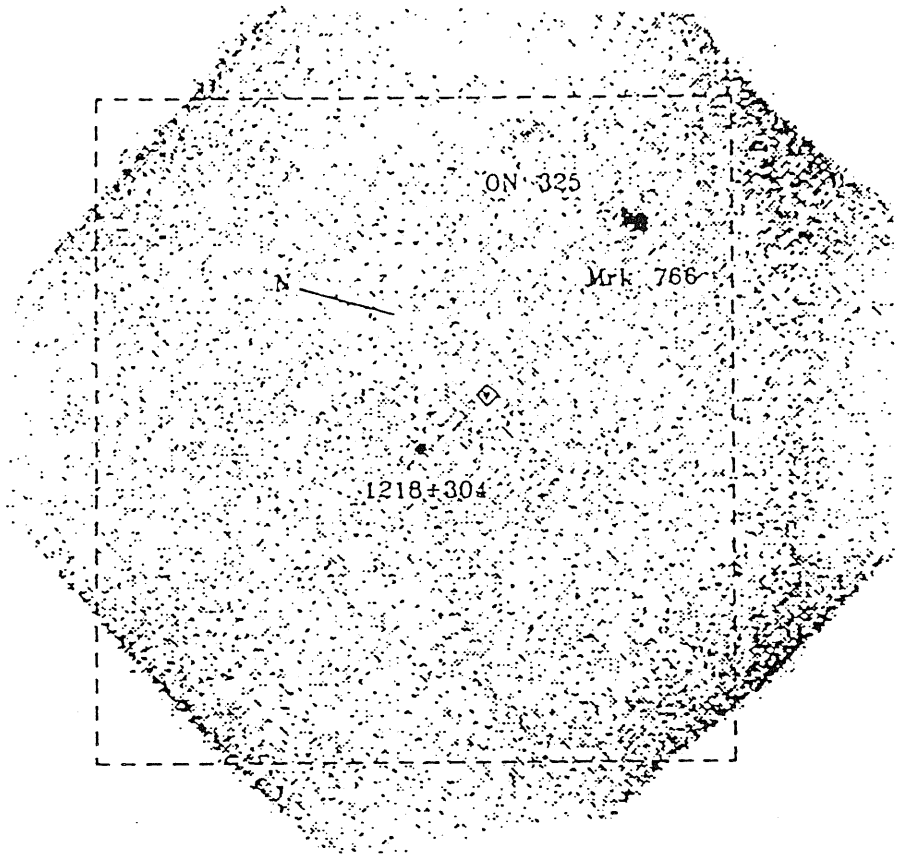

Figure 2.3: Image of 1218+304 taken with the CMA + 3Lexan filter. The diamond indicates the CMA 'hot spot'. Note the two contaminating sources Mrk 766 and ON 325, discussed in the text (from George 1988).

The image automatic analysis provides high-quality results in most cases, however some problems can arise. First of all, the program DETECT gives reliable count rates only for point-like sources, while if the source is extended its intensity can be underestimated. The program provides an error which includes both statistical and systematic effects. A more accurate determination of the count rates is given using the program SOSTA, which allows one to estimate the events both for the source and the background in user-specified boxes of size maximizing the s/n ratio. Other relevant problems are the presence in

the $2^\circ \times 2^\circ$ CMA field of view of other sources close to the target of the observation, and/or of spurious sources, such as background statistical fluctuations. In both cases the target intensity can be severely affected. Again, one can run the program SOSTA to extract a more reliable count rate.

Summarizing, for each object we retrieved for the relevant observations (see section above) the archival images in all the filters available. The source count rates were extracted in a box centered on the source position and with a size optimizing the s/n ratio using the program SOSTA, with a proper choice of the region for the background estimation. In the cases in which contaminating sources were detected close to the target source, as for example in Figure 2.3, the background was determined in two or more disjoint boxes chosen in the field of view in such a way that the spurious sources were avoided. Otherwise, the background was estimated in a rectangular corona centered on the source position, of typical radii 30 and 50 pixels (1 pixel = 4.6 arcsec).

CHAPTER III

Blazars observed by EXOSAT

3.1 The reference lists

To compile the list of blazars observed by EXOSAT, we used a number of published samples. The most relevant are briefly described in the following.

These reference lists have been grouped for clarity in four different sections. Earlier classical lists are treated in section 1, while more recent compilations from polarimetric, radio-IR, and X-ray surveys, performed to discover new objects, have been reported in sections 2, 3, and 4, respectively.

In addition to the previous lists, we also used the blazar compilations of Ghisellini *et al.* (1986) and Maraschi *et al.* (1986), which were formed using various data sets from the literature. These lists have no specific compilation criteria.

3.1.1 Earlier lists

• *Stein, O'Dell & Strittmatter (1976).*

This is the first BL Lac compilation and lists all the 32 BL Lacs known up to

1975. BL Lac were known as quasi-stellar objects with some combination of the following characteristics:

1) absence of emission lines in the core source;

2) rapid variability at radio, infrared, and optical wavelengths;

3) nonthermal continuum with the bulk of the luminosity in infrared;

4) strong and rapidly varying polarization.

• *Angel & Stockmann (1980).*

List of strongly polarized compact extragalactic objects, which are found to be the nuclei of giant ellipticals or quasi-stellar objects. Among them, the blazars are the class of 56 sources which have polarization greater than 3%.

• *Moore & Stockmann (1984).*

In order to study various properties of HPQ versus LPQ (Low Polarization Quasars), Moore & Stockmann compiled a list of 239 quasars which were selected as follows. The "bright QSO" sample includes all QSO in the Burbidge, Crown & Smith (1977) catalog with visual magnitude V $\leq$ 17 mag and declination DEC $>$ – 20°. The "spectrophotometry" sample consists of all quasars with V $<$ 18 mag for which multichannel spectrophotometry is available in the literature. Finally, the "variability" sample collects all QSO with V $<$ 18 for which any photometric variability information was published. Polarimetric data were collected from the literature for all quasars in the final sample. The criteria adopted for a QSO to be classified as an HPQ are P $>$ 3% , P / σ_P $>$ 3 (P = degree of linear polarization, σ_P = its standard deviation). The QSO are further classified as "possible" HPQ if only one measurement satisfies these criteria, and "definite" HPQ if two or more measurements satisfy these criteria. A second part of the classification is whether the first polarization measurement of the QSO satisfied the HPQ criteria, to avoid bias towards "good" candidates for additional measurements.

Because the polarization of HPQ may exhibit phases of P $< 3\%$, not all HPQ have been discovered, *i.e.*, the sample of Moore & Stockmann is not complete.

• *Ledden & O'Dell (1985).*

The primary purpose of this study is to search for correlations among the radio, optical, and X-ray properties of blazars, defined as the class of extragalactic objects showing a high (P $> 3\%$) degree of polarization. The list was compiled using those of Angel & Stockmann (1980) and Moore & Stockmann (1981, 1984), and keeping the sources (highly, optically polarized BL Lacs and quasars) for which radio, optical and X-ray data could be collected from the literature. The list contains a total of 98 sources, further classified as "possible" or "confirmed" BL Lac/HPQ.

• *Burbidge & Hewitt (1987).*

This is a list of BL Lac objects taken from the catalog of quasistellar objects and BL Lacs of Hewitt & Burbidge (1987). It contains 87 sources, classified as BL Lacs on the basis of the following criteria:

1) variability in radio, optical, or X-ray band;

2) highly compact radio source;

3) highly polarized emission;

4) no lines or very weak features in the optical spectrum.

For each object, the list provides the coordinate designation and the name, the equatorial coordinates information on the optical emission, and the redshift.

3.1.2 POLARIMETRIC SURVEYS

• *Impey & Tapia (1988).*

Impey & Tapia performed a campaign of optical polarimetry for a complete radio sample, including all sources stronger than 2 Jy at 5 GHz. The criterion for classification as a blazar was polarization greater than 2.5%. 31 new blazars were discovered, and five others were confirmed. These new observations increased the number of known polarized radio sources by 40%.

• *Impey, Lawrence & Tapia (1991).*

This paper presented new polarimetry data for 50 strong radio sources taken from the flux-density limited sample of extragalactic radio sources selected at 5 GHz by Pearson & Readhead (1981). The selection criteria were: DEC $> 35°$, galactic latitude $|b^{II}| > 10°$, and flux density at 5 GHz greater than 1.3 Jy.

In the list of Impey, Lawrence & Tapia, the highly polarized sources are those for which P $> 3\%$.

3.1.3 Radio and Infrared surveys

• *Impey and Neugebauer (1988).*

Impey & Neugebauer presented observations of 162 blazars made with the Infrared Astronomical Satellite (IRAS), and X-ray to radio wavelengths spectra for 93 objects. The list of blazars is compiled from the catalogs of Burbidge & Hewitt (1987), Ledden & O'Dell (1985), and Urry (1984). All sources should have at least two of the three primary properties of blazars:

1) strong compact radio emission;

2) optical variability;

3) high linear polarization.

There was no selection by emission-line properties. The list ranges from mini-blazars in nearby galaxies to distant luminous QSO.

• *Kühr and Schmidt (1990).*

This list provides a complete sample of RBL. Two catalogs of radio sources were used to compile the sample. The 1 Jy catalog (Kühr *et al.* 1981b) contains all the radio sources stronger than 1 Jy at 6 cm over virtually the entire sky. The S5 north polar region survey (Kühr *et al.* 1981a) contains all the sources stronger than 0.25 Jy at 6 cm. Kühr & Schmidt classified a BL Lac on the basis of the following criteria:

1) the radio spectral index $\alpha_{11-6} > -0.5$ ($F_\nu \propto \nu^{+\alpha}$);

2) DEC $> -20°$ and $|b^{II}| > 10°$;

3) V < 20 on POSS plates or deep CCD surveys;

4) no emission lines in the optical spectrum;

5) optical polarization P > 3 % and $P/\sigma_P > 3$ at least once.

A total of 43 BL Lacs are listed in the complete sample.

• *Stickel et al. (1991).*

All the BL Lacs from the 1 Jy catalog of Kühr *et al.* (1981b) are considered. The selection criteria are the first three of Kühr & Schmidt (1990), and

4) emission lines in the optical spectrum are absent or weak, with a rest-frame equivalent width < 5 Åfor the strongest line.

The resulting sample consists of 34 BL Lacs. For all but two objects the optical polarization exceeds 3%.

3.1.4 X-RAY SURVEYS

• *HEAO 1 - Schwartz et al. (1989).*

The Naval Research Laboratory's Large Area Sky Survey (LASS) instrument on board the HEAO 1 satellite produced a catalog of 842 bright, hard (1 – 10 keV)

X-ray sources over the entire celestial sphere (Wood *et al.* 1984). The sources are estimated by Wood *et al.* to be complete at 90% for fluxes $\geq 2 \times 10^{-11}$ ergs cm^{-2} s^{-1}. Schwartz *et al.* (1989) used the Scanning Modulation Collimator to identify the sources with optical counterparts. They obtained an incomplete set of 21 BL Lacs at $|b| \geq 20°$. The criteria for identifying BL Lac objects were:

1) the optical counterpart is an ultraviolet excess object as faint as 17th mag on two color (U, B) Schmidt plates;

2) it must have a featureless spectrum;

3) it must have any one of optical variability, optical polarization, radio emission.

• *EMSS – Stocke et al. (1991).*

The *Einstein* Observatory Extended Medium Sensitivity Survey (EMSS) is a flux-limited sample of faint X-ray sources discovered serendipitously in the IPC (0.3 – 3.5 keV) fields centered on targets at high galactic latitudes ($|b| \geq 20°$). The EMSS extends the *Einstein* Observatory Medium Sensitivity Survey (MSS; Maccacaro *et al.* 1982; Gioia *et al.* 1984) by using many more IPC fields and by analyzing the entire IPC image. The sensitivity threshold of the EMSS ranges from $\sim 5 \times 10^{-14}$ to $\sim 3 \times 10^{-12}$ ergs cm^{-2} s^{-1} in an area of 780 deg^2. Optical observations were taken for classification purposes for each of the 835 sources discovered. A subset of 348 sources bounded by F_X (0.3 – 3.5 keV) $\geq 5 \times 10^{-13}$ ergs cm^2 s^{-1} and declination DEC $\geq 20°$ have been virtually completely identified, some uncertainties remaining for four sources. This subset includes 22 BL Lacs, identified on the basis of the following criteria:

1) any emission line, or limit on emission line imposed by the s/n, must have equivalent width < 5 Å;

2) if CaII H and K break is present due to starlight in the host galaxy,

it must have a contrast $\leq 25\%$. [1]

• *HGLS – Giommi et al. (1991).*

In the EXOSAT High Galactic Latitude Survey (HGLS), 443 non overlapping CMA fields were examined for serendipitous sources. Only the fields with exposure greater than 2000 s, for which the pointing was at high Galactic latitude ($|b| \geq 20°$) were considered. HGLS covered an area of 783 deg^2 and included 210 sources, which defined a complete, flux-limited sample. These were identified with a program of optical and radio observations and with a cross-correlation with several catalogs of known objects. The identification was based on the coincidence (within the X-ray error circle) of the position of the X-ray source and the optical counterpart, and on the X-ray to optical flux ratio. Seven new BL Lacs were discovered serendipitously. A number of additional fields, in which the counterpart of the previously detected source was uncertain, were observed. The sources discovered were also identified with the same procedure as for the complete sample. This yielded a new BL Lac object and a candidate BL Lac.

3.2 Blazars observed by EXOSAT

[1] Here "contrast" means the relative flux depression blueward across the Ca II break, so that a normal elliptical would have a contrast of $\sim 50\%$.

3.2.1 BL LAC OBJECTS

The first list of BL Lacs observed by EXOSAT was provided by Giommi *et al.* (1990) in a paper devoted to the variability analysis of this class using the EXOSAT data. The BL Lacs reported were taken only from the Burbidge & Hewitt (1987) compilation.

We started from the Giommi *et al.* list and searched for additional BL Lacs in other compilations, described in the previous section. For each object reported in a given list, we interrogated the CMA and the ME databases, in the way which has been described in Appendix A. As a first step we were interested in all BL Lacs observed by EXOSAT at least once and in at least one experiment, to obtain a list as large as possible. The results of these searches are reported in Table 3.1.a. Column 1, 2, and 3 report the name of the object and its radio coordinates (R.A. and DEC). In column 4 the type of selection of the BL Lac is indicated (X = XBL, R = RBL), following Giommi *et al.* (1990) and Ghisellini *et al.* (1986). The acronyms in column 5 represent all the lists in which the object has been found. The objects of the EXOSAT survey are only recently discovered, and do not appear in any other list. Classification problems are present for objects like PKS 0537-441, B2 1308+326, and 3C 446 (see below), which are reported both in BL Lac and in HPQ compilations. Comments on single objects are referred to in column 6.

All the objects in Table 3.1.a were significantly detected by the LE experiment, *i.e.*, the LE count rates are > 0 within the errors. Some objects in Table 3.1.a were not significantly detected by the ME experiment.

In conclusion, Table 3.1.a provides all BL Lacs detected by the EXOSAT satellite *at least* in the LE experiment. It contains nine more objects than the Giommi *et al.* (1990) list, namely the BL Lacs of the HGLS EXOSAT survey,

1053+81, and PKS 0537-441.

Notes on particular objects in Table 3.1.a:

• *3C 66A.*

The radio source 3C 66 has two components: a flat spectrum, compact component 3C 66A, identified with a BL Lac object (Wills & Wills 1974), and the steep spectrum, radio extended component 3C 66B (Northover 1973). The field of 3C 66 was observed for the first time by the *Einstein* IPC detector, showing a complex X-ray image (Maccagni *et al.* 1983a). The EXOSAT images are much less complex than the *Einstein* ones (Maccagni *et al.* 1987). Only one source was found in the CMA fields, coincident in position with 3C 66A. The extended radio component 3C 66B is not visible, being below the detection threshold of the CMA. On the basis of the spectral information available from the previous *Einstein* observations, Maccagni *et al.* (1987) showed that the contribution of 3C 66B in the hard energy range can be neglected, and that the EXOSAT ME flux can be reasonably attributed entirely to the BL Lac.

• *EXO 0423.4-0840.*

This object was discovered in the EXOSAT HGLS as the counterpart of the HEAO 1 source 1H 0422-086. No other objects were found in the field. In the optical, it was identified with the galaxy MCG 01-12-005 (Giommi *et al.* 1991). Its optical to X-ray flux ratio is very close to the typical values found for BL Lacs. Since no strong emission lines were detected from the galaxy, and its X-ray luminosity is in excess of 10^{43} ergs s^{-1}, EXO 0423.4-0840 was classified as a BL Lac candidate. However, in the earlier HEAO 1 MC-LASS catalog (Remillard, in preparation), the source H0422-08 is designed either as or within a cluster. Edge & Stewart (1991) treat the object as a cluster.

• *EXO 0507.1-0404.*

The identification of this BL Lac is described in detail in a preliminary report

by Tagliaferri *et al.* (1989). A G8V star was observed in the CMA field, but its flux in the ME energy range was estimated to be negligible. Therefore, the hard X-rays are due to the BL Lac objects.

• *PKS 0537-441.*

PKS 0537-441 has been classified as a RBL, but it is actually a transition case between this and the HPQ classes. The ambiguity of the classification is due to the fact that, when the source is in the low state (*i.e.*, at the minimum of the light curve), a broad Mg II emission line is present which disappears when the continuum level increases (Falomo *et al.* 1989).

• *EXO0556.4-3838.*

This BL Lac was serendipitously detected in an EXOSAT CMA image and is located in the error box of H0557-385, a variable hard X-ray source. Two stars and a Seyfert 1 galaxy are also included in the error box of H0557-385. Giommi *et al.* (1989) showed that, because no significant contribution to the hard X-ray flux is expected from the stars, one of the two (or both) AGNs must be the counterpart of H0557-385. The soft X-ray flux of the BL Lac is 10 times higher than that of the Seyfert and the EXOSAT data are fully consistent with the BL Lac being the only counterpart of H0557-385. However, the authors noted that a contribution to the hard X-rays from the Seyfert galaxy can not be excluded.

• *PKS 0735+178.*

The CMA images show the presence of a serendipitous AGN $\sim$ 3 arcmin away from the BL Lac. The LE intensity of the AGN is comparable to that of PKS 0735+178, therefore its contribution to the ME flux could be relevant.

• *MS 1207.9+394.*

This object is located only $\sim$ 5 arcmin from the bright Seyfert galaxy NGC 4151. Therefore, the ME data can not be used to study MS 1207.9+394.

• *ON 325.*

In the CMA fields, two other objects are found: the Seyfert 1 galaxy Mrk 766 and the BL Lac 1218+304 (see below).

• *1218+304.*

The ME flux of this BL Lac is difficult to determine because of the proximity in the CMA images of two other sources: the BL Lac ON 325 (53 ′ away, visible in several images) and the Seyfert 1 galaxy Mrk 766, which lies 49 ′ from 1218+304 and is clearly detected in all images. An example is shown in Figure 2.3, discussed in the previous Chapter. George *et al.* (1988b), studying this field, were able to exclude a significant contribution from ON 325 to the ME flux. The Seyfert seems to contribute only $\sim$ 30% in two observations. Therefore, all the remaining ME observations could be used to study the X-ray spectrum of 1218+304.

• *B2 1308+326.*

This source is classified as a BL Lac (RBL) by some authors. In other lists, it is considered as an HPQ, because, as for PKS 0537-441, when it was in a low state, broad emission lines were detected.

• *1E 1415+255.*

This BL Lac is located $\sim$ 35 ′ from the bright source NGC 5548, which was the target of all the observations, except one. In fact, on one occasion, the pointing of the instrument was offset to avoid confusion in the ME detectors between the BL Lac and NGC 5548. This observation could be used to study 1E 1415+255.

• *3C 371.*

In the EXOSAT LE images, a second X-ray source, also seen in the IPC and identified with a K star (Worrall *et al.* 1984b), is present 20 ′ South West of 3C 371. Its contribution to the hard X-ray flux is negligible.

• *3C 446.*

It is confused in ME with PHL 5200, a radio quasar with broad absorption lines, which is located $\sim$ 22 ′ from 3C 446. Because of the occurrence of broad emission lines, the classification of 3C 446 is controversial.

3.2.2 Highly Polarized Quasars – Optically Violent Variables

For HPQ/OVV, the same selection criteria as for BL Lacs were applied. We started from published lists of blazars and checked if each reported object has at least one entry in either the LE or the ME databases. The HPQ/OVV observed by EXOSAT are listed in Table 3.1.b, structured as Table 3.1.a (we omitted here the type of selection). All objects in Table 3.1.b have been significantly detected in at least the LE experiment.

Notes on particular objects in Table 3.1.b:

• *NGC 1275.*

The nucleus of NGC 1275 has been pointed out in the past to display BL Lac properties (Veron 1978). However, in the EXOSAT images it is masked by the diffuse, bright X-ray emission of the Perseus cluster of galaxies, plus the cooling flow onto NGC 1275. Therefore, the EXOSAT data can not be used to study this active nucleus.

• *3C 273.*

This object is an intermediate case between blazars and LPQ (Valtaoja *et al.* 1990). The EXOSAT data were previously investigated by Turner *et al.* (1990).

• *Cen A.*

The radio galaxy Cen A shows a compact active nucleus. A BL Lac nature has been recently suggested (Morganti *et al.* 1992) on the basis of new radio

observations. A full report of the EXOSAT data, also involving the data from the ME Xenon detectors, has been done by Morini *et al.* (1989).

It is clear from above that Table 3.1 does not provide a statistical sample. However, for simplicity, in the following we will refer to the list of blazars observed by EXOSAT as to the "sample", without statistical meaning.

3.3 The final sample

The final sample contains all the objects for which at least one observation suitable for spectral analysis was available from the ME database or could be obtained from a re-extraction. The selection criteria rely entirely on the quality of the ME observations, as has been discussed in Chapter 2. First, we discarded the objects in Table 3.1.a and 3.1.b which were not significantly detected in the ME experiment, and the objects for which a contaminating source in the field of view was present. There are a few exceptions concerning the latter point. 1E 1415+255 was pointed at on one occasion (see above), which was therefore considered. For 1218+304, the contribution to the ME flux by the contaminating Seyfert was estimated to be relevant in only two occasions. This object was included in the final sample, and regarded as a " critical" case. Another critical source also included in the final sample is EXO 0556.4-3838, for which it is not clear if the ME flux is substantially contaminated by the Seyfert in the field (see above).

In Table 3.2.a and 3.2.b we report the log of the EXOSAT observations for all the BL Lacs and HPQ/OVV, respectively, which were selected for the spectral analysis according to the above criteria. In column 2 we report the

observing dates. In columns 3,4 and 5,6, the relevant information for the LE and ME experiments is summarized. The ME count rates (in cts s^{-1}) were obtained integrating the spectra in the channel range 4 – 34. An asterisk marks the observations which were re-extracted.

For most of the sources reported in Table 3.2.a-c, the EXOSAT data were studied in previous works by different investigators. A summary of these previous reports is provided in Table A and B (for BL Lacs and HPQ/OVV, respectively) in Appendix B. Photon indexes and absorption column densities from fits with a power law model to the LE + ME data are listed, except for 3C 66A, for which only the ME data were fitted. For the objects for which more than one observation was studied, which are indicated in Table A, the average values of the spectral parameters are given, and, where possible, the distinction between the high and the low intensity state is made. Table A is an updating of Table 2 in the review of Maraschi & Maccagni (1988). For PKS 0537-441, the results referred to in Table A were taken from the present work. They are in press, as part of a more extended project (Treves *et al.* 1992). All the objects in Table A and B were reconsidered here, for completeness. Cen A was not reconsidered, because, as we said above, the full analysis should also include the ME Xenon data, not available from the database.

Excluding EXO 0423-0840 (see above), 12 blazars are found in Table 3.2.a-c, for which the EXOSAT spectra are still unpublished. Within the criteria given above, the present work exhausts all usable material available from the EXOSAT database for blazars.

3.4 The target objects

For each object of the final sample we collected in Table 3.3.a-c the relevant references concerning the discovery (column 1), the identification (column 2), and the redshift (column 5) which is itself reported in column 4. The redshift references were mostly taken from the updated list of Veron-Cetty & Veron (1991). The EXOSAT observations for each selected object will be discussed later (see Chapter 4). Most of the sources in the final sample were also observed by other X-ray missions. These observations are summarized for each source in a separate history Table, with emphasis on the available spectral analysis results (Table 3.4.a-b). In column 1 the observing time is reported. The satellite and its operative band are indicated in columns 2 and 3. Columns 4 and 5 give the spectral parameters of a fit with an absorbed power law: the photon index α, and the absorption, parameterized in terms of the column density N_H, (in units of 10^{20} cm^{-2}). The references for the spectral analysis are listed in column 6. Other improved fits obtained with different models are referred to in the Notes (column 7). In the following for brevity the HPQ/OVV class will be shortly indicated with HPQ only.

Table 3.1.: Blazars observed by EXOSAT a) BL Lac objects

Object name	R.A. (1950) h m s	DEC (1950) ° ′ ″	Type	Lists	Notes
(1)	(2)	(3)	(4)	(5)	(6)
GC 0109+224	01 09 24.0	+22 28 44.0	R	BH,LOD1,GIO,IN,MA	
3C 66A	02 19 30.0	+42 48 30.0	R	SOS,BH,LOD1,GIO,IN,GHI	
AO 0235+164	02 35 53.0	+16 24 05.0	R	SOS,BH,STI,LOD1,GIO,IN,GHI,KS1	
4C 47.08	03 00 10.0	+47 04 34.0	R	BH,LOD1,GIO,IN	
MS0317.0+1834	03 17 00.3	+18 34 47.5	X	EMSS,BH,GIO,IN,MA	
H 0323+022	03 23 38.0	+02 14 47.0	X	BH,LOD1,HEAO,GIO,IN,GHI	
H0414+009	04 14 18.0	+00 58 53.0	X	BH,LOD2,IT,HEAO,GIO,IN,MA	
EXO 0423.4-0840	04 23 26.2	−08 40 28.0	X	HGLS	a
EXO 0507.1-0404	05 07 09.9	−04 04 20.0	X	HGLS	
PKS 0521-365	05 21 13.0	−36 30 16.0	R	SOS,BH,LOD1,GIO,IN,GHI	
PKS 0537-441	05 37 21.0	−44 06 45.0	R	STI,LOD4,IT,IN,GHI	
PKS 0548-322	05 48 50.0	−32 16 56.0	X	SOS,BH,LOD1,HEAO,GIO,IN,GHI	

Table 3.1.a (continued)

Object name	R.A. (1950) h m s	DEC (1950) ° ′ ″	Type	Lists	Notes
EXO 0556.4-3838	05 56 25.5	−38 38 39.0	X	HGLS	
EXO 0706.1+5913	07 06 07.5	+59 13 30.0	X	HGLS	
PKS 0735+178	07 35 14.0	+17 49 09.0	R	SOS,BH,STI,LOD1,GIO,IN,GHI,KS1	b
PKS 0754+100	07 54 23.0	+10 04 40.0	R	BH,LOD1,GIO,IN,GHI	
EXO 0811.2+2949	08 11 16	+29 49 31	X	HGLS	
OJ 287	08 51 57.0	+20 17 58.0	R	SOS,BH,STI,LOD1,GIO,IN,GHI,KS1	
EXO 1004.0+3509	10 04 00.1	+35 09 24.0	X	HGLS	
1053+81	10 53 39.2	+81 30 32.0	R	KS2	
MC 1057+100	10 57 44.0	+10 05 42.0	R	SOS,BH,LOD1,GIO,IN	
MKN 421	11 01 41.0	+38 28 43.0	X	SOS,BH,LOD1,HEAO,GIO,IN,GHI	
EXO 1118.0+4228	11 18 6.1	+42 28 10	X	HGLS	

Table 3.1.a (continued)

Object name	R.A. (1950) h m s	DEC (1950) ° ′ ″	Type	Lists	Notes
MKN 180	11 33 30.0	+70 25 00.0	X	BH,LOD1,HEAO,GIO,IN,GHI,KS2	
B2 1147+245	11 47 44.0	+24 34 35.0	R	BH,STI,LOD1,HEAO,GIO,IN,MA,KS1	
MS 1207.9+394	12 07 54.8	+39 45 51.5	X	EMSS,BH,GIO,IN,MA	b
ON 325	12 15 21.0	+30 23 40.0	R	SOS,BH,LOD1,GIO,IN,GHI	b
1218+304	12 18 52.0	+30 27 14.0	X	BH,LOD1,HEAO,GIO,IN	b
MS 1235.4+63	12 35 26.3	+63 15 35.3	X	EMSS,BH,GIO,IN,MA	
B2 1308+326	13 08 08.0	+32 36 40.0	R	BH,MS1,STI,LOD3,GIO,IN,GHI,KS1	E
MS 1402.3+041	14 02 19.7	+04 16 22.3	X	EMSS,BH,LOD1,GIO,IN,MA	
1E 1415.6+255	14 15 41.0	+25 57 15.0	X	BH,GIO,IT,IN	c
OQ 530	14 18 06.0	+54 36 57.0	R	BH,STI,LOD1,GIO,IN,GHI,KS1	
H 1427+42	14 26 36.0	+42 53 46.0	X	HEAO,GIO	

Table 3.1.a (continued)

Object name	R.A. (1950) h m s	DEC (1950) ° ′ ″	Type	Lists	Notes
AP LIB	15 14 45.0	−24 11 22.0	R	SOS,BH,STI,LOD1,GIO,IN,GHI	
4C 14.60	15 38 31.0	+14 57 25.0	R	BH,STI,LOD1,GIO,IN,MA,KS1	
MKN 501	16 52 12.0	+39 50 26.0	X	SOS,BH,STI,LOD1,HEAO,GIO,IN,GHI,ILT,KS1	d
H 1722+11	17 22 44.0	+11 54 52.0	X	HEAO,IN,GIO	
I ZW 186	17 27 04.0	+50 15 31.0	X	SOS,BH,LOD1,HEAO,GIO,IN,GHI	
1803+78	18 03 39.0	+78 27 54.0	R	BH,STI,LOD1,GIO,IN,MA,KS1,ILT,KS2	
3C 371	18 07 18.0	+69 48 59.0	R	BH,STI,LOD1,HEAO,GIO,IN,GHI,KS1,ILT	
EXO 1811.7+3143	18 11 43.1	+31 43 18	X	HGLS	
PKS 2005-489	20 05 47.0	−48 58 43.0	X	BH,STI,GIO,IN,GHI	
PKS 2155-304	21 55 58.0	−30 27 52.0	X	BH,LOD1,HEAO,GIO,IN,GHI	
BL LAC	22 00 39.0	+42 02 08.0	R	SOS,BH,STI,LOD1,GIO,IN,GHI,KS1,ILT	
3C 446	22 23 11.0	−05 12 17.0	R	BH,MS1,LOD3,GIO,IN,GHI	b

Table 3.1.: b) HPQ - OVV

Object name	R.A. (1950) h m s	DEC (1950) ° ′ ″	Lists	Notes
NGC 1275	03 16 29.63	+41 19 51.83	GHI,LOD1,ILT,IN	e
4C 55.17	09 54 14.30	+55 37 16.60	IN,ILT	f
TON 599	11 56 58.10	+29 31 24.00	GHI,LOD3,MS1,IN,AS	e
3C 273	12 26 33.32	+02 19 43.22	IN,	g
3C 279	12 53 35.84	−05 31 08.00	LOD3,MA,MS1,IN,AS	f
CEN A	13 22 33.00	−42 45 24.00	IN	
PKS 1510-089	15 10 08.97	−08 54 48.30	MS4,LOD4,IN	f
3C 390.3	18 45 43.00	+79 42.6	GHI,LOD3,ILT,IN,AS	e,f
PKS2208-137	22 08 42.70	−13 42 59.00	MS1,LOD3,IN,AS	f

Acronyms:

BH = Burbidge & Hewitt (1987)
AS = Angel & Stockmann (1980)
LOD1,2,3,4 = Ledden & O'Dell (1985): 1) confirmed BL Lac, 2) possible BL Lac, 3) confirmed HPQ, 4) possible HPQ
GIO = Giommi *et al.* (1990)
IN = Impey & Neugebauer (1988)
MA = Maraschi *et al.* (1986)
GHI = Ghisellini *et al.* (1986)
STI = Stickel *et al.* (1991)
KS1,2 = Kuhr & Schmidt (1990): 1) BL Lac at 1 Jy, 2) BL Lac at 0.25 Jy (see text)
EMSS = Stocke *et al.* (1991)
HEAO = Schwartz *et al.* (1989)
IT = Impey & Tapia (1988)
HGLS = Giommi *et al.* (1991)
MS1,3,4 = Moore & Stockmann (1984): 1) definite HPQ at first polarimetric measurement, 3) possible HPQ at first polarimetric measurement, 4) possible HPQ
ILT = Impey, Lawrence & Tapia (1991)
SOS = Stein, O'Dell & Strittmatter (1976)

Notes:

(a) candidate
(b) confused with another source in the field
(c) confused except in one occasion
(d) optical polarization $\sim 3\%$
(e) optical polarization $< 3\%$
(f) strongly polarized
(g) optical polarization $< 3\%$

Table 3.2.: Summary of the EXOSAT Observations a) RBL

Object	Date	LE Expo.Time (s)	LE Count Rate ($\times 10^{-3}$ cts s^{-1})	ME Expo. Time (s)	ME Count Rate[a] (cts s^{-1})
(1)	(2)	(3)	(4)	(5)	(6)
3C 66A	(*) 86.006	16172	3.8 ± 0.7 3LX	20890	0.56 ± 0.08
	(*) 86.015	20286	< 1.2 ± 0.5 3LX	36290	0.38 ± 0.09
	(*) 86.032	29468	2.5 ± 0.5 3LX	40060	0.81 ± 0.05
AO 0235+169	84.214	12938	3.0 ± 0.8 3LX	13940	0.42 ± 0.05
	86.015	10340	...[b]	15910	0.43 ± 0.09
PKS 0521-365	83.306	6040 6683	11.3 ± 1.8 3LX 6.8 ± 1.6 AP	17940	1.53 ± 0.08
	(*) 83.334	4718 4361	17.3 ± 2.4 3LX 8.3 ± 2.2 AP	9630	0.39 ± 0.06
PKS 0537-441	85.055	11688	2.6 ± 0.8 3LX	14350	0.58 ± 0.10
PKS 0754+100	(*) 84.043	13637 11755	7.1 ± 0.9 3LX 2.7 ± 0.7 AP	28540	0.39 ± 0.06
OJ 287	83.281	4812 4999	35.0 ± 3.0 3LX 18.2 ± 2.3 AP	6190	0.66 ± 0.07

Table 3.2.a (continued)

Object	Date	LE Expo.Time (s)	LE Count Rate ($\times 10^{-3}$ cts s^{-1})	ME Expo. Time (s)	ME Count Rate[a] (cts s^{-1})
(1)	(2)	(3)	(4)	(5)	(6)
	84.040	3141	47.8 ± 4.6 3LX	19000	0.81 ± 0.11
		6513	28.0 ± 2.5 AP		
		7390	2.6 ± 0.9 BO		
B2 1308+32	85.132	10523	6.7 ± 1.0 3LX	24920	0.48 ± 0.07
3C 371	(*) 84.256	25742	45.6 ± 1.6 3LX	17180	0.74 ± 0.08
		5415	25.1 ± 2.7 AP		
		7206	2.3 ± 0.9 BO		
	84.273	16512	21.9 ± 1.4 3LX	25670	0.44 ± 0.07
		5849	11.8 ± 1.8 AP		

Table 3.2: b) XBL

Object	Date	LE Expo.Time (s)	LE Count Rate ($\times 10^{-3}$ cts s^{-1})	ME Expo. Time (s)	ME Count Rate[a] (cts s^{-1})
(1)	(2)	(3)	(4)	(5)	(6)
MS 0317.0+1834	(*) 85.013	4487	8.9 ± 1.8 3LX	6320	0.74 ± 0.09
	(*) 85.039	8499	7.9 ± 1.3 3LX	18840	1.15 ± 0.08
H0323+022	(*) 84.265	3423	3.2 ± 0.4 3LX	21490	0.77 ± 0.04
		3610	2.8 ± 0.4 AP		
		11046	0.7 ± 0.1 BO		
	(*) 84.267	13218	2.8 ± 0.2 3LX	19270	1.14 ± 0.12
H0414+009	84.253	2635	3.5 ± 0.5 3LX	13820	1.94 ± 0.05
		3779	2.3 ± 0.3 AP		
		4829	1.2 ± 0.2 BO		
	84.258	4293	3.7 ± 0.4 3LX	14190	2.30 ± 0.05
		6652	2.6 ± 0.3 AP		
	(*) 84.266	2643	3.7 ± 0.5 3LX	12790	1.42 ± 0.05
		7091	2.1 ± 0.2 AP		
	84.274	3440	3.8 ± 0.4 3LX	10260	1.14 ± 0.05
		4153	2.4 ± 0.3 AP		
		2004	0.6 ± 0.2 BO		
EXO 0423.4-0840	85.048	6667	3.1 ± 1.0 3LX	7450	3.37 ± 0.14

Table 3.2.b (continued)

Object	Date	LE Expo.Time (s)	LE Count Rate ($\times 10^{-3}$ cts s^{-1})	ME Expo. Time (s)	ME Count Rate[a] (cts s^{-1})
(1)	(2)	(3)	(4)	(5)	(6)
	85.267	19482	$< 1.8 \pm 0.6$ 3LX	15100	2.73 ± 0.10
EXO 0507.1-0404	84.298	2328	16.7 ± 4.0 3LX	5998	1.71 ± 0.15
PKS 0548-322	83.306	2067	115.0 ± 7.0 3LX	12860	4.97 ± 0.10
		2153	62.0 ± 6.4 AP		
		6060	11.5 ± 2.2 BO		
	(*) 83.334	792	115.0 ± 0.2 3LX	10550	2.52 ± 0.07
		1713	59.0 ± 7.0 AP		
		4949	19.5 ± 3.0 BO		
	(*) 86.066	34721	92.0 ± 1.0 3LX	49410	3.08 ± 0.07
EXO 0556.4-3838	84.350	13699	43.0 ± 4.0 3LX	15090	4.50 ± 0.10
	86.021	25466	32.0 ± 3.0 3LX	31290	1.51 ± 0.06
Mrk 421	(*) 84.032	2976	500.0 ± 14.0 3LX	16710	1.11 ± 0.07
		8076	181.6 ± 5.4 AP		
	(*) 84.033	3084	328.4 ± 12.0 3LX	13010	0.09 ± 0.03 [c]
		2370	112.9 ± 8.1 AP		
		1471	22.8 ± 4.2 BO		

Table 3.2.b (continued)

Object	Date	LE Expo.Time (s)	LE Count Rate ($\times 10^{-3}$ cts s^{-1})	ME Expo. Time (s)	ME Count Rate[a] (cts s^{-1})
(1)	(2)	(3)	(4)	(5)	(6)
	(*) 83.035	1614	420.6 ± 18.0 3LX	14100	0.23 ± 0.03
		3995	156.2 ± 7.1 AP		
		4825	31.4 ± 3.5 BO		
	(*) 84.037	3257	482.8 ± 13.0 3LX	29380	0.58 ± 0.03
		3480	170.4 ± 7.9 AP		
		2648	32.9 ± 4.2 BO		
	84.340	1490	1082.0 ± 27.0 3LX	14340	12.30 ± 0.12
		3498	497.9 ± 13.0 AP		
		5025	126.2 ± 60.9 BO		
	84.337	1803	841.6 ± 23.0 3LX	12000	20.05 ± 0.13
		3673	362.7 ± 11.0 AP		
		4798	100.6 ± 5.6 BO		
	84.338	1995	1093.0 ± 21.0 3LX	24570	25.17 ± 0.11
		6755	469.5 ± 9.2 AP		
		10656	115.9 ± 4.3 BO		
	85.004	1125	474.3 ± 23.0 3LX	11010	3.00 ± 0.11
		1907	174.1 ± 11.0 AP		
		4835	29.2 ± 3.5 BO		

Table 3.2.b (continued)

Object	Date	LE Expo.Time (s)	LE Count Rate ($\times 10^{-3}$ cts s^{-1})	ME Expo. Time (s)	ME Count Rate[a] (cts s^{-1})
(1)	(2)	(3)	(4)	(5)	(6)
	85.112	6214	547.9 ± 10.0 3LX	19630	5.38 ± 0.09
		5105	235.4 ± 7.6 AP		
		4747	42.9 ± 3.9 BO		
	85.118	6303	499.1 ± 14.0 3LX	22650	5.41 ± 0.08
		5763	176.8 ± 6.2 AP		
		7536	35.8 ± 3.2 BO		
	85.126	6341	424.5 ± 8.6 3LX	23130	3.26 ± 0.07
		7688	173.0 ± 5.3 AP		
		8668	28.3 ± 2.5 BO		
	(*) 85.131	6391	488.1 ± 9.6 3LX	70530	3.62 ± 0.07
		6387	189.3 ± 6.1 AP		
		7088	34.1 ± 3.2 BO		
	(*) 85.132	3173	461.0 ± 9.6 3LX	5180	1.56 ± 0.08
	(*) 85.141	6279	382.2 ± 8.5 3LX	22020	3.20 ± 0.10
		5423	153.8 ± 6.0 AP		
		7735	31.4 ± 3.0 BO		
Mrk 180	84.308	3596	73.9 ± 7.6 3LX	14280	0.34 ± 0.09 [c]
		3560	30.4 ± 4.6 AP		

Table 3.2.b (continued)

Object	Date	LE Expo.Time (s)	LE Count Rate ($\times 10^{-3}$ cts s^{-1})	ME Expo. Time (s)	ME Count Rate[a] (cts s^{-1})
(1)	(2)	(3)	(4)	(5)	(6)
	(*) 84.333	3177	95.6 ± 6.0 3LX	10260	0.29 ± 0.07 [c]
		3218	45.4 ± 4.4 AP		
		8793	7.7 ± 1.5 BO		
	85.093	1332	172.5 ± 12.0 3LX	6110	1.06 ± 0.08
		3227	71.4 ± 5.4 AP		
		5297	18.3 ± 3.0 BO		
1218+304	84.356	3893	208.0 ± 8.0 3LX	12560	5.43 ± 0.13
		5081	102.0 ± 5.0 AP		
		3067	13.6 ± 2.7 BO		
	85.005	3083	203.0 ± 9.0 3LX	14450	5.24 ± 0.11
		2615	106.0 ± 8.0 AP		
		3662	24.7 ± 3.1 BO		
	85.029	4569	182.0 ± 7.0 3LX	11870	3.68 ± 0.11
		3417	101.0 ± 6.0 AP		
		1894	11.0 ± 3.1 BO		
MS 1235+63	85.079	9395	2.6 ± 0.9 3LX	39390	0.25 ± 0.05
	85.080	...[d]	...	40010	0.24 ± 0.06
1E 1402+04	(*) 85.031	17199	29.0 ± 2.0 3LX	19050	0.23 ± 0.05

Table 3.2.b (continued)

Object	Date	LE Expo.Time (s)	LE Count Rate ($\times 10^{-3}$ cts s^{-1})	ME Expo. Time (s)	ME Count Rate[a] (cts s^{-1})
(1)	(2)	(3)	(4)	(5)	(6)
	85.187	11504	13.4 ± 1.4 3LX	19740	0.44 ± 0.09
1E 1415+22	86.063	32437	4.0 ± 0.5 3LX	39330	1.40 ± 0.10
H1426+428	85.012	5741	32.7 ± 0.8 3LX	7940	4.21 ± 0.07
	(*) 85.055	3934	28.7 ± 1.2 3LX	46320	3.14 ± 0.06
		1308	11.6 ± 1.1 AP		
		6825	2.4 ± 0.2 BO		
Mrk 501	84.034	3622	421.0 ± 12.0 3LX	12040	3.99 ± 0.06
		2365	200.6 ± 11.0 AP		
		1983	50.2 ± 7.1 BO		
	(*) 84.036	4816	424.5 ± 11.0 3LX	18570	3.28 ± 0.12
		5005	190.3 ± 7.0 AP		
		4754	42.0 ± 3.8 BO		
	84.086	1781	370.0 ± 20.0 3LX	7130	4.02 ± 0.10
	(*) 84.183	1857	400.9 ± 17.0 3LX	26320	2.32 ± 0.07
		4222	164.9 ± 7.1 AP		
		4421	37.4 ± 3.9 BO		

Table 3.2.b (continued)

Object	Date	LE Expo.Time (s)	LE Count Rate ($\times 10^{-3}$ cts s^{-1})	ME Expo. Time (s)	ME Count Rate[a] (cts s^{-1})
(1)	(2)	(3)	(4)	(5)	(6)
	(*) 84.191	3230	364.4 ± 12.0 3LX	4330	1.79 ± 0.08
		2410	158.2 ± 9.2 AP		
		317	27.3 ± 4.7 BO		
	84.201	2342	351.0 ± 14.0 3LX	13320	4.92 ± 0.11
		3044	148.7 ± 8.0 AP		
		3702	25.4 ± 3.4 BO		
	(*) 84.207	1343	382.0 ± 19.0 3LX	25750	1.52 ± 0.08
		1627	182.1 ± 12.0 AP		
		6440	37.8 ± 3.4 BO		
	(*) 84.209	1638	362.0 ± 17.0 3LX	30640	2.80 ± 0.06
		3284	166.7 ± 8.1 AP		
		6158	37.8 ± 3.4 BO		
	(*) 85.099	2677	363.0 ± 13.0 3LX	30890	3.07 ± 0.08
		5862	164.5 ± 6.0 AP		
			34.0 ± 3.0 BO		
	(*) 86.074	78126	379.7 ± 2.5 3LX	87590	6.82 ± 0.04
H1722+119	85.246	5243	2.5 ± 0.3 3LX	20110	0.75 ± 0.04
		5549	1.7 ± 0.2 AP		
		5665	0.4 ± 0.1 BO		

Table 3.2.b (continued)

Object	Date	LE Expo.Time (s)	LE Count Rate ($\times 10^{-3}$ cts s^{-1})	ME Expo. Time (s)	ME Count Rate[a] (cts s^{-1})
(1)	(2)	(3)	(4)	(5)	(6)
I ZW 186	(*) 84.063	5534	61.5 ± 3.9 3LX	14390	0.15 ± 0.03
			40.5 ± 3.3 AP		
		29932	5.6 ± 0.6 BO		
	84.181	5439	80.2 ± 4.2 3LX	29030	1.29 ± 0.07
		3708	43.0 ± 4.4 AP		
		13745	6.0 ± 0.9 BO		
PKS 2005-489	84.254	3244	235.6 ± 18.0 3LX	21530	5.43 ± 0.09
		4674	249.6 ± 11.0 AP		
		10964	44.8 ± 2.7 BO		
	(*) 84.287	2643	596.2 ± 24.3 3LX	46320	6.11 ± 0.06
		2708	320.0 ± 15.3 AP		
		3662	60.0 ± 5.0 BO		
	(*) 85.145	5819	51.6 ± 3.8 3LX	20040	0.37 ± 0.08
		6053	29.3 ± 2.8 AP		
		5667	4.0 ± 1.2 BO		
	(*) 85.276	5641	61.0 ± 4.2 3LX	18300	0.47 ± 0.12
		9843	36.0 ± 2.5 AP		
	(*) 85.289	4886	150.0 ± 7.6 3LX	36800	0.48 ± 0.06
		6285	82.5 ± 4.8 AP		
		6674	10.0 ± 1.6 BO		

Table 3.2.b (continued)

Object	Date	LE Expo.Time (s)	LE Count Rate ($\times 10^{-3}$ cts s^{-1})	ME Expo. Time (s)	ME Count Rate[a] (cts s^{-1})
(1)	(2)	(3)	(4)	(5)	(6)
PKS 2155-304	(*) 84.311 A	1766	1966.0 ± 35.0 3LX	1860	5.40 ± 0.14
	B	2458	685.0 ± 18.0 AP	2580	6.62 ± 0.13
	C	7730	164.0 ± 6.0 BO	7250	16.52 ± 0.21
	D		2259.0 ± 5.0 3LX	2080	10.85 ± 0.13
	(*) 84.312 A	2106	2060.0 ± 40.0 3LX	1660	5.19 ± 0.13
	B	1731	783.0 ± 0.23 AP	2680	6.72 ± 0.11
	C	7396	207.0 ± 7.0 BO	6880	23.32 ± 0.22
	D		3190.0 ± 50.0	1820	19.86 ± 0.16
	(*) 84.316	1729	2300.0 ± 34.0 3LX	12590	14.82 ± 0.13
		655	890.0 ± 40.0 AP		
		5800	158.0 ± 7.4 BO		
	(*) 85.306	40233	1850.0 ± 7.0 3LX	49640	9.49 ± 0.06
	(*) 85.316	42535	1349.0 ± 6.0 3LX	57460	5.03 ± 0.05
	(*) 85.297	38643	3730.0 ± 10.0 3LX	50660	23.43 ± 0.08
	(*) 85.305	1414	1790.0 ± 30.0 3LX	15920	2.26 ± 0.06

Table 3.2.b (continued)

Object	Date	LE Expo.Time (s)	LE Count Rate ($\times 10^{-3}$ cts s^{-1})	ME Expo. Time (s)	ME Count Rate[a] (cts s^{-1})
(1)	(2)	(3)	(4)	(5)	(6)
	(*) 83.304	9110	763.0 ± 12.0 3LX	44830	3.97 ± 0.06
		14066	245.0 ± 6.0 AP		
		14316	45.0 ± 3.0 BO		
	(*) 83.333	122	1350.0 ± 4.0 3LX	43170	3.15 ± 0.07
		1121	468.0 ± 20.0 AP		
		4821	76.0 ± 5.0 BO		

Table 3.2.: c) HPQ

Object	Date	LE Expo.Time (s)	LE Count Rate ($\times 10^{-3}$ cts s^{-1})	ME Expo. Time (s)	ME Count Rate[a] (cts s^{-1})
(1)	(2)	(3)	(4)	(5)	(6)
Ton 599	84.151	3346	14.0 ± 3.0 3LX	13940	0.31 ± 0.09 [c]
		6335	6.2 ± 1.0 AP		
	85.136	4589	19.0 ± 3.0 3LX	13570	0.51 ± 0.10
		7407	5.8 ± 1.0 AP		
	85.127	14174	6.5 ± 1.0 3LX	15910	0.43 ± 0.09
PKS 1510-08	84.216	30582	4.1 ± 0.6 3LX	23980	1.10 ± 0.07
		31048	3.5 ± 0.6 AP		
	84.217	...[d]	...[d]	50180	1.10 ± 0.05
	85.212	31048	4.5 ± 0.7 3LX	35560	0.72 ± 0.06
3C 390.3	84.153	10799	3.0 ± 0.8 3LX	23760	0.49 ± 0.07
		12555	2.9 ± 0.7 AP		
	85.033 A	3460	16.0 ± 3.0 3LX	27610	2.72 ± 0.07
		10621	13.0 ± 2.0 AP		
		22697	4.0 ± 0.6 BO		
	85.033 B	...	...	23800	2.59 ± 0.08

Table 3.2.c: (continued)

Object	Date	LE Expo.Time (s)	LE Count Rate ($\times 10^{-3}$ cts s^{-1})	ME Expo. Time (s)	ME Count Rate[a] (cts s^{-1})
(1)	(2)	(3)	(4)	(5)	(6)
	85.311	5893	30.0 ± 3.0 3LX	3250	1.86 ± 0.09
		18315	6.4 ± 0.8 BO		
	86.076	6821	20.0 ± 2.0 3LX	26210	2.91 ± 0.06
		9599	13.0 ± 2.0 AP		
		14027	6.3 ± 0.9 BO		
	86.077	5184	18.0 ± 2.0 3LX	6440	1.24 ± 0.08
PKS 2208-137	84.146	8584	9.0 ± 2.0 3LX	3260	0.43 ± 0.09

Notes:

(a) In the channel range 4 – 34 (2 – 10 keV).
(b) Not detected in 3LX.
(c) High background in the range considered.
(d) Not detected in the 4000 Lexan filter.

(*) re-extracted spectrum (see text).

Table 3.3: The target objects.

Object	Discovery	ID	z	Refs. z
(1)	(2)	(3)	(4)	
		a) RBL		
3C 66A	1,2	1,2	0.444	3
AO 0235+164	4	5	0.852	6
PKS 0521-365	7	8	0.055	9
PKS 0537-441	10	11	0.894	12
PKS 0754+100	13	13,14	...	...
OJ 287	15	16	0.306	17
B2 1308+32	8	8	0.996	17
3C 371	18, 19	18,19	0.050	20
		b) XBL		
MS 0317.0+1834	21	21	0.190	21
H0323+022	22,23	24	0.147	25
H0414+009	26	26	0.287	27
EXO 0423.4-0840	28	28	0.039	28
EXO 0507.1-0404	28	28	0.304	28
PKS 0548-322	29	30, 31	0.069	32
EXO 0556.4-3838	28	28	...	...
Mrk 421	33	34	0.031	34
Mrk 180	35	35	0.046	35
1218+304	36, 37	37	0.130g	38
MS 1235+63	21	21	0.297	21

Table 3.3 (continued)

Object	Discovery	ID	z	Refs. z
(1)	(2)	(3)	(4)	
1E 1402+04	21	21	0.210	21
1E 1415+22	39	39	0.237g	39
H1426+428	40	40	0.129g	40
Mrk 501	23	24	0.034	24
H1722+119	41, 42	41, 42	...	...
I Zw 187	43	30	0.055	44
PKS 2005-489	45	46	0.071	47
PKS 2155-304	48	48	0.117a	49
		c) HPQ		
Ton 599	50	50, 51	0.729	52
PKS 1510-08	53	54, 55	0.361	56
3C 390.3	57, 58	59	52	
PKS 2208-137	60	60	0.392	52

References: (1) Wills & Wills (1974); (2) Butcher *et al.* (1976); (3) Burbidge & Hewitt (1987); (4) Argue *et al.* (1973); (5) Spinrad & Smith (1975); (6) Rieke *et al.* (1976); (7) Bolton *et al.* (1965); (8) Angel & Stockmann (1980); (9) Searle & Bolton (1968); (10) Peterson & Bolton (1972); (11) Maraschi *et al.* (1985); (12) Peterson *et al.* (1976); (13) Tapia *et al.* (1977); (14) Worrall *et al.* (1984a); (15) Blake (1970); (16) Altschuler & Wardle (1975); (17) Miller *et al.* (1978); (18) Miller (1975); (19) Worrall *et al.* (1984b); (20) Sandage (1973); (21) Stocke *et al.* (1985); (22) Doxsey *et al.* (1983); (23) Piccinotti *et al.* (1982); (24) Feigelson *et al.* (1986); (25) Filippenko *et al.* (1986); (26) Ulmer *et al.* (1983); (27) Halpern *et al.* (1991); (28) Giommi *et al.* (1991); (29) Shimmins & Bolton (1974); (30) Stein *et al.* (1976); (31) Mushotzky *et al.* (1978); (32) Fosbury & Disney (1976); (33) Colla *et al.* (1972); (34) Ulrich *et al.* (1975); (35) Ulrich (1978); (36) Cooke *et al.* (1978); (37) Wilson *et al.* (1979); (38) Schwartz *et al.* (1979); (39) Halpern *et al.* (1986); (40) Remillard *et al.* (1989); (41) Griffiths *et al.* (1989); (42) Brissenden *et al.* (1990); (43) Zwicky (1966); (44) Oke (1978); (45) Wall *et al.* (1975); (46) Wall *et al.* (1986); (47) Falomo *et al.* (1987); (48) Griffiths *et al.* (1979); (49) Bowyer *et al.* (1984); (50) Wills (1966); (51) Burbidge (1968); (52) Angel & Stockmann (1980); (53) Bolton & Ekers (1966); (54) Appenzeller & Hiltner (1967); (55) Liller & Liller (1975); (56) Burbidge & Kinman (1966); (57) Burbidge & Burbidge (1971); (58) Penston & Penston (1973); (59) Ledden & O'Dell (1985); (60) Moore & Stockmann (1981).

Table 3.4. History Table: a) RBL

Object	Date	Experiment	Energy Range (keV)	Photon Index	N_H ($\times 10^{20}$ cm^{-2})	Refs.	Notes
(1)	(2)	(3)	(4)	(5)	(6)	(7)	(8)
3C 66A	1979 Jul-Aug	*Einstein* IPC+MPC	0.2-10	3.10 ± 0.60	< 35.0	1	
	1979 Aug	*Einstein* IPC	0.2-4.0	5.20 ± 0.30	~ 10.0	1	a
AO 0235 +164	···	*Einstein* IPC	0.2-4.0	$2.20^{+1.10}_{-1.66}$	$88.0^{+150}_{-60.0}$	2	
PKS 0521-365	1979.279	*Einstein* IPC	0.2-4.0	$1.60^{+0.80}_{-0.40}$	~ 3.2	2	
PKS 0537-441	1980 Apr-Sep	*Einstein* IPC	0.2-4.0	1.55 ± 0.40	···	3	b
	1991 Apr	ROSAT PSPC	0.1-2.4	2.10 ± 0.40	3.0 ± 1.0	4	
OJ 287	1979 Oct	*Einstein* IPC	0.2-4.0	$2.60^{+1.00}_{-0.40}$	$5.0^{+5.0}_{-2.5}$	1	
	1980 Apr	*Einstein* IPC	0.2-4.0	3.40 ± 1.00	$6.3^{+6.3}_{-4.3}$	1	
	1980 May 14	*Einstein* IPC	0.2-4.0	2.17 ± 0.23	$1.5^{+1.1}_{-0.7}$	1	
	1980 May 15	*Einstein* IPC	0.2-4.0	2.00 ± 0.30	$1.0^{+1.5}_{-0.9}$	1	
	1980 May 16	*Einstein* IPC	0.2-4.0	$3.20^{+2.20}_{-0.60}$	$7.9^{+7.9}_{-3.9}$	1	
3C 371	1990 Aug-Sep	ROSAT PSPC	0.1-2.4	2.66 ± 0.09	···	5	b,c

Table 3.4. History Table: b) XBL

Object	Date	Experiment	Energy Range (keV)	Photon Index	N_H ($\times 10^{20}$ cm^{-2})	Refs.	Notes
(1)	(2)	(3)	(4)	(5)	(6)	(7)	(8)
H0323+022	1981 Feb	*Einstein* IPC	0.2-4	~ 2.4	$14.0^{+7.0}_{-5.0}$	6	
		Einstein MPC	1.2-10	~ 2.8	...	6	b
	...	GINGA LAC	2-38	2.90 ± 0.20	...	7	b
	...	GINGA LAC	2-38	2.10 ± 0.10	...	7	b
H0414+009	1980	*Einstein* IPC+MPC	0.2-10	2.6 ± 0.5	$35.0^{+18.0}_{-14.0}$	8	d
PKS 0548-322	1977 Sep	HEAO 1 LED	0.15-2.0	3.20 ± 0.40	$2.5^{+1.3}_{-0.8}$	9	e
		HEAO 1 MED	2-10	1.30 ± 0.40	...	9	
	1978 Mar	HEAO 1 MED	2-10	$5.00^{+3.00}_{-1.50}$	...	10	
	1978 Sep	HEAO 1 MED	2-10	2.80 ± 0.70	< 320	10	
	1979 Feb	*Einstein* MPC	1.2-10	2.10 ± 0.20	< 50	1	
		Einstein IPC	0.2-4.0	~ 2.10	< 4.5	1	f
	1979 Mar	*Einstein* SSS	0.6-4.5	1.60 ± 0.70	$11.0^{+8.0}_{-6.0}$	11	

Table 3.4.b (continued)

Object	Date	Experiment	Energy Range (keV)	Photon Index	N_H ($\times 10^{20}$ cm^{-2})	Refs.	Notes
(1)	(2)	(3)	(4)	(5)	(6)	(7)	(8)
		Einstein MPC	1.2-10	1.90 ± 0.20	< 40	2	
	1979 Mar	*Einstein* IPC+MPC	0.2-10	~ 2.10	< 4.4	1	
	1979 Apr	*Einstein* SSS	0.6-4.5	$1.84^{+0.66}_{-0.24}$	$14.0^{+8.0}_{-6.0}$	11,12	d
		Einstein MPC	1.2-10	2.30 ± 0.30	< 60	2	
PKS 0538-322	1979 Aug	*Einstein* MPC	1.2-10	$2.30^{+1.00}_{-0.50}$	< 100	13	
	1980 Mar	*Einstein* IPC+MPC	0.2-10	~ 2.10	< 4.8	1	
Mrk 421	1976 Apr	SAS 3 LE	0.15-0.8	2.10 ± 0.40	< 3.0	14	
	1977 May 18-20	OSO 8	2-30	0.90 ± 0.50	< 8.0	15	g
	1977 Nov	HEAO 1 LED+MED	0.15-10	$3.50^{+1.70}_{-1.30}$	$2.0^{+3.0}_{-1.0}$	16	
	1978 May	HEAO 1 SMC	2-6	3.00 ± 1.00	...	17	
		HEAO 1 MED+HED	2-60	$3.90^{+1.30}_{-0.70}$	< 70	18	
	1978 Dec	HEAO LED	0.15-2.0	2.70 ± 0.40	1.0 ± 0.6	16	

Table 3.4.b (continued)

Object	Date	Experiment	Energy Range (keV)	Photon Index	N_H ($\times 10^{20}$ cm^{-2})	Refs.	Notes
(1)	(2)	(3)	(4)	(5)	(6)	(7)	(8)
	1978 Dec	*Einstein* SSS	0.6-4.5	$3.30^{+1.30}_{-1.00}$	$26.0^{+16.0}_{-12.0}$	11	
		Einstein MPC	1.2-10	$2.80^{+0.60}_{-0.40}$	< 100	2	
	1979 May	*Einstein* SSS	0.6-4.5	$1.30^{+0.80}_{-0.50}$	$6.0^{+8.0}_{-6.0}$	11,12	h
		Einstein MPC	1.2-10	$1.10^{+1.30}_{-0.60}$	< 250	2	
	1980 Jan-Feb	*Ariel 6*	1-10	$2.90^{+0.90}_{-0.40}$	< 3.0	19	i
	1980 May	*Einstein* IPC	0.2-4.0	2.31 ± 0.18	···	20	
	1984 Jan	TENMA	1.5-10	2.1 ± 0.2	···	21	g
			4-10	2.6 ± 0.1	···	21	g
	1984 Mar	TENMA	1.5-10	2.8 ± 0.3	···	21	g
Mrk 421	1984 Mar	TENMA	4-10	2.7 ± 0.2	···	21	g
	1990 Nov	ROSAT PSPC	0.1-2.4	2.41 ± 0.08	1.7 ± 2.0	22	
Mrk 180	1979 Nov	*Einstein* IPC	0.2-4.0	2.30 ± 0.30	$2.5^{+0.7}_{-0.5}$	23	j

Table 3.4.b (continued)

Object	Date	Experiment	Energy Range (keV)	Photon Index	N_H ($\times 10^{20}$ cm^{-2})	Refs.	Notes
(1)	(2)	(3)	(4)	(5)	(6)	(7)	(8)
		Einstein MPC	1.2-10	3.90 ± 0.80	$158.5^{+157.7}_{-118.5}$	23	
	1980 Dec	*Einstein* IPC	0.2-4.0	$1.70^{+1.00}_{-0.20}$	$0.4^{+0.6}_{-0.4}$	23	
1218+304	1977 Dec	HEAO 1 MED	2-10	2.10 ± 0.90	...	10	
	1978 May	HEAO 1 SMC	2-6	1.50 ± 0.50	< 300	17	
		HEAO 1 MED	2-10	2.10 ± 0.20	< 86.0	10	
	1978 Dec	*Einstein* SSS	0.6-4.5	$1.40^{+2.00}_{-0.50}$	< 16.0	11	
		Einstein MPC	1.2-10	$2.40^{+0.90}_{-0.30}$	< 100	2	
	1978 Dec	HEAO 1 MED	2-10	$4.00^{+1.80}_{-0.90}$	...	10	
	1979 Jun	*Einstein* SSS	0.6-4.5	3.60 ± 0.50	~ 17.0	11	d
		Einstein MPC	1.2-10	$2.80^{+0.60}_{-0.20}$	< 60	2	
H1426+428	1990	ROSAT PSPC	0.1-2.4	2.10 ± 0.10	...	24	k
Mrk 501	1975 Mar	*Ariel 5*	2.0-10	1.8 ± 0.5	< 50	25	

Table 3.4.b (continued)

Object	Date	Experiment	Energy Range (keV)	Photon Index	N_H ($\times 10^{20}$ cm^{-2})	Refs.	Notes
(1)	(2)	(3)	(4)	(5)	(6)	(7)	(8)
	1977 Aug	HEAO 1 LED	0.15-2.0	3.4 ± 0.4	1.2 ± 0.5	16	
		HEAO 1 MED+HED	2-60	1.2 ± 0.4	< 180	15	
Mrk 501	1978 Sep	HEAO 1 MED	2-10	$2.50^{+0.50}_{-0.30}$	< 45.7	26	
	1979 Jan	*Einstein* SSS	0.6-4.5	$2.20^{+0.70}_{-0.50}$	$20.0^{+8.1}_{-6.0}$	27	
		Einstein MPC	1.2-10	2.50 ± 0.40	< 100	2	
	1979 Mar	*Einstein* SSS	0.6-4.5	$1.70^{+0.60}_{-0.20}$	$12.0^{+5.0}_{-3.0}$	27	
		Einstein MPC	1.2-10	2.50 ± 0.2	< 60	2	
	1979 Aug	*Einstein* SSS	0.6-4.5	2.60 ± 0.15	18.0 ± 2.0	27	l
		Einstein MPC	1.2-10	2.6 ± 0.2	< 40	2	
	1980 Jan	*Einstein* IPC	0.2-4.0	2.4 ± 0.2	$3.2^{+1.8}_{-1.2}$	23	d
		Einstein MPC	1.2-10	2.5 ± 0.2	$10.0^{+30.0}_{-7.5}$	23	
	1980 Aug	*Einstein* IPC	0.2-4.0	$1.80^{+0.50}_{-0.20}$	$2.0\ ^{+2.0}_{-1.0}$	23	

Table 3.4.b (continued)

Object	Date	Experiment	Energy Range (keV)	Photon Index	N_H ($\times 10^{20}$ cm^{-2})	Refs.	Notes
(1)	(2)	(3)	(4)	(5)	(6)	(7)	(8)
		Einstein MPC	1.2-10	2.7 ± 0.2	$20.0^{+12.0}_{-16.8}$	23	
	1991 Aug	ROSAT PSPC	0.1-2.4	2.41 ± 0.08	1.6 ± 0.4	22	
H1722+119	1979 Feb	*Einstein* MPC	1.2-10	2.70 ± 0.70	...	28	
I Zw 187	1977 Aug-Sep	HEAO 1 MED	2-10	$2.30^{+0.60}_{-0.40}$	...	29	
	1992	ROSAT PSPC	0.2-2.4	2.09 ± 0.15	...	24	
PKS 2155-304	1977 Nov	HEAO 1 LED	0.15-2.0	2.40 ± 0.30	2.0 ± 1.0	30	
	1977 Nov	HEAO 1 MED+HED	2-60	$2.50^{+1.70}_{-0.7}$	< 1500	31	
	1978 Nov	HEAO 1 SMC	2-6	2.00 ± 0.60	...	32	m
		HEAO 1 MED+HED	2-60	$3.00^{+2.00}_{-0.60}$	< 100	31	
	1979 May	*Einstein* SSS	0.6-4.5	2.50 ± 0.30	15.0 ± 3.0	11	
		Einstein MPC	1.2-10	2.90 ± 0.20	< 25.0	2	
	1979 May	*Einstein* SSS	0.6-4.5	2.60 ± 0.10	13.0 ± 2.0	11	

Table 3.4.b (continued)

Object	Date	Experiment	Energy Range (keV)	Photon Index	N_H ($\times 10^{20}$ cm^{-2})	Refs.	Notes
(1)	(2)	(3)	(4)	(5)	(6)	(7)	(8)
		Einstein MPC	1.2 -10	2.90 ± 0.20	< 40	2	
	1979 Oct-Nov	*Einstein* MPC	1.2-10	$3.10^{+1.00}_{-0.40}$	< 100	13	
	1979 Nov	*Einstein* IPC	0.2-4.0	$2.15^{+0.16}_{-0.13}$	···	20	
	1980 May	*Einstein* IPC	0.2-4.0	$2.61^{+0.17}_{-0.19}$	···	20	
	1980 May	*Einstein* OGS	0.4-1.5	$6.00^{+0.20}_{-0.40}$	≤ 4.0	33	n
	1983 Oct	TENMA	1.5-10	2.11 ± 0.19	< 2.0	34	
	1987 May	GINGA LAC	2-9.8	2.74 ± 0.05	< 30	35	o
			9.8-38	2.61 ± 0.24	···	35	b
	1987 May	GINGA LAC	2-9.8	2.84 ± 0.05	< 30	35	o,p
			9.8-38	2.40 ± 0.40	···	35	b

Notes to Table 3.4

a= IPC flux 30% fainter than in the previous observation; no detection in the MPC
b= N_H fixed at the Galactic value
c= absorption edge at 0.6 keV
d= data consistent with a 0.6 keV absorption edge
e= combined LED-MED spectrum is best fitted by a two power law photon spectrum with $E_0 \sim 2$ keV
f= Worral and Wilkes give $\alpha = 1.69 \pm 0.12$
g= soft excess below 3.2 keV
h= concave up continuum ($\alpha_1 = 3.51^{+0.40}_{-0.49}$, $\alpha_2 = 1.41^{+0.16}_{-0.17}$, $E_0 \sim 1.4$) + absorption edge at 0.6 keV
i= Two component: $\alpha_1 = 3.4 \pm 0.4$, $\alpha_2 = 1.0 \pm 0.1$,E_0=3 keV
j= Worrak and Wilkes 1990 report a photon index = $1.97^{+0.16}_{-0.18}$
k= BBXRT data available (see Chapter 4)
l= Worral and Wilkes 1990 report a photon index = $2.09^{+0.18}_{-0.16}$
m= Soft excess in the lowest SMC channels
n= Two-component model fitted to tha data, with the higher energy index fixed (2.9, from MPC data)
o= No significant Fe emission line (E.W. < 50 eV) nor Fe K absorption edge ($N_H < 2 \times 10^{17}$ cm^{-2}) was observed
p= Other GINGA observations (Sembay *et al.* 1992) require a broken power law with break at ~ 4 keV

References to Table 3.4:

1 = Maccagni *et al.* (1983b); 2 = Madejski (1985); 3 = Maraschi *et al.* (1985); 4 = Treves *et al.* (1992);
5 = Fink *et al.* (1992a); 6 = Feigelson *et al.* (1986); 7 = Ohashi (1989); 8 = Halpern *et al.* (1990);
9 = Riegler *et al.* (1979); 10 = Worral *et al.* (1981); 11 = Urry *et al.* (1986); 12 = Madejski *et al.* (1991a);
13 = Agrawal *et al.* (1983); 14 = Hearn *et al.* (1979); 15 = Mushotzky *et al.* (1978); 16 = Singh & Garmire (1985);
17 = Schwartz *et al.* (1979); 18 = Mushotzky *et al.* (1979); 19 = Hall *et al.* (1981); 20 = Worral & Wilkes (1990);
21 = Makino *et al.* (1987); 22 = Fink *et al.* (1991); 23 = Mufson *et al.* (1984); 24 = Fink *et al.* (1992b);
25 = Snijders *et al.* (1979); 26 = Kondo *et al.* (1981); 27 = Urry (1984); 28 = Brissenden *et al.* (1990);
29 = Weistrop *et al.* (1981); 30 = Agrawal & Riegler (1979); 31 = Urry & Mushotzky (1982); 32 = Griffiths *et al.* (1979);
33 = Canizares & Kruper (1984); 34 = Miyoshi *et al.* (1986); 35 = Ohashi *et al.* (1989).

CHAPTER IV

Spectral analysis and results

4.1 The X-ray spectral analysis

In general, the ME spectra described in Chapter 2 (in cts s^{-1}) are the result of the convolution of the incident (or photon) spectra with the detector response. This is expressed by means of a matrix, in which each element is the probability that a photon of given energy is detected in a given channel, multiplied by numerical factors (detector resolution, efficiency, gain). However, it is not possible to obtain the photon spectrum with a simple deconvolution (Blisset & Cruise 1979; Kahn & Blisset 1979). It is more convenient to convert a chosen spectral slope, using the device characteristics, into something directly comparable to the observed data. In practice, assuming a incident spectrum ($\frac{dN}{dE}$ in ph cm^{-2} s^{-1} keV^{-1}), dependent on a number of free parameters, we calculate

$$f(E_i) = \int_{E_i}^{E_{i+1}} \frac{dN}{dE} R(E) dE \qquad i = 0, N,$$

where R(E) is the response matrix, and E_i, E_{i+1} the energy boundaries of the N-th energy bin. The function $f(E_i)$ is therefore compared to the observed spectrum through a fit (Bevington 1969). The best - fit parameters are determined through the χ^2 minimization technique (Lampton *et al.* 1976), where

$$\chi^2 = \sum_{i=1}^{N} \frac{(y_i - f(E_i))^2}{{\sigma_i}^2},$$

and $y_i \pm \sigma_i$ is the experimental value. Usually, the reduced minimum χ^2 is given, *i.e.*, the minimum χ^2 divided by the degrees of freedom (d.o.f., N – number of fitted parameters). In general, for an acceptable fit, the reduced $\chi^2_{min} = 1$.

It is important to note that in the method above there need not be a unique solution. Different models are found to provide acceptable fits to the same data sets. A number of tests can be performed to check the statistical significance of the different fits, for example the F-test (Bevington 1969).

4.2 Spectral analysis of the EXOSAT data

4.2.1 Fit with the power law model

The spectral analysis of the EXOSAT data was performed using the XSPEC fitting program (Shafer *et al.* 1991). A number of trial models, folded with the instrumental responses, were compared to the data in the way described above. Besides the ME spectra, we also considered the overall LE + ME energy distributions, obtained by adding the LE data points from the various filters to the ME spectra. Both distributions have been first studied using an absorbed power law of the form

$$\frac{dN}{dE} = N \times \exp(-N_H \sigma(E)) \times E^{-\alpha},$$

where N is the normalization and α the photon index. The term $exp(-N_H\sigma(E))$ takes into account the effects of photoelectric absorption by cold gas, between the source and us, on the incoming X-ray photons. This absorption term is parameterized with the column density of atomic hydrogen along the line of sight, N_H (in cm^{-2}). In general, blazars are expected not to have large amounts of intrinsic absorption and this parameter is usually fixed to the Galactic value, *i.e.*, the absorption is totally attributed to the interstellar matter along the line of sight. Carbon, oxygen, and helium primarily contribute to the absorption cross section $\sigma(E)$ in the energy range of interest here. In this analysis, the absorption cross section of Morrison & McCammon (1983) is assumed. It is important to note that $\sigma(E)$ decreases roughly with the cube of the energy, therefore the low energy X-ray data are much more affected by absorption than are the high energy ones.

Two models have been used in the present analysis. In model (a) N_H has been fixed to the Galactic value; in model (b) N_H has been allowed to vary. In Table 4.1.a and 4.1.b we list the results from the fits to the ME data with model (a) and to the LE + ME data with both models (a) and (b), for RBL and XBL, respectively. Results for HPQ – OVV are reported in Table 4.1.c. Only the interesting parameters (α and N_H) are reported, together with the reduced χ^2 per d.o.f. The errors quoted in Table 4.1.a-c for the spectral parameters are 90% confidence limits for model (a), and 68% for model (b). The Galactic values for N_H, also listed in Table 4.1.a-c, are taken from the SAO EINLINE database, which interpolates the values in the HI map of the Galaxy (Stark *et al.* 1992). Errors on the quoted Galactic absorbing columns are typically on the order of $\sim 10^{19}$ cm^{-2} (Elvis *et al.* 1989). Columns 3 and 4 of Table 4.1.a-c give the fluxes in the LE (3LX filter) and in the 2 – 6 keV energy range, corrected for absorption. The LE fluxes were calculated assuming a power law with photon index 2.0 and

absorption fixed at the Galactic value. The ME fluxes were calculated using the best fit values for the slope and the absorption in columns 9 and 10, respectively.

For each object, we show the most representative spectrum or spectra, deconvolved with model (b) above, in Appendix C. For simplicity, in Table 4.2.a-c we report only the values of the photon indexes from the fits with model (a) to the ME and to the LE + ME data.

4.2.2 Fit with the broken power law model

In some individual observations we found that the fit with a simple power law was not acceptable because the reduced χ^2 is high, and, in addition, the corresponding residuals are rather poor (see below). Since in the literature a two component X-ray continuum has often been claimed for BL Lacs (see Introduction), we fit these data with a broken power law model.

In other cases we found that, even if the power law was formally acceptable, evidence was present for curvature at lower energies. This was inferred by comparing the photon indexes derived from the fits to the ME and to the LE + ME data with model (a). If two components are present one might expect that the LE data points do not lie on the extrapolation of the ME slope, being below for a convex down spectrum and above for a concave up spectrum. In addition, one might also expect that the fit to the overall spectrum with N_H free would converge towards an absorbing column greater or less than the Galactic one, as a compensation for the downward or upward curvature of the spectrum, respectively. These observations were also reanalyzed with a broken power law model.

We used an absorbed broken power law of the form (neglecting the normaliza-

tion)

$$\frac{dN}{dE} \propto \begin{cases} exp(-N_H\sigma(E)) \times E^{-\alpha_1} & \text{if } E \leq E_0 \\ E^{-\alpha_2} & \text{if } E \geq E_0, \end{cases}$$

where α_1 and α_2 are the photon indexes below and above the break energy E_0, respectively. Because of the limited statistics of our data we fitted the spectra by fixing N_H and the E_0 and allowing only three parameters to vary (α_1, α_2, and the normalization). We repeated the fit, varying E_0 in the range permitted by the data coverage. We checked the statistical significance of the broken power law, with respect to a single power law, using the F-test (Bevington 1969), which gives the probability that adding two free parameters (a spectral index and the break point) should significantly improve the fit. The results of the fits with the broken power law are listed in Table 4.3.a-c.

The results reported in Table 4.1.a-c and 4.3.a-c are discussed separately for each source in the following sections. In addition, they are compared with the results obtained from the previous X-ray missions, summarized in the Tables 3.4.a-b.

The results of the spectral analysis for four XBL of the HEAO-1 survey (H 0323+022, 0414+009, 1426+428, and 1722+119) have recently been submitted to *The Astrophysical Journal* (Sambruna *et al.* 1992).

4.3 Results for individual objects: RBL

4.3.1 3C 66A

3C 66A was observed by EXOSAT on three occasions. An important point must be discussed before describing the ME data reduction. As we saw in Chapter 3, the extended radio component 3C 66B was not visible in the LE images. However, its contribution to the ME flux can not be excluded *a priori*. To decide if the ME flux of 3C 66A was contaminated by the extended component, we relied on the information about the X-ray energy distribution of 3C 66B available from the previous *Einstein* observations (Maccagni *et al.* 1983b). On one occasion, the BL Lac was found by the *Einstein* IPC in a low state, but with a flux still higher than the extended component (Maccagni *et al.* 1983b). No flux was detected in the simultaneous MPC (1.2 – 10 keV) observations. This indicates that 3C 66B is likely not to have a flat X-ray spectrum, and we can reasonably attribute the EXOSAT ME flux to the BL Lac.

In all observations the signal in the ME band was detected with a significance $\geq 5\sigma$. The background monitoring was complicated by the fact that not all the detectors were on. This affected the quality of the resulting spectra, which were all re-extracted. The LE and ME count rates are reported in Table 3.2.a. It is interesting to note that, when the source intensity is higher in the LE band, it is lower in the ME one. It is the first time that this behavior has been observed. In the previous *Einstein* observations, in fact, the flux decreases simultaneously in the soft and in the hard energy bands, although much faster in the latter (Maccagni *et al.* 1983b).

The ME signal was detected in a rather restricted energy range (2 – 5 keV). We fitted the spectra with models (a) and (b) above, with the results reported in Table 4.1.a. The results obtained for the 86.015 observing epoch must be considered with caution because of the fading of the source in the soft

energy range (only a 3σ upper limit on the LE intensity could be given, Table 3.2.a). In general, we obtained satisfactory χ^2's only in the case of the ME data (column 6) and LE + ME data with N_H free (column 11). In these fits, the slope of the power law is variable, and there is an indication for a flattening in the high (ME) state. In addition, one can see that the spectral indexes in column 7 are flatter than those in column 5, and the absorption in column 10 is in excess to the Galactic value. As discussed above, this may suggest the presence of curvature with a break at lower energies. A fit with the broken power law model was performed in the way described above, with the results reported in Table 4.3.a. The improvement with respect to a simple power law model is significant in the 86.015 and 86.032 observing epochs. In both cases the break point is found at $\sim$ 2 keV.

The ME spectra of 3C 66A were studied by Maccagni *et al.* (1987). It is unclear if these spectra were taken from the database or re-extracted. The results are listed in Table A (Appendix 2). They were obtained from a fit (with free N_H) to the sum of the three ME spectra. The ME high state of 86.015 seems to give the dominant contribution, yielding a photon index of $\sim$ 2.80. This value is similar to what we found for a fit to the LE + ME data with free N_H.

We collected all the spectral information derived from the *Einstein* data in Table 3.4.a. No evidence for curvature was found in these data. In the first observing epoch, the simultaneous IPC and MPC data were fit by a simple power law, with a slope consistent within the errors to those in Table 4.1.a. However, it is remarkable that in the second observation the source was entirely in a soft state, with a dramatic steepening of the spectrum ($\alpha \sim 5.0$). This behavior is opposite to that found in the EXOSAT data, in which, when the high energy intensity is low, the spectrum is harder.

4.3.2 AO 0235+164

EXOSAT observed AO 0235+164 nine times. Only two ME spectra could be retained, corresponding to a high detection rate and acceptable QF. The observing log is reported in Table 3.2.a. The ME intensity is the same in both observations, while in 86.015 the source was not detected in LE, although the exposure is not short. We treated the two spectra together in the spectral analysis.

The source emits in the energy range 0.1 – 6 keV. A fit with a power law (Table 4.1.a) is acceptable in all cases. The photon index of $\sim$ 1.9 from the fit with fixed N_H is consistent within the 90% errors with that found from the previous *Einstein* IPC data (Table 3.4.a), $\alpha \sim 2.2$. No evidence for curvature is present, because the ME slope is consistent, within the errors with the slope obtained when the LE data point is added. The absorption is also in agreement within the uncertainties with the Galactic value.

4.3.3 PKS 0521-365

PKS 0521-365 was observed twice with the EXOSAT satellite (Table 3.2.a). In both ME observations the emission was significant at the 5σ level. However, only the first spectrum (83.306) was of high enough quality to be retrieved from the database. In this case, all the detectors were on and the background was estimated through an array swap manoeuvre. For the 83.334 spectrum, for which the background was determined during a slew, a re-extraction was required.

The source was found to emit signal in the range 0.1 – 8 keV. In Table 4.1.a we report the results of the fits with a power law (see above). This model satisfactorily fits the data in both observations, resulting in a power law slope

among the flattest found for the RBL sample. The spectral parameters are in total agreement, within the errors, with the values obtained by Garilli & Maccagni (1990). However, for the 83.306 epoch, from column 10 of Table 4.1.a indication is found for a fitted absorption (9.0×10^{20} cm^{-2}) in slightly excess to the Galactic one (3.5×10^{20} cm^{-2}); in addition, the slope from column 7 is flatter than the slope in column 5, which causes us to suspect the presence of a spectral break. A significant improvement to the fit was obtained with a broken power law model with $E_0 \sim 4$ keV, as shown in Table 4.3.a. For the 83.334 observation, this model is not preferred over a simple power law. In this case, the slope in Table 4.1.a is in good agreement with that obtained from the fit to the *Einstein* IPC spectrum (Table 3.4.a).

4.3.4 PKS 0537-441

EXOSAT observed PKS 0537-441 on two close occasions in 1985. Only the spectrum obtained on the second date (85.055) could be used, the detected signal being significant at $> 5\sigma$ and having QF=3. The count rates in the LE and ME energy ranges are listed in Table 3.2.a. On the first date, the source was not detected in the hard energy range, although it was in a higher state in the LE. This behavior, *i.e.*, a high state in the ME concurrently with low state in the LE, is analogous to that found for 3C 66A (see above).

The ME signal was detected in 1.5 – 7 keV. The fit with a single power law yields acceptable results (Table 4.1.a). No indication for curvature is found. The photon index of $\sim$ 1.3 is the flattest found for the RBL sample. It is interesting to compare this slope with those found from the other X-ray missions, *Einstein* and ROSAT (Table 3.4.a), although both operated in a softer

(< 2.4 keV) energy range. The EXOSAT slope is totally in agreement with that obtained from the *Einstein* IPC experiment, and both are flatter than the ROSAT one. Therefore, ROSAT found PKS 0537-441 in a softer state. Quasi-simultaneously with the ROSAT observations, a non zero flux was detected in γ-rays (Michelson *et al.* 1992). This can imply that in the spectrum of PKS 0537-441 there may be a second component, rising up at higher energies.

4.3.5 PKS 0754+100

PKS 0754+100 was pointed at by the EXOSAT satellite on one occasion in 84.043 (Table 3.2.a). The spectrum provided by the ME database was of poor quality and was re-extracted. The low QF was due to the fact that only one detector array was operative at the time, and the background was estimated during a slew.

After the background subtraction, a positive signal was found in a rather restricted range (2 – 5 keV). The results of the fits with the power law model are reported in Table 4.1.a. The power law model does not satisfactorily fit the spectrum, as can be inferred from the high χ^2s. Large errors are found on the parameters, and the absorption is not well constrained ($< 5.3 \times 10^{21}$ cm^{-2}). We attribute this to the low s/n of these data. Therefore, we do not expect that the data could be better fit with another model. In fact, a broken power law, even if is formally acceptable, does not provide a significantly improved modeling of the data.

4.3.6 OJ 287

The EXOSAT archive provides 11 observations for this BL Lac. However, only two could be retained for spectral analysis. As apparent from Table 3.2.a, where the observing log is given, OJ 287 was in different emission levels, the 83.281 observation corresponding to a lower state.

Signal was detected in a restricted energy range, 0.1 – 5 keV. The power law fit results are listed in Table 4.1.a. The most striking feature is the extremely steep spectrum found in the 83.281 low state. A photon index of ~ 5.2 is obtained when the ME data are fitted, and of 5.8 when the overall spectrum is fitted with N_H free. This is not an isolated case among RBL, because a similar steep slope ($\alpha \sim 5.0$) was found for 3C 66A on one occasion in the *Einstein* data (see above), corresponding to a vanishing of the hard energy flux with an increase of the soft flux. It is remarkable that here the 83.281 observation corresponds to a lower state both in the LE and the ME bands. This trend, *i.e.*, a steepening of the spectrum in the low state, is in agreement with that found for the other BL Lac in the sample (see below) An indication for curvature at lower energies is also found in the 83.281 observations. In fact, when the LE data points are included in the fit, the slope flattens considerably and the absorption is greater than the Galactic one. The fit with a two component model is preferred with high significance over a single power law (Table 4.3.a). Evidence for curvature also seems to be present in the higher state, but it is not significant.

Beside EXOSAT, the only spectral information available is from the *Einstein* IPC data (Madejski 1985). It is summarized in Table 3.4.a. The *Einstein* observations are consistent in slope with the 84.040 EXOSAT one. The steepest spectrum reported in Table 3.4.a is that from 1980 April, with $\alpha \sim 3.4$; within the errors, it is consistent with the 83.281 EXOSAT observation.

We conclude that the spectrum of OJ 287 is characterized by a large spectral variability. In the EXOSAT data, there is indication for a hardening of the spectrum when the source is in a higher state.

4.3.7 B2 1308+32

Ten observations are available from the EXOSAT database for B2 1308+32, of which only one could be considered for spectral analysis purposes. Although the corresponding spectrum satisfied the ME selection criteria it is a marginal case and the results should be regarded as indicative.

The spectrum was studied up to 7 keV. A power law fit (see Table 4.1.a) yields a rather flat slope. Values from 1.3 to 1.6 are allowed. Because of the limited quality of the data, a fit with N_H free is not able to constrain this parameter.

4.3.8 3C 371

3C 371 was pointed at by EXOSAT two times (Table 3.2.a). In the ME experiment, the source was detected at a level $\geq 5\sigma$. In the first epoch (84.255), at the beginning of the observation, an increase of the background was recorded, probably due to solar flares. This spectrum was therefore re-extracted taking into account only the time sequences free of flares. The 84.273 observation could be retrieved.

Signal from the source extends up to $\sim$ 7 keV. We fitted the ME and the LE + ME energy distributions with the power law model. As can be seen

from Table 4.1.a, the ME spectra are satisfactorily fit by this model, with a slope $\sim$ 1.9 in both cases. Adding the LE data points causes the fit to get worse, except for the 84.273 data (N_H free case). The slope in column 7 is steeper than in column 5, while the fitted absorption (2.0 $\times 10^{20}$ cm^{-2}) is less than the Galactic one (4.9 $\times 10^{20}$ cm^{-2}). As was discussed above, this indicates the fact that the LE points lie above the ME slope, yielding a soft excess. Fitting with a broken power law, we find (Table 4.3.a) that a break at $\sim$ 1 keV with a flattening above this energy is required, with a maximum confidence ($> 99.9\%$). It is quite interesting to note that, above the break, the photon index is $\sim$ 1.86 in both observing epochs, a value close to the "canonical" value of $\sim$ 1.7 determined for Seyfert galaxies (Turner & Pounds 1989) which are also characterized by a soft excess at lower energies.

Staubert *et al.* (1986b) studied the 84.256 spectrum of 3C 371 (see Table A). The fit to the LE + ME data with fixed N_H yielded a slope in agreement with ours. Considering separately the LE and the ME data, the authors were able to infer evidence for a soft excess, which we confirm.

Recently 3C 371 was observed with the PSPC experiment on board the ROSAT satellite in the energy range 0.1 – 2.4 keV (Fink *et al.* 1992a). The spectrum was fitted with a power law, and a better fit was obtained when an absorption edge at 0.6 keV was added. This feature was found for the first time by Canizares & Kruper (1984) in the *Einstein* data of PKS 2155-304 and attributed to ionized oxygen. The slope was determined to be 2.66 $\pm$ 0.09. If compared to the EXOSAT data it is steeper than the slope of the ME data, but flatter than that of the soft excess. We checked if the EXOSAT data could be consistent with an absorption feature with energy at 0.6 keV, but we did not find convincing results. Our data do not have enough intrinsic resolution to see such a feature, which therefore could not be confirmed nor ruled out in the EXOSAT

spectra.

4.4 Results for individual objects: XBL

4.4.1 MS 0317+18

The EXOSAT satellite observed MS 0317+18 twice in 1985. In both cases, the ME spectra were re-extracted with a more careful analysis for the background subtraction. These are the first X-ray spectra available for this source. Signal from the source was observed up to $\sim 7 - 8$ keV.

The power law fits results are listed in Table 4.1.b. For the 85.039 observation the fit is acceptable and gives a rather flat slope (~ 1.8). The results obtained for this observation are consistent with those obtained by Giommi *et al.* (1987), reported in Table A. Instead, for the 85.013 observation the χ^2 is high and there is indication that the index from the fit to the LE + ME data for fixed N_H (column 7) is flatter than the index for the ME data (column 5). Moreover, the fitted value for the absorption is high ($\sim 26.0 \times 10^{20}$ cm^{-2}) if compared to the Galactic one (9.8×10^{20} cm^{-2}), which could suggest the presence of some spectral curvature at lower energies. We fitted the 85.013 spectrum with a broken power law in the way described in section 4.2. Even if the spectral parameters are well constrained the improvement in the χ^2 is not significant. We could expect this because of the low s/n and the presence of fluctuations in the data.

4.4.2 H0323+022

The source was observed with the EXOSAT satellite on 7 times at different emission levels. Of these, only two observations (84.265 and 84.267) satisfied the selection criteria of Chapter 2, having a signal significance above the 5σ level and QF = 3. However, both the spectra needed to be re-extracted because of technical problems.

Signal from the source was detected in the energy range 0.1 – 6 keV. The results of the fits to the data are listed in Table 4.1.b. We note that the spectral index varied between the observations, being $\sim$ 2.6 – 2.8 in 84.265 and lower ($\sim$ 2.4 – 2.5) in 84.267. The change is in the sense of a hardening of the spectrum when the source brightens, as apparent from Table 4.1.b. A similar trend, although more dramatic, was also found in the GINGA data (Table 3.4.b). In our data, the intensity change is remarkable only in the hard energy range. At soft energies the source remains essentially constant (Table 3.2.b).

It is interesting to note that the *Einstein* observations (Table 3.4.b), which covered an energy range similar to the EXOSAT one, were consistent with a two component spectrum. The fit to the IPC data resulted in a flatter slope than to the simultaneous MPC data, and in an absorbing column density greater than the Galactic one. This difference suggested to Madejski & Schwartz (1989), in the context of their global analysis, a steepening of the spectrum in 1 – 3 keV.

In summary, the EXOSAT spectrum of H0323+022 is adequately represented by a single power law. The spectral index seems to vary with the intensity, in such a way that the spectrum hardens when the source brightens.

4.4.3 H0414+009

The EXOSAT satellite observed H0414+009 on four close occasions 1984 (see Table 3.2.b), and in all cases but one (84.266) the quality of the spectrum was high. In each observation the background was determined through array swaps. We retained the high quality observations from the database and re-extracted the 84.266 spectrum to perform the spectral analysis. From Table 3.2.b it is clear that the source varied in intensity, in particular in the high energy range, being in a high state in 84.258 and in a low state in 84.274. A previous study on the EXOSAT data was performed in an unpublished work by George (1988).

The source was found to emit up to $\sim$ 8 keV. On one occasion (84.274), a positive signal was detected up to $\sim$ 10 keV. The spectral analysis results are shown in Table 4.1.b. The spectral slope is rather variable, ranging from $\sim$ 1.8 in 84.258 to $\sim$ 2.4 in 84.274. As discussed above, simultaneously with the spectral variations the source also varied in intensity. The 2 – 6 keV flux ranged from $\sim$ 19.0 $\times 10^{-12}$ ergs cm^{-2} s^{-1} in 84.258, to $\sim$ 9.0 $\times 10^{-12}$ ergs cm^{-2} s^{-1} in 84.274. As for H0323+022, the change is in the sense of a spectral hardening when the source brightens. For H0414+009, due to the greater number of observations and to the higher s/n, the correlation is more reliable than for H0323+022. As an example, we plot in Figure 4.1 the highest state ME spectrum of 84.258 (triangles) and the lowest state ME spectrum of 84.274 (circles). A steepening of the spectrum when the source is in the low state is apparent. As for H0323+022, the intensity remains quite constant in the softer energy band.

The indexes determined from fitting the ME spectrum and the combined LE + ME data are all consistent, except for the two low states (84.266 and 84.274), where curvature is possibly present. We checked if our data could be modeled by a broken power law, following the procedure described above. An

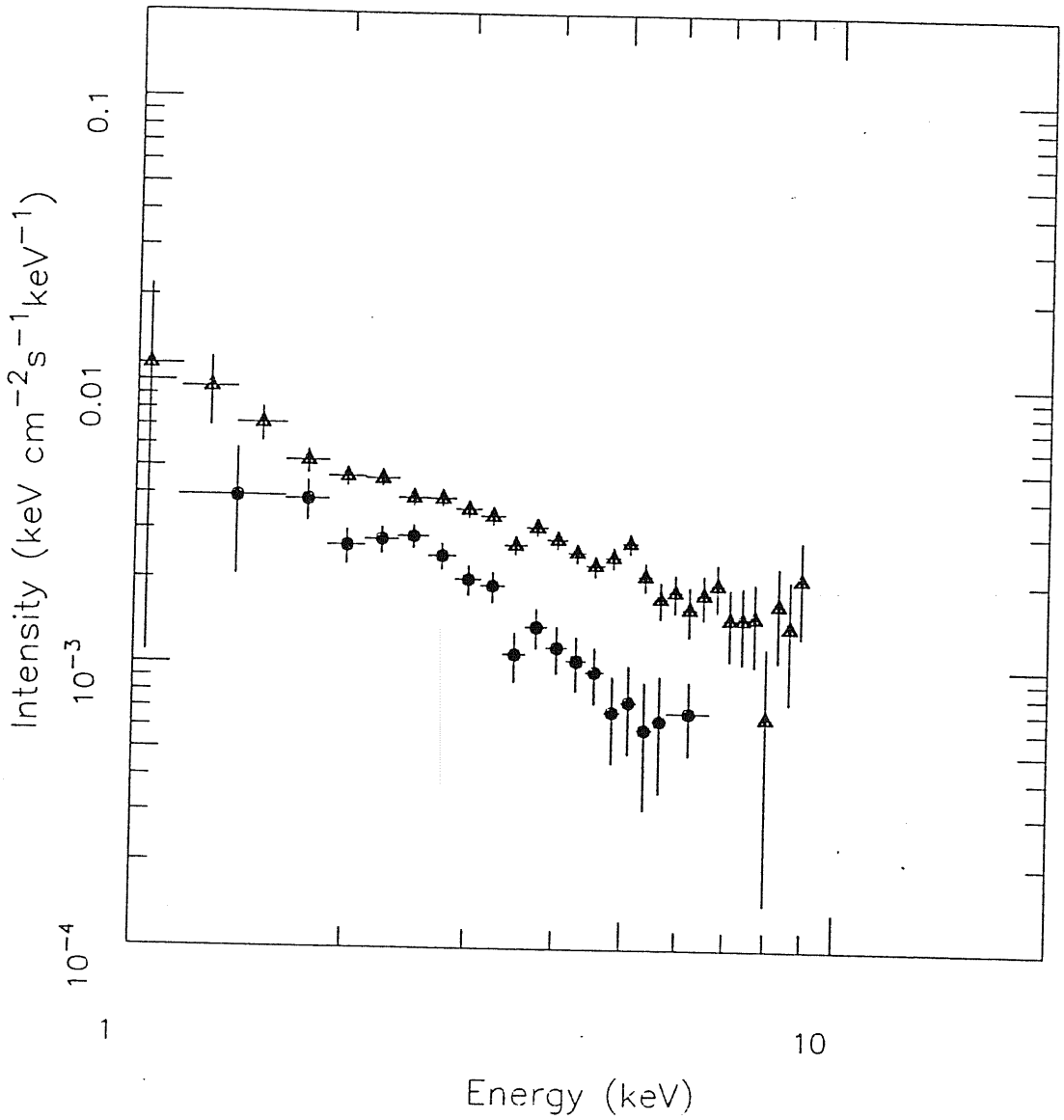

Figure 4.1: Spectral variability of H0414+009. Comparison between the high state of 84.258 (*triangles*) and the low state of 84.274 (*circles*). Only the hard energy data are plotted.

indication for curvature was found for the lowest state of 84.274, with $E_0 \sim 3$ keV, $\alpha_1 \sim 2.3$ and $\alpha_2 \sim 2.8$. However, as for H0323+022, the fit did not improve significantly with respect to a simple power law model ($\Delta\chi^2 = 3.8$).

A remarkable result of the analysis of the *Einstein* data (Table 3.4.b) was that an absorption column density in excess to the Galactic value was found (Halpern *et al.* 1990). The extra absorption was convincingly attributed to highly ionized gas, intrinsic to the BL Lac. It was found that a neutral absorber does not adequately reproduce the X-ray spectrum, and that instead a model including an absorption line between 0.5 and 0.6 keV, probably due to ionized oxygen as in other few BL Lac objects (Canizares & Kruper 1984; Madejski *et al.* 1991), did provide an improved fit. We checked if including a feature at 0.6 keV would be consistent with both the low state spectra, but we did not find convincing results in either case. As discussed for 3C 371, the lack of spectral resolution in our data below $\sim$ 1 keV does not allow us to exclude the presence of a feature in the soft energy range.

In summary, the EXOSAT spectrum of H0414+009 is well represented by a single power law over the energy range 0.1 – 10 keV. Apparently, the intensity and the slope are correlated, the spectrum becoming harder when the source brightens.

4.4.4 EXO 0423-0840

The candidate BL Lac EXO 0423-0840 was observed by EXOSAT twice. Both the ME observations fulfilled the selection criteria described in Chapter 2 and were therefore retained from the database. In Table 3.2.b the log of the observations is reported. In 85.267, only an upper limit could be given in the LE

band. In this case, only the fit to the ME data alone is reliable and the fit to the composite spectrum must be considered with caution.

The emission was detected up to $\sim$ 10 keV. In both cases, a fit with a power law was first attempted, with the results listed in Table 4.1.b. The LE + ME data are better fit by a power law with low energy absorption in large excess to the Galactic value (although the big error bars). Because the source was found in a region where there seems to be a cluster of galaxies (see Chapter 3), a fit with a thermal bremsstrahlung was also performed on the LE + ME data. In both spectra the fit is not preferred. The χ^2s were 1.3 and 2.0 for the 85.048 and 85.267 observations, respectively. The fitted temperature was of few keV.

Indication for curvature is present in both epochs. As reported in Table 4.3.b, a broken power law with $E_0 \sim 2$ keV is highly preferred over a single component spectrum. The fit gives a negative low energy slope even for the more reliable observation (85.048). As we said above, the source was not detected in the soft energy range in the 85.267 epoch, where in fact there is an indication for a fitted N_H larger than in the 85.048 data. It does not seem clear whether the spectrum is intrinsically curve, or if a great amount of intrinsic absorption is present, or both.

It must be noted that in the work of Edge & Stewart (1991) the EXOSAT data are treated in the hypothesis of a cluster of galaxies. The authors made a fit with an optically-thin metal-enriched plasma bremsstrahlung model (Raymond & Smith 1977). They found a good fit, $\chi^2 = 19.22$ for 18 d.o.f. (kT $\sim$ 3 keV, absorption $\sim$ Galactic).

4.4.5 EXO 0507-04

This BL Lac was observed by EXOSAT only once in 1984. The ME data satisfied our selection criteria (Chapter 2) and were retained from the database.

The spectrum was studied in the energy range 0.1 – 5 keV, in which a positive emission has been detected. A power law with photon index $\sim$ 1.8 and absorption in total agreement with the Galactic value (7.5×10^{20} cm^{-2}) provides an acceptable fit to the data.

4.4.6 PKS 0548-322

EXOSAT observed PKS 0548-322 on three occasions during 1983 and 1986 (Table 3.2.b). All the ME observations satisfied the 5σ selection criterion explained in Chapter 2. However, the automatic procedure provided a satisfactory background subtraction only for the 83.306 epoch. The 86.066 and 83.334 spectra were re-extracted.

In all observations the signal from the source covered a rather extended energy range (up to $\sim$ 9 keV). The results of the fits to the ME and to the LE + ME data with a power law model are summarized in Table 4.1.b. The quality of the fit is acceptable only for the 83.334 observation. However, the fit with a broken power law following the procedure described above, gives an improvement at the 95% confidence level (Table 4.3.b). We can therefore conclude that for the 83.334 observation the broken power law is consistent with, although not required by, the data.

For the 83.306 and 86.066 observations the fit with a single power law is clearly not acceptable. For the 83.306 data we expect a break at lower energies,

because of the flattening of the spectrum when N_H is fixed (column 7), and because the fitted absorption is greater than the Galactic value (column 10). These features are not present in the 86.066 epoch. In this case, from the poor residuals at higher energies a break point at $\sim$ 5 – 6 keV is expected. Fitting both distributions with a broken power law model in the way described above yields highly improved ($>$ 99.9%) results in both cases, as reported in Table 4.3.b. The break point moves, being at lower energies when the source is bright and at higher energies in the low states. In addition, the slopes below and above E_0 are also related to the flux, both being flatter in the high state. The results found for the three observations, both in the case of the power law and of the broken power law, are consistent with those found by Barr *et al.* (1988) and Garilli & Maccagni (1990), listed in Table A.

It is not the first time that a two component spectrum is reported for PKS 0548-322. As was noted in Table 3.4.b the first HEAO-1 measurements were consistent with a clear break near 2 keV, the low energy data (LED) being steeper than the high energy (MED) ones (Riegler *et al.* 1979). Worrall *et al.* (1981) found a single steep power law for the 1978 Sep MED (2 – 10 keV) data with indication for high N_H. The authors noticed that the spectrum was likely dominated by the steep component because of the vanishing of the high ($>$ 10 keV) energy flux and the corresponding decrease of the flatter component. From the *Einstein* SSS data a large amount of absorption was inferred at low energies (Urry *et al.* 1986), not found in the IPC data (Maccagni *et al.* 1983b). This extra absorption was interpreted as due to the presence of a warm absorber at 0.6 keV, transparent to the lower energies sampled by the IPC. A flux depression was explicitly modelled with an absorption edge at 0.6 keV in the 1979 SSS data by Madejski *et al.* (1991). The presence of extra absorption in the previous X-ray observations of PKS 0548-322 can indicate an intrinsic steepening. On

one occasion, however, it was entirely attributed to a flux depression at lower energies caused by a warm absorber, and no spectral change was required. The EXOSAT data are not consistent with such a feature.

In summary, in at least two of the EXOSAT observations of PKS 0548-322, a simple power law model is not adequate to describe the data, which instead are modeled with a two component spectrum. The break point seems to move depending on the continuum emission level. A two component spectrum was also found in previous reports, together with the presence of an absorption feature at 0.6 keV, suggesting that this source does not have a simple X-ray spectrum.

4.4.7 EXO 0557-3838

Two observations are available from the EXOSAT database for EXO 0557-38, all satisfying our ME selection criteria. This object is "critical" (see Chapter 3), and the results of the spectral analysis must be considered with caution.

The signal was detected up to $\sim$ 5 keV in the first date and to 10 kev in the second one. As apparent from Table 4.1.b, a power law fit is acceptable only in the 84.350 observation. In the 86.021 observation, an indication for a soft excess can be inferred, the slope of the ME data alone being flatter than when the LE data points are added (columns 5 and 7, respectively), and the fitted N_H less than the Galactic value. In fact, a concave up model, with a soft excess below 2 keV gives a highly significant fit (Table 4.3.b).

4.4.8 MRK 421

Mrk 421 was observed with EXOSAT in 1984 – 1985, on a total of 14 occasions. The log of the observations is reported in Table 3.2.b. Signal from the source was detected with a significance level well above 5σ. For the 84.033 observation, a positive signal was detected only in a restricted energy range, 2 – 4 keV; this explains why in a larger range, such as that where the ME count rates of Table 3.2.b were calculated, the signal is not significant. In a few cases some of the detectors were off during the observation and the spectra needed to be re-extracted using a more careful background subtraction. These observations are marked with an asterisk in Table 3.2.b. The source varied in intensity both in the LE and in the ME energy bands. In particular it was found in an outburst during the latest 1984 observations (84.337, 84.338, and 84.340), with low and intermediate intensity in the remaining dates. The EXOSAT observations of Mrk 421 were previously studied by George *et al.* (1988a; see Table A).

Mrk 421 was found to emit in an extended energy range (0.1 – 9 keV) and on a few occasions up to 11 keV. The s/n ratio was good, except for the 84.032 epoch, for which the background determination was poorer than in the other cases. The spectra were first fit with a power law model with the results listed in Table 4.1.b. Except for the latest 1984 observations, for which high χ^2's were found (see below), the power law gave acceptable fits, with slopes and absorbing column densities in agreement with the results of George *et al.* (1988a). The average absorption from column 10 is$(1.7 \pm 0.4) \times 10^{20}$ cm^{-2}, in good agreement with the Galactic value (1.8×10^{20} cm^{-2}), while for the slope the values in columns 7 give 2.55 with standard deviation 0.23. The high dispersion of the photon indexes around the mean reflects the spectral variability of the source. The photon index varies in such a way that the spectrum is harder

when the intensity is higher. To see this more clearly, we plotted α_{LE+ME} for free N_H versus the 2 – 6 keV count rates in Figure 4.2. A global trend of flatter α with increasing intensity is apparent. A large spectral variability is also inferred from the results obtained from data collected by the other X-ray missions (Table 3.4.b), but the correlation between the slope and the intensity found in the EXOSAT data was not always supported by all the previous missions. For example, in the GINGA data (Ohashi 1989), a dramatic variation in intensity in 2 – 35 keV was not accompanied by a spectral change. The ROSAT observations in 0.2 – 2.4 keV detected a flattening with fading intensity (Fink *et al.* 1991).

As we said above, the fit with a simple power law is not completely satisfactory in the high state observations (84.337, 84.338, and 84.340). This is probably due to a deficiency of photons at higher energies. An example is shown in Appendix C. We fitted these data with a broken power law model as described above. We found (Table 4.3.b) a significant improvement (P > 99.9%) of the fit when we fixed the break point at $\sim$ 3 – 4 keV. The average slopes are $\langle\alpha_1\rangle = 2.12 \pm 0.01$ and $\langle\alpha_2\rangle = 2.37 \pm 0.14$. We can conclude that, in the high state, the spectrum of Mrk 421 is convex with a slope change of $\Delta\alpha \sim 0.25$ at 3 keV. This is in agreement with the findings of George *et al.* (1988a), who modelled these data including an exponential cut off at 3 – 4 keV (Table A).

Some other observations in Table 4.1.b should be noted. They are the 85.131, 85.118, and 85.004 dates. For these observations, comparing the indexes in columns 5 and 7, we see that the slope found when we add the LE points is steeper than that of the ME data alone. In addition, the inferred value for the absorption is lower than the Galactic value. As for 3C 371, this is a suggestion for a possible soft excess in the data. We modelled these data with a broken power law (Table 4.3.b). A significantly improved fit could be obtained describing the spectra with a steepening soft component. In the 85.118 and 85.131 observations

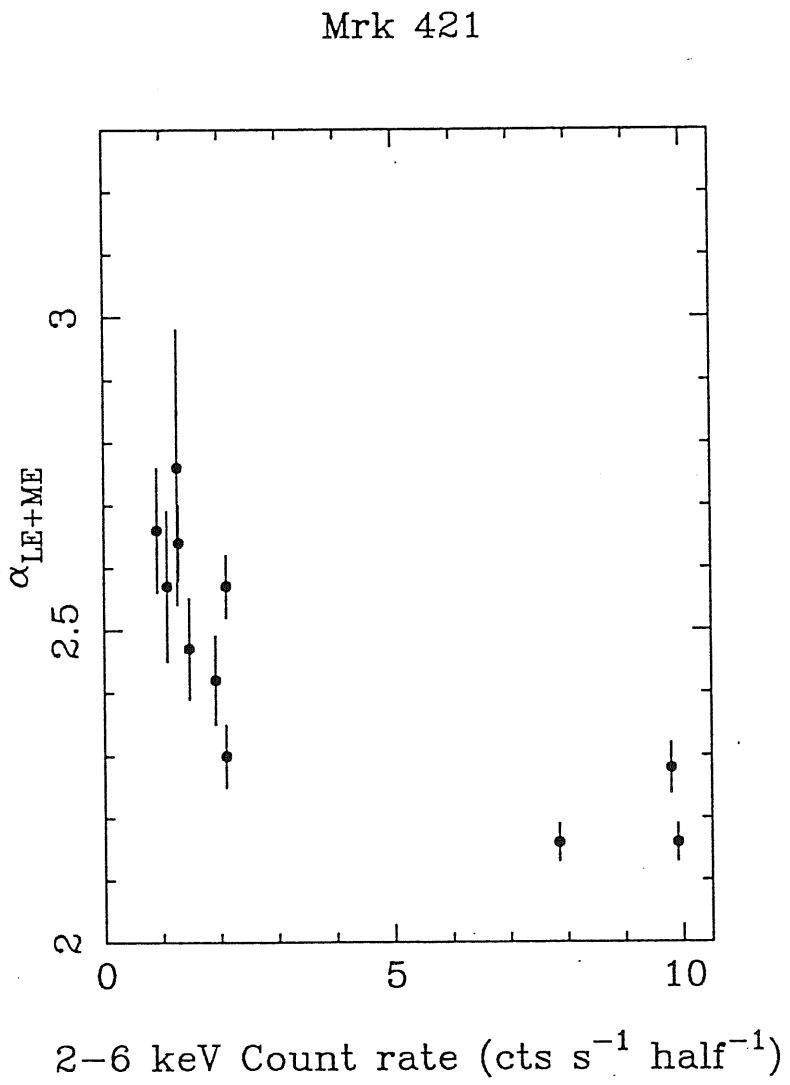

Figure 4.2: Spectral variability of Mrk 421. The spectral index from the fit to the 0.1 – 10 keV spectra with a power law (free absorption) is plotted against the 2 – 6 keV count rate. Uncertainties on the slope are at 90% confidence errors.

E_0 is found at $\sim$ 1 keV, thus indicating a soft excess. For the 85.004 observation $E_0 \sim 5$ keV and α_2 is consistent with zero (high tail). It is interesting to note that all these observations correspond to intermediate intensity states, with the 85.118 and 85.131 states very similar each other and higher than the 85.004. The remaining epochs, which are the lowest states, are fit with a power law with $\langle\alpha\rangle = 2.65 \pm 0.10$.

It is not the first time that a double component spectrum has been reported for Mrk 421. A soft excess below 3.2 keV was found in the 2 – 30 keV spectrum from the OSO-8 satellite and in the later *Ariel 6* spectrum (Table 3.4.b). The spectral parameters obtained in these earlier observations are similar to those found for the EXOSAT 85.004 observation, in particular the zero-consistent high energy slope. It is interesting to note that only concave up spectra were detected in these previous observations, while in the EXOSAT data a downward convexity is found in the high states. In Table 3.4.b a high amount of absorption is found only for the *Einstein* SSS data of 1978 Dec 6 (Urry *et al.* 1986), due to a 0.6 keV absorption feature (Madejski *et al.* 1991). The latter authors found also that the continuum required a concave up model with an excess below 1.4 keV. None of the EXOSAT spectra is consistent with a model involving the 0.6 keV edge. As we said previously, our data do not allow us to detect discrete features below $\sim$ 2 keV, therefore the edge at 0.6 keV can be neither excluded nor confirmed in the EXOSAT observations.

In summary, the principal results are the following. As for other BL Lacs in our sample, Mrk 421 shows remarkable spectral variability, in the sense of a hardening when the intensity increases. In addition, we found different modelling of the spectrum depending on the continuum level. In the highest states a downward curved spectrum is found. In the lowest state it is described by a simple, steeper power law ($\alpha \sim 2.6$), while in the intermediate states a concave up

spectrum is detected, with a high tail/soft excess. Absorption features, claimed in previous reports, can not be excluded from our data.

4.4.9 MRK 180

The source was observed by EXOSAT four times in 1984 when it was in a low state, and once in 1985 during an outburst. The latter observation (high state) satisfied the ME selection criteria illustrated in Chapter 2, and was retrieved from the database. Only two out of 1984 four spectra could be taken into account. Signal from the source was detected up to $\sim 5 - 6$ keV, a rather restricted energy range. The log of the selected observations is reported in Table 3.2.b.

The spectra were not of high statistical quality, except the 85.093 epoch (the highest state) for which the s/n was good. The results of the fits with a power law, reported in Table 4.1.b, show that this model adequately reproduces the energy distribution only for the better quality data (85.093), yielding a photon index ~ 2.3 and absorbing column density of 1.4 $\times 10^{20}$ cm^{-2}, consistent within the errors with the results of George *et al.* (1988b) reported in Table A. In the other cases, a rather high value of the χ^2 was found. These data have a poor s/n, and, not surprisingly, a fit with a two component model is not significant. Within the errors, the fit results for these observations are in agreement with those found by George *et al.*.

The spectral fits to the data from the other X-ray experiments are summarized in Table 3.4.b. Fitting the IPC and simultaneous MPC data, Mufson *et al.* (1984) found that the low energy data are flatter than the high energy ones, even if no absorption in excess to the Galactic one is substantially deduced. A later IPC observation gave an indication for a flatter slope. Recent ROSAT

PSPC (0.1 – 2.4 keV) observations (Fink *et al.* 1992b) gave a value for the photon index of $\sim$ 2.3, in total agreement with the EXOSAT high state.

Summarizing, the X-ray spectrum of Mrk 180 is represented by a single power law, with variable slope. The spectral variability inferred from the EXOSAT data is similar to that found for other BL Lacs in this sample, *i.e.*, the spectrum is flatter in the high state.

4.4.10 1218+304

1218+304 was observed by EXOSAT on nine occasions. As explained in Chapter 3, in two epochs the contribution to the ME flux from the contaminating Seyfert in the field, Mrk 766, was maximum. Among the remaining observations only three satisfied the ME selection criteria (Chapter 2), and could be retained from the database.

The data could be studied up to $\sim$ 8 – 9 keV with a power law model (Table 4.1.b), with results in agreement, within the errors, with those of George *et al.* (1988b), listed in Table A. The LE + ME data are not well fit when N_H is set to the Galactic value. In all cases evidence for curvature is present, because the ME slope flattens when the LE data points are added and the fitted absorption in column 10 is greater than the Galactic value. The fit with a broken power law model yields an improved results in two cases (84.356 and 85.005), as reported in Table 4.3.b. In both cases a steepening is found above $\sim$ 2 keV. Note that the χ^2 for broken power law model in the 84.356 date is still rather high due to some fluctuating points in the spectrum.

In Table 3.4.b, all the X-ray spectral information available from the literature is summarized. The first HEAO 1 A2 and A3 spectra of 1977 December

and 1978 May are rather flat and consistent with the *Einstein* SSS observations of 1978 Dec. However, as is remarked by Urry *et al.* (1986), these latter observations were not of high quality, as is apparent from the great uncertainty on the spectral index; values from 0.9 to 3.4 are equally allowed within the 95% confidence level, in agreement with the simultaneous MPC data. The A2 observation taken only five days later (Worrall *et al.* 1981) indicates a much steeper spectrum in the same (hard) energy range. No substantial intensity variability is observed. In the EXOSAT data, the same uncertainty remains: no significant spectral changes accompany the intensity variations, noteable in particular in the softer energy range.

The SSS data of 1979 Jun were of good quality. In this case, a steep slope of $\sim$ 3.6 and a column density one order of magnitude greater than the Galactic value are found, attributed to a warm absorber. These data were reanalyzed by Madejski *et al.* (1991) who found a better fit by adding an absorption edge at 0.6 keV.

In conclusion, our data for 1218+304 are consistent with a two component spectrum in all observing epochs. Previous spectral analyses does not always support this scenario. The spectral index apparently varies without a clear correlation with the intensity.

4.4.11 2A 1235+63

The EXOSAT satellite observed this BL Lac three times. Only two observations fulfilled the ME selection criteria described in Chapter 2, having detection significant at 5σ level and QF = 3. The spectra were retrieved from the archive. As reported in Table 3.2.b, in the 85.080 epoch the LE observations were taken

only with the thick 4000 Å Lexan filter. Because the source was not significantly detected on this occasion in LE, although the exposure long, and because of the ME intensity similar to that of 85.079, the two ME spectra were treated together. EXOSAT provided the first spectrum of MS 1235+63 because in the previous *Einstein* observations (see Table 3.4.b) the s/n was not sufficient for a spectral analysis.

The signal covers the energy range 0.1 – 5 keV. The power law model gives the results listed in Table 4.1.b. It can be see that the addition of the LE data points flattens the spectrum considerably, indicating a spectral break. In fact, a broken power law model with a steepening above 4 keV is highly preferred over a single power law model (Table 4.3.b).

4.4.12 MS 1402+04

This BL Lac was observed four times in 1985 by EXOSAT at different emission levels. Only two observations were found to be suitable for spectral analysis according to the selection criteria explained in Chapter 2. The observing dates are reported in Table 3.2.b. The 85.031 observation could be retained from the database, while the 85.187 data needed to be re-extracted.

In the ME energy band the source was detected up to $\sim$ 7 keV. Due to the limited s/n ratio the spectral analysis gave only indicative results. We studied the two spectra with models (a) and (b) above, with the results listed in Table 4.1.b. In the high state (85.031 observation) the power law model yields acceptable χ^2s with a photon index $\sim$ 2.3. This observation was also studied by Giommi *et al.* (1987), with consistent results (Table A). The χ^2's values are higher in the second observing data (85.187). The fit with N_H free was unable

to constrain this parameter, and only an upper limit could be obtained in both epochs. We can conclude that the X-ray spectrum of MS 1402+04 is consistent with a power law model.

4.4.13 1E 1415+22

EXOSAT pointed at 1E 1415+22 only once in 1986 (Table 3.2.b). The ME data satisfied the selection criteria described in Chapter 2, having been detected at $\geq 5\sigma$ level and flagged 3.

Signal from the source covers an energy range up to $\sim$ 5 keV only. As shown in Table 4.1.b, a power law with N_H fixed to the Galactic value is not acceptable because of the high χ^2, and yields a slope much flatter than the ME one. Notwithstanding the large errors the fitted absorption is still in excess to the Galactic value. This is an indication for a break at 2 – 3 keV. The fit with a broken power law with $E_0 \sim 2$ keV gives a highly significant improvement, as shown in Table 4.3.b. This fit yields $\alpha_1 \sim -0.4$ and $\alpha_1 \sim 2.9$. With the candidate BL Lac EXO 0423-084 (see above), 1E 1415+22 is the only object in which a negative low energy slope and absorption well above the Galactic value by $\sim$ two orders of magnitude were found.

The results of the fit to the LE + ME data with a power law model with free absorption are in agreement with those of Giommi *et al.* (1987).

4.4.14 H1426+428

H1426+428 was observed by the EXOSAT satellite two times, on 85.012 and 85.055. Both these observations satisfied the 5σ detection criterion, but only the first spectrum had an acceptable QF. This spectrum was previously studied by Remillard *et al.* (1989), with similar results. In the second case the low quality of the archival spectrum could be attributed to the fact that during the observation only 3 detectors were on, requiring a more accurate background subtraction. The re-extraction gave improved results (Figure 2.2).

The signal from the source covers the range from 0.1 keV to $\sim 8-9$ keV. The spectral analysis results are shown in Table 4.1.b. For both observations we obtained very close indexes for all the fits, without evidence for curvature at lower energies. The source did not change in intensity nor in spectral shape between the two observing epochs. Because of this, and to improve the s/n, we fitted the two spectra together. We obtained $\alpha = 2.03 \pm 0.05$, and $N_H = (1.6 \pm 0.3) \times 10^{20}$ cm^{-2}, in excellent agreement with the Galactic value (1.4×10^{20} cm^{-2}). It is also remarkable that the slope found for H1426+428 is among the flattest in Table 4.1.b. This is consistent with the findings by Fink *et al.* (1992b), in a preliminary report of the ROSAT observations in the soft energy range 0.1 – 2.4 keV for a sample of 10 bright BL Lac objects (Table 3.4.b). For H1426+428 they give a spectral index of 2.10 ± 0.10 while the average for the entire sample was 2.39 ± 0.07.

Recently, Madejski *et al.* (1992) published a preliminary description of the BBXRT spectrum of H1426+428. They found that the data require an absorption feature at ~ 0.6 keV and a spectral break with a steepening of $\Delta\alpha \sim 0.7$ at $\sim 1.5 - 2.0$ keV. The 0.6 keV feature is similar to that discovered in PKS 2155-304 by Canizares & Kruper (1984) and in a few other BL Lac objects

by Madejski *et al.* (1991) in the *Einstein* data. It is interpreted as an O VIII resonant line.

With reference to the line, we can not exclude its presence because of the lack of resolution below 1 keV in our data. As can be seen in Appendix C, upper panel, a systematic downward trend above $\sim$ 5 keV is present in the 85.055 observation, although the error bars on the data points are large. A similar less pronounced trend is also present in the 85.012 spectrum. A fit to the spectra with a broken power law, as described in section 4.2, resulted in an indication of a steepening at $E_0 \sim 5$ keV, with $\alpha_1 \sim 2.00$ and $\alpha_2 \sim 3.00$ in both cases. The quality of the fit improved by $\Delta\chi^2 = 5.3$ and $\Delta\chi^2 = 11$ in the 85.012 and 85.055 data, respectively. The improvement is significant only in the second case (at $\sim$ 95%) and is more evident if we fit the two spectra together. In fact, this yielded $\Delta\chi^2$ =16.7 and a significance > 99.9 %.

In summary, in the EXOSAT spectra of H1426+428 well defined evidence for curvature at higher energies is found. The spectra are among the flattest known for X-ray selected BL Lac objects.

4.4.15 MRK 501

Ten observations are available for Mrk 501 from the EXOSAT database. Only two were taken from the archive. In the remaining cases problems with the array detectors required a re-extraction.

The range where the signal was detected is extended, 0.1 – 9 keV, except for the 84.036 date when it covers the range up to 6 keV only. The spectra were studied with the power law model with the results shown in Table 4.1.b. The ME data were all satisfactorily fitted with this model, with a variable index, which

is $\sim$ 2.6 in the lowest state (84.183) and $\sim$ 2.1 in the highest (84.086). The slope changes are related to the intensity variations in the sense illustrated in Figure 4.3, where α_{LE+ME} (free N_H) is plotted versus the 2 – 6 keV count rate. As for Mrk 421, a general trend of decreasing index with increasing intensity is clearly seen. At the lowest and highest states the data points do not obey the general trend; this could indicate 'local' deviations as in PKS 2155-304 (see below), although it can not be excluded that they are fluctuations.

The LE + ME data are better fit when the absorption is allowed to vary. The average value for N_H is, from column 10, (2.2 $\pm$ 0.4) $\times 10^{20}$ cm^{-2}, with indication for a slight excess with respect to the Galactic value (1.7 $\pm$ 0.1) $\times 10^{20}$ cm^{-2}. An indication for a curve spectrum is present, the slope of the ME data being steeper than when the LE data points are added, while in the 84.207 epoch the indication is for a soft excess. The fit with a two component model improves significantly in half of the spectra, as reported in Table 4.3.b, with a break energy at $\sim$ 2 keV, and on one occasion (the low state of 84.191) at 4 keV.

All but the 84.207 observation were previously studied by George *et al.* (1988b) with a power law model, with the results reported in Table A. They are in good agreement with ours, both for the high and the low states.

Mrk 501 is a bright, frequently observed BL Lac. The observations for which spectral information is available are summarized in Table 3.4.b. The first *Ariel 5* spectrum was rather flat, $\alpha \sim 1.8$, in a hard energy range (2 – 10 keV). In the same (hard) energy range the slope of the HEAO 1 spectrum varies from a flatter value of $\sim$ 1.2 in 1977 August to a steeper value, $\sim$ 2.5, 13 months later. Until the first *Einstein* observations (Urry *et al.* 1986), intensity and spectral variability were separately noted, without any correlation. In the *Einstein* data, as well, no clear relationship between the intensity and slope changes was noted. Urry *et al.* observed a flattening of the spectrum simultaneously with an increase

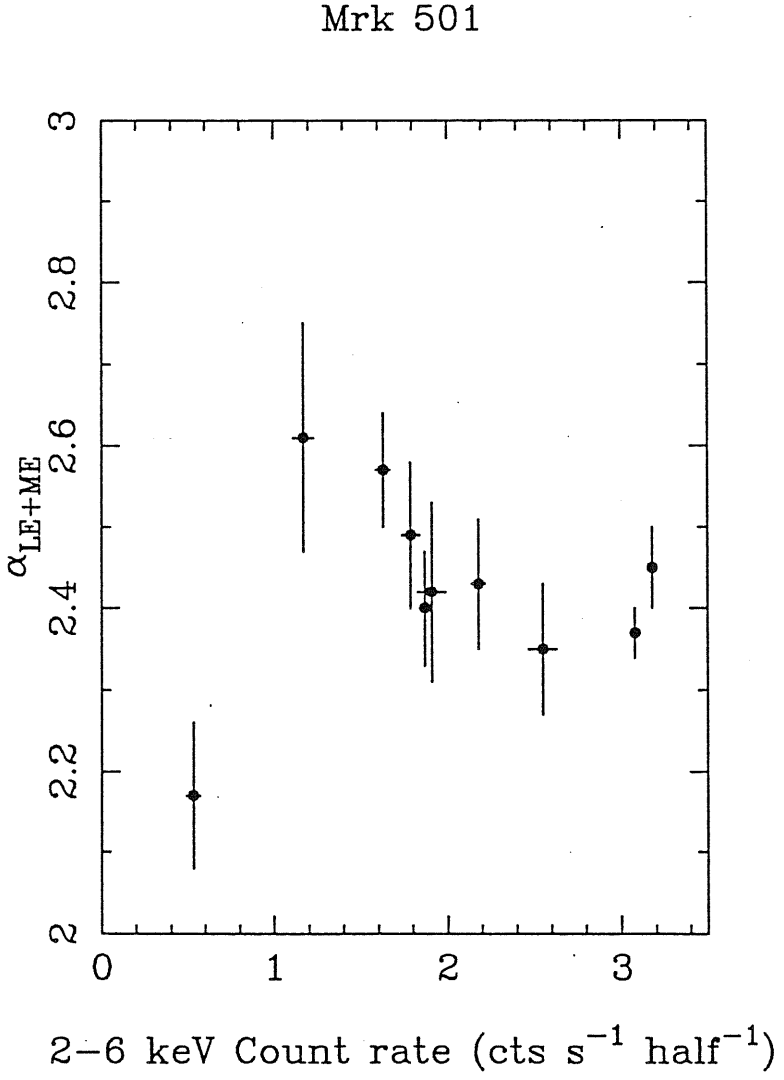

Figure 4.3: Spectral variability of Mrk 501. The spectral index from the fit to the 0.1 – 10 keV spectra with a power law (free absorption) is plotted against the 2 – 6 keV count rate. Uncertainties on the slope are at 90% confidence errors.

of intensity in the 1979 March observations. Five months later the spectrum steepened as the source brightened. As discussed above, in the EXOSAT data a clear trend is instead present.

In some cases in Table 3.4.b the X-ray spectrum of Mrk 501 is consistent with a two component model. The HEAO 1 spectrum of 1977 Aug is steeper ($\alpha \sim$ 3.4) in the soft energy range 0.15 – 2.5, and harder ($\alpha \sim 1.2$) at higher energies (> 2 keV). The *Einstein* SSS data have a slope consistent with the simultaneous MPC data, except for the March observations, where the spectrum gets steeper in the harder energy range. Finally, the IPC data of 1980 August are flatter than the simultaneous MPC ones.

However, the X-ray spectrum of Mrk 501 seems more complex. In the SSS data N_H in excess to the Galactic value is found. Urry *et al.* attribute this extra absorption to a warm absorber acting below ~ 0.8 keV and transparent at energies lower than 0.3 keV (the IPC data do not reveal excess absorption). The August observations, reanalyzed by Madejski *et al.* (1991), were better fitted by adding an absorption edge at 0.6 keV. Only one of the EXOSAT spectra of Mrk 501 is consistent with the a power law plus the 0.6 keV edge ($\chi^2_r = 1.0/25$).

In conclusion, the X-ray spectrum of Mrk 501 seems more complex than a single power law. Half of the EXOSAT spectra, all high states except one, are better represented by a two component model. Some spectra from the previous missions are also consistent with such a scenario, and, in addition, evidence for an absorption edge at 0.6 keV has been found.

4.4.16 H1722+119

H1722+119 was observed only once by EXOSAT, at a relatively bright emission level (Table 3.2.b). The count rates of the source are comparable to the low state of H0323+022, both in the LE and in the ME bands. The good quality of the spectrum (QF=4) allowed us to retain it from the database and to perform a spectral study. Signal was found in the range 0.1 – 6 keV.

The fits to the LE + ME data are not good. Inspection of the residuals in the figure of Appendix C reveals that the fit with a simple power law is poor between 1 and 3 keV. As a comparison of the indexes in columns 5 and 7 of Table 4.1.b suggests weak indication for a spectral break is present in the data. Modelling the data with a broken power law (section 4) is consistent with a steepening at $E_0 \sim 2$ keV, with $\alpha_1 \sim 2.2$ and $\alpha_2 \sim 2.6$, $\Delta\chi^2 = 3$, but the probability that the improvement is significant is negligible. A comparison of the intensities of the source in the previous X-ray missions (Table 3.4.b) shows that at the time of the EXOSAT observations H1722+119 was in a low state.

4.4.17 I ZW 186

I ZW 186 was observed twice by EXOSAT in 1984. In both cases, the ME count rates were significant at $\geq 5\sigma$ level. The log of the EXOSAT observations is reported in Table 3.2.b. The 84.063 observation, during which not all the detectors were on, required a re-extraction.

The source flux was detected in the range 0.1 – 6.0 keV. We studied the spectra with a single power law model (Table 4.1.b). The high χ^2 values must be attributed to the low s/n, in particular for the 84.063 observation. There is a

weak indication for a variable photon index, which is flatter in the 84.063 date, in agreement with that found in the previous HEAO 1 spectrum (Table 3.4.b). For the 84.181 epoch, during which the source was in a soft mode, it is steeper. Our results are in close agreement with those found by Garilli & Maccagni (1990; see Table A).

If compared to the EXOSAT results, the ROSAT slope is flatter. This slope is also the flattest (with that found for H1426+428, see above) for the entire sample of BL Lacs observed by ROSAT, for which the average slope is 2.39 ± 0.07 (Fink *et al.* 1992b). In the 84.181 observation an indication for a break at lower energies is present. A fit with a broken power law gave maximum improvement when $E_0 = 2$ keV, but this was not significant.

We conclude that the X-ray spectrum of I ZW 186 is consistent with being described by a single power law.

4.4.18 PKS 2005-489

This BL Lac was observed by EXOSAT on several occasions (Table 3.2.b). All the ME observations satisfied the 5σ detection criterion. However, only the 84.254 spectrum could be retrieved from the database, having a satisfactory background subtraction. The remaining observations were re-extracted.

The signal covers the energy range 0.1 – 6 keV, except for the 84.254 and 84.287 observations, in which positive emission was detected up to 9 keV. In these latter epochs PKS 2005-489 was in a high state, as Table 3.2.b shows. These are the better quality spectra, while the lowest s/n is found in the low state (85.145 observation). The results of the spectral fits with a single power law are reported in Table 4.1.b. Except for the high states the power law fits

the data well. The index is variable with an indication of steepening when the intensity decreases.

The better quality observations (84.254 and 84.287) were previously studied by Wall *et al.* (1986). It is unclear whether these observations were retrieved from the database or re-extracted. For the 84.254 epoch, which was retained from the database and which corresponds to the low state in Table A, our results are marginally consistent with those obtained by Wall *et al.*, while they are in agreement for the 84.287 (high state in Table A) observing epoch.

In Table 4.1.b, the fits with a single power law are not acceptable in the 84.254 and 84.287 observations. Fitting with a two component model yields the results reported in Table 4.3.b. Both high state spectra are well fitted by a convex broken power law, with a break at $E_0 \sim 2$ keV in the 84.254 epoch, and at $E_0 \sim 4$ keV in the 84.287 epoch. In the latter observation the 2 – 6 keV flux is $\sim 55\%$ higher than in the former one. A dependence of the energy break on the intensity was previously noted for PKS 0548-322. Weak indication for a two component spectrum is present also in the 84.145 and 85.276 data. However, in the former case the evidence is not actually believable due to the large errors on the index in column 5. In the latter case, the F-test showed it is not significant.

In the 84.287 epoch, the χ^2 of the fit with the broken power law (1.58/27) gets even better if an absorption feature at low energy is added. In fact, this model yields $\chi^2 = 0.90/25$, with $E_{line} = 0.55^{+0.10}_{-0.07}$ keV.

We conclude that only in the high states, where the quality of the data is better, there is indication for a two component (convex) spectrum. The energy break moves depending on the intensity level. There is also evidence for a correlation between the spectral index and the intensity, in the sense of a hardening when the source brightens.

4.4.19 PKS 2155-304

The EXOSAT observations of PKS 2155-304 are nine in total. All were re-extracted. The observing log is given in Table 3.2.b. In the 84.311 and 84.312 epochs the source was extremely variable and these observations were split into four parts (A, B, C, and D) corresponding to different filters used in the LE experiment. Because of the variability these data were treated as from separate observations.

In general a net signal was detected in an extended range, up to 9 – 10 keV, except on a few occasions corresponding to lower states. The spectra were fitted first with a power law model and the results are reported in Table 4.1.b. In general, the simple power law is not adequate to describe the data. One can see this from the large values of the χ^2 in Table 4.1.b. For clarity, each spectrum will be discussed briefly below. In addition to the broken power law model, we also tried on the data models involving an absorption edge at 0.6 keV. This feature was originally discovered in the *Einstein* spectrum by Canizares & Kruper (1984). Its presence has been more recently confirmed in the *Einstein* SSS data by Madejski *et al.* (1991) and in the BBXRT spectrum by Madejski *et al.* (1992).

• *84.311 A.*

In this case the poorer fit is that performed on the overall spectrum when N_H is fixed. The photon index is greater than that of the ME data alone (columns 7 and 5). When N_H is allowed to vary the fitted absorption in column 10 is less than the Galactic value. This indicates a soft excess. The results of the fit with a two component model are given in Table 4.3.b. A concave up spectrum, with a flattening above 1 keV, is highly preferred to the power law and is a good description of the data ($\chi^2_r = 1.00/17$). A power law with an absorption edge at

0.6 keV is also acceptable but gives a higher χ^2 (1.17/16).

• *84.311 C.*

The fit with a power law is not acceptable for this spectrum. The χ^2 is large both for the ME and the LE + ME data. The slope obtained when the LE data point is added is higher than the slope of the ME data alone, and the fitted absorption is less than the Galactic value. Also in this case indication for a soft excess is derived. The fit with a soft excess is highly preferred over a simple power law, as reported in Table 4.3.b, but the χ^2 obtained is still rather high. The inspection of the residuals of the fit shows that a deficiency of photons is present at $\sim$ 7 keV. If an absorption feature at $\sim$ 7 keV is added to the broken power law, the fit improves (χ^2_r = 1.17/24). Actually, E_{line} = 6.6 $\pm$ 0.3 keV. A fit with a single power law plus an absorption edge at 0.6 keV is unable to converge.

• *84.311 D.*

This case is analogous to 84.311 A above. The fit with a power law is unacceptably high when the LE + ME data are fitted with fixed N_H and yields a slope steeper than that of the ME data alone. Here also the fit with a two component model is preferred with high significance when a flattening above 1 keV is included. The fit with a single power law plus an absorption edge is equally acceptable (χ^2_r = 1.09/24), even though the line edge is best fitted at 1.4 $\pm$ 0.7 keV.

• *84.312 D.*

As Table 4.1.b shows unacceptable results are obtained when fitting both the ME and the combined LE + ME spectrum with a simple power law. The inspection of the residuals shows that a systematic downward trend is present above 5 keV, suggesting a convex down spectrum with a break at higher energies. In fact, the fit with a broken power law model with $E_0 \sim$ 5 keV is preferred at

the 97.5% confidence level (Table 4.3.b). However, this fit is also not completely satisfactory. A even better description of the data is obtained when an absorption edge at 0.6 keV is added to the broken power law. This yields χ^2_r= 1.09/24. A broken power law with a break at 2 – 3 keV plus a 0.6 keV edge was required to explain the BBXRT data of PKS 2155-304 (Madejski *et al.* 1992).

• *84.316.*

The fit to the ME data with a power law with N_H fixed is not good. However, if the absorption is allowed to vary a better fit is obtained, with the fitted N_H in excess to the Galactic value. Equally unacceptable fits are obtained for the LE + ME data. However, no indication for curvature can be found. The fact that the ME data alone are better fit by a power law model with N_H greater than the interstellar value may indicate that some depression is present below 1 keV, not due to the interstellar matter. In fact, adding an absorption edge at 0.6 keV yields a better fit to the overall spectrum ($\chi^2_r = 1.12/27$).

• *85.306.*

Here the same happens as for the 84.312 D spectrum above. The large χ^2 of the power law model is due to a loss of photons at higher energies. The fit with a broken power law model with a break at 5 keV is highly preferred.

• *85.316.*

The spectrum covers a restricted energy range. The cause of the bad fit with a power law can be attributed to two data points at 4 and 6 keV, respectively, which are below the fit. Excluding these two points, the power law is acceptable, $\chi^2_r = 0.79/16$. We can not conclude however that the power law is the only representation of the data. If a break were present at higher energies, as discussed above, we could not detect it because of the limited energy coverage.

• *85.297.*

This corresponds to the highest state of the source. A bad fit with the power law

model is obtained both for the ME and LE + ME data. In addition, the slope derived when the LE data point is added is less than the ME slope, evidence for a curved spectrum. A two component model (convex spectrum) with $E_0 \sim$ 4 keV is highly preferred (Table 4.3.b).

• *85.305.*

In this case the power law is formally acceptable but indication for spectral curvature is derived from the slopes in columns 7 and 5. The spectrum flattens when the LE data is added. As reported in Table 4.3.b, a broken power law yields a better fit at the 95% confidence level, with $E_0 \sim 1$ keV and indicates a convex spectrum.

• *83.304.*

This observation was obtained when the source was in the lowest state. The high χ^2 should be attributed to fluctuations of the data points due to the subtraction of a high background.

• *83.333.*

The fit with a single power law is not acceptable here for the LE + ME data. The broken power law model is not preferred over a power law. Instead, a power law plus an absorption edge at low energy gives a better fit ($\chi^2 = 0.73/22$), even if the spectral parameters are poorly determined ($\alpha \sim 2.75$, $E_{line} \sim 0.44$ keV).

The EXOSAT observations were previously examined by Treves *et al.* (1989), with the results summarized for the high and the low states in Table A. All the considered spectra were re-extracted. The 84.311 and 84.312 observations were not split into four parts, and correspond, with the 85.297 epoch, to the higher state of the source. The remaining observations (83.304, 83.333, 84.316, 85.305, 85.306, and 85.316) correspond to the lower state in Table A. Concerning the higher state, our results agree well with the results of Treves *et al.* only for the 84.311 epoch ($\langle\alpha\rangle \sim 2.4$, $\langle N_H\rangle \sim 1.2 \times 10^{20}$ cm^{-2}). In the case of the 84.312

epoch Treves *et al.* found values for the photon index and the absorption which are equal to those of the 84.312 D date in Table 4.3.b. Note, however, that this segment of the 84.312 observation corresponds to the higher flux and should be dominant in a joint fit. For the 85.297 observation, the results of Treves *et al.* are marginally consistent with ours, the photon index being slightly flatter. In the case of the lower state, our results and those of Treves *et al.* are in good agreement, except for the 85.305 and 85.306 dates, in which the reported photon indexes are flatter than ours, as for the 85.297 high state. This may be attributed to a different background subtraction. Note that in all cases the above authors found a better fit including a 0.6 keV absorbing feature (see Chapter 6).

PKS 2155-304 is a bright and frequently observed BL Lac, therefore a large body of data is available. Two main points are addressed by the results summarized in Table 3.4.b, the first concerning the shape of the spectrum and the second the spectral variability.

As discussed in Urry *et al.* (1986), the spectra obtained from the HEAO 1 and the *Einstein* observations are compatible with a two component, concave up model. The HEAO 1 A2 data reported by Urry & Mushotszky (1982), in fact, required a hard tail, dominant above $\sim$ 10 keV. In the *Einstein* observations, the MPC data of 1979 May 15 and 26 indicate keV a flat component above $\sim$ 10 at roughly the same intensity as in the HEAO 1 A2 observations, $\sim 10^{-4}$ photons cm^{-2} s^{-1} keV^{-1} (Urry *et al.* 1986). In general, as apparent from Table 3.4.b, the HEAO 1 A2 and the *Einstein* SSS observations suggest a low energy, steep spectrum with $\alpha \sim 2.5$ (Agrawal & Riegler 1979; Urry & Mushotzky 1982; Urry *et al.* 1986). An even steeper spectrum is obtained at the lower energies sampled by the OGS observations (Canizares & Kruper 1984).

The hard tail found in the HEAO 1 data is not confirmed in the GINGA data, (Ohashi *et al.* 1989; Sembay *et al.* 1992), although this satellite sampled

an energy range up to 35 keV. In early 1987 observations, Ohashi *et al.* found consistent spectral indexes in two disjoint energy ranges, 2 – 10 keV and 10 – 37 keV. In later data Sembay *et al.* fitted the best quality spectrum with a broken power law and found a steepening above $E_0 \sim 3.3$ keV. All these latter data are best fitted by a convex down model, with $\langle E_0 \rangle = 3.8 \pm 0.2$ keV and $\Delta\alpha \sim 0.2$, with a constant degree of curvature. No spectral features in emission nor in absorption were significantly detected in the GINGA data.

A more complex spectrum is that suggested by the BBXRT data (Madejski *et al.* 1992), which requires a broken power law with a steepening above 2 – 3 keV, plus an absorption feature at 0.6 keV. Such a feature, originally discovered in the OGS data by Canizares & Kruper (1984), was also confirmed in the *Einstein* SSS data (Madejski *et al.* 1991).

Therefore, a complex picture emerges from the discussion above. It seems that the spectrum of PKS 2155-304 consists of more components. Evidence for a hard tail was found on a few occasions, and a downward curved spectrum has also been claimed. In addition, an absorption edge at lower energies is sometimes detected in the experiments with the best spectral resolution. As we discussed above, the EXOSAT data fully support these previous findings. Both convex and concave spectra are found, the latter having, however, a soft excess rather than a hard tail (this could suggest that the break can move). In the best exposed spectra an emission feature at 7 keV is detected, and the absorption edge at low energy can not be ruled out.

Concerning the spectral variability, no clear information can be derived from the data collected by the early X-ray missions. Urry *et al.* (1986), who analyzed the *Einstein* SSS data, first reported a brightening of the source accompanied by a steepening of the spectrum. In the early GINGA data a dramatic intensity variability is found unaccompanied by substantial spectral

change (Ohashi *et al.* 1989), while in the later observations a discontinuous trend is found (Sembay *et al.* 1992). In fact, in these latter data the hardness ratio of the count rates in different energy ranges shows an anti-correlation between the intensity and the spectral index, in the sense of a hardening when the source brightens. However, in some flaring episodes a positive correlation is found instead. In the EXOSAT data, as is shown is Figure 4.4 where the LE+ME spectral index is plotted against the 2 – 6 keV count rate, a general trend pointing towards an anti-correlation is visible. However, if some small portions of the plot are isolated the trend is no longer the same, the slope *increasing* with increasing intensity. These 'local' deviations were also noted by Treves *et al.* (1989) from the analysis of the hardness ratios, and show that the spectral variability in PKS 2155-304 is more complex than apparent.

In summary, it seems that the X-ray spectrum of PKS 2155-304 is much more complex than a simple power law. The correlation slope-intensity also seems more complex than a linear one.

4.5 Results for individual objects: HPQ – OVV

4.5.1 Ton 599

The HPQ Ton 599 was observed 13 times by EXOSAT. Only three observations satisfied the ME selection criteria, the relevant information is summarized in Table 3.2.c.

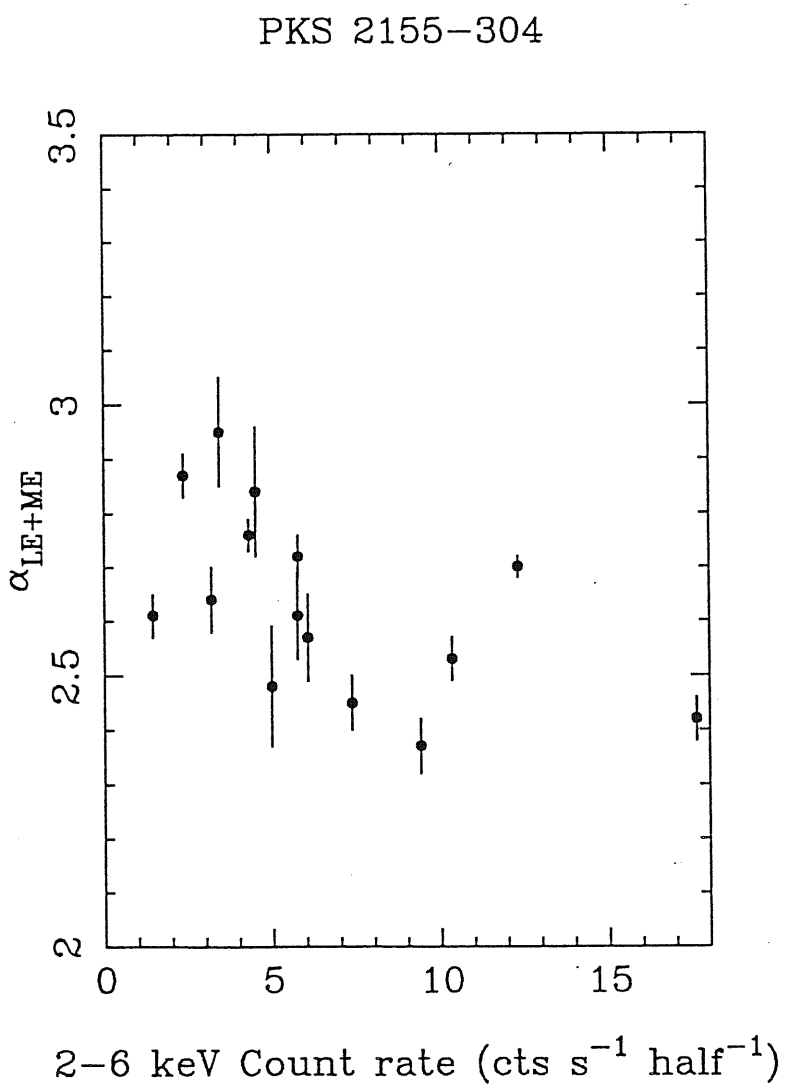

Figure 4.4: Spectral variability of PKS 2155-304. The spectral index from the fit to the 0.1 – 10 keV spectra with a power law (free absorption) is plotted against the 2 – 6 keV count rate. Uncertainties on the slope are at 90% confidence errors.

The emission is found up to $\sim$ 5 keV. The spectra were fitted with a power law model (Table 4.1.c). Except for the first observation, the power law fits the data well. Apparently a flattening is obtained when the LE data points are added to the ME ones. The fit with the broken power law model is not significantly improved in any case. No spectral variability is present; the average index from a fit to the 0.1 – 10 keV spectrum (with fixed N_H) is 1.66 $\pm$ 0.03.

4.5.2 PKS 1510-08

Three observations are available from the EXOSAT database for this source. All three satisfied the selection criteria described in Chapter 2 and were retained from the archive. As can be seen from Table 3.2.c the 1984 observations were taken on two consecutive days, with no difference in ME count rate, and are higher with respect to the 1985 observing date. All three spectra were studied by Singh *et al.* (1990), whose results are consistent with ours (Table A).

The source emits in an extended energy range, 0.1 – 8 keV. The power law model fits gave the results reported in Table 4.1.c. The ME data for the 84.216 and 84.217 observations were fitted together. It can be seen that the spectrum of PKS 1510-08 is consistent with a rather flat slope, $\alpha \sim 1.3$, in the 1984 observations, and is slightly steeper, $\alpha \sim 1.6$, in the lower state of 1985. The power law model is not completely satisfactory in both occasions. However, in the 1985 observation, the high χ^2 should be due to some fluctuations in the data. More complex models, like the broken power law (which seems to be suggested by the flattening of the spectrum when the LE data points are added), do not improve the fit. For the 1984 data an inspection of the residuals shows a marginal

evidence for an emission line at $\sim$ 5 keV. An improved fit is actually obtained if the data are modelled with a power law plus a gaussian centered at 5 keV and with σ fixed at 0.1 keV ($\alpha = 1.44 \pm 0.10$, $\chi^2_r = 1.05/52$). No improvement of the fit to the 1985 data is obtained by the addition of a feature. As discussed by Singh *et al.* (1990), the feature at $\sim$ 5 keV is consistent with redshifted 6.4 keV and 6.7 keV iron lines.

4.5.3 3C 390.3

3C 390.3 was observed seven times by EXOSAT. Only one observation was rejected. The observing log is reported in Table 3.2.c. On 85.033 the ME observations were taken at two different times. The difference in intensity is only $\sim$ 5%. These two observations, together with the 86.076 epoch, were previously studied by Ghosh & Soundararajaperumal (1991), with results consistent with ours (Table A).

The source was found to emit in the range 0.1 – 9 keV, except on two dates when signal only up to 5 keV was detected. A spectral fit was attempted with the power law model (Table 4.1.c). Although the intensity has not changed between the two observing times of 85.033, the two observations were fitted separately (see below). In all cases except the 86.077 and 85.033 dates, the simple power law is an adequate representation of the data. The slope is variable, ranging from $\sim$ 1.34 in 84.153 to $\sim$ 1.68 in 85.311, with an average 1.47 $\pm$ 0.13. Correlations with intensity changes are not noted.

The worse fits are obtained in the 86.077 and 85.033 observations. In the first case curvature is suggested by the fact that the addition of the LE points considerably flattens the slope of the harder energy points (columns 7 and 5),

and by the fact that, although the errors are large, the fitted N_H is higher than the Galactic one. A fit with a broken power law model with a steepening above 3 keV is preferred at the 97% confidence level (Table 4.3.c).

For the 85.033 observation, case A, the inspection of the residuals reveals a deficiency of photons centered at 5 keV, suggesting the presence of an absorption edge (Appendix C). In fact, the fit improves when an absorption edge is added to the power law. The energy of the edge is best fitted at 5.5 keV, its width at 0.3 keV, and the χ^2 is 1.1/25, yielding an improvement of 16.8 with respect to a simple power law. The 85.033 B data can not be modeled by the inclusion of such a feature. As argued by Ghosh & Soundararajaperumal (1991), the line could be the redshifted 6.4 keV fluorescence line of iron.

Summarizing, 3C 390.3 is, among our HPQ sample, the source for which the most observations are available from EXOSAT. The X-ray spectrum has a variable slope, uncorrelated with the intensity changes. In one occasion, a two component model is preferred, while in another case a well detected absorption feature is present at 5 keV.

4.5.4 PKS 2208-137

EXOSAT observed PKS 2208-137 only once. The ME selection criteria were satisfied by this observation, which was retained from the database (Table 3.2.c).

The signal from this source could be detected up to 7 keV. The spectrum is acceptably described by a single power law with index $\sim$ 1.7, and is among the steepest in Table 4.1.c.

Table 4.1.: Spectral fit results a) RBL

Object	Energy Range	F_{3LX} ($\times 10^{-12}$ ergs cm^{-2} s^{-1})	F_{2-6keV}	ME α	ME χ^2_r/d.o.f.	LE + ME: N_H fixed α	LE + ME: N_H fixed χ^2_r/d.o.f.	LE + ME: N_H free α	LE + ME: N_H free N_H ($\times 10^{20}$ cm^{-2})	LE + ME: N_H free χ^2_r/d.o.f.
(1)	(2)	(3)	(4)	(5)	(6)	(7)	(8)	(9)	(10)	(11)
3C 66A N_H (Gal) = 7.5 × 10^{20} cm^{-2}										
86.006	2 – 5	0.94	3.12	2.17 ± 0.55	1.13/12	1.62 ± 0.2	1.2/13	2.29 ± 0.64	28^{+29}_{-19}	1.1/12
86.015	2 – 5	< 0.30	4.3	2.41 ± 0.65	0.89/12	$1.21^{+0.14}_{-0.12}$	1.5/13	$2.72^{+0.96}_{-0.83}$	68^{+120}_{-37}	0.87/12
86.032	2 – 6	0.61	3.5	2.39 ± 0.27	0.9/16	1.52 ± 0.11	2.9/17	$2.59^{+0.38}_{-0.34}$	48^{+10}_{-10}	1.00/16
0235+169 N_H (Gal) = 9.1 × 10^{20} cm^{-2}										
84.214 + 86.015	2.5 – 6	0.8	1.8	2.10 ± 0.80	1.0/28	$1.89^{+0.25}_{-0.32}$	0.98/29	$2.10^{+0.96}_{-0.85}$	15^{+35}_{-14}	1.0/28
PKS 0521-365 N_H (Gal) = 3.5 × 10^{20} cm^{-2}										
83.306	1.5 – 8.5	2.23	7.2	1.74 ± 0.20	0.76/21	1.52 ± 0.09	0.88/23	1.76 ± 0.22	$9.0^{+7.0}_{-5.0}$	0.75/22
83.334	1.5 – 8	3.4	7.1	1.85 ± 0.33	0.84/20	1.68 ± 0.12	0.85/22	$1.74^{+0.42}_{-0.33}$	$4.0^{+9.0}_{-3.0}$	0.88/21
PKS 0537-441 N_H (Gal) = 4.0 × 10^{20} cm^{-2}										
85.055	1.5 – 7	0.56	2.8	1.3 ± 0.60	0.5/19	$1.26^{+0.24}_{-0.31}$	0.4/20	1.30 ± 0.60	< 30.	0.5/19

Table 4.1.a (continued)

Object	Energy Range	F_{3LX} ($\times 10^{-12}$ ergs cm^{-2} s^{-1})	F_{2-6keV}	ME		LE + ME: N_H fixed		LE + ME: N_H free		
				α	χ^2_r/d.o.f.	α	χ^2_r/d.o.f.	α	N_H ($\times 10^{20}$ cm^{-2})	χ^2_r/d.o.f.
(1)	(2)	(3)	(4)	(5)	(6)	(7)	(8)	(9)	(10)	(11)
PKS 0754+100 N_H (Gal) = 2.7 × 10^{20} cm^{-2}										
84.043	2 – 5	1.25	6.4	2.11 ± 0.65	1.12/11	1.31 ± 0.14	1.6/13	$2.16^{+0.82}_{-1.37}$	< 53.0	1.6/12
OJ 287 N_H (Gal) = 2.7 × 10^{20} cm^{-2}										
83.281	1.5 – 5	6.4	2.7	5.2 ± 1.0	1.2/13	2.16 ± 0.10	4.8/14	$5.87^{+2.00}_{-1.30}$	96^{+64}_{-38}	1.4/13
84.040	2 – 5	8.7	3.7	2.98 ± 0.60	0.53/11	2.37 ± 0.10	1.4/14	2.34 ± 0.20	$2.5^{+1.2}_{-1.0}$	1.5/13
B2 1308+32 N_H (Gal) = 1.1 × 10^{20} cm^{-2}										
85.132	2 – 7	0.73	2.0	$1.65^{+0.78}_{-0.75}$	1.7/19	$1.52^{+0.14}_{-0.16}$	1.6/20	$1.64^{+0.81}_{-0.62}$	2.0 (< 12.0)	1.7/19
3C 371 N_H (Gal) = 4.9 × 10^{20} cm^{-2}										
84.256	1.5 – 7	10.1	3.0	$1.95^{+0.47}_{-0.45}$	0.98/21	$2.86^{+0.10}_{-0.09}$	1.86/24	2.39 ± 0.14	$2.0^{+7.0}_{-5.0}$	1.38/23
84.273	1.5 – 6	4.8	1.6	1.86 ± 0.52	0.38/15	2.73 ± 0.10	54/17	2.36 ± 0.24	2.0 ± 1.0	0.43/16

Table 4.1.: b) XBL

Object	Energy Range	F_{3LX} ($\times 10^{-12}$ ergs cm^{-2} s^{-1})	F_{2-6keV}	ME		LE + ME: N_H fixed		LE + ME: N_H free		
				α	χ^2_r/d.o.f.	α	χ^2_r/d.o.f.	α	N_H ($\times 10^{20}$ cm^{-2})	χ^2_r/d.o.f.
(1)	(2)	(3)	(4)	(5)	(6)	(7)	(8)	(9)	(10)	(11)
MS 0317+18 N_H *(Gal)* $= 9.8 \times 10^{20}$ cm^{-2}										
85.013	1 – 8	2.24	6.9	2.21 ± 0.45	1.7/22	1.80 ± 0.20	1.8/23	$2.20^{+0.53}_{-0.57}$	26^{+170}_{-16}	1.76/22
85.039	1 – 7	1.98	5.0	1.83 ± 0.27	0.7/15	1.84 ± 0.20	0.66/16	1.84 ± 0.30	12^{+10}_{-6}	0.70/15
H 0323+022 N_H *(Gal)* $= 8.4 \times 10^{20}$ cm^{-2}										
84.265	1 – 6	6.8	4.3	$2.81^{+0.34}_{-0.31}$	0.72/16	2.73 ± 0.10	0.67/19	$2.83^{+0.30}_{-0.27}$	$10^{+6.0}_{-9.9}$	0.70/18
84.267	1 – 6	8.0	6.5	2.45 ± 0.30	0.64/13	2.37 ± 0.09	0.78/14	2.46 ± 0.36	$9.9^{+7.3}_{-5.0}$	0.83/13
H 0414+009 N_H *(Gal)* $= 8.6 \times 10^{20}$ cm^{-2}										
84.253	1.5 – 10	9.0	16.2	1.90 ± 0.10	1.07/25	1.94 ± 0.07	1.03/28	1.91 ± 0.11	$7.4^{+3.7}_{-2.3}$	1.06/27
84.258	1.5 – 10	9.5	18.9	1.89 ± 0.09	0.73/30	1.90 ± 0.08	0.9/32	1.89 ± 0.09	$7.7^{+2.3}_{-2.1}$	0.7/31
84.266	1.5 – 6.5	9.5	12.0	2.34 ± 0.16	0.73/21	2.15 ± 0.07	1.00/23	2.36 ± 0.18	14.0 ± 5.0	0.83/22
84.274	1.5 – 6.5	9.8	9.3	2.49 ± 0.20	0.94/21	2.34 ± 0.08	1.05/24	2.42 ± 0.21	$10.2^{+5.8}_{-4.0}$	1.07/23

Table 4.1.b (continued)

Object	Energy Range	F_{3LX}	F_{2-6keV}	ME		LE + ME: N_H fixed		LE + ME: N_H free		
		($\times 10^{-12}$ ergs cm^{-2} s^{-1})		α	χ^2_r/d.o.f.	α	χ^2_r/d.o.f.	α	N_H ($\times 10^{20}$ cm^{-2})	χ^2_r/d.o.f.
(1)	(2)	(3)	(4)	(5)	(6)	(7)	(8)	(9)	(10)	(11)
EXO 0423-0840 N_H *(Gal)* $= 6.2 \times 10^{20}$ cm^{-2}										
85.048	1.5 – 10	0.12	24	2.27 ± 0.10	1.05/25	1.13 ± 0.07	7.0/26	2.80 ± 0.30	133^{+600}_{-39}	1.13/25
85.267	1.5 – 10	< 0.44	14	2.46 ± 0.08	1.3/25	1.09 ± 0.06	16.8/26	3.41 ± 0.33	218^{+57}_{-44}	1.5/25
EXO 0507-04 N_H *(Gal)* $= 7.5 \times 10^{20}$ cm^{-2}										
84.298	1.5 – 5	4.2	10.4	1.79 ± 0.63	0.65/12	$1.77^{+0.23}_{-0.28}$	0.60/13	$1.79^{+0.70}_{-0.67}$	$7.9^{+0.70}_{-7.2}$	0.65/12
PKS 0548-322 N_H *(Gal)* $= 2.3 \times 10^{20}$ cm^{-2}										
83.306	1.5 – 8	19.0	22.0	2.37 ± 0.08	0.99/22	1.99 ± 0.03	4.2/25	$2.28^{+0.12}_{-0.08}$	6.0 ± 1.0	2.4/24
83.334	1.5 – 9	18.8	21.0	1.77 ± 0.33	1.16/25	1.98 ± 0.06	0.7/28	2.09 ± 0.11	4.0 ± 1.6	0.6/27
86.066	1.5 – 9	15.0	14.6	2.08 ± 0.09	1.56/25	2.01 ± 0.02	1.56/26	2.09 ± 0.09	2.8 ± 0.5	1.53/25
EXO 0557-3838 N_H *(Gal)* $= 3.9 \times 10^{20}$ cm^{-2}										
84.350	1.5 – 5	9.1	19.6	1.76 ± 0.10	0.87/13	1.72 ± 0.05	0.87/14	1.77 ± 0.11	$4.8^{+2.1}_{-1.5}$	0.87/13

Table 4.1.b (continued)

Object	Energy Range	F_{3LX} ($\times 10^{-12}$ ergs cm^{-2} s^{-1})	F_{2-6keV} ($\times 10^{-12}$ ergs cm^{-2} s^{-1})	ME α	ME χ^2_r/d.o.f.	LE + ME: N_H fixed α	LE + ME: N_H fixed χ^2_r/d.o.f.	LE + ME: N_H free α	LE + ME: N_H free N_H ($\times 10^{20}$ cm^{-2})	LE + ME: N_H free χ^2_r/d.o.f.
(1)	(2)	(3)	(4)	(5)	(6)	(7)	(8)	(9)	(10)	(11)
86.021	1.5 – 10	6.8	7.14	1.40 ± 0.15	1.06/26	1.85 ± 0.13	2.4/27	1.43 ± 0.15	$0.4^{+0.5}_{-0.0}$	1.06/26
Mrk 421	N_H (Gal) = 1.8×10^{20} cm^{-2}									
85.126	1 – 8	61.2	13.0	2.67 ± 0.09	0.82/19	2.63 ± 0.02	1.06/22	2.64 ± 0.06	2.0 ± 0.1	1.11/21
85.141	1 – 9	55.0	14.5	2.48 ± 0.13	0.6/26	2.53 ± 0.02	0.6/25	2.47 ± 0.08	1.6 ± 0.2	0.53/24
85.112	1 – 9	80.	21.2	2.60 ± 0.07	0.73/26	2.53 ± 0.02	0.7/27	2.57 ± 0.05	2.0 ± 0.2	0.65/26
85.118	1 – 9	72.	21.2	2.33 ± 0.33	0.68/27	2.44 ± 0.02	1.8/30	2.30 ± 0.05	1.1 ± 0.2	0.92/29
85.131	1 – 7	70.	21.2	2.41 ± 0.07	1.27/20	2.52 ± 0.02	1.88/23	2.42 ± 0.07	1.4 ± 0.2	1.5/22
85.132	1 – 8	66.	13.	2.78 ± 0.22	0.81/23	2.66 ± 0.03	0.81/24	2.76 ± 0.22	2.3 ± 1.0	0.81/23
84.032	1 – 7	72.	9.7	2.93 ± 0.22	1.77/19	2.79 ± 0.03	1.87/21	...	...	...
84.033	2 – 4	47.	4.1	$4.19^{+1.59}_{-1.22}$	0.74/9	$2.85^{+0.14}_{-0.10}$	1.08/12	$2.72^{+0.21}_{-0.19}$	1.4 ± 0.5	1.02/11
84.035	1 – 6	61.	7.8	$2.01^{+0.49}_{-0.46}$	1.1/17	2.82 ± 0.07	1.33/20	2.75 ± 0.14	1.5 ± 0.4	1.3/19
84.037	1.5 – 5	69.6	9.7	2.94 ± 0.21	0.9/12	2.73 ± 0.03	1.3/16	2.66 ± 0.10	$1.5^{+0.4}_{-0.3}$	1.2/15

Table 4.1.b (continued)

Object	Energy Range	F_{3LX} ($\times 10^{-12}$ ergs cm^{-2} s^{-1})	F_{2-6keV} ($\times 10^{-12}$ ergs cm^{-2} s^{-1})	ME		LE + ME: N_H fixed		LE + ME: N_H free		
				α	χ^2_r/d.o.f.	α	χ^2_r/d.o.f.	α	N_H ($\times 10^{20}$ cm^{-2})	χ^2_r/d.o.f.
(1)	(2)	(3)	(4)	(5)	(6)	(7)	(8)	(9)	(10)	(11)
85.004	1.5 – 9	68.	12.	2.50 ± 0.17	0.95/27	2.67 ± 0.04	1.14/30	2.57 ± 0.12	1.4 ± 0.4	1.1/29
84.340	1.5 – 10	156	99.4	2.34 ± 0.04	1.7/25	2.18 ± 0.02	3.4/28	2.28 ± 0.04	2.6 ± 0.3	2.4/27
84.337	1.5 – 11	120	80	2.18 ± 0.03	1.17/31	2.14 ± 0.02	1.53/34	2.16 ± 0.03	1.9 ± 2.0	1.5/33
84.338	1.5 – 11	160	100	2.18 ± 0.02	1.9/31	2.15 ± 0.01	2.5/34	2.16 ± 0.02	1.9 ± 0.1	2.52/33
Mrk 180	N_H (Gal) = 1.4 × 10^{20} cm^{-2}									
84.308	1.5 – 6	9.3	1.12	$3.80^{+1.46}_{-1.18}$	1.44/15	2.80 ± 0.20	1.44/17	$3.10^{+0.50}_{-0.40}$	2.6 ± 2.0	1.43/16
84.333	1.5 – 5	12.	2.8	$3.73^{+0.97}_{-0.83}$	2.3/15	2.50 ± 0.10	1.5/15	$2.83^{+0.30}_{-0.26}$	$3.0^{+0.1}_{-10}$	1.22/14
85.093	1.5 – 5	22	7.3	$2.29^{+0.37}_{-0.35}$	0.68/14	2.34 ± 0.06	0.6/18	2.34 ± 0.16	$1.4^{+0.8}_{-0.5}$	0.6/17
1218+304	N_H (Gal) = 1.7 × 10^{20} cm^{-2}									
85.029	1 – 8	26.1	15.0	2.46 ± 0.14	0.7/21	2.21 ± 0.03	1.7/25	2.41 ± 0.09	$2.8^{+0.7}_{-0.5}$	1.2/24
85.005	1 – 9	29.2	22.0	2.35 ± 0.08	0.8/25	2.11 ± 0.03	1.65/28	2.32 ± 0.07	3.2 ± 0.6	0.78/27
84.356	1 – 7.5	30.0	22.0	2.53 ± 0.11	1.3/20	2.11 ± 0.03	4.3/23	2.35 ± 0.08	3.5 ± 0.7	3/22

Table 4.1.b (continued)

Object	Energy Range	F_{3LX} ($\times 10^{-12}$ ergs cm^{-2} s^{-1})	F_{2-6keV}	ME		LE + ME: N_H fixed		LE + ME: N_H free		
				α	χ^2_r/d.o.f.	α	χ^2_r/d.o.f.	α	N_H ($\times 10^{20}$ cm^{-2})	χ^2_r/d.o.f.
(1)	(2)	(3)	(4)	(5)	(6)	(7)	(8)	(9)	(10)	(11)
2A 1235+63 N_H (Gal) = 1.7 × 10^{20} cm^{-2}										
85.079	1.5 – 5	0.4	1.7	2.34 ± 0.43	0.93/40	1.41 ± 0.10	1.23/42	$2.45^{+0.53}_{-0.48}$	$24.^{+17}_{-23}$	0.9/41
1402+04 N_H (Gal) = 2.2 × 10^{20} cm^{-2}										
85.031	1.5 – 7	4.64	2.18	$2.43^{+0.77}_{-0.73}$	0.9/12	$2.32^{+0.12}_{-0.10}$	0.84/13	$2.43^{+0.82}_{-0.74}$	< 100	0.9/12
85.187	2 – 5	2.14	1.4	$2.66^{+1.15}_{-1.03}$	1.27/9	2.10 ± 0.15	1.22/10	$2.70^{+1.30}_{-1.00}$	< 30	1.27/9
E 1415+22 N_H (Gal) = 1.6 × 10^{20} cm^{-2}										
86.063	1.5 – 5	0.23	6.0	2.74 ± 0.34	0.61/11	0.83 ± 0.10	8.0/12	$3.34^{+0.58}_{-0.51}$	110^{+43}_{-32}	0.8/11
H 1426+428 N_H (Gal) = 1.4 × 10^{20} cm^{-2}										
85.012	1.5 – 9	41	34.7	2.10 ± 0.07	0.80/25	2.06 ± 0.02	0.80/26	2.10 ± 0.07	1.8 ± 0.3	0.80/25
85.055	1.5 – 9	36	33.8	2.08 ± 0.10	0.70/25	1.95 ± 0.03	1.30/28	1.98 ± 0.09	$1.5^{+0.5}_{-0.4}$	1.34/27
Mrk 501 N_H (Gal) = 1.7 × 10^{20} cm^{-2}										
84.183	1.5 – 9	56.	4.3	2.64 ± 0.14	0.97/25	2.44 ± 0.03	1.13/28	2.49 ± 0.09	2.0 ± 0.5	1.13/27

Table 4.1.b (continued)

Object	Energy Range	F_{3LX} ($\times 10^{-12}$ ergs cm^{-2} s^{-1})	F_{2-6keV}	ME		LE + ME: N_H fixed		LE + ME: N_H free		
				α	χ^2_r/d.o.f.	α	χ^2_r/d.o.f.	α	N_H ($\times 10^{20}$ cm^{-2})	χ^2_r/d.o.f.
(1)	(2)	(3)	(4)	(5)	(6)	(7)	(8)	(9)	(10)	(11)
84.191	1.5 – 9	51.	4.7	2.52 ± 0.18	1.03/25	2.37 ± 0.03	1.10/28	2.42 ± 0.11	2.0 ± 0.5	1.1/27
84.201	1.5 – 9	50	20	2.46 ± 0.09	1.10/23	2.35 ± 0.03	1.4/26	2.40 ± 0.07	2.0 ± 0.4	1.4/25
84.207	1.5 – 9	53.4	12	2.30 ± 0.22	0.45/25	2.62 ± 0.04	0.8/27	2.61 ± 0.14	$1.6^{+0.7}_{-0.4}$	0.84/26
84.209	1.5 – 9	50.6	23	2.50 ± 0.10	1.07/25	2.31 ± 0.01	1.3/28	2.43 ± 0.08	2.4 ± 0.5	1.1/27
84.086	1.5 – 9	52.	33	2.21 ± 0.11	0.6/25	2.16 ± 0.04	0.85/28	2.17 ± 0.09	$1.9^{+7.0}_{-5.0}$	0.87/27
84.034	1.5 – 10	59	33	2.48 ± 0.06	1.03/25	2.23 ± 0.02	3.00/28	2.45 ± 0.05	$3.0^{+0.6}_{-0.3}$	1.22/27
84.036	1.5 – 6	59	27	2.60 ± 0.17	1.06/14	2.28 ± 0.03	1.45/18	2.35 ± 0.08	2.0 ± 0.4	1.42/17
85.099	1.5 – 9	51	16.4	2.64 ± 0.11	1.00/24	2.45 ± 0.03	1.23/28	2.57 ± 0.07	$2.3^{+7.0}_{-1.0}$	0.97/27
86.074	1.5 – 9	53	31.1	2.37 ± 0.03	1.1/24	2.19 ± 0.01	5.11/26	2.37 ± 0.03	3.0 ± 0.1	1.24/25
H 1722+119 N_H (Gal) = 8.6 × 10^{20} cm^{-2}										
85.246	1 – 6	6.4	6.1	2.65 ± 0.25	0.74/18	2.35 ± 0.09	1.10/21	$2.44^{+0.26}_{-0.24}$	$11.0^{+7.0}_{-4.0}$	1.13/20

Table 4.1.b (continued)

Object	Energy Range	F_{3LX} ($\times 10^{-12}$ ergs cm^{-2} s^{-1})	F_{2-6keV}	ME		LE + ME: N_H fixed		LE + ME: N_H free		
				α	χ^2_r/d.o.f.	α	χ^2_r/d.o.f.	α	N_H ($\times 10^{20}$ cm^{-2})	χ^2_r/d.o.f.
(1)	(2)	(3)	(4)	(5)	(6)	(7)	(8)	(9)	(10)	(11)
I Zw 186 N_H *(Gal)* $= 2.7 \times 10^{20}$ cm^{-2}										
84.063	1.5 – 6	10.8	6.0	$2.26^{+0.62}_{-0.58}$	0.73/15	2.30 ± 0.12	1.72/18	2.25 ± 0.21	2.5 ± 0.9	1.8/17
84.181	1.5 – 6	14.	5.83	2.82 ± 0.21	1.08/15	2.41 ± 0.05	2.13/18	$2.72^{+0.22}_{-0.19}$	$5.0^{+2.0}_{-1.0}$	1.2/16
PKS 2005-489 N_H *(Gal)* $= 4.6 \times 10^{20}$ cm^{-2}										
84.254	1.5 – 9	95	21.3	3.06 ± 0.07	0.84/25	2.88 ± 0.03	1.7/28	2.96 ± 0.06	5.5 ± 0.7	1.5/27
84.287	1.5 – 9	130	47.6	2.68 ± 0.04	1.69/25	2.62 ± 0.02	2.60/28	2.65 ± 0.05	5.0 ± 0.6	2.7/27
85.145	1.5 – 4.5	11.2	1.1	$3.70^{+1.60}_{-1.30}$	0.3/11	$3.20^{+0.20}_{-0.14}$	0.3/14	$3.19^{+0.41}_{-0.34}$	4.5 ± 3.0	0.3/13
85.276	1.5 – 6	13	2.87	$3.56^{+1.07}_{-0.86}$	0.5/15	2.90 ± 0.15	0.54/17	$2.97^{+0.50}_{-0.30}$	$5.2^{+5.0}_{-2.0}$	0.6/16
85.289	1.5 – 6	26.3	3.3	3.20 ± 0.70	0.52/17	$3.27^{+0.10}_{-0.09}$	0.65/18	$3.17^{+0.21}_{-0.19}$	4.0 ± 1.0	0.64/17
PKS 2155-304 N_H *(Gal)* $= 1.8 \times 10^{20}$ cm^{-2}										
84.311 A	1.5 – 6	283	44	2.49 ± 0.11	1.02/17	2.75 ± 0.02	1.87/18	2.48 ± 0.11	$0.9^{+0.3}_{-0.2}$	1.02/17
84.311 B	1.5 – 6	...[a]	54	2.54 ± 0.08	0.9/18	2.58 ± 0.03	0.9/19	2.57 ± 0.08	1.4 ± 0.6	0.9/18

Table 4.1.b (continued)

Object	Energy Range	F_{3LX} ($\times 10^{-12}$ ergs cm^{-2} s^{-1})	F_{2-6keV}	ME		LE + ME: N_H fixed		LE + ME: N_H free		
				α	χ^2_r/d.o.f.	α	χ^2_r/d.o.f.	α	N_H ($\times 10^{20}$ cm^{-2})	χ^2_r/d.o.f.
(1)	(2)	(3)	(4)	(5)	(6)	(7)	(8)	(9)	(10)	(11)
84.311 C	1.5 – 10	...[b]	66	2.45 ± 0.05	1.5/25	2.53 ± 0.04	1.93/26	2.45 ± 0.05	1.0 ± 0.2	1.54/25
84.311 D	1.5 – 10	255	85	2.37 ± 0.05	0.97/25	2.54 ± 0.01	1.90/26	2.37 ± 0.05	1.7 ± 0.2	0.97/25
84.312 A	1.5 – 9	300	40	2.83 ± 0.12	0.4/25	2.82 ± 0.02	0.4/24	2.84 ± 0.12	1.8 ± 0.5	0.4/23
84.312 B	1.5 – 8	...[a]	51.3	2.62 ± 0.08	1.04/20	2.68 ± 0.03	1.04/21	2.61 ± 0.08	$1.4^{+0.5}_{-1.3}$	1.04/20
84.312 C	1.5 – 9	...[b]	94	2.52 ± 0.04	0.9/23	2.51 ± 0.02	0.8/24	2.53 ± 0.03	1.8 ± 0.3	0.8/23
84.312 D	1.5 – 10	460	130	2.42 ± 0.04	2.7/30	2.42 ± 0.01	2.6/31	2.42 ± 0.04	1.8 ± 0.2	2.7/30
84.316	1.5 – 9	330	58	2.72 ± 0.06	1.25/25	2.72 ± 0.04	1.51/28	2.72 ± 0.04	2.9 ± 0.3	1.6/27
84.306	1.5 – 10	270	43	2.76 ± 0.03	2.3/30	$2.74^{+0.0}_{-0.04}$	2.3/31	2.76 ± 0.03	1.8 ± 0.1	2.34/30
85.316	1.5 – 6.5	194	24	2.87 ± 0.04	1.6/17	2.85 ± 0.00	1.5/18	2.87 ± 0.04	1.9 ± 0.2	1.6/17
85.297	1.5 – 10	540	130	2.69 ± 0.02	4.13/25	2.59 ± 0.01	9.6/26	2.70 ± 0.02	2.3 ± 0.1	4.06/25
85.305	1.5 – 10	260	34.3	2.95 ± 0.10	0.6/25	2.81 ± 0.02	0.74/26	2.95 ± 0.11	2.4 ± 0.6	0.6/25

Table 4.1.b (continued)

Object	Energy Range	F_{3LX} ($\times 10^{-12}$ ergs cm^{-2} s^{-1})	F_{2-6kev}	ME		LE + ME: N_H fixed		LE + ME: N_H free		
				α	χ^2_r/d.o.f.	α	χ^2_r/d.o.f.	α	N_H ($\times 10^{20}$ cm^{-2})	χ^2_r/d.o.f.
(1)	(2)	(3)	(4)	(5)	(6)	(7)	(8)	(9)	(10)	(11)
83.304	1.5 – 6	110	15	2.72 ± 0.07	1.0/17	2.77 ± 0.01	4.2/20	2.61 ± 0.04	1.2 ± 0.2	2.5/19
83.333	1.5 – 7	194	34	2.70 ± 0.10	0.96/24	2.70 ± 0.01	2.8/24	2.64 ± 0.06	1.5 ± 0.2	2.8/23

Table 4.1.: c) HPQ

Object	Energy Range	F_{3LX}	F_{2-6keV}	ME		LE + ME: N_H fixed		LE + ME: N_H free		
		($\times 10^{-12}$ ergs cm^{-2} s^{-1})		α	χ^2_r/d.o.f.	α	χ^2_r/d.o.f.	α	N_H ($\times 10^{20}$ cm^{-2})	χ^2_r/d.o.f.
(1)	(2)	(3)	(4)	(5)	(6)	(7)	(8)	(9)	(10)	(11)
Ton 599 N_H *(Gal)* $= 1.5 \times 10^{20}$ cm^{-2}										
84.151	1.5 – 5	2.4	3.0	2.03 ± 0.52	1.2/15	$1.69^{+0.78}_{-0.31}$	1.2/17	$1.70^{+0.77}_{-0.32}$	$2.0^{+15}_{-1.6}$	1.3/16
85.136	1.5 – 5	1.3	2.0	2.60 ± 0.8	0.3/15	1.68 ± 0.31	0.5/17	1.68 ± 0.30	$0.5^{+2.0}_{-0.4}$	0.6/16
85.127	1.5 – 5	1.0	1.5	$2.30^{+0.04}_{-0.90}$	0.7/15	$1.62^{+0.18}_{-0.16}$	0.8/16	$2.30^{+1.10}_{-0.90}$	9.0^{+25}_{-8}	0.7/15
PKS 1510-08 N_H *(Gal)* $= 6.8 \times 10^{20}$ cm^{-2}										
84.216 + 84.217	2 – 9	1.0	4.7	1.34 ± 0.15	1.23/46	1.36 ± 0.11	1.15/53	1.35 ± 0.16	$6.6^{+6.4}_{-3.3}$	1.16/52
85.212	2 – 7	1.1	3.8	1.88 ± 0.32	1.38/18	$1.61^{+0.12}_{-0.14}$	1.4/19	$1.91^{+0.37}_{-0.34}$	$16^{+14}_{-9.0}$	1.4/18
3C 390.3 N_H *(Gal)* $= 4.2 \times 10^{20}$ cm^{-2}										
86.076	1.5 – 9.5	4.5	13	1.58 ± 0.09	0.9/28	1.56 ± 0.06	0.8/31	1.59 ± 0.09	$5.0^{+2.3}_{-1.6}$	0.9/30
86.077	1.5 – 5.	4.7	11.6	2.12 ± 0.22	0.9/13	1.52 ± 0.08	2.6/14	2.23 ± 0.25	$23^{+11}_{-7.0}$	0.9/13
84.153	1.5 – 5	0.7	2.7	2.01 ± 0.53	0.7/11	1.34 ± 0.17	0.9/13	$2.03^{+0.64}_{-0.59}$	23^{+26}_{-17}	0.7/12

Table 4.1.c (continued)

Object	Energy Range	F_{3LX} ($\times 10^{-12}$ ergs cm^{-2} s^{-1})	F_{2-6keV}	ME		LE + ME: N_H fixed		LE + ME: N_H free		
				α	χ^2_r/d.o.f.	α	χ^2_r/d.o.f.	α	N_H ($\times 10^{20}$ cm^{-2})	χ^2_r/d.o.f.
(1)	(2)	(3)	(4)	(5)	(6)	(7)	(8)	(9)	(10)	(11)
85.311	1.5 – 9	6.7	14.2	1.74 ± 0.20	0.8/25	1.68 ± 0.08	0.8/27	1.65 ± 0.15	4.0 ± 2.0	0.8/26
85.033 A	1.5 – 9	4.0	17.0	1.61 ± 0.10	0.7/25	1.36 ± 0.06	1.6/28	1.58 ± 0.14	$16^{+12}_{-8.0}$	1.2/27
85.033 B	1.5 – 9	4.0	16.0	1.53 ± 0.13	1.12/25	1.35 ± 0.07	1.4/28	$1.42^{+0.18}_{-0.12}$	$7.0^{+8.0}_{-4.0}$	1.4/27
PKS 2208-137 N_H *(Gal)* $= 3.3 \times 10^{20}$ cm^{-2}										
84.146	1.5 – 7	1.9	4.0	1.40 ± 0.9	0.97/20	1.66 ± 0.26	0.9/21	$1.39^{+0.90}_{-0.56}$	< 1.4	0.97/20

Notes to Table 4.1

(a) Al-P flux
(b) Bo flux

Table 4.2.: Summary of spectral results a) RBL

Object	Date	α_{ME}	α_{LE+ME}
(1)	(2)	(3)	(4)
3C 66A	86.066	2.17 ± 0.55	1.62 ± 0.2
	86.015	2.41 ± 0.65	$1.21^{+0.14}_{-0.12}$
	86.032	2.39 ± 0.27	1.52 ± 0.11
0235+169	84.214 + 86.015	2.10 ± 0.80	$1.89^{+0.25}_{-0.32}$
PKS 0521-365	83.306	1.74 ± 0.20	1.52 ± 0.09
	83.334	1.85 ± 0.33	1.68 ± 0.12
PKS 0537-441	85.055	1.3 ± 0.60	$1.26^{+0.24}_{-0.31}$
PKS 0754+100	84.043	2.11 ± 0.65	1.31 ± 0.14
OJ 287	83.281	5.20 ± 1.00	2.16 ± 0.10
	84.040	2.98 ± 0.60	2.37 ± 0.10
B2 1308+32	85.132	$1.65^{+0.78}_{-0.75}$	$1.52^{+0.14}_{-0.16}$
3C 371	84.25	$1.95^{+0.47}_{-0.45}$	$2.86^{+0.10}_{-0.09}$
	84.273	1.86 ± 0.52	2.73 ± 0.10

Table 4.2.: b) XBL

Object	Date	α_{ME}	α_{LE+ME}
(1)	(2)	(3)	(4)
MS 0317+18	85.013	2.21 ± 0.45	1.80 ± 0.20
	85.039	1.83 ± 0.27	1.84 ± 0.20
H 0323+022	84.265	$2.81^{+0.34}_{-0.31}$	2.73 ± 0.10
	84.267	2.45 ± 0.30	2.37 ± 0.09
H 0414+009	84.253	1.90 ± 0.10	1.94 ± 0.07
	84.258	1.89 ± 0.09	1.90 ± 0.08
	84.266	2.34 ± 0.16	2.15 ± 0.07
	84.274	2.49 ± 0.20	2.34 ± 0.08
EXO 0423-0840	85.048	2.27 ± 0.10	1.13 ± 0.07
	85.267	2.46 ± 0.08	1.09 ± 0.06
EXO 0507-04	84.298	1.79 ± 0.63	$1.77^{+0.23}_{-0.28}$
PKS 0548-322	83.306	2.37 ± 0.08	1.99 ± 0.03
	83.334	1.77 ± 0.33	1.98 ± 0.06
	86.066	2.08 ± 0.09	2.01 ± 0.02
EXO 0557-3838	84.350	1.76 ± 0.10	1.72 ± 0.05
	86.021	1.40 ± 0.15	1.85 ± 0.13
Mrk 421	85.126	2.67 ± 0.09	2.63 ± 0.02
	85.141	2.48 ± 0.13	2.53 ± 0.02
	85.112	2.60 ± 0.07	2.53 ± 0.02
	85.118	2.33 ± 0.33	2.44 ± 0.02

Table 4.2.b (continued)

Object	Date	α_{ME}	α_{LE+ME}
(1)	(2)	(3)	(4)
	85.131	2.41 ± 0.07	2.52 ± 0.02
	85.132	2.78 ± 0.22	2.66 ± 0.03
	84.032	2.93 ± 0.22	2.79 ± 0.03
	84.033	$4.19^{+1.59}_{-1.22}$	$2.85^{+0.14}_{-0.10}$
	84.035	$2.01^{+0.49}_{-0.46}$	2.82 ± 0.07
	84.037	2.94 ± 0.21	2.73 ± 0.03
	85.004	1.50 ± 0.17	2.67 ± 0.04
	84.340	2.34 ± 0.04	2.18 ± 0.02
	84.337	2.18 ± 0.03	2.14 ± 0.02
	84.338	2.18 ± 0.02	2.15 ± 0.01
Mrk 180	84.308	$3.80^{+1.46}_{-1.18}$	2.80 ± 0.20
	84.333	$3.73^{+0.97}_{-0.83}$	2.50 ± 0.10
	85.093	$2.29^{+0.37}_{-0.35}$	2.34 ± 0.06
1218+304	85.029	2.46 ± 0.13	1.94 ± 0.06
	85.005	2.35 ± 0.08	1.89 ± 0.05
	84.356	2.53 ± 0.10	2.11 ± 0.03
2A 1235+63	85.079	2.34 ± 0.43	1.41 ± 0.10
1402+04	85.031	$2.43^{+0.77}_{-0.73}$	$2.32^{+0.12}_{-0.10}$
	85.187	$2.66^{+1.15}_{-1.03}$	2.10 ± 0.15
E 1415+22	86.063	2.74 ± 0.34	0.83 ± 0.10

Table 4.2.b (continued)

Object	Date	α_{ME}	α_{LE+ME}
(1)	(2)	(3)	(4)
H 1426+428	85.012	2.10 ± 0.07	2.06 ± 0.02
	85.055	2.08 ± 0.10	1.95 ± 0.03
Mrk 501	84.183	2.64 ± 0.14	2.44 ± 0.03
	84.191	2.52 ± 0.18	2.37 ± 0.03
	84.201	2.46 ± 0.09	2.35 ± 0.03
	84.207	2.30 ± 0.22	2.62 ± 0.04
	84.209	2.50 ± 0.10	2.31 ± 0.01
	84.086	2.21 ± 0.11	2.16 ± 0.04
	84.034	2.48 ± 0.06	2.23 ± 0.02
	84.036	2.60 ± 0.17	2.28 ± 0.03
	85.099	2.64 ± 0.11	2.45 ± 0.03
	86.074	2.37 ± 0.03	2.19 ± 0.01
H 1722+119	85.246	2.65 ± 0.25	2.35 ± 0.09
I Zw 186	84.063	$2.26^{+0.62}_{-0.58}$	2.30 ± 0.12
	84.181	2.82 ± 0.21	2.41 ± 0.05
PKS 2005-489	84.254	3.06 ± 0.07	2.88 ± 0.03
	84.287	2.68 ± 0.04	2.62 ± 0.02
	85.145	$3.70^{+1.60}_{-1.30}$	$3.20^{+0.20}_{-0.14}$
	85.276	$3.56^{+1.07}_{-0.86}$	2.90 ± 0.15
	85.289	3.20 ± 0.70	$3.27^{+0.10}_{-0.09}$

Table 4.2.b (continued)

Object	Date	α_{ME}	α_{LE+ME}
(1)	(2)	(3)	(4)
PKS 2155-304	84.311 A	2.49 ± 0.11	2.75 ± 0.02
	84.311 B	2.54 ± 0.08	2.58 ± 0.03
	84.311 C	2.45 ± 0.05	2.53 ± 0.04
	84.311 D	2.37 ± 0.05	2.42 ± 0.01
	84.312 A	2.83 ± 0.12	2.82 ± 0.02
	84.312 B	2.62 ± 0.08	2.68 ± 0.03
	84.312 C	2.52 ± 0.04	2.51 ± 0.02
	84.312 D	2.42 ± 0.04	2.42 ± 0.01
	84.316	2.72 ± 0.06	2.72 ± 0.04
	84.306	2.76 ± 0.03	$2.74^{+0.0}_{-0.04}$
	85.316	2.87 ± 0.04	2.85 ± 0.00
	85.297	2.69 ± 0.02	2.59 ± 0.01
	85.305	2.95 ± 0.10	2.81 ± 0.02
	83.304	2.67 ± 0.07	2.77 ± 0.01
	83.333	2.74 ± 0.10	2.71 ± 0.01

Table 4.2.: c) HPQ

Object	Date	α_{ME}	α_{LE+ME}
(1)	(2)	(3)	(4)
Ton 599	84.151	2.03 ± 0.52	$1.69^{+0.78}_{-0.31}$
	85.136	2.60 ± 0.8	1.68 ± 0.31
	85.127	$2.30^{+0.04}_{-0.90}$	$1.62^{+0.18}_{-0.16}$
PKS 1510-08	84.216(7)	1.34 ± 0.15	1.36 ± 0.11
	85.212	1.88 ± 0.32	$1.61^{+0.12}_{-0.14}$
PKS 2208-137	84.146	1.40 ± 0.9	1.66 ± 0.26
3C 390.3	86.076	1.58 ± 0.09	1.56 ± 0.06
	86.077	2.12 ± 0.22	1.52 ± 0.08
	84.153	2.01 ± 0.53	1.34 ± 0.17
	85.311	1.74 ± 0.20	1.68 ± 0.08

Table 4.3.: Broken Power Law Results a) RBL

Object	Date	E_o (keV)	α_1	α_2	χ^2_r/d.o.f.	$\Delta\chi^2$	P (%)
(1)	(2)	(3)	(4)	(5)	(6)	(7)	(8)
3C 66A	86.015	2	$0.37^{+0.45}_{-0.37}$	$2.54^{+0.78}_{-0.72}$	0.88/12	8.97	95
	86.032	2	$0.57^{+0.38}_{-0.57}$	$2.40^{+0.35}_{-0.33}$	1.09/16	31.7	> 99.9
PKS 0521-365	83.306	4	$1.41^{+0.12}_{-0.14}$	$2.42^{+0.71}_{-0.60}$	0.62/22	6.7	97
OJ 287	83.281	2	1.47 ± 0.20	$4.17^{+0.85}_{-0.69}$	0.86/13	56.02	> 99.9
3C 371	84.256	1	$3.91^{+0.42}_{-0.39}$	1.86 ± 0.36	0.94/23	23	> 99.9
	84.273	1	3.72 ± 0.92	1.86 ± 0.78	0.36/16	53	> 99.9

Table 4.3.: Broken Power Law Results b) XBL

Object	Date	E_o (keV)	α_1	α_2	χ^2_r/d.o.f.	$\Delta\chi^2$	P (%)
(1)	(2)	(3)	(4)	(5)	(6)	(7)	(8)
EXO 0423-084	85.048	2	$-1.10^{+0.63}_{-1.24}$	2.42 ± 0.19	1.12/25	154	> 99.9
	85.267	2	$-2.50^{+0.80}_{-1.35}$	2.70 ± 0.11	1.33/25	404	> 99.9
PKS 0548-322	83.306	2	1.73 ± 0.07	2.40 ± 0.09	1.4/24	71.9	> 99.9
	83.334	2	1.88 ± 0.11	2.13 ± 0.13	0.6/27	4.4	95
	86.066	5	2.00 ± 0.02	$3.48^{+0.85}_{-0.69}$	0.99/25	15.8	97.5
EXO 0557-38	86.021	2	2.34 ± 0.14	1.38 ± 0.16	1.08/26	36.72	> 99.9
Mrk 421	85.118	1	2.62 ± 0.08	2.30 ± 0.06	1.2/29	19.78	> 99.9
	85.131	1	2.67 ± 0.08	2.37 ± 0.08	1.4/22	11.87	95
	84.340	3	2.12 ± 0.02	2.52 ± 0.08	1.04/27	67.05	> 99.9
	84.337	3	2.11 ± 0.02	2.25 ± 0.05	1.08/33	16.4	> 99.9
	84.338	4	2.13 ± 0.01	2.33 ± 0.05	1.46/33	36.85	> 99.9
	85.004	5	2.70 ± 0.05	$0.60^{+0.72}_{-0.60}$	0.71/29	13.44	> 99.9

Table 4.3.b (continued)

Object	Date	E_o (keV)	α_1	α_2	χ^2_r/d.o.f.	$\Delta\chi^2$	P (%)
(1)	(2)	(3)	(4)	(5)	(6)	(7)	(8)
1218+304	84.356	2	1.95 ± 0.05	2.57 ± 0.10	1.86/22	57.96	> 99.9
	85.005	2	2.00 ± 0.05	2.38 ± 0.10	0.73/27	26.56	> 99.9
2A 1235+63	85.079	4	1.22 ± 0.12	$6.00^{+4.00}_{-2.43}$	0.84/41	17.22	> 99.9
1E 1415+22	86.063	2	-0.41 ± 0.4	2.97 ± 0.43	1.0/11	84.32	> 99.9
H 1426+428	85.055	5	1.93 ± 0.03	3.40 ± 0.80	0.94/27	11.02	95
Mrk 501	84.034	2	2.13 ± 0.03	2.51 ± 0.07	0.92/27	59.28	> 99.9
	86.074	2	2.13 ± 0.01	2.38 ± 0.03	1.1/25	105.3	> 99.9
	84.209	2	2.25 ± 0.06	2.51 ± 0.11	1.00/27	8.61	97.5
	84.191	4	2.34 ± 0.04	$3.72^{+1.24}_{-0.88}$	0.86/27	7.68	95
	84.036	3	2.24 ± 0.04	2.94 ± 0.37	0.92/17	10.47	95
PKS 2005-489	84.254	2	2.81 ± 0.04	3.07 ± 0.07	1.1/27	17.88	> 97.5
	84.287	4	2.57 ± 0.03	3.16 ± 0.16	1.56/27	30.57	> 99.9

Table 4.3.b (continued)

Object	Date	E_o (keV)	α_1	α_2	χ^2_r/d.o.f.	$\Delta\chi^2$	P (%)
(1)	(2)	(3)	(4)	(5)	(6)	(7)	(8)
PKS 2155-304	84.311 A	1	2.97 ± 0.09	2.50 ± 0.12	1.0/17	16.38	> 99.9
	84.311 C	1	2.77 ± 0.11	2.45 ± 0.05	1.52/25	12.06	> 99.9
	84.311 D	1	2.69 ± 0.05	2.38 ± 0.05	0.97/25	25.22	> 99.9
	84.312 D	5	2.41 ± 0.01	3.00 ± 0.20	1.84/30	25.36	97.5
	85.297	4	2.57 ± 0.01	3.00 ± 0.05	1.33/25	216.3	> 99.9
	83.333	1	2.82 ± 0.07	2.58 ± 0.08	2.2/23	27.83	97.5
	85.305	1	2.70 ± 0.09	2.95 ± 0.10	0.6/25	5.00	95
	85.306	5	2.73 ± 0.01	3.52 ± 0.27	1.31/30	31.98	> 99.9

Table 4.3.: Broken Power Law results c) HPQ-OVV

Object	Date	E_o (keV)	α_1	α_2	χ^2_r/d.o.f.	$\Delta\chi^2$	P (%)
(1)	(2)	(3)	(4)	(5)	(6)	(7)	(8)
3C 390.3	86.077	3	1.26 ± 0.16	$2.96^{+0.55}_{-0.49}$	0.64/13	28.05	97

CHAPTER V

Average X-ray properties of the EXOSAT blazars.

In this Chapter we examine the global X-ray properties of the blazars of our sample, paying particular attention to whether differences are present among XBL, RBL, and HPQ. Our sample contains 19 XBL, 8 RBL, and only 4 HPQ. Therefore, while the number of XBL and RBL does allow a statistical study, the results concerning the HPQ class are not conclusive.

5.1 Luminosity distributions.

We considered both the ME and LE luminosity distributions. The luminosities were computed from the fluxes listed in Table 4.1.a-c and the redshifts listed in Table 3.3.a-c, assuming $H_o = 50$ km s^{-1} Mpc^{-1} and $q_o = 0.5$. Because of variability, for each object we considered all the listed values of the fluxes, that is, no averages have been done for sources with more than one observation.

The 2 – 6 keV luminosity distributions for XBL, RBL, and HPQ are plotted in Figures 5.1.a-c, respectively. It is apparent that the three distributions span the same luminosity interval, from 10^{43} to 10^{46} ergs s^{-1}. In Table 5.1.a, the average values are given for the three classes individually and for all the blazar group. The three classes have very close average luminosities. Using the Kolmogorov-Smirnov (KS) test (Bevington 1969), the probability P_{KS} that

the three distributions are different is $\sim$ 94% (the threshold for significance is commonly fixed at 95%). Because of the limited number of objects and the lack of a "statistical" sample, nothing can be said about the luminosity functions of the three classes.

The same considerations apply for the LE luminosity distributions, which are plotted in Figures 5.2.a-c and whose averages are reported in Table 5.1.a.

As we said above, no average luminosity was computed for objects with more than one observation because of variability. However, we find that there is no significant difference in the distributions if the average luminosity for each object is used.

In conclusion, no significant difference in luminosity distribution is apparent among the XBL, RBL, and HPQ classes, which span the same interval both in the LE and the ME energy band and have very close average luminosities.

5.2 Spectral index distributions.

We studied the distributions both in α_{ME} and in α_{LE+ME} using the best fit values reported in Table 4.2.a-c. As for the luminosity distributions, first, to take into account the spectral variability, we did not average the values of the slopes.

The distributions obtained considering the single spectral indexes are shown in Figures 5.3.a-c and 5.4.a-c for α_{ME} and α_{LE+ME}, respectively. In both cases, using the KS test, RBL and HPQ are not differently distributed ($P_{KS} \sim$ 68%). On the contrary, XBL are significantly different ($P_{KS} > 99.9\%$) from

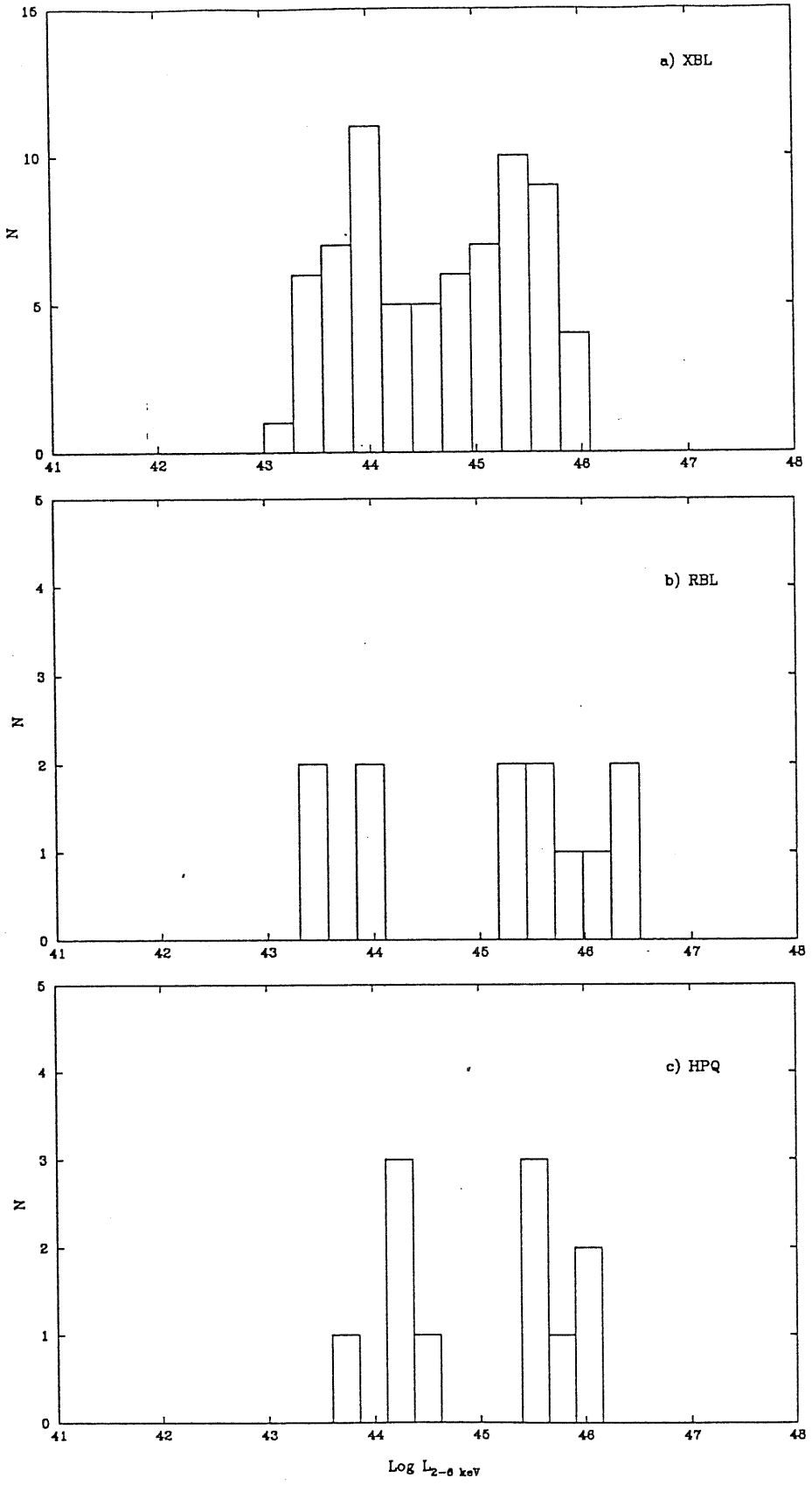

Figure 5.1: 2 – 6 keV luminosity distributions of blazars. (a) X-ray selected BL Lacs, (b) Radio selected BL Lacs, and (c) Highly Polarized Quasars.

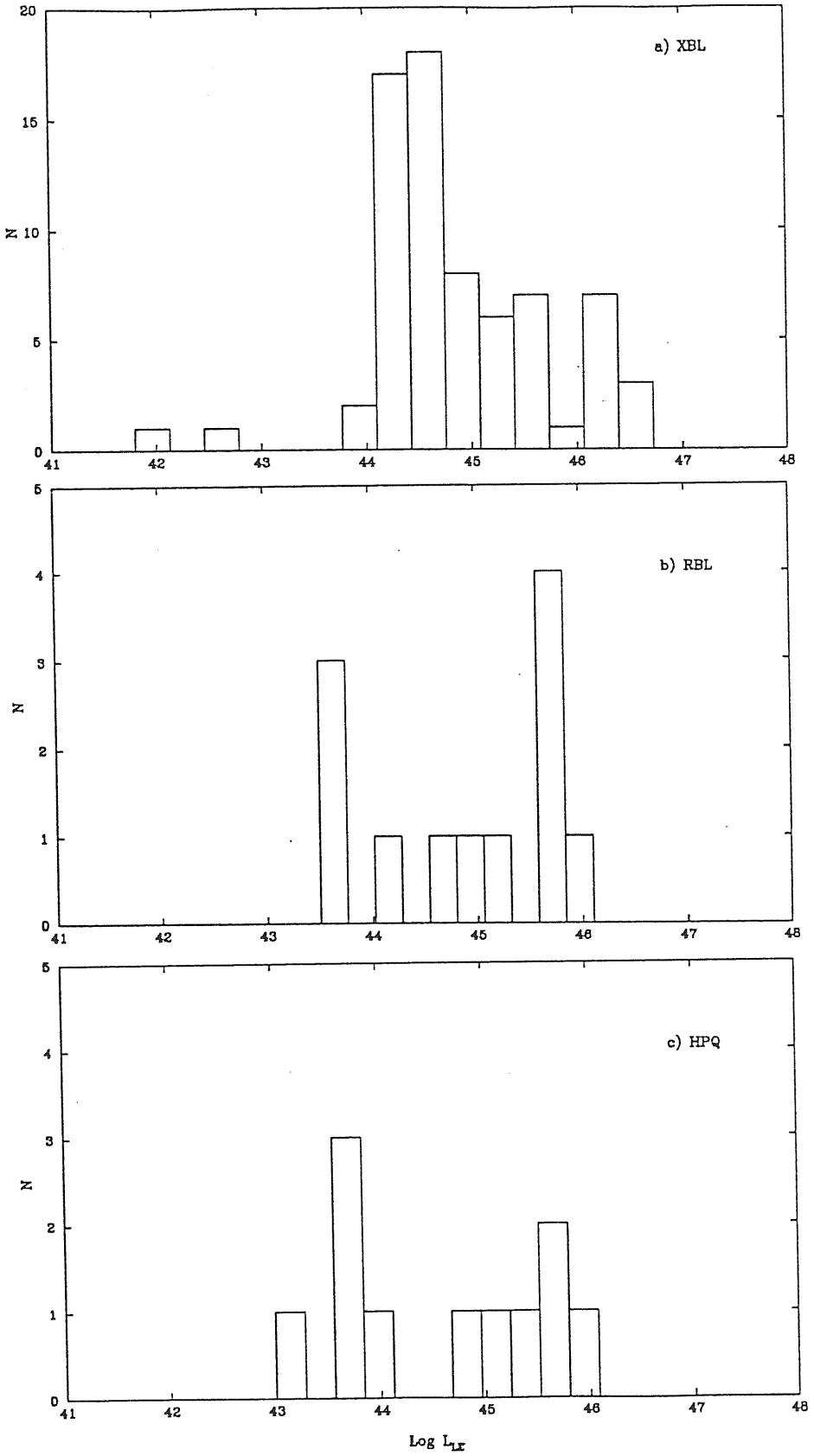

Figure 5.2: LE luminosity distributions of blazars. (a) X-ray selected BL Lacs, (b) Radio selected BL Lacs, and (c) Highly Polarized Quasars.

both the RBL and the HPQ. The average values the two slopes are reported in Table 5.1.b, for XBL, RBL, HPQ. Because the RBL and HPQ distributions do not differ, we also report in Table 5.1.b the average values for the joint class RBL-HPQ. For XBL, the α_{ME} distribution is not different from the α_{LE+ME} one. The two distributions are instead different at 98% confidence level for RBL and HPQ, although only the best fit values, without the observational uncertainties, have been used (see below).

Another way to look at the difference between XBL and RBL-HPQ is to plot α_{ME} versus α_{LE+ME} for all blazars (Figure 5.5). Filled circles represent XBL, open circles RBL, and crosses HPQ. The solid line in the Figure is the locus $\alpha_{ME} = \alpha_{LE+ME}$. It is apparent that RBL and HPQ are, on average, flatter than the XBL class. A few single objects do not obey this trend. Among RBL, OJ 287 was found in an exceptionally soft mode ($\alpha_{ME} \sim 5.0$) on one occasion; 3C 371 has a soft excess which cause the α_{LE+ME} to steepen (Table 4.3.a). Some XBL (1E 1415+22, MS 1235+63, EXO 0423.4-0840, and EXO 0507.1-0404) are found in the region of flatter α_{LE+ME}. However, the power law model does not adequately fit the LE + ME spectra of these objects, and the broken power law model was instead required. Therefore, as discussed in Chapter 4, in these cases α_{LE+ME} flattens because of the spectral breaks at lower energies. Taking into account the errors in Figure 5.5, the two indexes (α_{ME} and α_{LE+ME}) are consistent with each other both for RBL-HPQ and XBL, although the data point distributions are slightly skewed in the region above the solid line.

As we discussed in the section above, considering the single slopes could favor the most observed objects. Therefore we also considered the distributions obtained using the average slope for each object in the sample. Results obtained are consistent with the previous ones.

We can conclude that strong evidence is found in our data for XBL

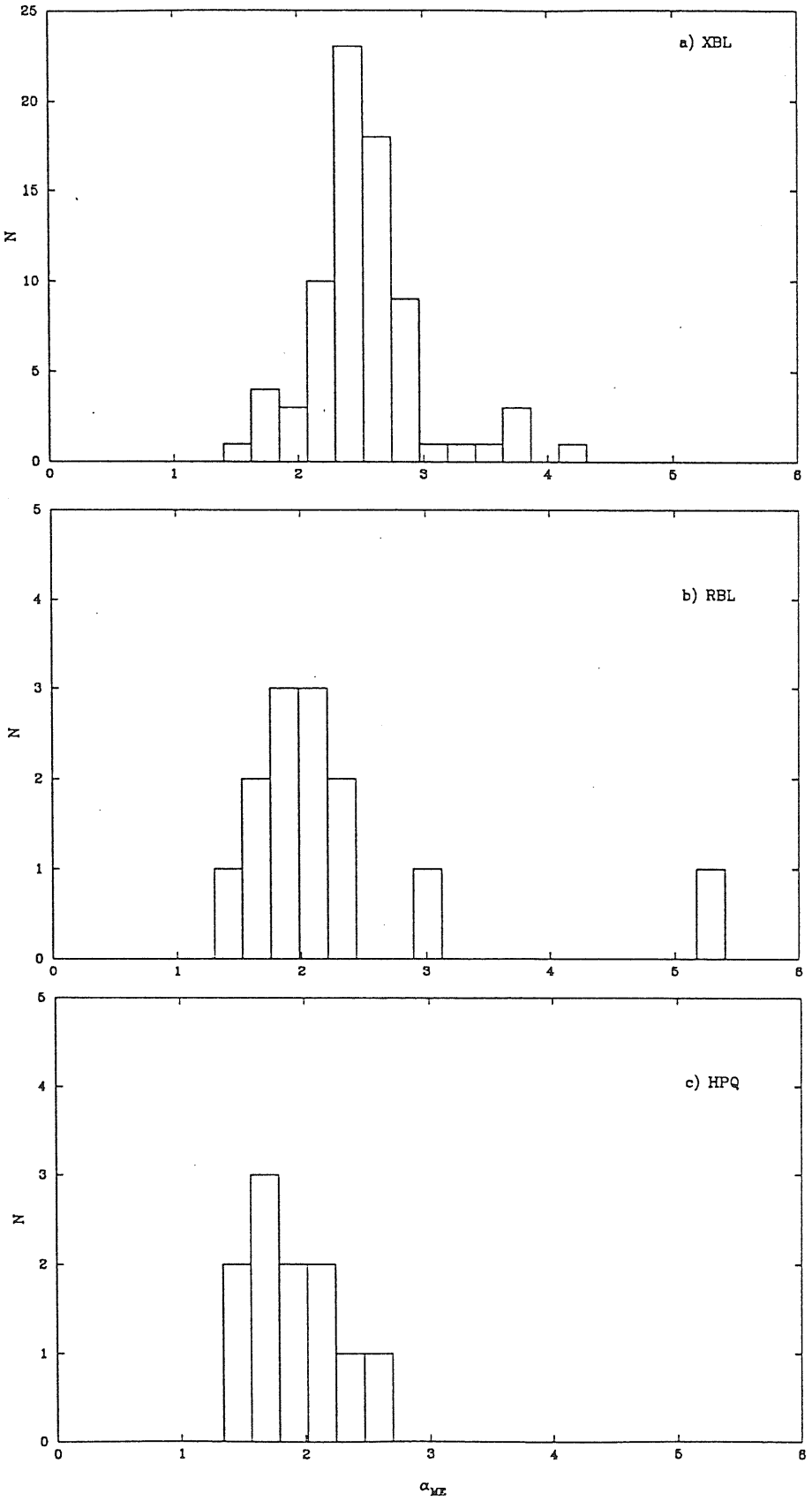

Figure 5.3: Spectral index distributions of blazars: α_{ME}. (a) X-ray selected BL Lacs, (b) Radio selected BL Lacs, and (c) Highly Polarized Quasars.

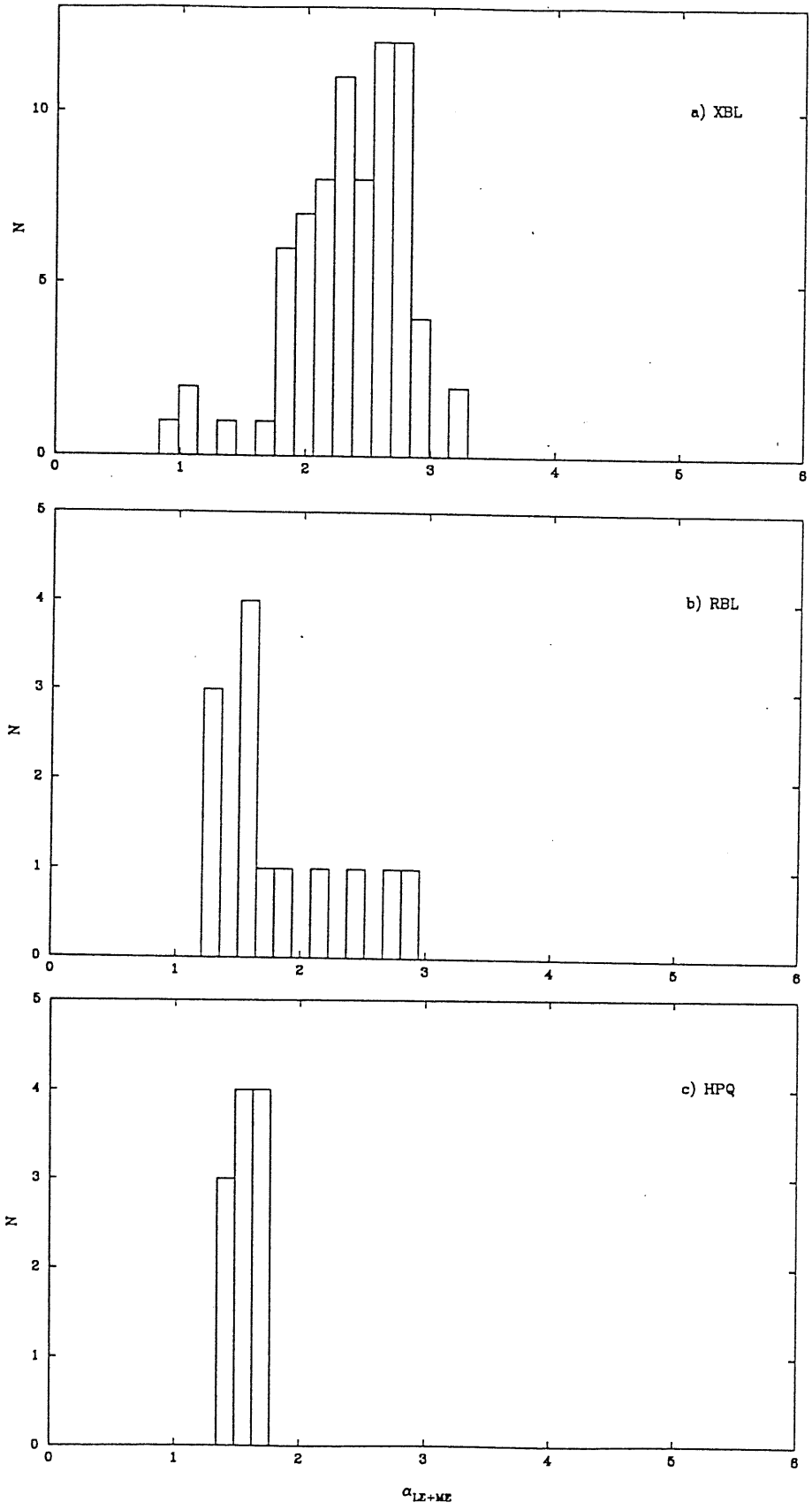

Figure 5.4: Spectral index distributions of blazars: α_{LE+ME}. (a) X-ray selected BL Lacs, (b) Radio selected BL Lacs, and (c) Highly Polarized Quasars.

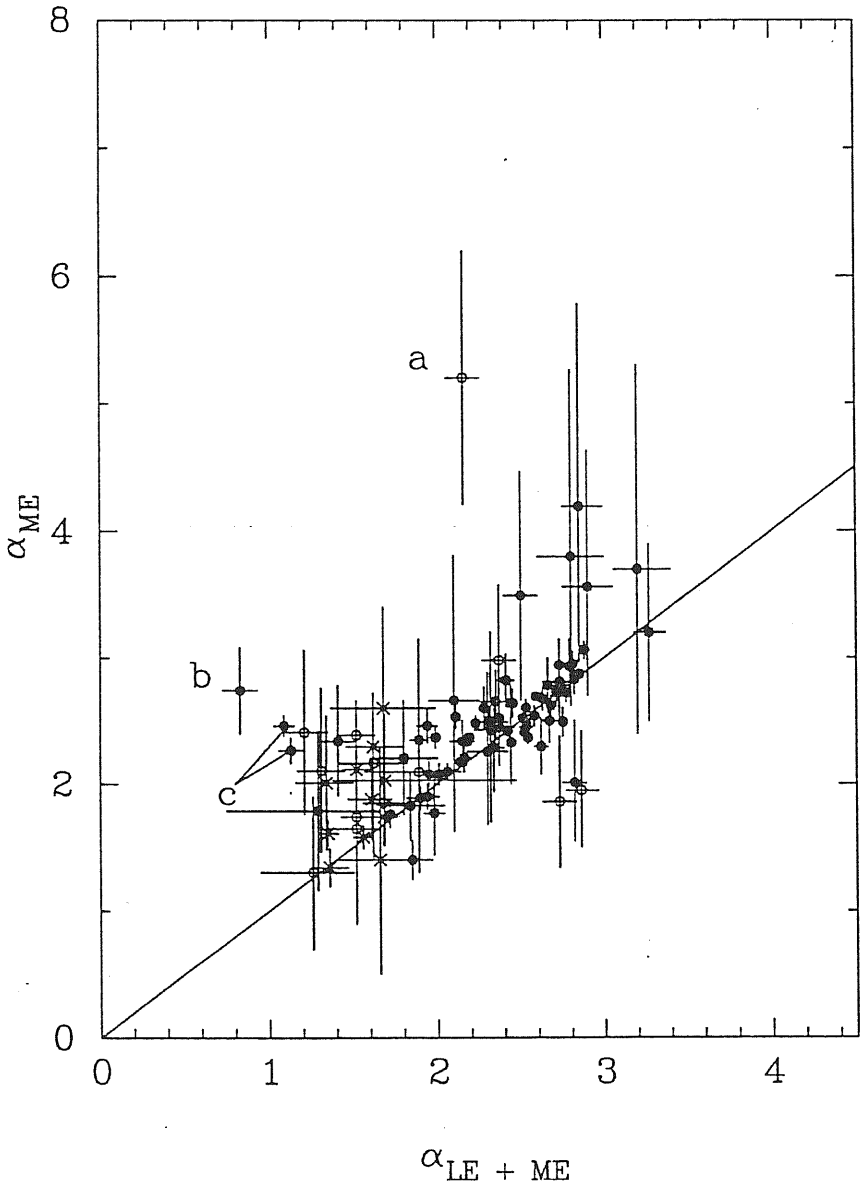

Figure 5.5: α_{ME} versus α_{LE+ME} for X-ray selected BL Lacs (*filled circles*), radio selected BL Lacs (*open circles*), and Highly Polarized Quasars (*crosses*). (a) OJ 287; (b) 1E 1415+22; (c) EXO 0423.4–0840.

being, in general, steeper than RBL and HPQ. The addition of the LE data does not affect, on average, the hard energy slopes.

5.3 Intrinsic absorption.

To investigate whether blazars as a class have intrinsic absorption we plotted the histograms of the *residual* column densities, defined as log [N_H] - log [N_H (Galactic)]. We used the values reported in Table 4.1.a-c. Because of the large errors on single values, we averaged the fitted N_H for objects having more than one observation.

In Figures 5.6.a-c the residual column density distributions for the three classes are shown. The average values are reported in Table 5.2.c, where the value for the whole class of blazars is also given. The average residuals are consistent with zero in each case, as expected if the intrinsic absorption of blazars is negligible.

Another way to study the intrinsic absorption, which takes the uncertainties into account, is shown in Figure 5.7 where the fitted N_H values are plotted versus the Galactic ones. Filled circles represent XBL, open circles RBL, and crosses HPQ. We plotted the average values of the fitted N_H and their standard deviations for the sources observed more than once. The solid line is the $N_H = N_H$ (Galactic) locus. Points in the region above the line indicate extra absorption while those in the region below correspond to a deficiency of absorption. In general, for all the three classes the data indicate absorption consistent with the Galactic one at the 3σ confidence level, although the point distributions seem skewed toward the region above the line. Points labelled 'a' and 'b'

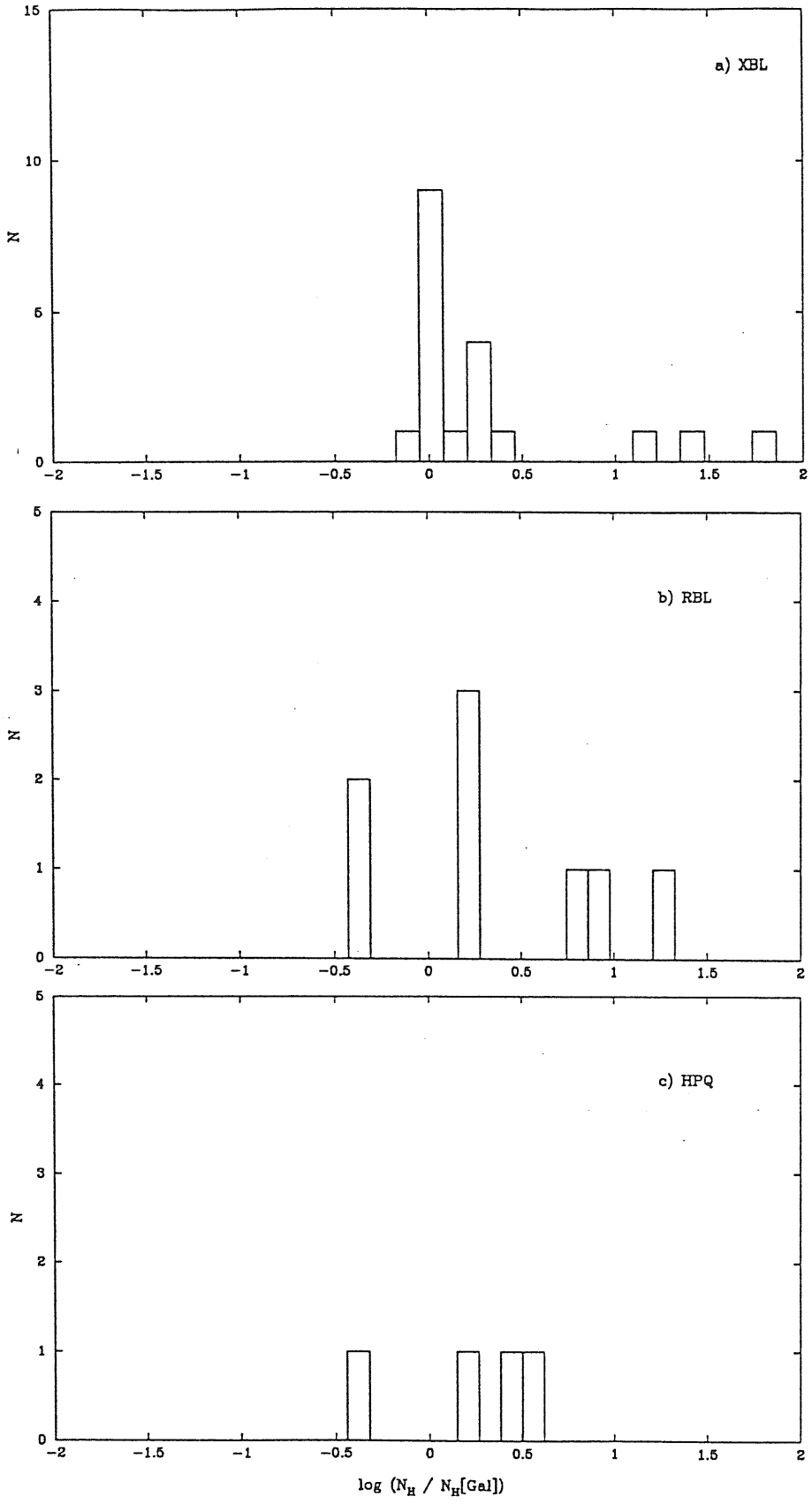

Figure 5.6: Intrinsic absorption. Distribution in residual column densities of (a) X-ray selected BL Lacs, (b) Radio selected BL Lacs, and (c) Highly Polarized Quasars.

correspond to EXO 0423.4-0840 and 3C 66A, respectively, whose apparent extra absorption has been discussed in Chapter 4. The points labelled 'c' and 'd' (3C 371 and PKS 2208-137, respectively) seem related to a deficiency of absorption. For 3C 371, this is due to the presence of the soft excess (Chapter 4).

We conclude that, on average, blazars seem not to have significant intrinsic absorption in excess to the Galactic value.

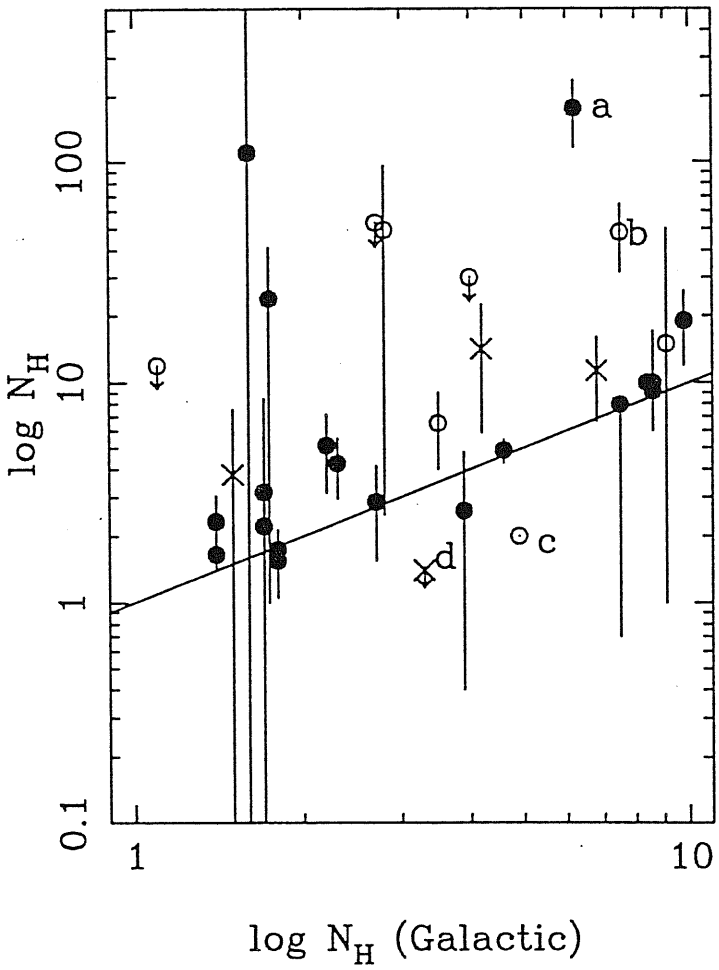

Figure 5.7: Comparison of fitted N_H and Galactic N_H of X-ray selected BL Lacs (*filled circles*), radio selected BL Lacs (*open circles*), and Highly Polarized Quasars (*crosses*). (a) EXO 0423.4–0840; (b) 3C 66A; (c) 3C 371; (d) PKS 2208–137.

5.4 The average X-ray spectrum.

As we discussed in Chapter 4, in some individual cases a broken power law preferred over a single power law (Table 4.3.a-c). The break point is mostly found at lower energies (2 – 3 keV), but in some cases also above 4 keV. In Figure 5.5, spectra with a break at 2 – 3 keV are represented by data points in the regions above (convex spectra) or below (concave spectra) the solid line. In fact, above the line $\alpha_{LE+ME} < \alpha_{ME}$, while below $\alpha_{LE+ME} > \alpha_{ME}$ (see Chapter 4). The most representative examples are the points labelled 'a', 'b', and 'c' in the Figure, which correspond to OJ 287, 1E 1415+22, and EXO 0423.4-0840. Instead, spectra with a break at higher energies are not visible in Figure 5.5, because in these cases the ME slope is not affected when the LE data are added.

An important point is whether the spectra that do not appear in Table 4.3.a-c are actually described by a single power law, or whether they are intrinsically too weak for a double power law to be seen with a fit to the *single* spectrum. In the latter case one could sum all the spectra to increase the s/n ratio, and then fit the resulting spectrum with a broken power law model. For blazars this solution does not appear advisable because in the summed spectra the high states of the brightest sources would dominate the statistics. In addition, in the hypothesis that the spectra were actually curved, the break points can be at different energies, as found in Chapter 4. In the sum it may occur that the individual broken power laws "compensate" giving, for the summed spectrum, a single power law. That is, spectral information could be lost by summing spectra, due to the variable nature of blazars.

Alternatively, one can use the additivity of the χ^2 statistics. It has been demonstrated that fitting the individual spectra and then adding the χ^2s

is formally equivalent to summing the spectra and then fitting the resulting spectrum (see *e.g.* Canizares & White 1989). The summed χ^2 is usually referred to as the "cumulated" χ^2. Therefore, one fits the single spectra with the given model, and thus sums the single minima χ^2s and degrees of freedom (dofs), obtaining the cumulated minimum χ^2 and the total dofs.

To investigate which model better represents the spectra not in Table 4.3.a-c, we followed this procedure. We fitted the individual observations with a broken power law model, in the way described in Chapter 4. We summed the single χ^2_{min}s and dofs, obtaining the cumulated χ^2_{min} and total dofs for the broken power law model. The cumulated χ^2_{min} and dofs for the single power law model were calculated from Table 4.1.a-c. We then applied the F-test to the cumulated statistics to decide which of the corresponding models is preferred. The results are shown in Table 5.2, where we list in rows 1 and 2 the cumulated χ^2_{min}/dof for the power law and the broken power law models, respectively, the $\Delta\chi^2$ in row 3, and the probability P of the F-test (Chapter 4) in row 4. The results show that the broken power law model is globally preferred over a single power law with high confidence (P $>$ 99.9%). The average break point is $\langle E_0 \rangle = 2.4 \pm 1.0$ keV.

The dominant contribution to the cumulated χ^2s comes from the BL Lac class. In fact, no significant improvement over a single power law is found for the HPQ class alone, which, however, contains a limited number of objects. We can therefore conclude that for BL Lacs a broken power law is globally preferred to represent the EXOSAT data. The average spectrum is convex down with a break at $\sim$ 2.4 keV.

A final note should be made. The conclusions stated in the above sections, concerning the luminosity and the spectral index distributions, were based on the assumption of power-law shaped spectra. They are not affected by the finding that the spectra are instead represented by a broken power law. In

regard to the luminosity distributions, in fact, it is sufficient to note that the LE luminosities have been calculated assuming a universal power law, with fixed slope ($\alpha = 2.00$) and interstellar absorption (Chapter 4). The ME luminosities were calculated in the 2 – 6 keV energy range, *i.e.*, in a range where the single power law approximation holds. The statement that the XBL spectra are, on average, steeper than those of the other blazars is also still valid. In fact, in Figure 5.8 α_2 versus α_1 is plotted for all blazars, using the values in Table 4.3.a-c and those obtained from a fit with a broken power law with E_0 fixed at the average value (2.4 keV). In the Figure, filled dots represent XBL, open dots RBL, and crosses HPQ. As for Figure 5.5, one can conclude that RBL and HPQ are, on average, flatter than XBL.

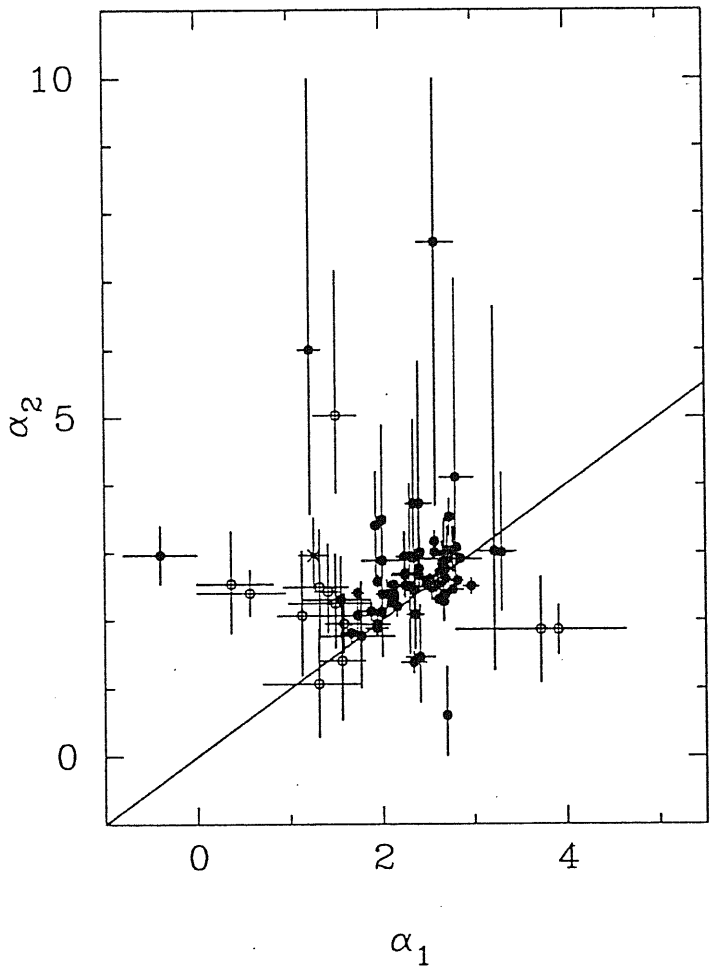

Figure 5.8: Comparison of low-(α_1) and high-(α_2) energy slopes from a broken power law model; X-ray selected BL Lacs (*filled circles*), radio selected BL Lacs (*open circles*), and Highly Polarized Quasars (*crosses*). The X-ray selected BL Lac in the region of flatter α_1 is 1E 1415+22. The very soft radio-selected BL Lac is OJ 287 (83.281 observation).

Table 5.1. Average X-ray Properties of the EXOSAT Blazars:

a) Luminosity

	XBL (1)	RBL (2)	HPQ (3)	ALL (4)
$\langle logL_{(2-6keV)} \rangle$	44.65	45.10	45.08	44.76
σ	0.83	1.11	0.85	0.88
$\langle logL_{LE} \rangle$	44.89	44.85	44.65	44.86
σ	0.85	0.91	1.01	0.87

b) Spectral Index

	XBL (1)	RBL (2)	HPQ (3)	RBL-HPQ (4)
$\langle \alpha_{ME} \rangle$	2.54	2.29	1.83	2.10
σ	0.47	0.97	0.40	0.77
$\langle \alpha_{LE+ME} \rangle$	2.34	1.82	1.54	1.70
σ	0.45	0.55	0.14	0.43

c) Residual Column density

	XBL (1)	RBL (2)	HPQ (3)	ALL (4)
$\langle log(N_H/N_H(Gal)) \rangle$	0.32	0.37	0.18	0.33
σ	0.54	0.61	0.43	0.54

Table 5.2. Cumulative spectral results

P.Law χ^2_{min}/dof	1136.4/1145
Broken P.Law χ^2_{min}/dof	1074.6/1115
$\Delta\chi^2$	62
P(%)	> 99.9

CHAPTER VI

Discussion and Conclusions

We have studied the archival EXOSAT data for a sample of blazars, containing 8 RBL, 19 XBL, and 4 HPQ. For 12 objects, these data were still unpublished. Basically, three distinct areas are addressed by the data presented here:

a) Shape of the X-ray spectrum. The X-ray spectrum of BL Lacs is globally curved. In general, it is convex down, with the break mainly at lower energies. In two individual objects, Mrk 421 and PKS 2155-304, soft excesses are found in the lowest states.

b) Spectral variability. All the sources which were observed more than once show substantial spectral variability. For BL Lacs the slope changes are related to intensity changes with the general trend of spectral hardening when the source brightens.

c) Average properties of blazars. Studying the global properties of blazars we have found that no difference is present in the X-ray luminosity distributions (the three classes are distributed in the same interval and have similar average luminosities), while, on average, XBL have steeper X-ray slopes than do RBL and HPQ.

We will now discuss each of the above points in more detail.

a) Shape of the X-ray spectrum.

As we highlighted in Chapter 1, before EXOSAT the true shape of the X-ray spectrum of BL Lacs was difficult to determine because of the lack of data collected simultaneously in an extended energy range for a large sample of objects. For this reason, EXOSAT provides the most suitable set of data.

The X-ray spectra of BL Lacs are consistent with a broken power law model. For the weakest cases a global analysis indicates that the spectrum steepens above 2 – 3 keV (Chapter 5). However, the study of the individual cases (Chapter 4) has shown that the situation is more complex. For example the break energy, E_0, is not constant in different spectra of the same object. In PKS 0548-322 E_0 is found at lower energies in the high states and at $\sim$ 5 keV in the low state. The opposite trend is seen in Mrk 501.

Another interesting feature recently found in the X-ray spectra of BL Lacs is the absorption edge of Oxygen VIII at 0.6 keV (Canizares & Kruper 1984; Urry *et al.* 1986; Madejski *et al.* 1991). Our data do not have intrinsic resolution below 1 keV, therefore the 0.6 keV edge can not be confirmed nor ruled out in the EXOSAT data. We can not directly detect the edge, though we could expect that its presence might be revealed by a flattening of the ME data below 2 – 3 keV, unaccompanied by a depression of the LE flux, collected in a broader band. Thus, this may result in an apparent excess of the softer energy data with respect to the harder ones.

In fact, we find evidence for a soft excess in a number of objects, namely Mrk 421, PKS 2155-304, and 3C 371. Indeed for these objects an absorption edge at 0.6 keV has been found in other X-ray experiments, as discussed in Chapter 4. Several high quality EXOSAT spectra of PKS 2155-304 are also consistent with an edge at 0.6 keV, confirming the findings of Treves *et al.* (1989). However, it is not clear whether the soft excess in the EXOSAT data

is intrinsic or whether it is a result of the aforementioned 0.6 keV feature. A particular example demonstrating this uncertainty is Mrk 421 for which concave up spectra (indicative of a soft excess) have been reported in the earlier X-ray missions (see Table 3.4.b). In addition, Madejski *et al.* (1991) fitted the *Einstein* SSS data with a concave up spectrum *plus* the 0.6 keV feature.

Two possible scenarios exist to describe the overall shape of the spectra. One is that all of the EXOSAT spectra are effectively represented by the superposition of two distinct power law components. The best evidence of this is found for individual objects at higher intensities, perhaps due to the better quality of the data in these states (*e.g.*, PKS 2005-489). Two component fits with sharp breaks have been found in the data from the other X-ray missions for the brightest XBL (PKS 0548-322, Mrk 421, Mrk 501, 1218+304, and PKS 2155-304).

The major problem with the two components scenario is the justification of the break points. As Barr *et al.* (1989) has outlined, sharp breaks are very difficult to produce in nature. In the context of the synchrotron-self Compton model, even if one supposes a neat break in the power law shaped electron distribution, the emerging photon spectrum seems to have a continuous degree of curvature instead of a break point (Landau *et al.* 1986). The second possibility is therefore that the spectra are continuously curved. However, because of the limited energy range sampled, EXOSAT is not sensitive to continuous curvature, and therefore the broken power law is the most straightforward modelling of these data. Break points do not necessarily have a physical meaning, and their location might merely reflect the location of the peak sensitivity.

Strong evidence for a continuously curved spectrum would come if a break well above 10 keV were detected. This requires operative bands larger than EXOSAT, such as, for example, that of the LAC experiment on board

the GINGA satellite, which covers intervals up to $\sim$ 40 keV. For example, PKS 2155-304 was observed several times by the LAC, with a positive signal up to $\sim$ 20 keV (Sembay *et al.* 1992). A two power-law model was required to explain the data; however the break point was found at $\sim$ 4 keV. While this appears, instead, to favor the two component model, more work is required to determine which of models is preferred.

In conclusion, the EXOSAT results show that the 0.1 – 10 keV spectra of BL Lacs are, in general, convex down. It is not clear whether the continuum is smoothly curved or whether two components and sharp breaks are present instead. Observations with a larger operative band are required to solve the puzzle.

b) Spectral variability.

As shown in Chapter 4, all the BL Lacs observed more than once show spectral changes generally anti-correlated with intensity changes, in the sense that the spectrum hardens in the high state. This behavior is peculiar to the BL Lacs class; no related slope-intensity changes were found for the four HPQ in the sample.

In the literature spectral variability was first noted in the EXOSAT observations of a sample of BL Lacs by Giommi *et al.* (1990). By plotting the ME/LE count rate ratio versus the ME intensity for the 6 brightest sources in their sample (which included Mrk 421, Mrk 501, and PKS 2155-304), an increase of the hardness ratio with intensity was observed, implying that the sources' spectra harden as their intensity increases. Our data increase the number of sources for which this trend has been observed individually.

However, the slope-intensity relationship is more complex than appar-

ent. The best examples are provided by Mrk 421, Mrk 501, and PKS 2155-304, for which larger time coverage exists. From Figures 4.2, 4.3, 4.4, where the spectral indexes versus the 2 – 6 keV count rates are plotted, two important points must be made. The correlation trend between slope and intensity is not linear; at higher count rates α_{LE+ME} no longer decreases and a 'saturation' value, different for each object, is reached. This is most apparent for Mrk 421 and 501. The second point concerns the 'local' shape of the relationship. For example, PKS 2155-304 shows, at lowest intensities, an *increase* of α with increasing count rates, *i.e.*, a positive correlation. For Mrk 421 and Mrk 501 there is less strong evidence. A positive correlation has been noted in other X-ray missions in nearby or overlapping energy bands. For example, the ROSAT observations of Mrk 421 in 0.2 – 2.4 keV detected a hardening of the spectrum with fading intensity (Fink *et al.* 1991). In the GINGA data of PKS 2155-304 (Sembay *et al.* 1992), a steeper (softer) spectrum with increasing flux was observed during flaring episodes.

In the above considerations the spectral indexes of the single power law model were used. However, for Mrk 421, Mrk 501, and PKS 2155-304 a broken power law is required in some spectra. We checked if this model can account for the spectral variability found in these BL Lacs by plotting the fitted spectral parameters α_1, α_2, and E_0, versus the 2 – 6 keV count rate in Figures 6.1,6.2, and 6.3. Only the low energy spectral index correlates with the count rate, in the above sense of a hardening in the higher states. No clear trends are apparent in the cases of α_2 and E_0. However, in the GINGA observations of PKS 2155-304 (Sembay *et al.* 1992), fitted with a broken power law, both low and high energy indexes flattened (hardened) with increasing intensity.

In summary, the general trend of spectral variability (*i.e.*, the hardening of the spectrum when the source brightens) claimed for BL Lacs is found to be much

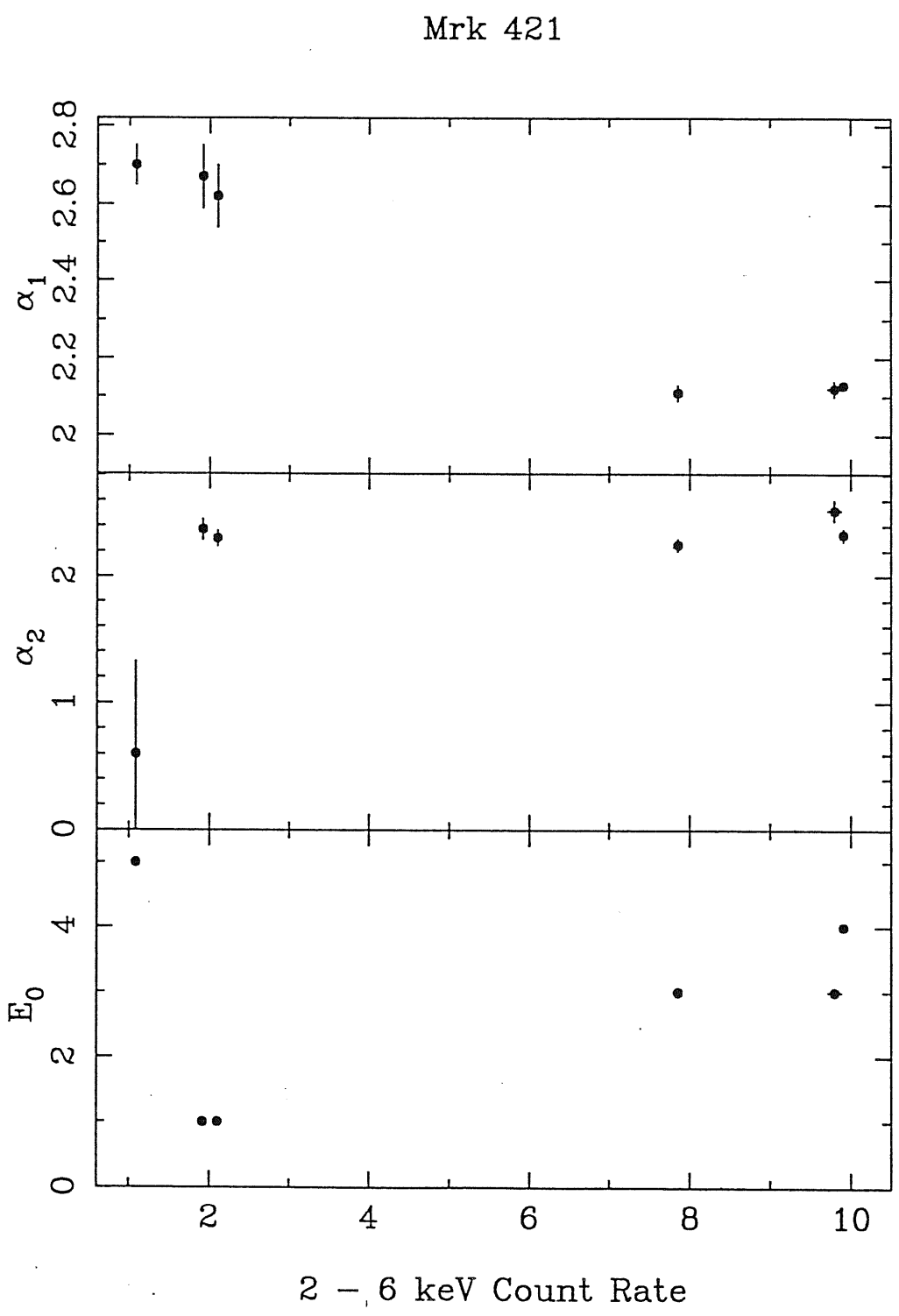

Figure 6.1: Spectral variability of Mrk 421 (broken power law). We plot the low-(a) and the high-(b) energy indexes, and the break point (c) versus the 2 – 6 keV count rate.

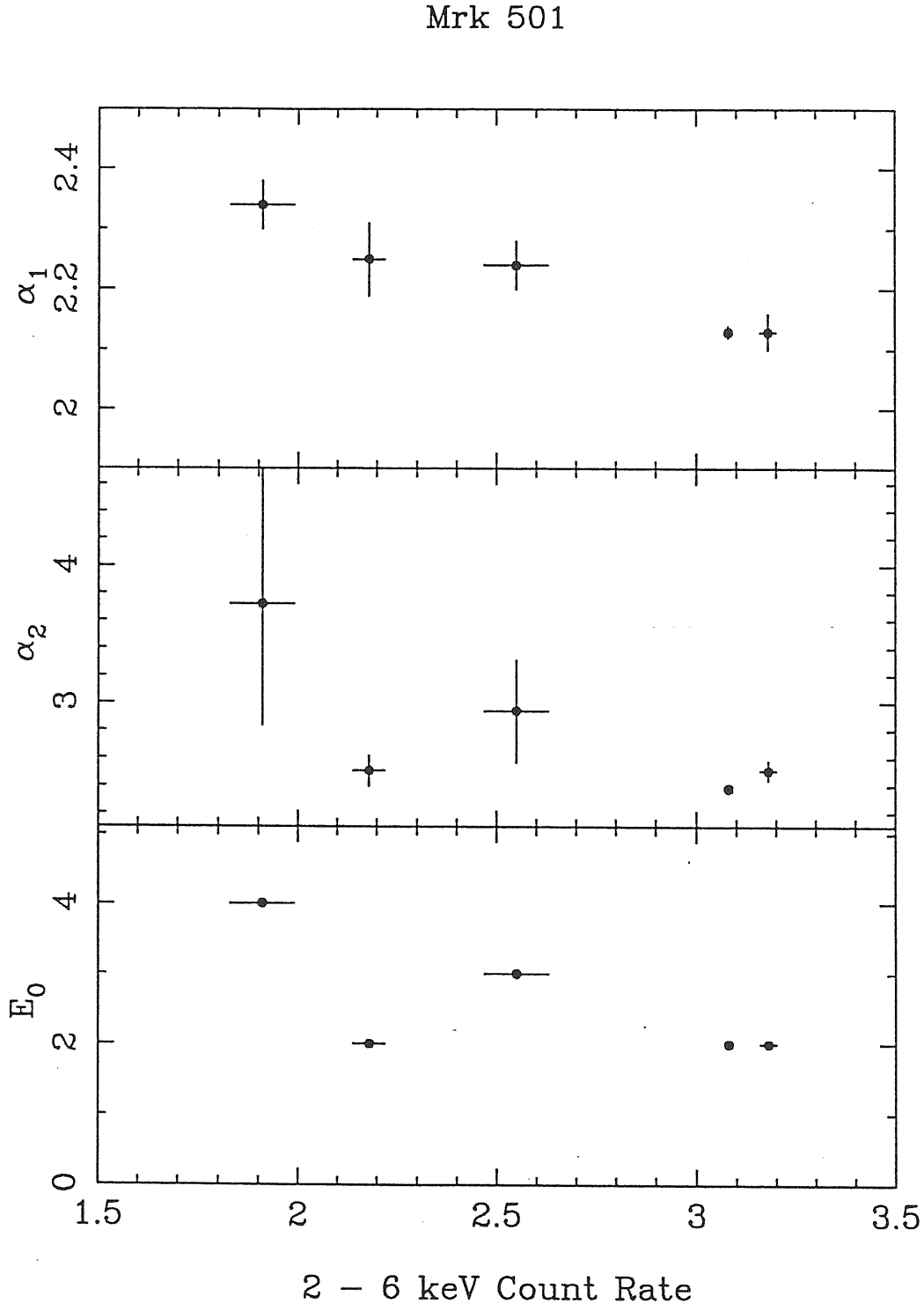

Figure 6.2: Spectral variability of Mrk 501 (broken power law). We plot the low-(a) and the high-(b) energy indexes, and the break point (c) versus the 2 – 6 keV count rate.

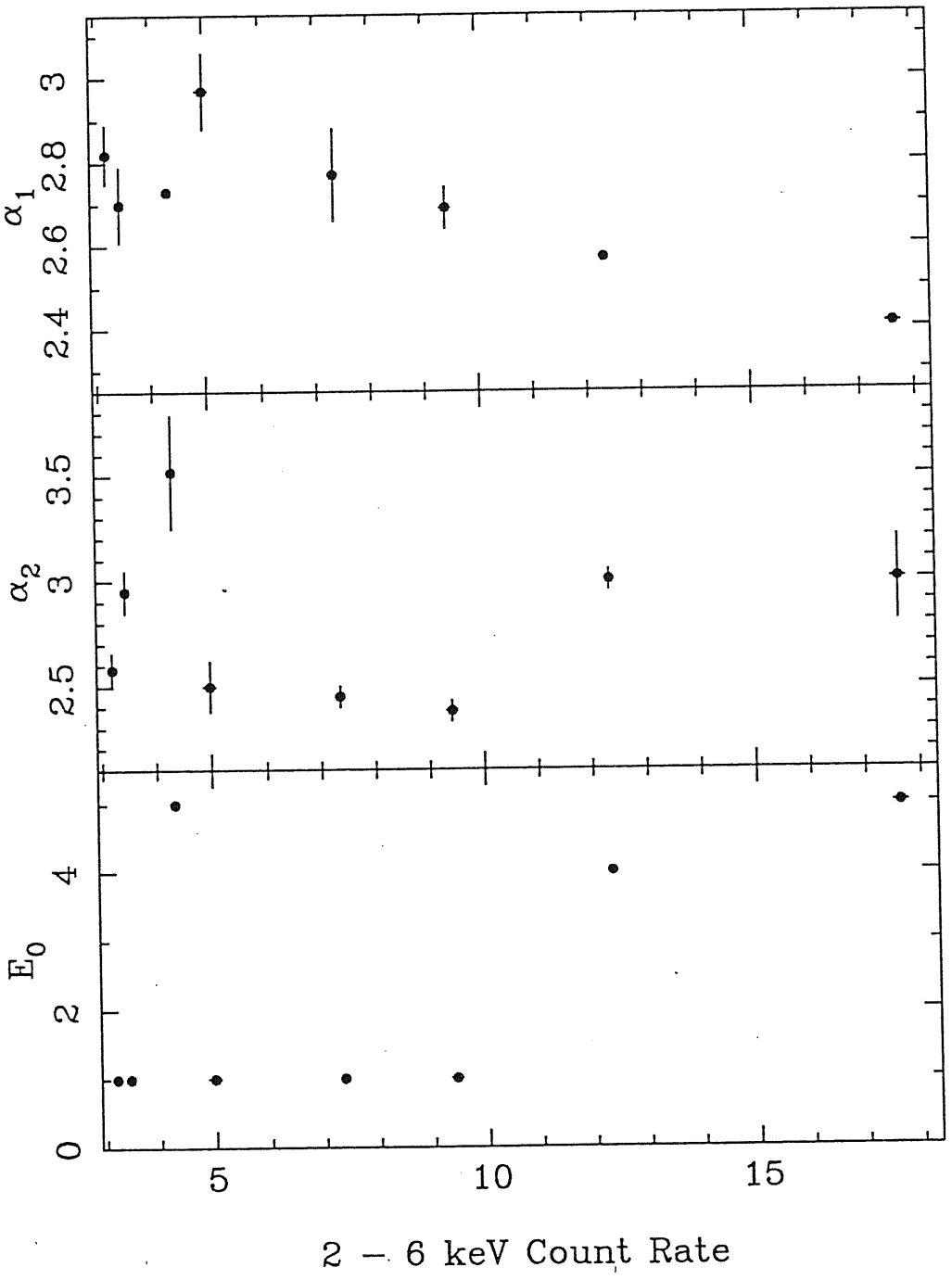

Figure 6.3: Spectral variability of PKS 2155-304 (broken power law). We plot the low-(a) and the high-(b) energy indexes, and the break point (c) versus the 2 – 6 keV count rate.

more complex than it appears.

c) Average properties of blazars.

Our results concerning the luminosity and spectral index distributions of blazars can be fully understood in the context of the current observational and theoretical framework. In particular, they confirm the findings of Maraschi *et al.* (1986). Studying the multiwavelength energy distributions of blazars, for which data from the literature were available, Maraschi *et al.* found that XBL are, on average, less luminous in radio, IR, and optical than RBL, but that the X-ray luminosity distributions for the two classes are the same. Interpreting the blazar emission in the context of the inhomogeneous jet model (Ghisellini *et al.* 1985), the authors proposed that the X-ray emission is radiated isotropically via synchrotron at the base of the jet, while emission at decreasing frequencies should come from outer regions of the jet where the beaming factor becomes greater. In this scenario, the emission properties of XBL are explained assuming that the line of sight is at large angles with respect to the jet axis, thus intercepting radiation from the inner regions of the jet, but only a small amount from the outer regions, whose radiation is concentrated in a narrower cone. On the contrary, in the case of RBL, for which the radio to optical power is enhanced, the line of sight is at small angles with respect to the jet axis. These results were based on data taken from the literature and for a sample of 13 XBL only. Our results from the analysis of the EXOSAT data confirm that XBL and RBL-HPQ are equally distributed in X-ray luminosity and support the scenario proposed by Maraschi *et al.*

Another important finding from the EXOSAT data is that RBL are, on average, flatter in X-ray slope than XBL. This is also expected from the

inhomogeneous jet model (Ghisellini & Maraschi 1989). As discussed above, in the context of this model the X-ray radiation is primarily emitted via synchrotron in the inner regions of the jet and therefore should have a steep slope due to the short radiative lifetime and the high energy cut offs in the particle spectra. In the outer regions of the jet, however, a second X-ray component, due to the Inverse Compton (IC) emission, is supposed to be important. The IC component should share the properties of the outer regions, and therefore it should be more beamed and have a flatter spectrum. XBL, seen at intermediate angles, are thus predicted to have steeper slopes in X-ray than RBL. Our results are totally in agreement with the predictions of this scheme.

Finally, we note that 30% EXOSAT spectra studied here were not previously published. This work contributed to improve our knowledge of the X-ray emission in many individual blazars.

One of the principle merits of the EXOSAT observatory is its coverage of two decades in soft and hard energy ranges. This allowed us to better investigate the shape of the X-ray spectra of BL Lacs. The present analysis finds strong evidence for spectral curvature. However, the present data do not permit us to approach a universal model to describe the curvature. In addition, spectral variability is found, and is shown to follow a general trend, in the sense of a hardening of the spectrum when the source brightens, although this behavior is extremely complex.

Contrary to the other classes of AGNs, for example quasars and Seyferts, BL Lacs are found to show individual peculiarities, both in shape and spectral variability, which can not be simply reconciled within a single model. This sug-

gests that these objects are governed by intrinsically more complex emission processes.

More progress appears to be made in understanding the geometry of this class of blazars. Our results concerning the distributions in luminosity and slope confirm and support the current theoretical framework.

It is thus apparent that more observational work has to be done to fully understand the complex emission properties of BL Lacs. In particular, broader data coverage is required to investigate which model can be used to describe the spectral curvature. Long duration temporal coverage of individual objects are also needed to determine the details of the spectral variability. A larger sample of objects is required to better clarify the situation for BL Lacs themselves, as well as the differences between BL Lacs and other classes of blazars.

APPENDICES

APPENDIX A

Login to the EXOSAT system

The EXOSAT system is installed at:

1) the EXOSAT Observatory/ESTEC in the Netherlands;
2) the University of Leicester X-ray astronomy group in the UK;
3) the HEASARC/NSSDC at the Goddard Space Flight Center in the USA.

To login to one of the above sites, you have to type:

1) **SET H EXOSAT** (or EXOSA0 or 29343)
2) **SET H LTXDB** (or 19847)
3) **SET H NDADSA** (or NDADS or 7069)

After receiving **Username:**, type XRAY; no password is required. At the first session, you are prompted for your username:

EXOSAT username >

enter your first initial and last name as ONE word. Example:

EXOSAT username > rsambruna

For the subsequent sessions, you are automatically recognized.

You are now in the EXOSAT system. If you want to enter in one of the available databases, you should use the command BROWSE followed by the name of the desired database. Then you can look at the tables of results, plot the available products (images, light curves, spectra), and extract what you are interested in for a more detailed analysis.

• *Plotting.* To plot the database products you need a graphic terminal. If you are using a Workstation, you should login to the EXOSAT system from a ReGIS VT200 window or a TEK4014/4125 Tektronix window. Thereafter, before doing the command for plotting, you must set the device for plotting. This is done using the command **cpd** (change plot device). For a Tektronix window:

EXOSAT> cpd /te

For the other options, you can use HELP. The command to plot any database products, is **pp**/*qualifier*, where the *qualifier* refers to the type of product you want to look at:

/im = image
/li = light curve
/bgli = background light curve
/sp = spectrum

You must also specify the number of the entry you are interested in:

pp/sp 1

This plots the spectrum of entry 1.

• *Extracting.* To extract any database result you can use the command xp/*qualifier*, where *qualifier* is the same as above. Again, you must specify the entry as above. You can extract more than one entry at a time:

xp/sp 1-4

This extracts the spectra of entries 1 to 4. For any information you need, you can use the on-line HELP.

EXAMPLE 1: to search for LE observations of the source 3C 66A.

```
EXOSAT> br le                          ! go in the LE database

LE_SOURCES_DEC> log 3c66a              ! create a log file named 3c66a.log

LE_SOURCES_DEC> sn 3C66A               ! search by name; you get

    name        seq  off  expos   time    count  filt   ra          dec    inst
(field name)    (#) (min) (sec) (yr.day)  rate          (1950)      (1950)

> 1 3C66A      2026   1   29468  86.032  2.8E-03  7  2 19 30.0 +42 48 30 L1
  2 3C66A      1992   1   16172  86.006  4.5E-03  7  2 19 30.0 +42 48 28 L1

LE_SOURCES_NAM 2> sc                                  ! search by coordinates

R.A. (1950  d/f=  2  h 19 m 29.97sec): 02 19 29   ! enter the right ascen.
Dec  (1950 d/f= 42 deg 48 m 29.57sec): 42 48      ! enter the declination
Radius in arcmin.  (d/f=  30.00): 60

    name        seq  off  expos   time     count filt   ra          dec    inst
(field name)    (#) (min) (sec) (yr.day)   rate        (1950)      (1950)

> 1 3C66A      1992   1   16172  86.006  4.5E-03  7  2 19 30.0 +42 48 28 L1
  2 3C66A      2026   1   29468  86.032  2.8E-03  7  2 19 30.0 +42 48 30 L1

LE_SOURCES_DEC 2> dp 1              ! display the first entry; you get

+-------------------------------------------------------------------------+
|                    EXOSAT Database -- LE results      EXO0219.4+4248    |
+-------------------------------------------------------------------------+
| Sequence No 1992 Field name 3C66A          Date 860106:1033  Instr L1   |
|                                                                         |
| Source type Extragalactic Object BL Lac                 mV=15.2 Z=0.444 |
|                                                                         |
| Position : R.A.  2 h 19 m 30.0 s  (1950)                                |
|            Dec +42 d 48 ' 28.0    (1950) Error radius  15 arcsec       |
|              L (II) 140.14  B (II) -16.77      Galactic NH = 6.60E+20   |
|                                                                         |
| Exp time  16172 X-pix  34.0  Y-pix  24.7 Offset from centre   7.1 min   |
|                                                                         |
| Offset from target location    1.4 min                                  |
|                                                                         |
| Image name A68817     Rates file C68817         Back/sqpix/s 1.07E-05   |
|                                                                         |
| Count rate   0.45E-02+/-0.8E-03 Counts     72+/-  13  Signf   0.1E-33   |
| Filter      Thin lexan                                   Volume # 49    |
|                                                                         |
| Count rate: Al/P : Not available         Boron : Not available          |
|             ME   :  4.37E-01+/- 4.0E-02  IPC   :  3.09E-02+/- 3.1E-03   |
| Comment:  Prop code AGN                                                 |
+-------------------------------------------------------------------------+

LE_SOURCES_DEC 2>                      ! you want to display an image;

LE_SOURCES_DEC 2>cpd /te               ! to set up the graphic mode
                                         from a TEK window on VAX

LE_SOURCES_DEC 2>pp/im 1               ! display image of entry 1

LE_SOURCES_DEC 2>pp/li 1               ! display the light curve of entry 1

LE_SOURCES_DEC 2> xp/li/name=3c66a 1   ! extract the light curve of entry 1
                                         and name it 3c66a.rbf

LE_SOURCES_DEC 2>ex                    ! exit from the LE database.
```

EXAMPLE 2: now search for the ME observations of 3C 66A:

```
EXOSAT> br me                          ! go in the ME database

ME_TOTAL_DEC 3> log 3c66a              ! create a log file named 3c66a.log

ME_TOTAL_DEC 3> sn 3C66A               ! search by name; you get
```

	name	time (yy.day)	seq (#)	QF	exp (sec)	count rate error	ra (1950)	dec (1950)
>	1 3C66A	86.015	2008	3	36290	0.49 +/- 0.07	02 19 30	+42 48.5
	2 3C66A	86.006	1992	2	20570	0.43 +/- 0.04	02 19 30	+42 48.5
	3 3C66A	86.032	2026	2	40060	0.44 +/- 0.02	02 19 30	+42 48.5

```
ME_TOTAL_NAM 3> sc                                  ! search by coordinates

R.A. (1950  d/f=  2  h 19 m 30.00sec): 02 19 27     ! enter right ascension
Dec  (1950 d/f= 42 deg 48 m 29.95sec): 42 48        ! enter declination
Radius in arcmin. (d/f=  60.00):
```

	name	time (yy.day)	seq (#)	QF	exp (sec)	count rate error	ra (1950)	dec (1950)
>	1 3C66A	86.015	2008	3	36290	0.49 +/- 0.07	02 19 30	+42 48.5
	2 3C66A	86.032	2026	2	40060	0.44 +/- 0.02	02 19 30	+42 48.5
	3 3C66A	86.006	1992	2	20570	0.43 +/- 0.04	02 19 30	+42 48.5

```
ME_TOTAL_DEC 3> dp 1                   ! display entry 1; you get
```

```
+-----------------------------------+-----------------------------------+
|   EXOSAT ME Database              |            Source: 3C66A          |
+-----------------------------------+-----------------------------------+
|   Pointing direction (1950)       |  Ct/s (1-8 keV):   0.49 +/-  0.07 |
|    R.A.(h m s):  2 19 23.0        |       (1-3 keV):   0.22 +/-  0.04 |
|    Dec (d m s): 42 46 33.6        |       (3-6 keV):   0.25 +/-  0.04 |
|    LII (d): 140.14                |      (6-10 keV):  -0.11 +/-  0.05 |
|    BII (d): -16.77                |     (10-15 keV):   0.00 +/-  0.06 |
|    Beta angle: 109                |  HR (6-10keV/3-6keV): -0.454+/- 0.200|
|  Start: 1986 Day  15, 10h 32m 20s |  SR (1-3keV/3-6keV) :  0.894+/- 0.219|
|  Stop : 1986 Day  15, 17h 45m  8s |                                   |
|  Exposure:  36290 s               +------+-------Spectral Results-----+
|                                   |                                   |
|  Int-tint =   0.03906 s           | Spectrum:S69478 with quality flag 3 (3-5 OK)|
|  Pha-tint =   10.0000 s           | Best fit: Power law               |
|                                   |                                   |
|                                   |                                   |
|                                   |  Warning: Auto-specfit not always reliable |
|  Variability at pha-tint          |  If in doubt, extract spectrum and use xspec|
|  1-3keV RMS Var:  <925.4   %      |                                   |
|  3-8keV RMS Var:  <999.9   %      | chi2=   0.00  Norm=  1.0000 alpha=  0.000 |
|  1-8keV RMS Var:  <691.6   %      |  Nh=0.00E+00                      |
|  Bgnd   RMS Var:  < 18.0   %      |                                   |
|      at 10*(pha tint)             |                                   |
|  1-8keV RMS Var:  Not Calc %      |                                   |
|  Tape no:   2                     |  Mod  Chi-2   Norm     Alpha   kT      Nh  |
|  Sequence number: 2008            |  th    0.0  0.00E+00    -     0.00  0.0E+00|
|  Macro code:SWAP1                 |  pl    0.0  0.00E+00   0.00    -    0.0E+00|
|  Proposal code:AGN3-077           |  bb    0.0  0.00E+00    -     0.00  0.0E+00|
|  Created on: 1987 Day 303         |  co    0.0  0.00E+00   0.00   0.00  0.0E+00|
+-----------------------------------+-----------------------------------+
```

```
ME_TOTAL_DEC 3> cpd /te              ! set the graphic mode from a TEK window on VAX
ME_TOTAL_DEC 3> pp/sp 1              ! plot the spectrum of entry 1
ME_TOTAL_DEC 3> xp/sp/name=3c66a 1 ! extract the spectrum and name it 3c66a.pha

ME_TOTAL_DEC 3> ex                   ! exit from the ME database.
```

To transfer any files from your EXOSAT area to your actual account, you can use the MAIL command from the EXOSAT system, or the COPY command from your system.
To exit from the system type LOG.

APPENDIX B

Summary of the published EXOSAT spectra

Table A and B list the results of a literature search concerning the published results of spectral analysis of the EXOSAT data. The BL Lacs listed in Table A, column 1, were studied individually in the works referred to in column 5. In column 2 the number of EXOSAT observations which were considered is given. The parameters of a fit with a single power law (photon index, α, and absorbing column density, N_H) are reported in columns 3 and 4, respectively. When more than one observation was studied, the average with the standard deviation is given. Finally, notes concerning the single objects are given in column 7.

Table A is an updated version of Table 2 given by Maraschi & Maccagni (1988). Excluding PKS 0537-441 (see section 3.2), three additional objects were found with respect to this work, *i.e.,* EXO 0556.4-3838, Mrk 180, and 2A 1219+305, while for other objects (PKS 0521-365, Mrk 501, I ZW 186) more recent references, involving an increased number of observations, are quoted. In addition, alternative (better) fits with different models are referred to in the notes.

The HPQ–OVV of the final sample for which the EXOSAT spectra were already published are listed in Table B with the same format as Table A.

Table A: Published spectral results from EXOSAT for BL Lacs

Object	N. of obs.	α	N_H ($\times 10^{20}$ cm^{-2})	References	Notes
3C 66A	3	$2.80^{+0.80}_{-0.60}$	≤ 100	1	a
MS 0317.0+1834	1	$2.00^{+0.50}_{-0.40}$	$11.5^{+15.0}_{-8.0}$	2	
PKS 0521-365	2	1.68 ± 0.03	4.0 ± 1.0	3	
EXO0556.4-3838	2	1.53 ± 0.13	5.3 ± 4.1	4	b
PKS 0537-441	1	1.30 ± 0.13	≤ 30	5	
PKS 0548-322	3	2.15 ± 0.04	3.6 ± 0.8	6,3	c
Mrk 421	3	2.18 ± 0.05	2.4 ± 0.4	7	d
	11	2.62 ± 0.17	2.0 ± 0.4		e
Mrk 180	1	$2.44^{+0.20}_{-0.07}$	$2.0\ ^{+1.2}_{-0.8}$	8	f
	2	2.67 ± 0.19	2.3 ± 0.0		e
1218+304	7	2.23 ± 0.08	3.3 ± 0.5	8	f,b
	1	$2.44^{+0.14}_{-0.05}$	$3.6^{+1.3}_{-0.9}$		e,b
MS 1402.3+041	1	$2.60^{+0.30}_{-0.10}$	2.0 (< 12.0)	2	f
1E 1415.6+255	1	3.00 ± 0.20	8.0 ± 2.5	2	g
H1426+428	1	$2.19^{+0.09}_{-0.06}$	$2.7^{+0.9}_{-0.6}$	9	
Mrk 501	5	2.29 ± 0.09	2.3 ± 0.5	8	f
	5	2.46 ± 0.08	2.4 ± 0.5	8,10	e
I ZW 186	2	2.45 ± 0.11	3.6 ± 0.1	3	
3C 371	1	2.7 ± 0.10	...	11	f,g
PKS 2005-489	1	$2.60^{+0.10}_{-0.05}$	$5.1^{+1.4}_{-1.0}$	12	f
	1	$3.10^{+1.10}_{-0.05}$	$7.2^{+1.6}_{-1.1}$		e
PKS 2155-304	6	2.73 ± 0.05	1.8 ± 0.2	13	e,h
	3	2.51 ± 0.08	1.7 ± 0.5		f,h

Table B: Published spectral results from EXOSAT for HPQ

Object	N. of obs.	α	N_H ($\times 10^{20}$ cm^{-2})	References	Notes
PKS 1510-089	2	1.30 ± 0.20	8.5 ± 3.4	14	j
3C 390.3	3	1.52 ± 0.09	4.8 ± 1.1	15	j

References: 1 = Maccagni *et al.* (1987), 2 = Giommi *et al.* (1987), 3 = Garilli & Maccagni (1990), 4 = Giommi *et al.* (1989), 5 = Treves *et al.* (1992), 6 = Barr *et al.* (1988), 7 = George *et al.* (1988a), 8 = George *et al.* (1988b), 9 = Remillard *et al.* (1989), 10 = Staubert *et al.* (1986a), 11 = Staubert *et al.* (1986b), 12 = Wall *et al.* (1986), 13 = Treves *et al.* (1989), 14 = Singh *et al.* (1990), 15 = Ghosh & Soundararajaperumal (1991).

Notes:

(a) Only ME data, 2 – 7 keV
(b) Possible contaminating Seyfert in the field
(c) Better fit to the lowest and highest states by a broken power law with break at 5 and 3 keV, respectively
(d) High state, better fit by adding an exponential cut-off above 3 keV
(e) Low state
(f) High state
(g) The data are consistent with a break at 2 keV
(h) Evidence for Fe and OVIII absorption edges at 7 and 0.6 keV, respectively
(i) Soft excess
(j) Evidence for redshifted 6.4 keV fluorescence line of cold Iron

APPENDIX C

Spectra

The following spectra are reported:

- 3C 66A: 86.006, 86.032
- AO 0235+169: 84.214 + 86.015
- PKS 0521-365: 83.306
- PKS 0537-441: 85.055
- PKS 0754+100: 84.045
- OJ 287: 83.281, 84.040
- B2 1308+32: 85.132
- 3C 371: 84.256, 84.273
- MS 0317.0+1834: 85.013, 85.039
- H0323+022: 84.265, 84.267
- H0414+009: 84.258, 84.274
- EXO 0423.4-0840: 85.048
- EXO 0507.1-0404: 84.298
- PKS 0548-322: 83.306, 86.066
- EXO 0556.4-3838: 84.350, 86.021
- Mrk 421: 84.338, 85.118, 84.037
- Mrk 180: 84.308, 85.093
- 1218+304: 85.005, 85.029
- MS 1235+63: 85.079 + 85.080
- 1E 1402+04: 85.031, 85.187
- 1E 1415+22: 86.063
- Mrk 501: 84.034, 84.086, 84.201
- H1722+119: 85.246
- I ZW 187: 84.063, 84.181
- PKS 2005-489: 84.254, 84.287, 85.276
- PKS 2155-304: 83.304, 84.311 C, 85.297
- Ton 599: 84.151, 85.136
- PKS 1510-08: 85.212, 84.216 + 84.217
- 3C 390.3: 84.153, 85.033, 86.077
- PKS 2208-137: 84.146

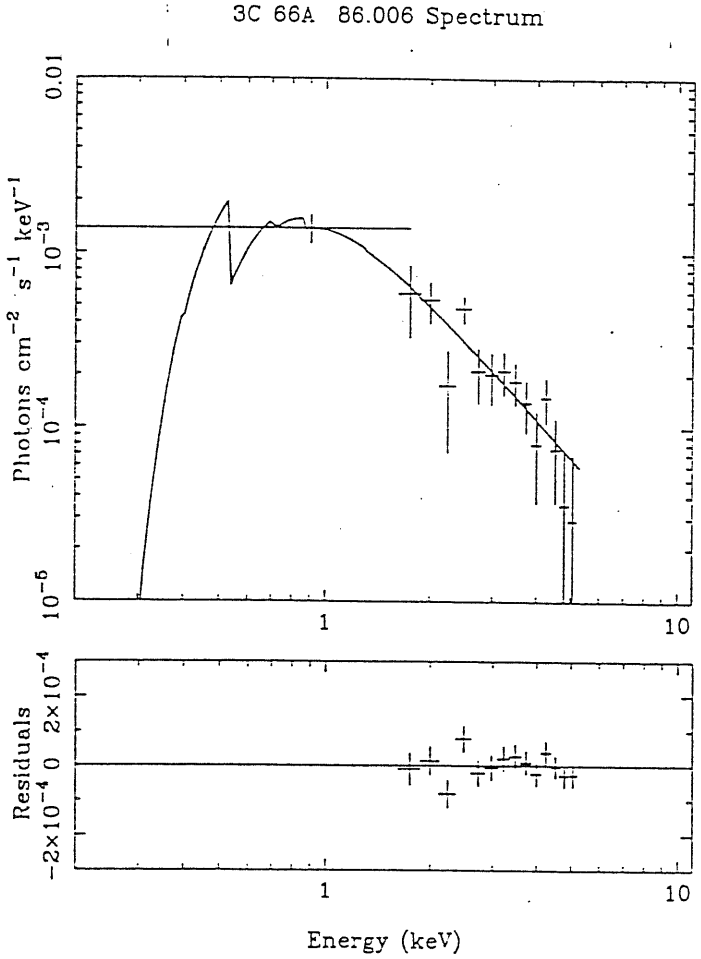

Figure C.1: The most representative spectra of the blazars studied in Chapter 4 are shown. *Upper panels:* 0.1 – 10 keV spectra deconvolved with the power law model with free N_H. *Lower panels:* residuals of the above model.

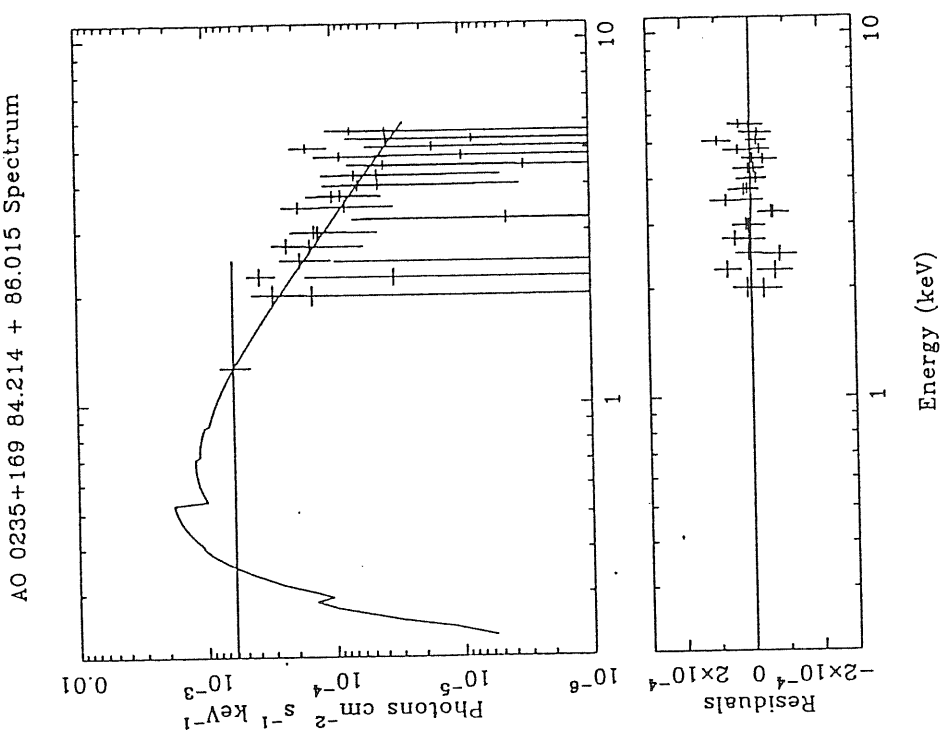
AO 0235+169 84.214 + 86.015 Spectrum
Photons cm^{-2} s^{-1} keV^{-1}
Residuals
Energy (keV)

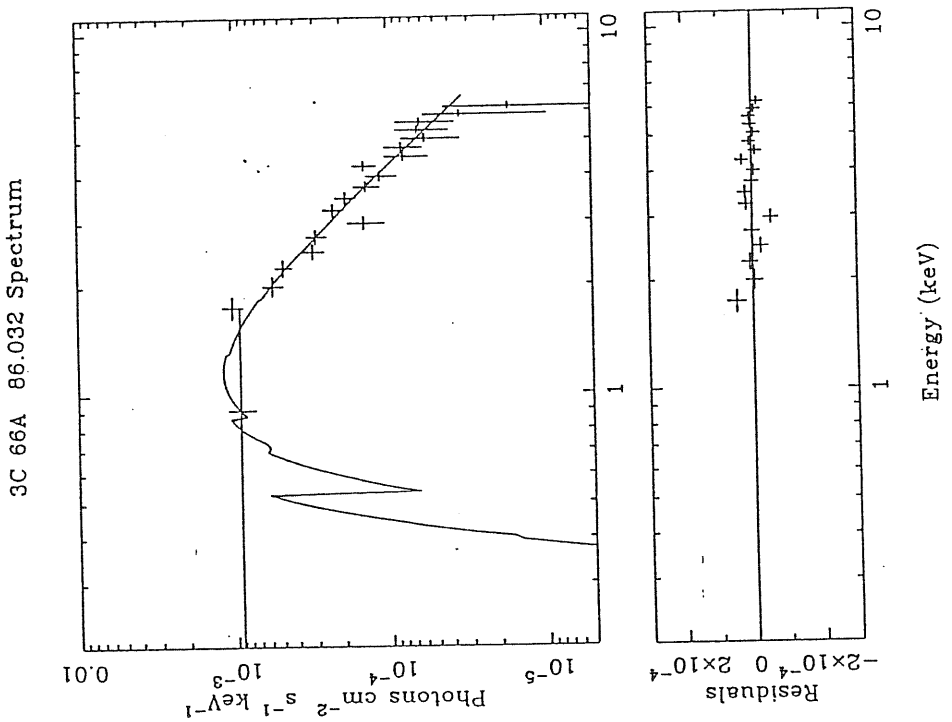
3C 66A 86.032 Spectrum
Photons cm^{-2} s^{-1} keV^{-1}
Residuals
Energy (keV)

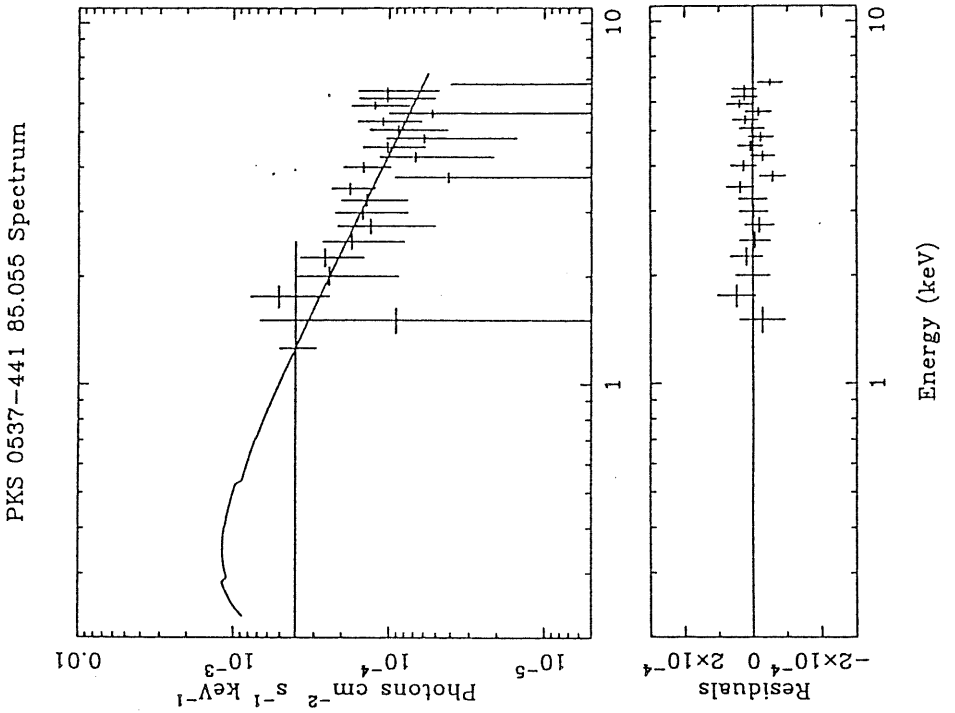
PKS 0537−441 85.055 Spectrum
Photons cm^{-2} s^{-1} keV^{-1}
0.01
10^{-3}
10^{-4}
10^{-5}
Residuals
-2×10^{-4} 0 2×10^{-4}
1
10
Energy (keV)

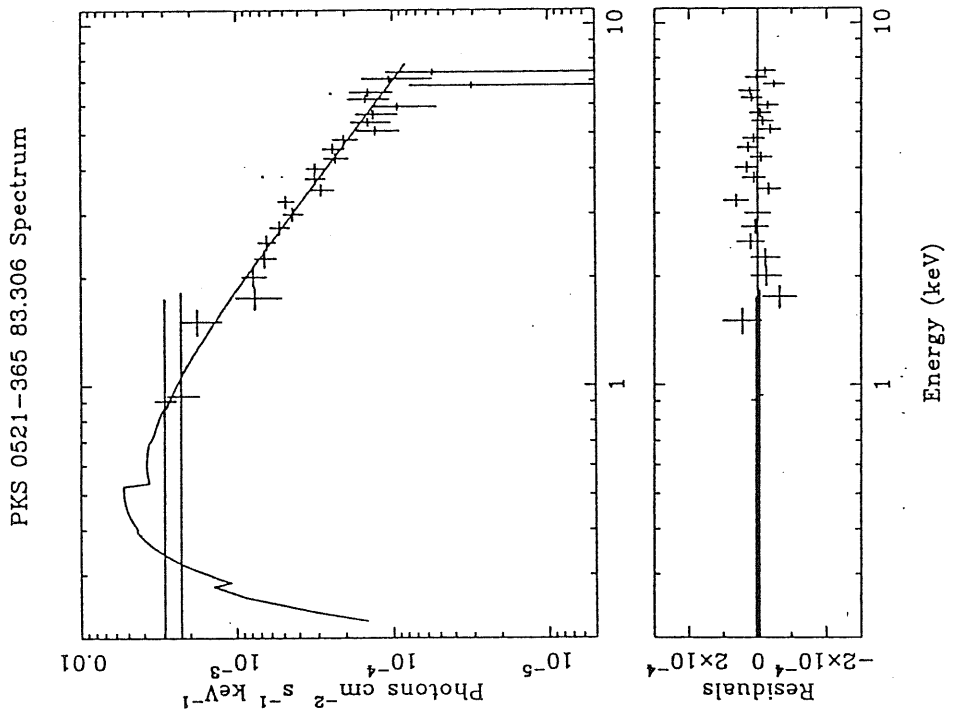
PKS 0521−365 83.306 Spectrum
Photons cm^{-2} s^{-1} keV^{-1}
0.01
10^{-3}
10^{-4}
10^{-5}
Residuals
-2×10^{-4} 0 2×10^{-4}
1
10
Energy (keV)

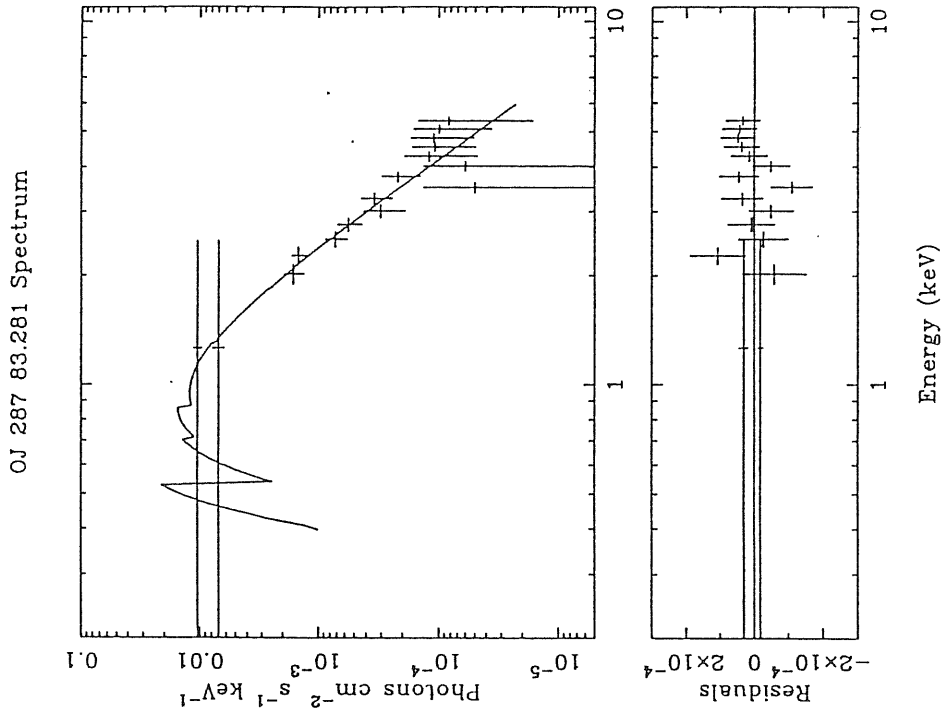
OJ 287 83.281 Spectrum
Photons cm^{-2} s^{-1} keV^{-1}
Residuals
Energy (keV)

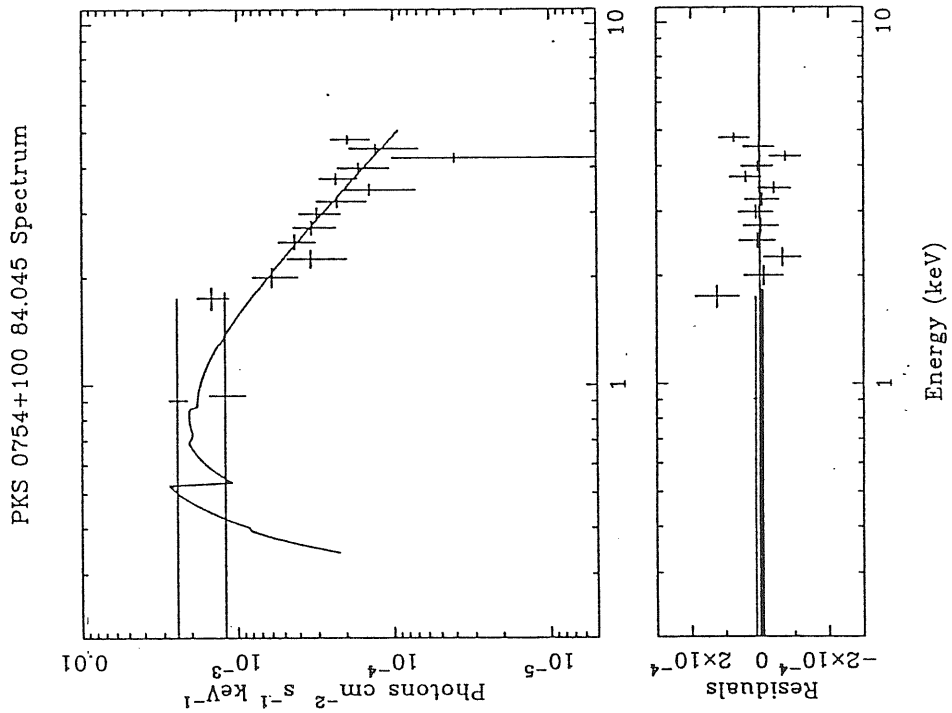
PKS 0754+100 84.045 Spectrum
Photons cm^{-2} s^{-1} keV^{-1}
Residuals
Energy (keV)

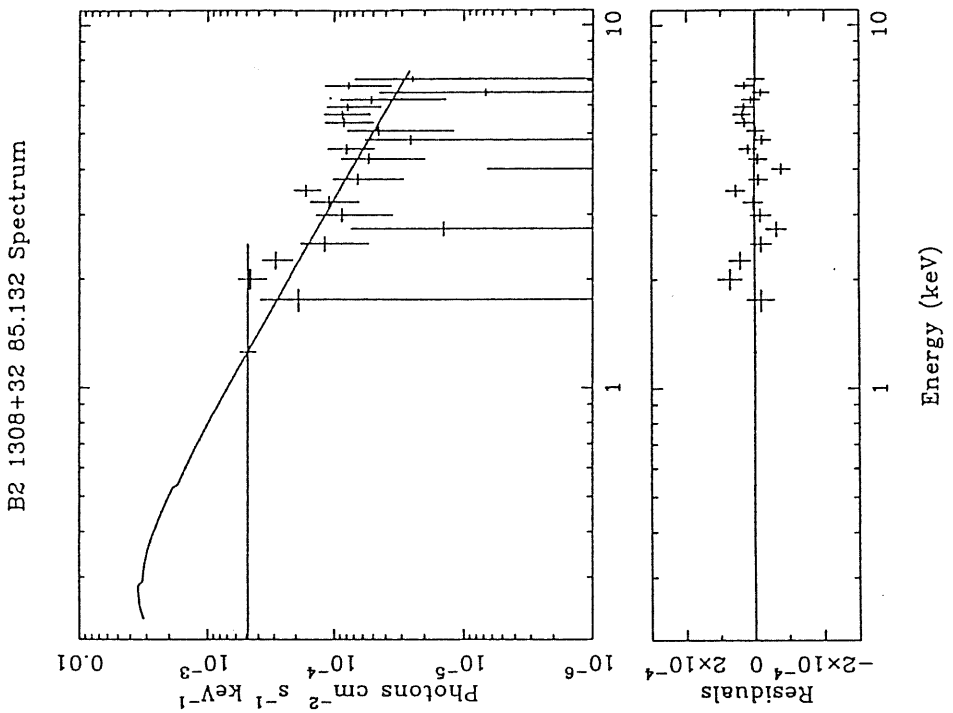
B2 1308+32 85.132 Spectrum
Photons cm^{-2} s^{-1} keV^{-1}
Residuals
Energy (keV)

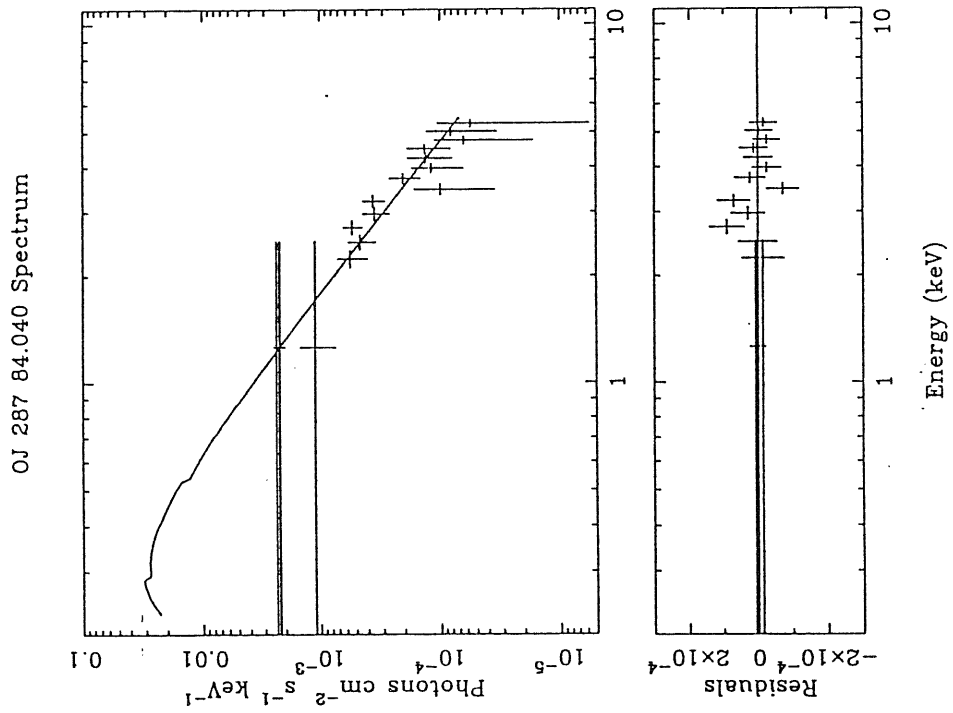
OJ 287 84.040 Spectrum
Photons cm^{-2} s^{-1} keV^{-1}
Residuals
Energy (keV)

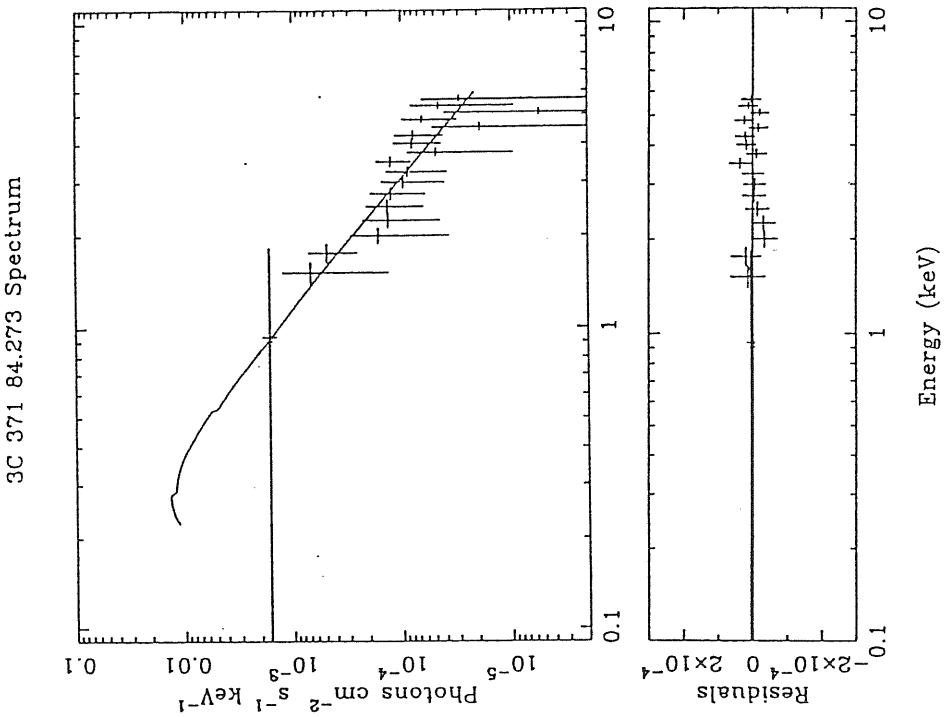
3C 371 84.273 Spectrum
Photons cm^{-2} s^{-1} keV^{-1}
Residuals
Energy (keV)

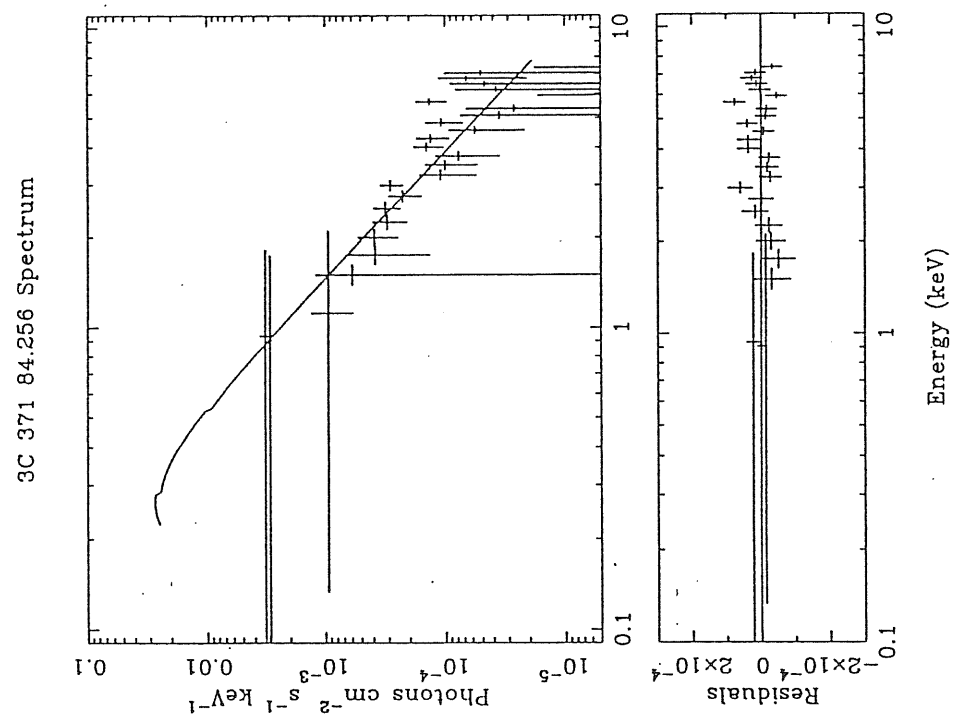
3C 371 84.256 Spectrum
Photons cm^{-2} s^{-1} keV^{-1}
Residuals
Energy (keV)

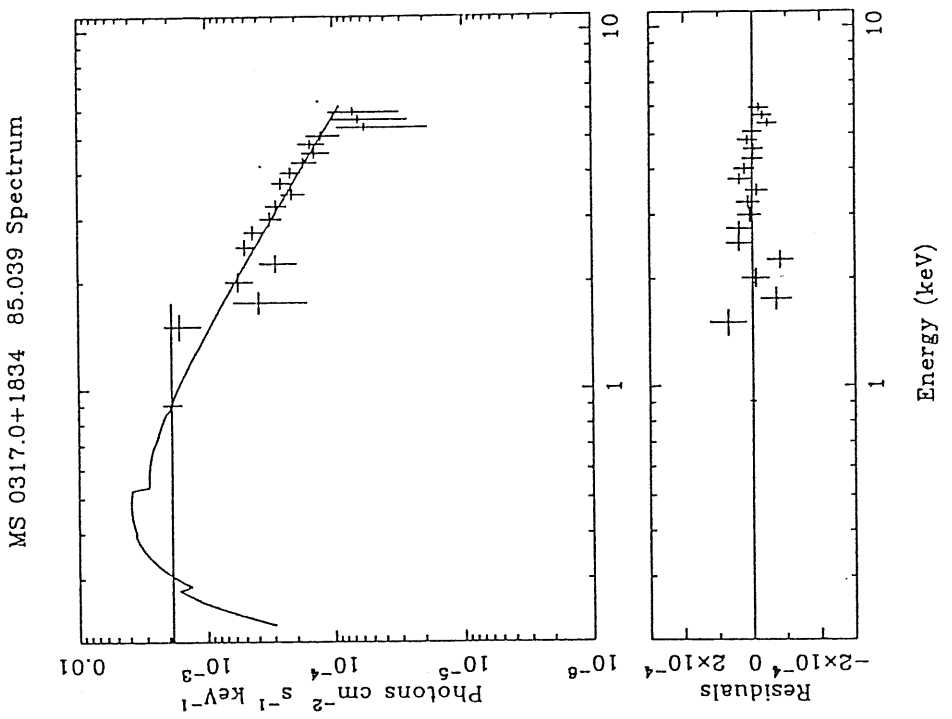
MS 0317.0+1834 85.039 Spectrum
Photons cm^{-2} s^{-1} keV^{-1}
Residuals
Energy (keV)

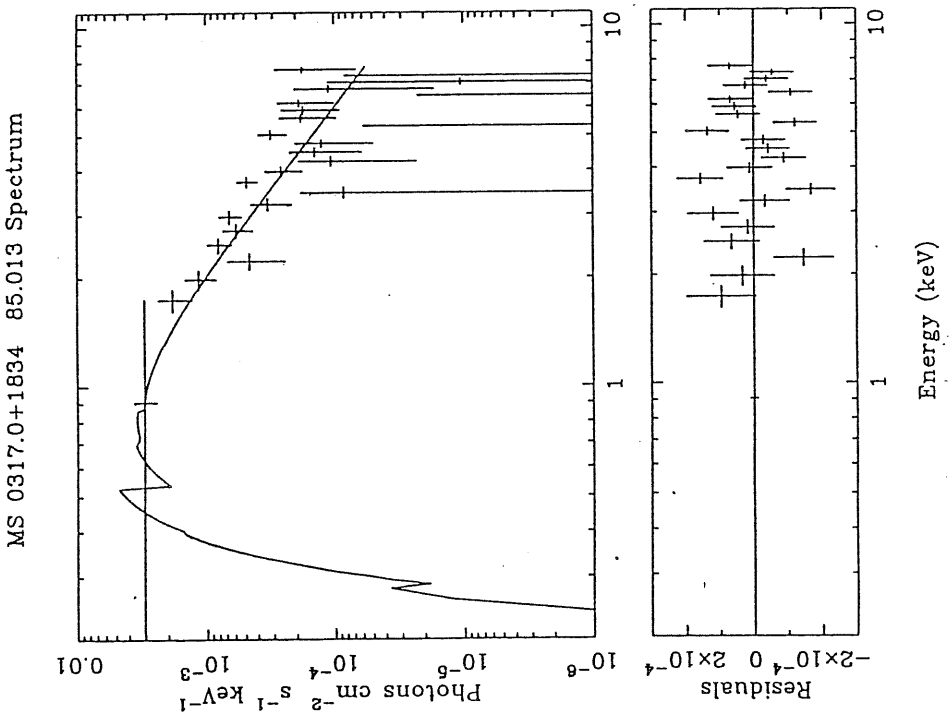
MS 0317.0+1834 85.013 Spectrum
Photons cm^{-2} s^{-1} keV^{-1}
Residuals
Energy (keV)

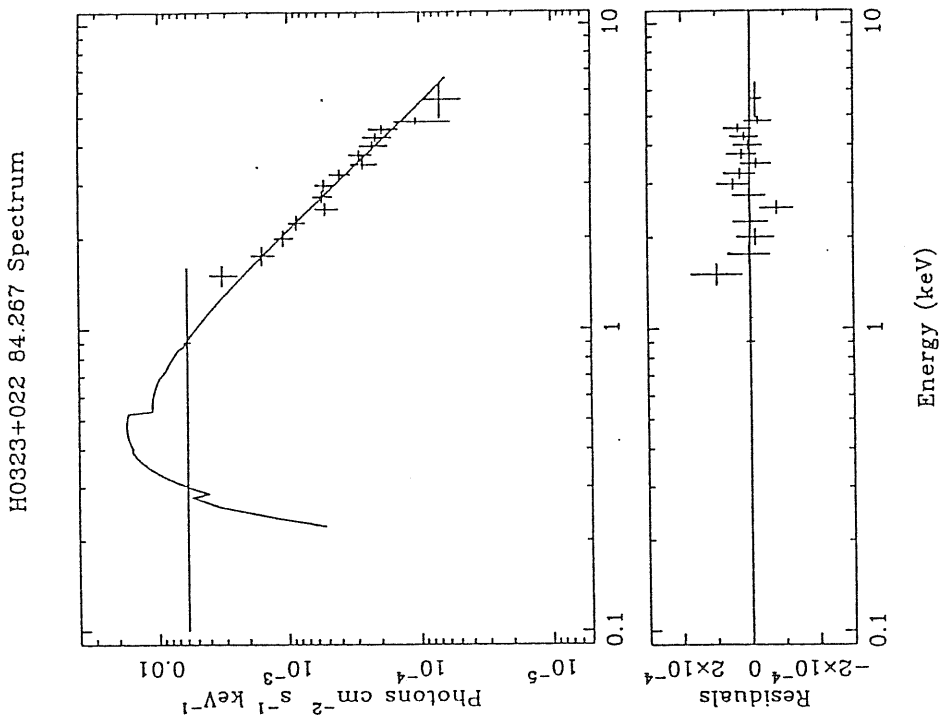
H0323+022 84.267 Spectrum
Photons cm^{-2} s^{-1} keV^{-1}
Residuals
Energy (keV)

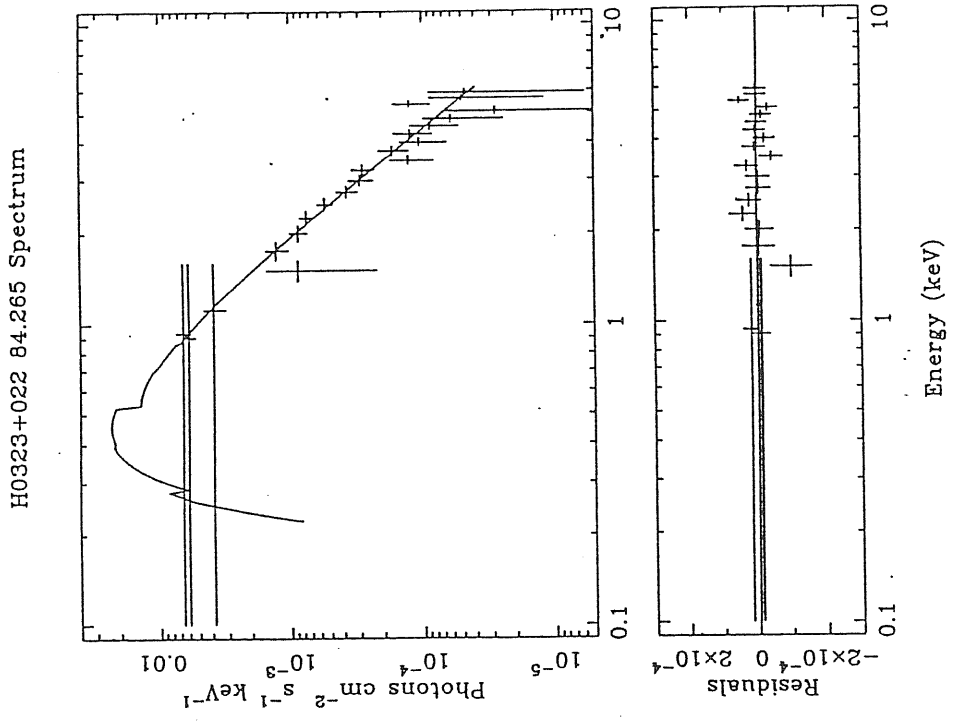
H0323+022 84.265 Spectrum
Photons cm^{-2} s^{-1} keV^{-1}
Residuals
Energy (keV)

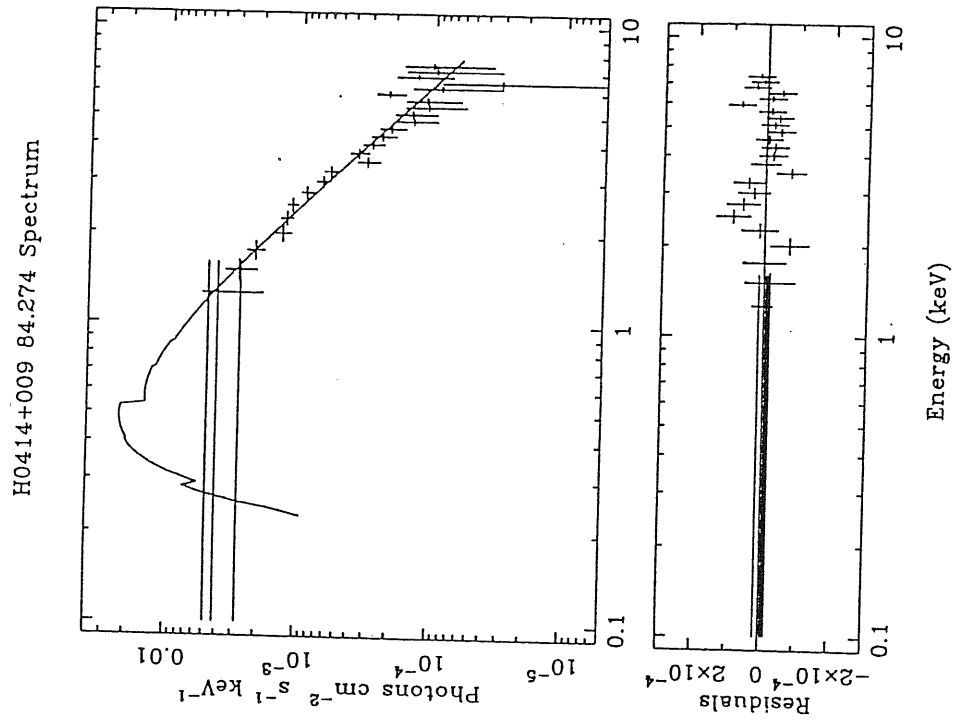
H0414+009 84.274 Spectrum
Photons cm^{-2} s^{-1} keV^{-1}
Residuals
Energy (keV)

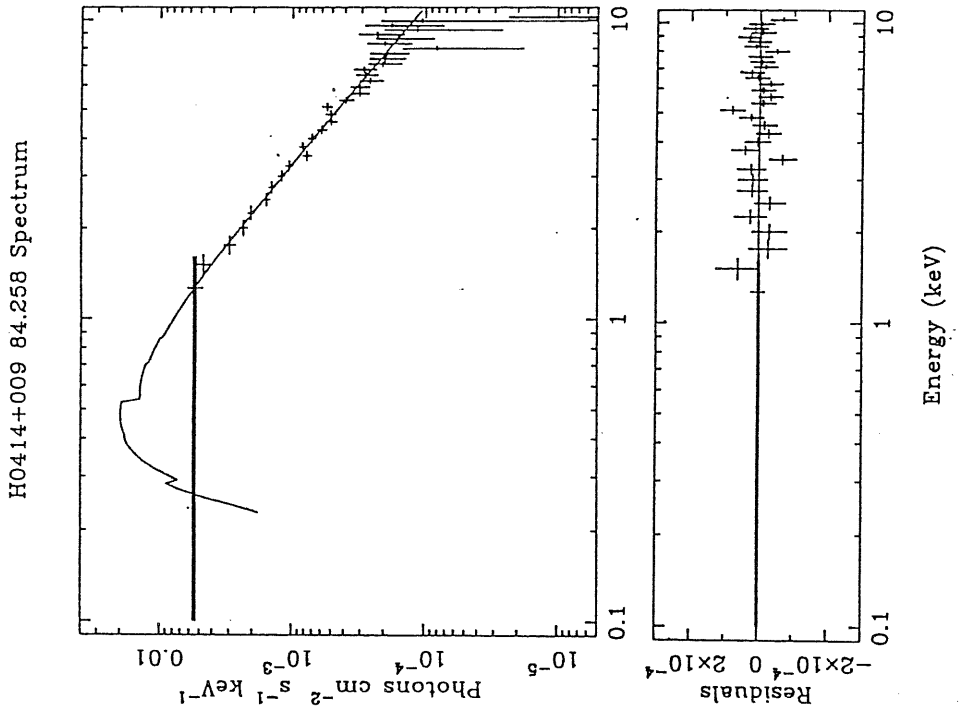
H0414+009 84.258 Spectrum
Photons cm^{-2} s^{-1} keV^{-1}
Residuals
Energy (keV)

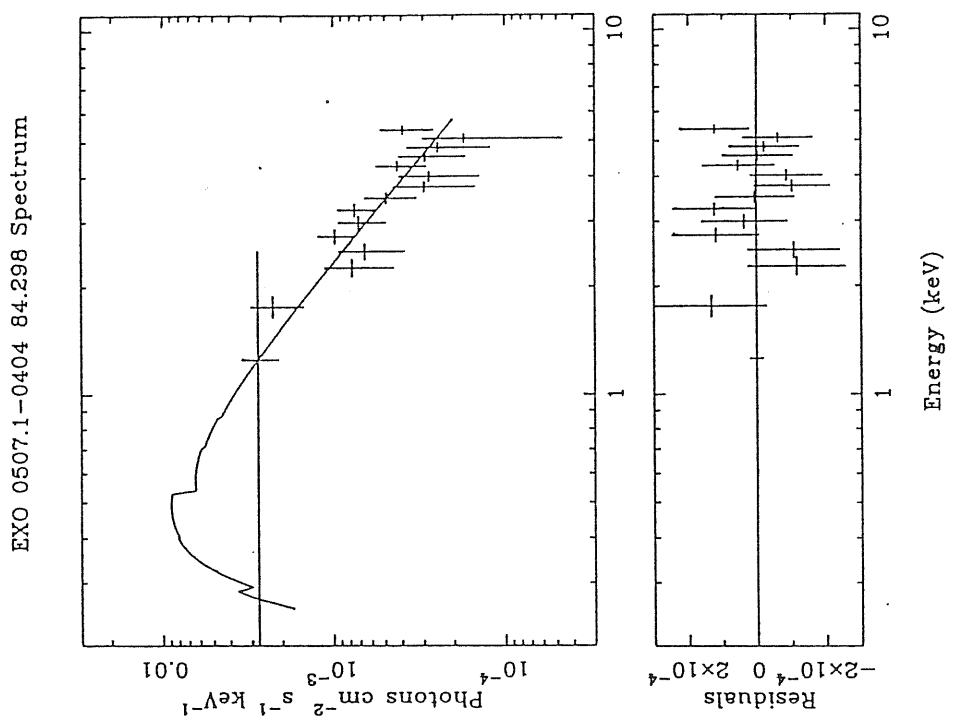
EXO 0507.1−0404 84.298 Spectrum
Photons cm^{-2} s^{-1} keV^{-1}
Residuals
Energy (keV)

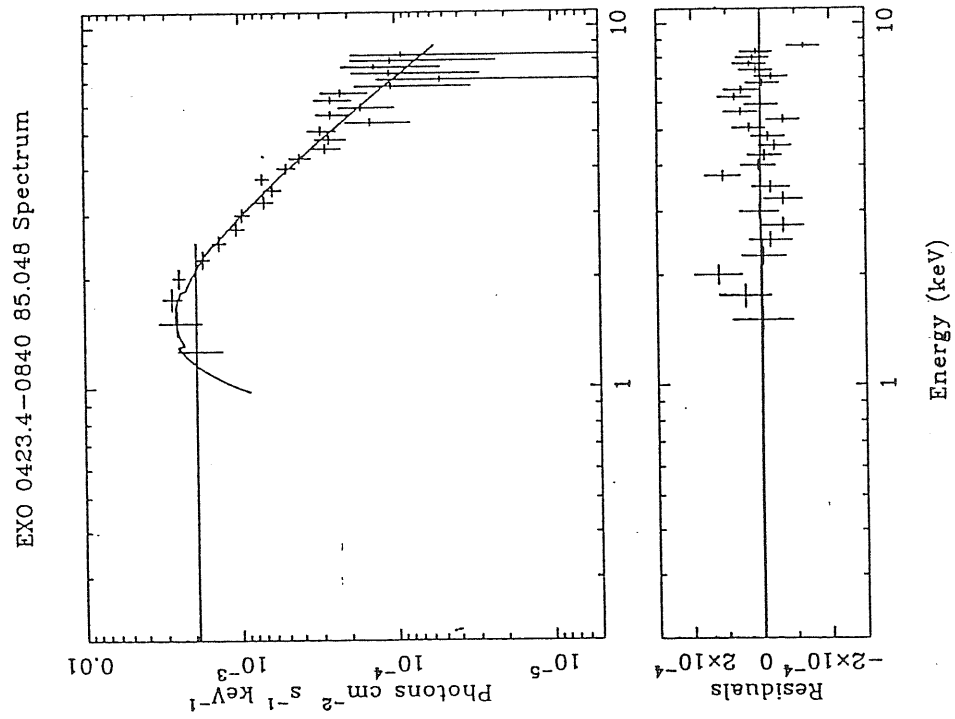
EXO 0423.4−0840 85.048 Spectrum
Photons cm^{-2} s^{-1} keV^{-1}
Residuals
Energy (keV)

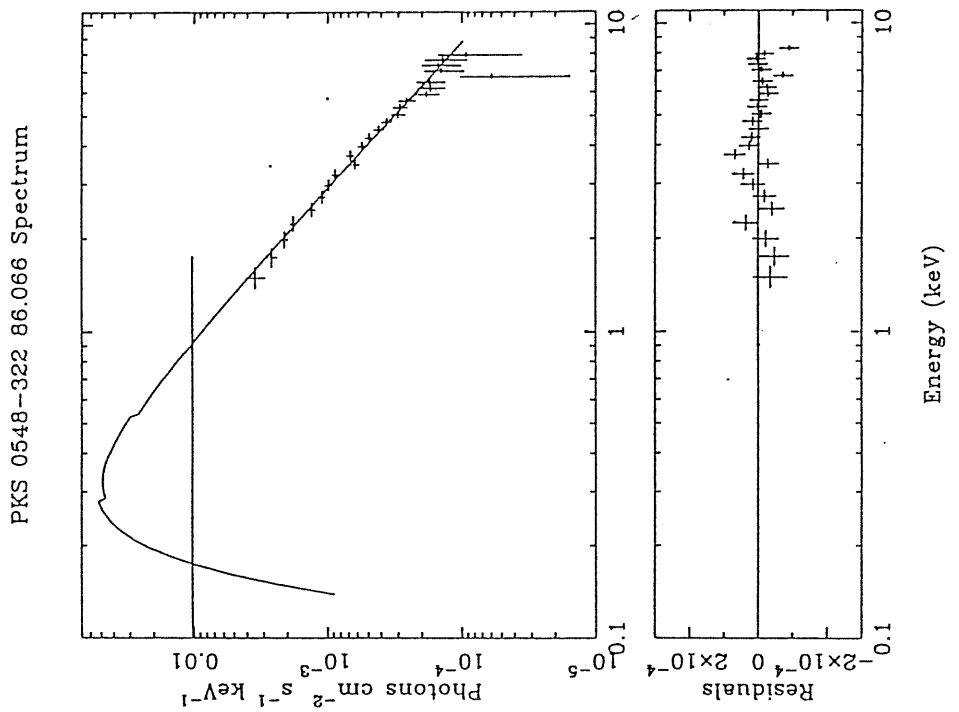
PKS 0548−322 86.066 Spectrum
Photons cm^{-2} s^{-1} keV^{-1}
Residuals
Energy (keV)

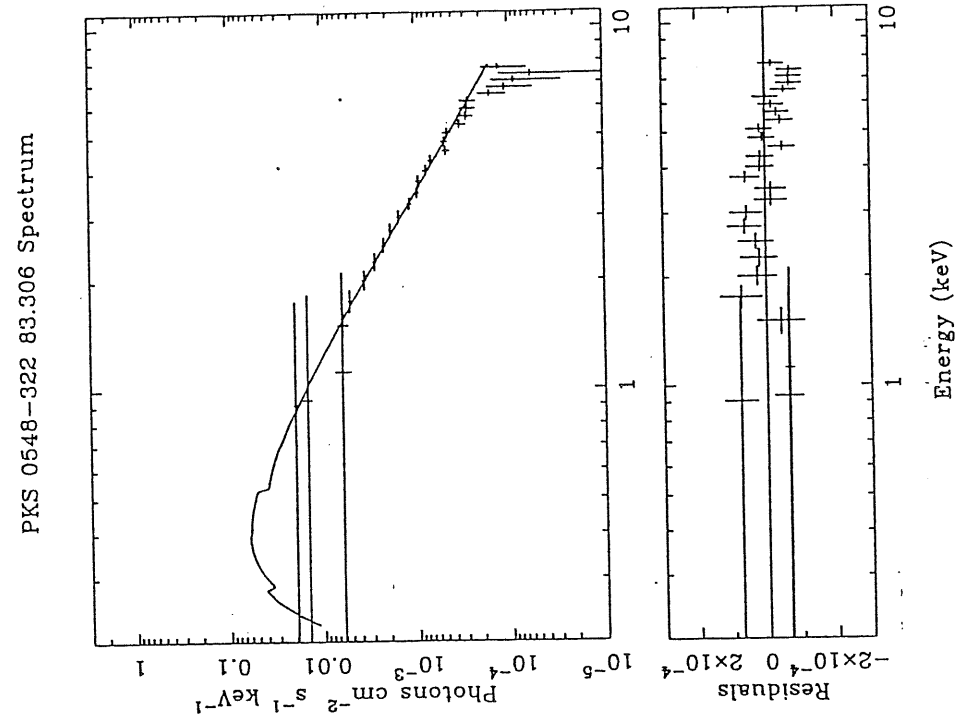
PKS 0548−322 83.306 Spectrum
Photons cm^{-2} s^{-1} keV^{-1}
Residuals
Energy (keV)

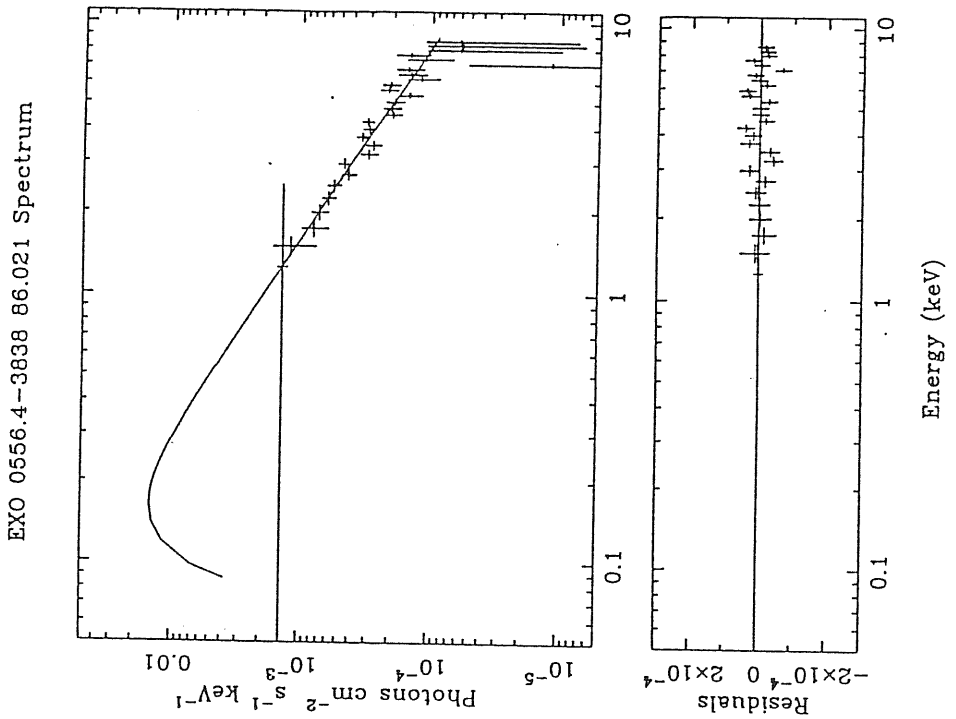
EXO 0556.4−3838 86.021 Spectrum
Photons cm^{-2} s^{-1} keV^{-1}
Residuals
Energy (keV)

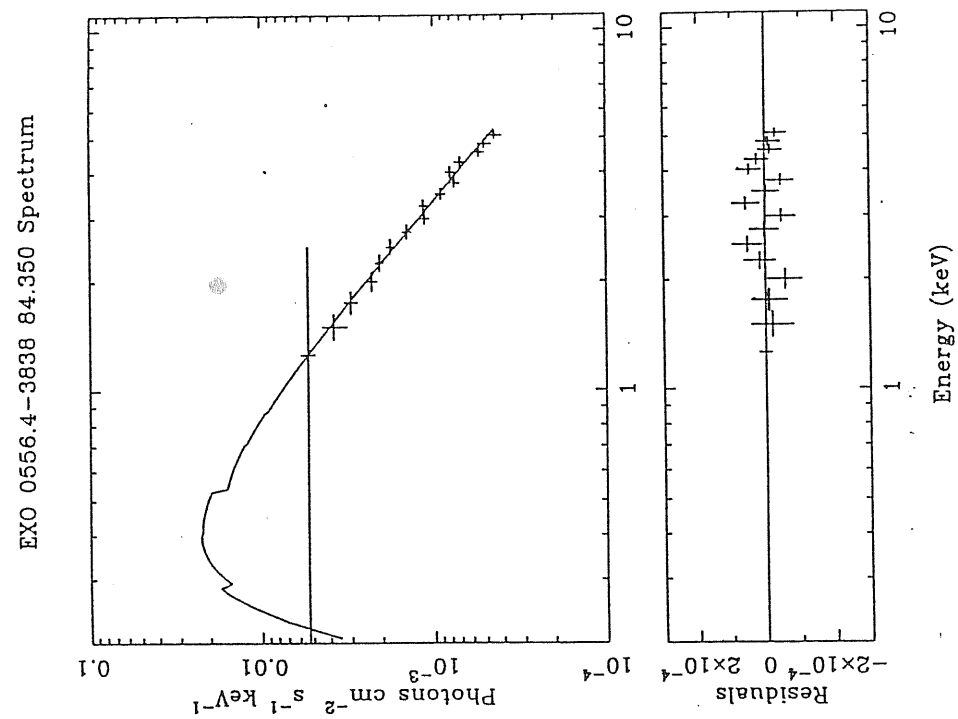
EXO 0556.4−3838 84.350 Spectrum
Photons cm^{-2} s^{-1} keV^{-1}
Residuals
Energy (keV)

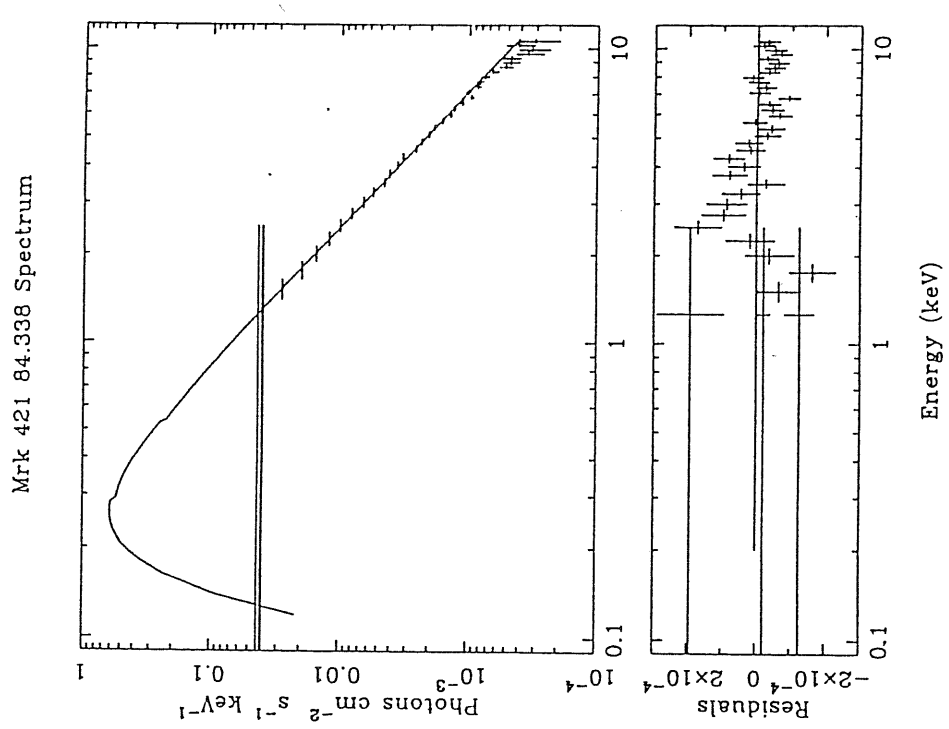
Mrk 421 84.338 Spectrum
Photons cm^{-2} s^{-1} keV^{-1}
Residuals
Energy (keV)

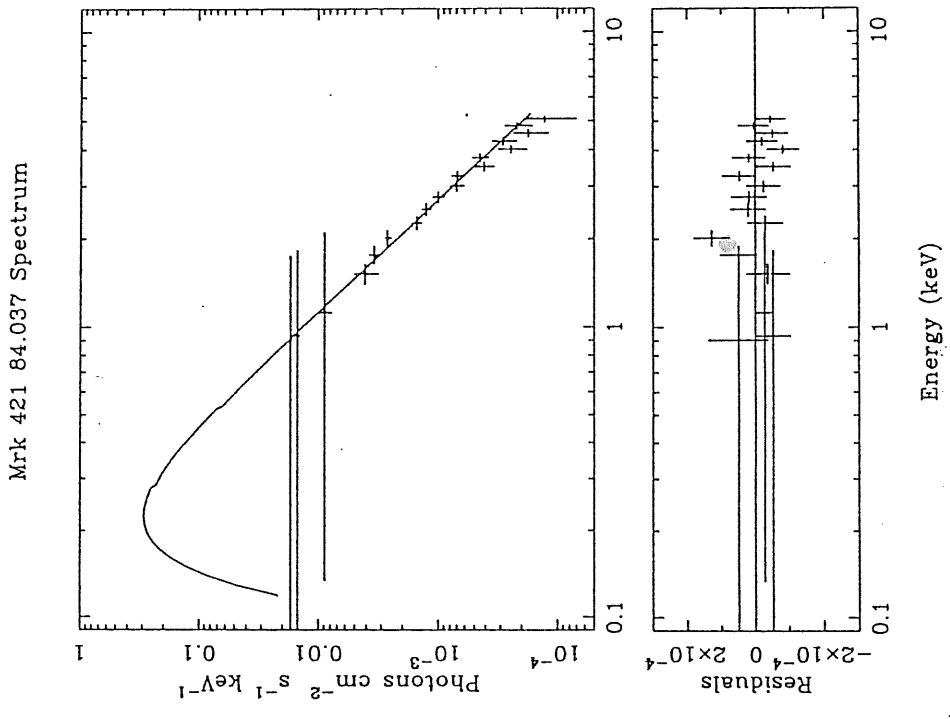
Mrk 421 84.037 Spectrum
Photons cm^{-2} s^{-1} keV^{-1}
Residuals
Energy (keV)

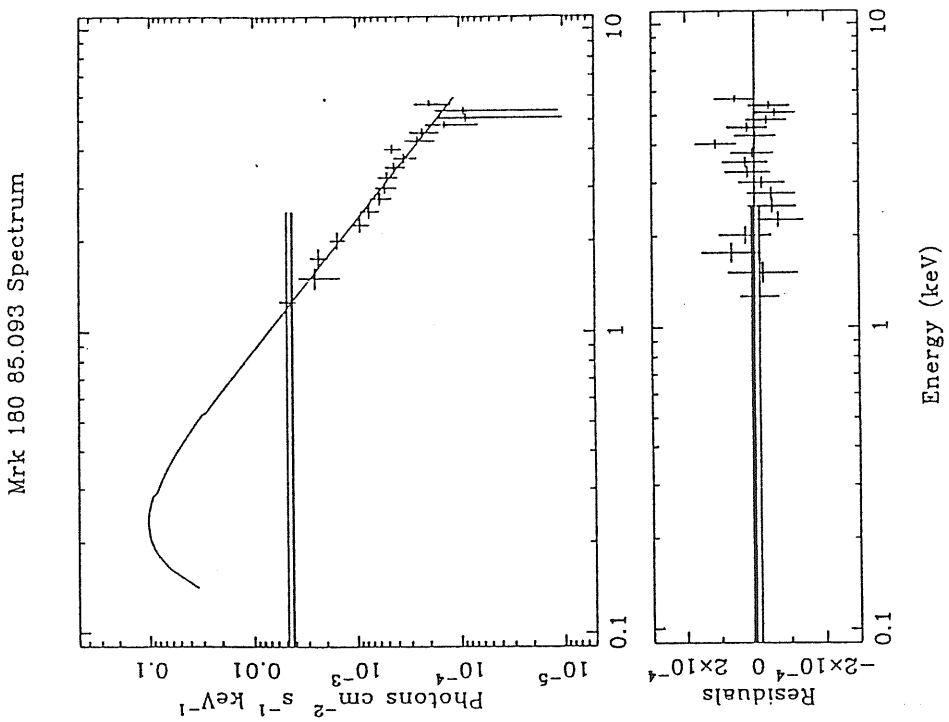
Mrk 180 85.093 Spectrum
Photons cm^{-2} s^{-1} keV^{-1}
Residuals
Energy (keV)

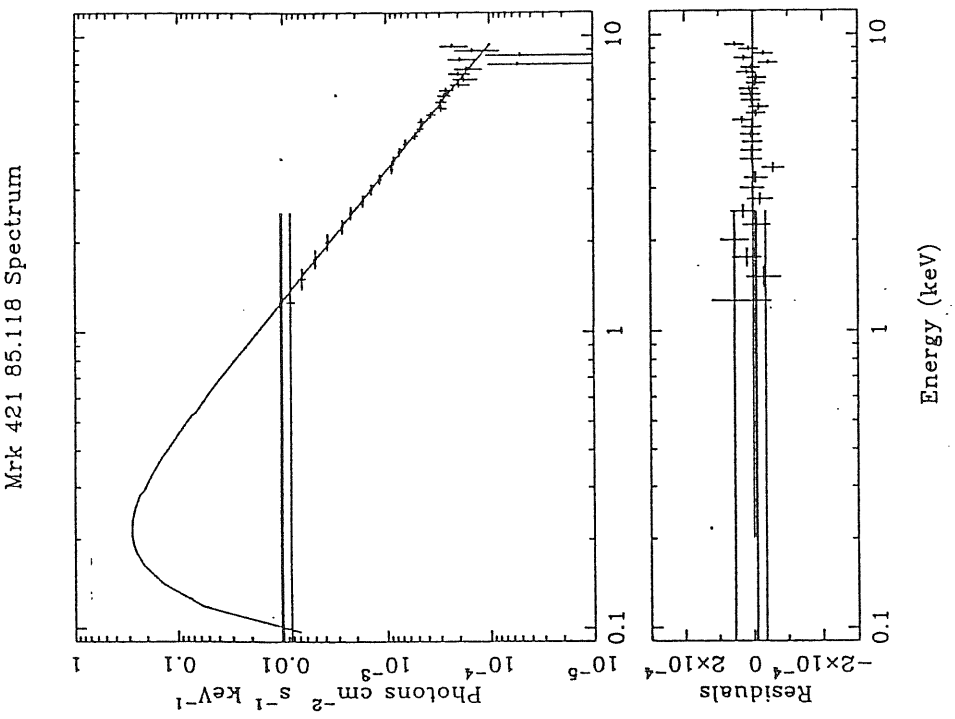
Mrk 421 85.118 Spectrum
Photons cm^{-2} s^{-1} keV^{-1}
Residuals
Energy (keV)

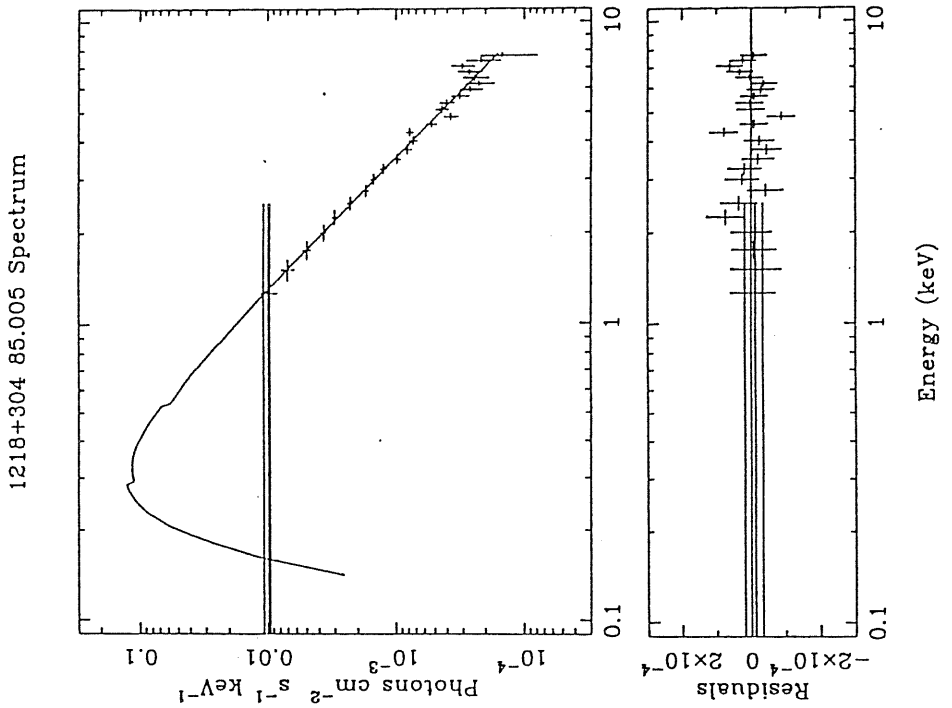
1218+304 85.005 Spectrum
Photons cm^{-2} s^{-1} keV^{-1}
Residuals
Energy (keV)

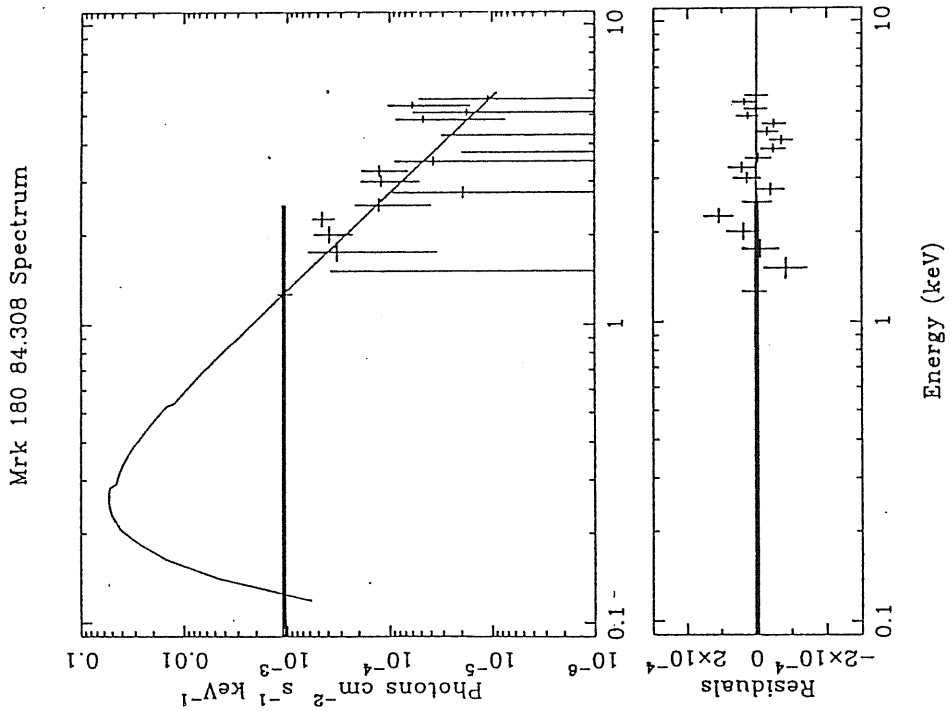
Mrk 180 84.308 Spectrum
Photons cm^{-2} s^{-1} keV^{-1}
Residuals
Energy (keV)

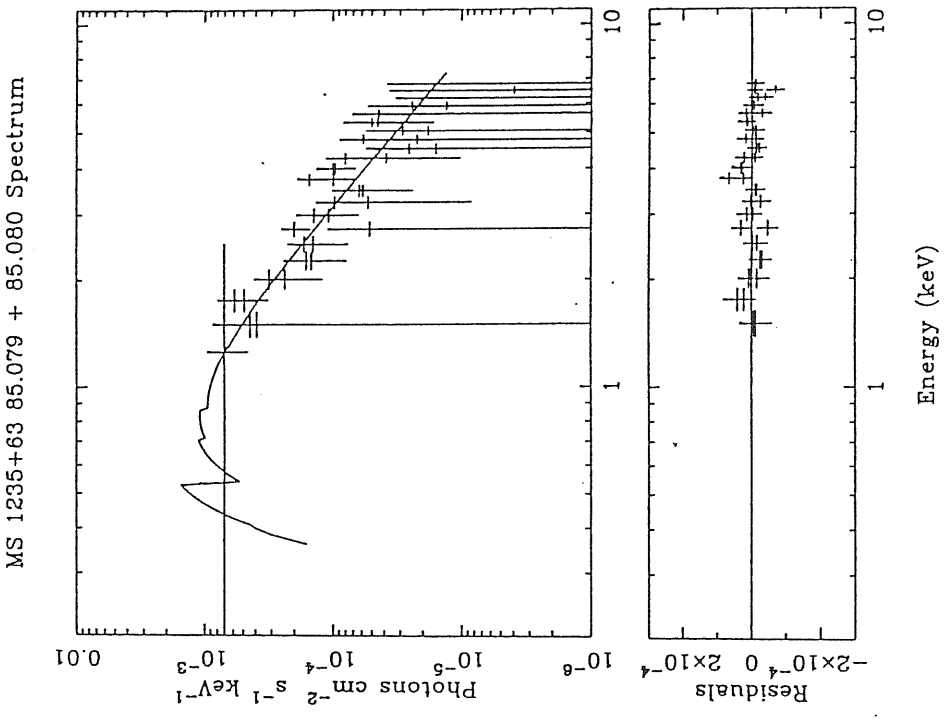
MS 1235+63 85.079 + 85.080 Spectrum
Photons cm^{-2} s^{-1} keV^{-1}
Residuals
Energy (keV)

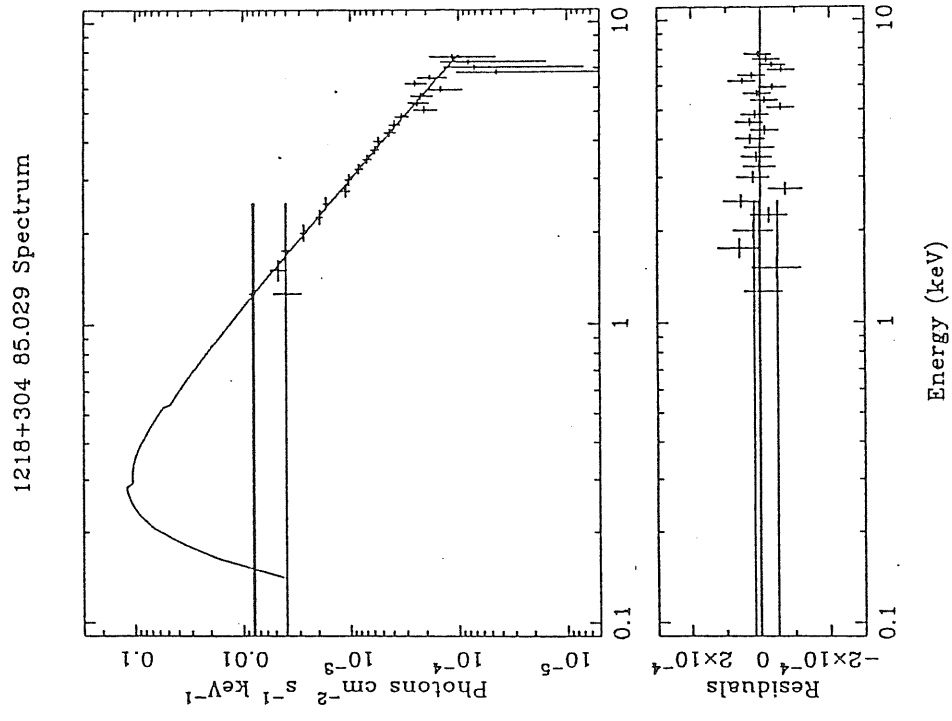
1218+304 85.029 Spectrum
Photons cm^{-2} s^{-1} keV^{-1}
Residuals
Energy (keV)

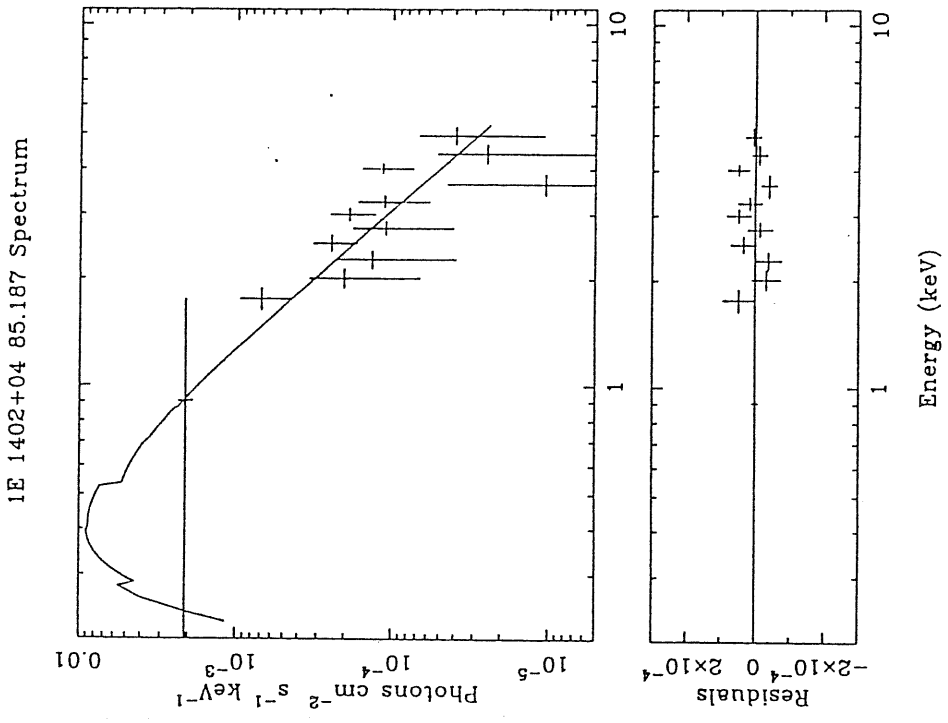
1E 1402+04 85.187 Spectrum
Photons cm^{-2} s^{-1} keV^{-1}
0.01
10^{-3}
10^{-4}
10^{-5}
1
10
Residuals
-2×10^{-4} 0 2×10^{-4}
Energy (keV)

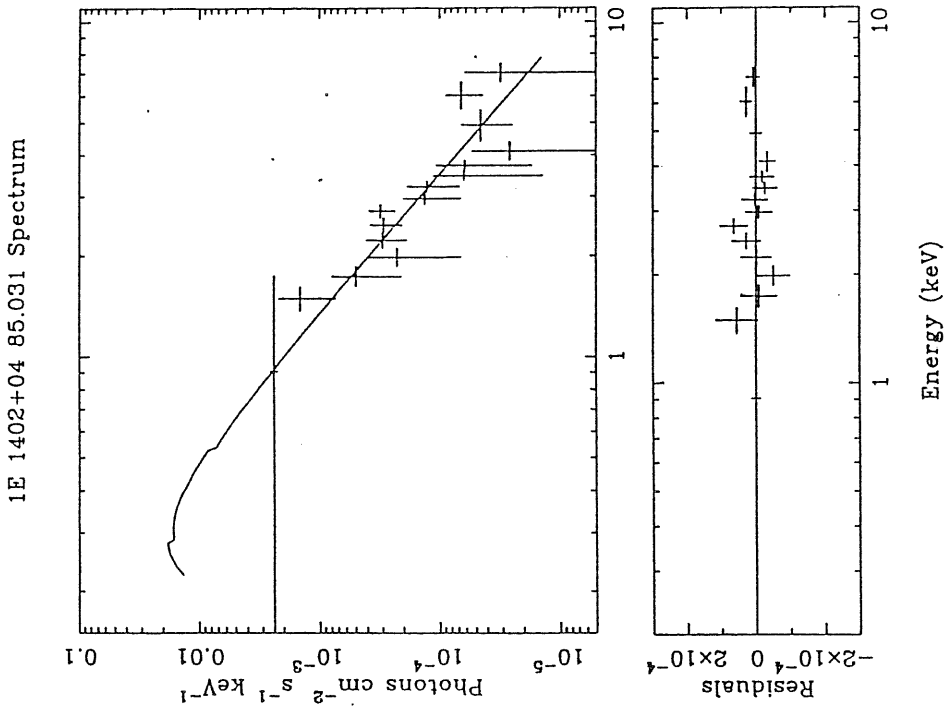
1E 1402+04 85.031 Spectrum
Photons cm^{-2} s^{-1} keV^{-1}
0.1
0.01
10^{-3}
10^{-4}
10^{-5}
1
10
Residuals
-2×10^{-4} 0 2×10^{-4}
Energy (keV)

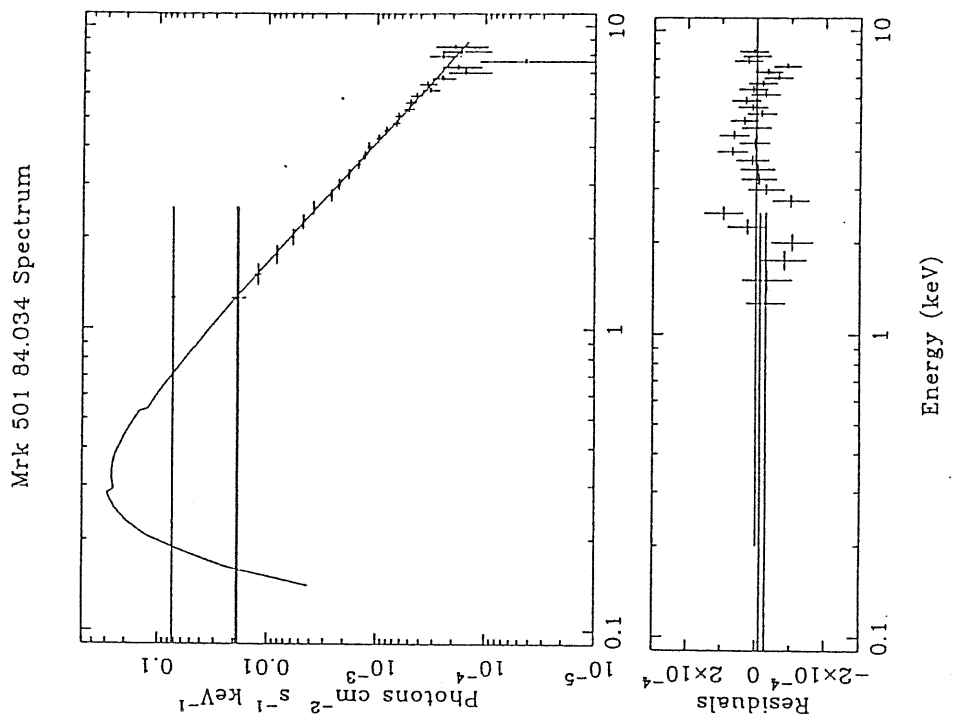
Mrk 501 84.034 Spectrum
Photons cm^{-2} s^{-1} keV^{-1}
Residuals
Energy (keV)

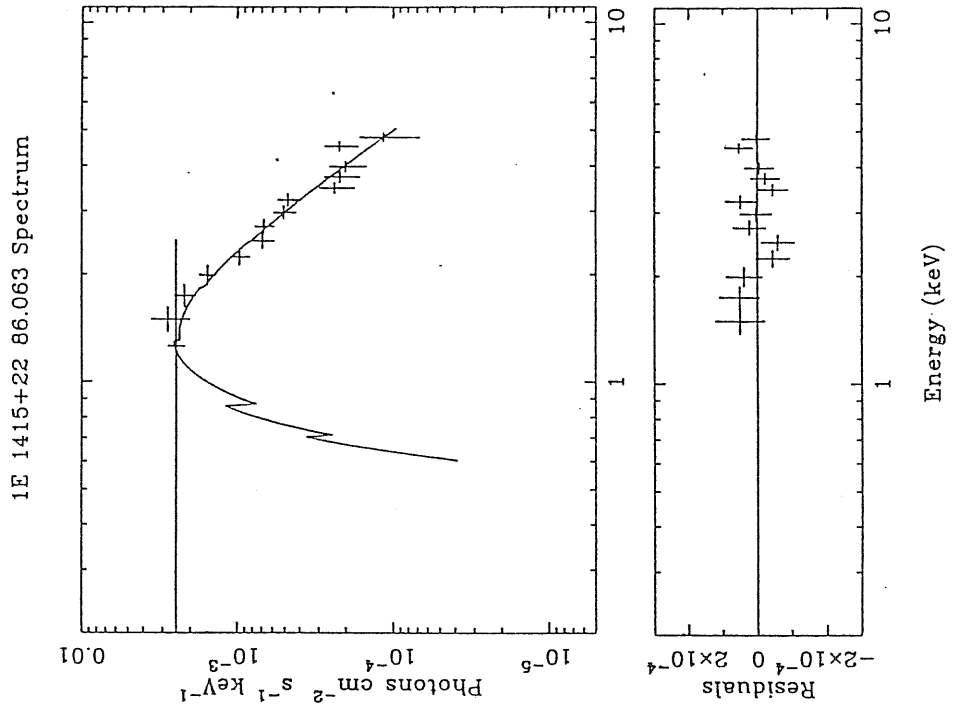
1E 1415+22 86.063 Spectrum
Photons cm^{-2} s^{-1} keV^{-1}
Residuals
Energy (keV)

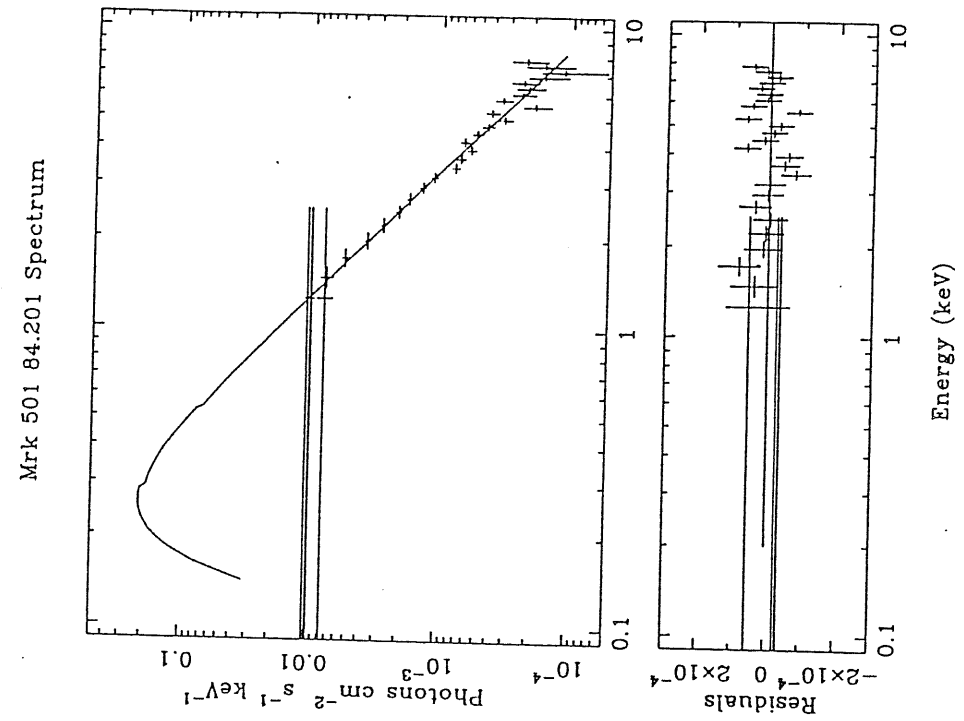
Mrk 501 84.201 Spectrum
Photons cm^{-2} s^{-1} keV^{-1}
Residuals
Energy (keV)

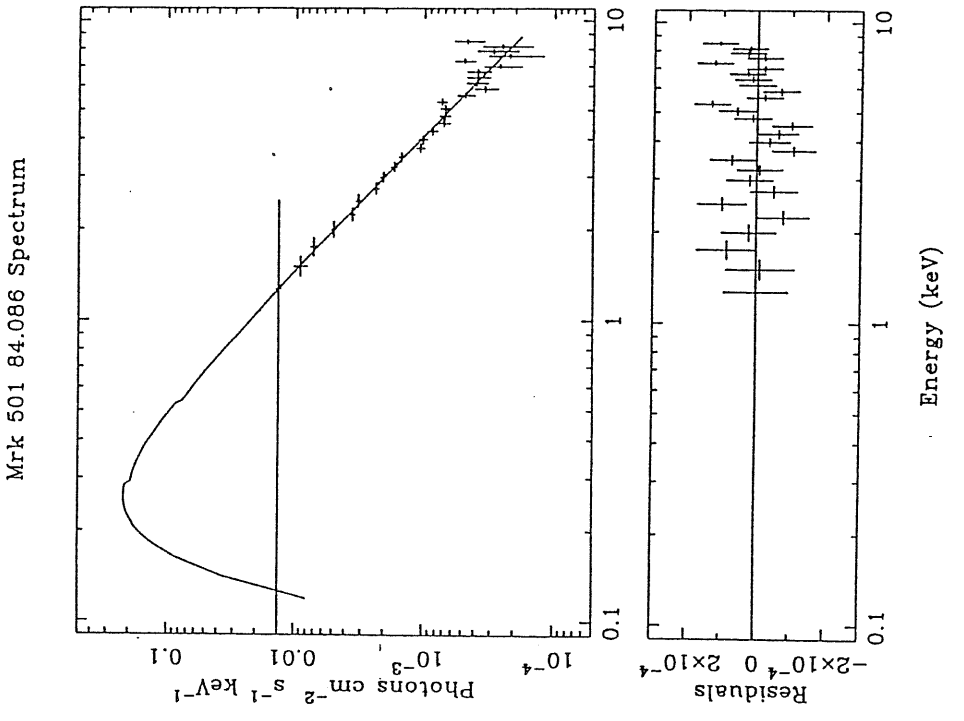
Mrk 501 84.086 Spectrum
Photons cm^{-2} s^{-1} keV^{-1}
Residuals
Energy (keV)

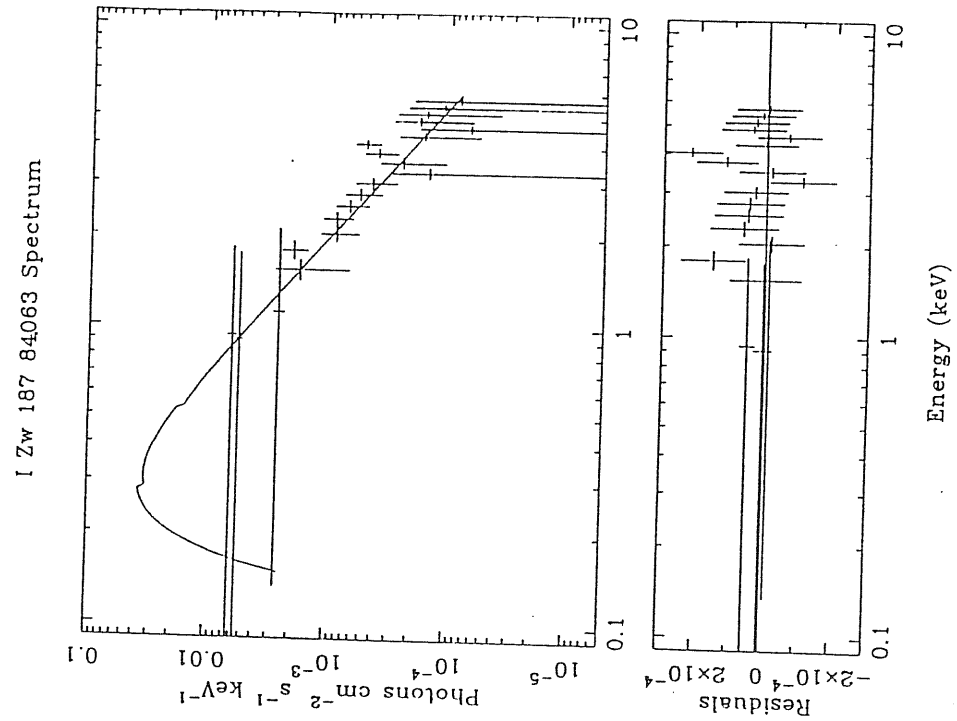
I Zw 187 84063 Spectrum
Photons cm^{-2} s^{-1} keV^{-1}
Residuals
Energy (keV)

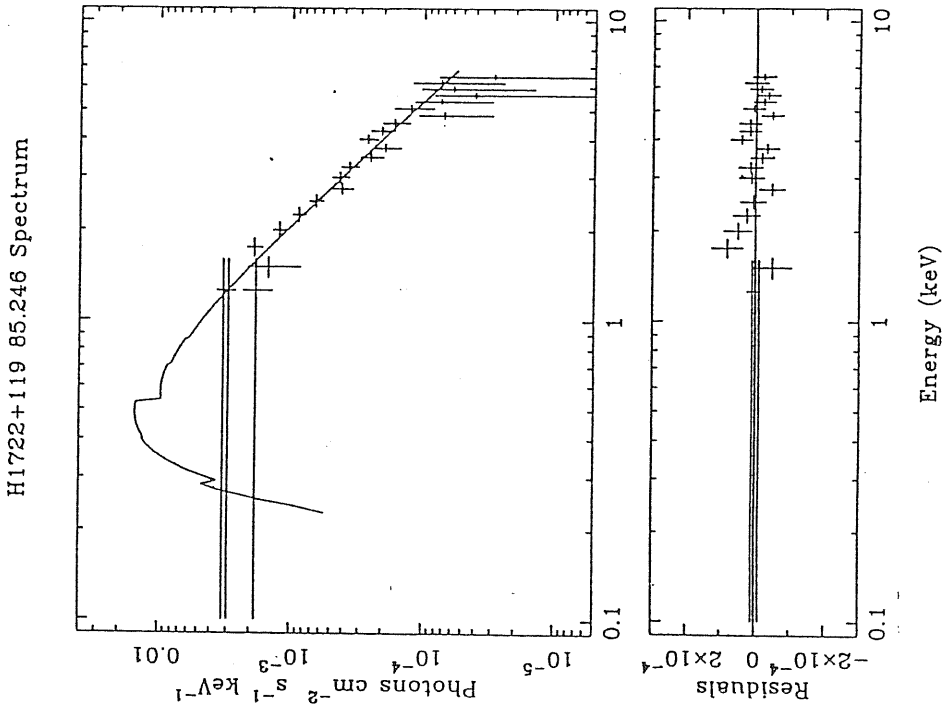
H1722+119 85.246 Spectrum
Photons cm^{-2} s^{-1} keV^{-1}
Residuals
Energy (keV)

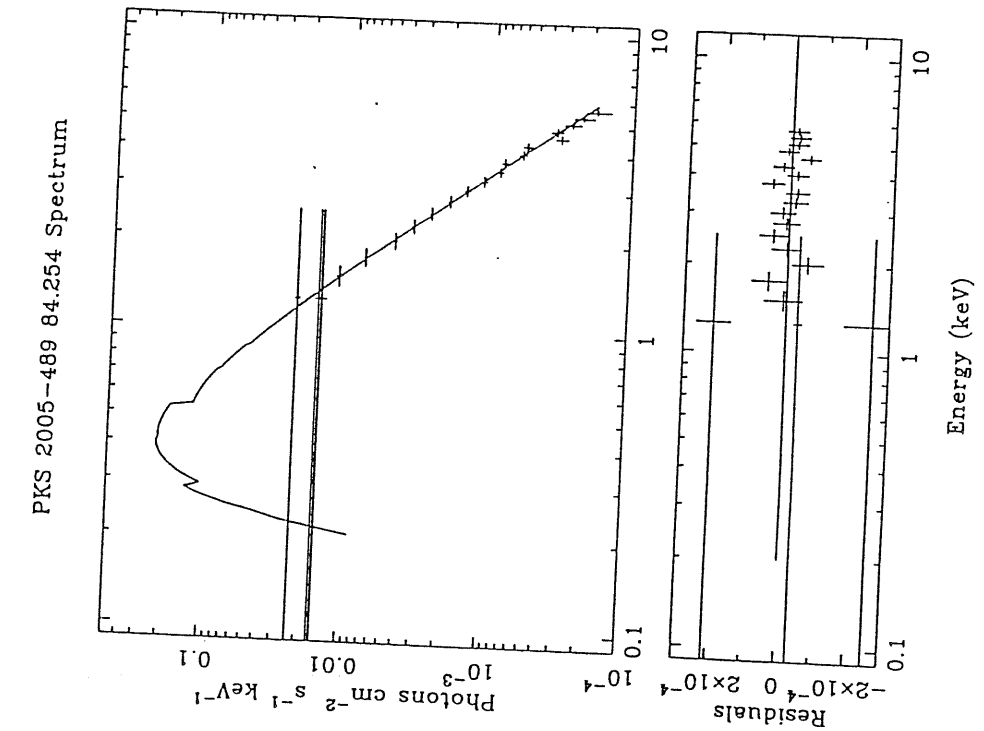
PKS 2005-489 84.254 Spectrum
Photons cm^{-2} s^{-1} keV^{-1}
Residuals
Energy (keV)

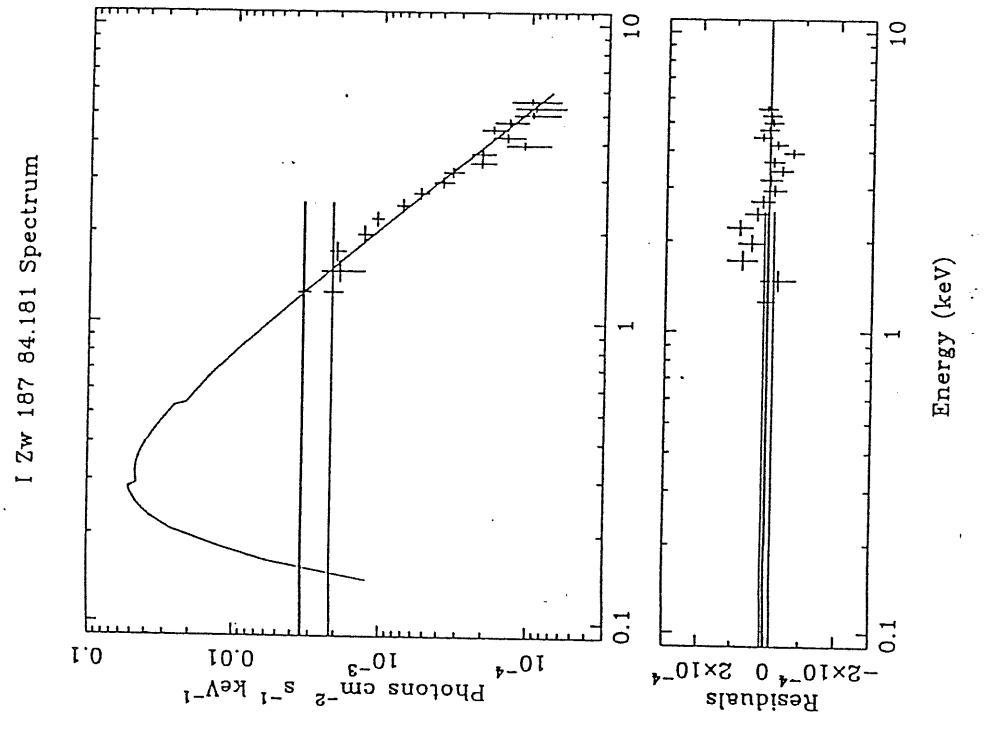
I Zw 187 84.181 Spectrum
Photons cm^{-2} s^{-1} keV^{-1}
Residuals
Energy (keV)

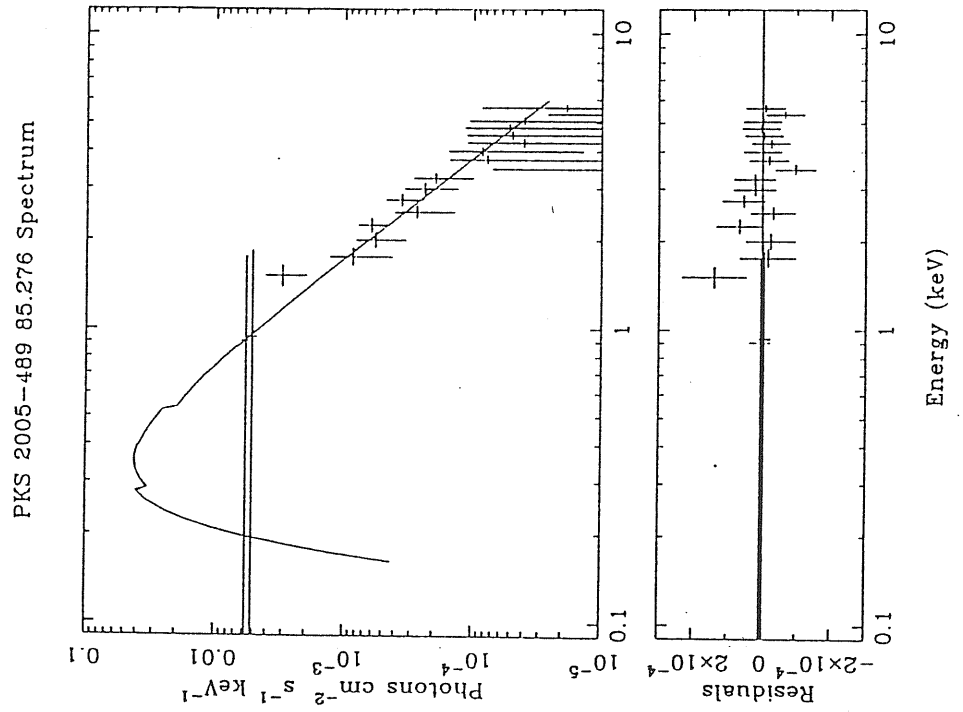
PKS 2005−489 85.276 Spectrum
Photons cm^{-2} s^{-1} keV^{-1}
Residuals
Energy (keV)

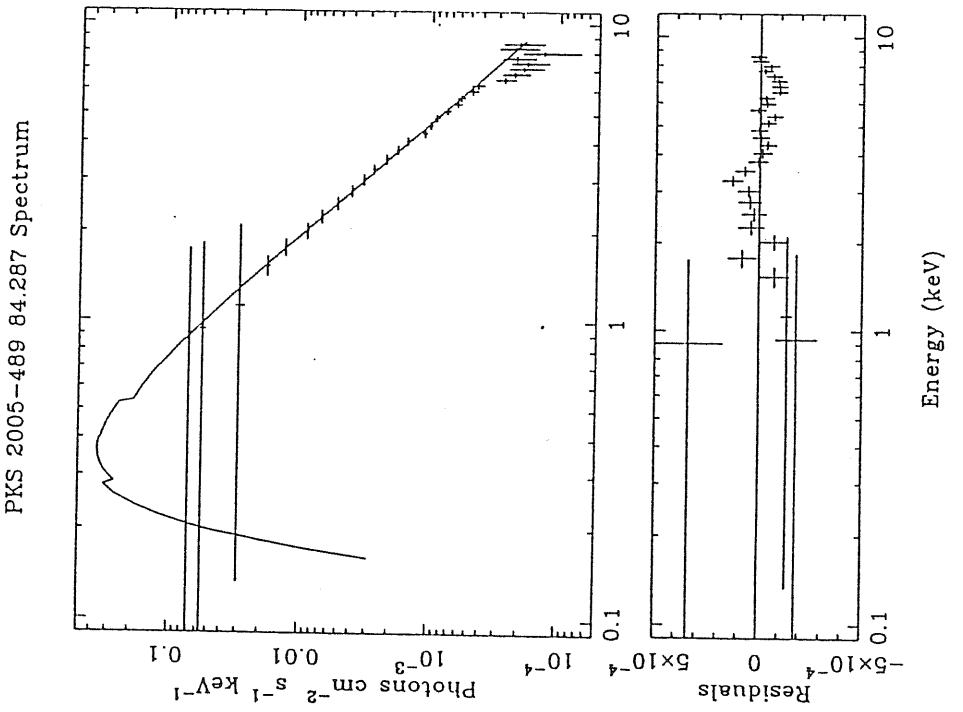
PKS 2005−489 84.287 Spectrum
Photons cm^{-2} s^{-1} keV^{-1}
Residuals
Energy (keV)

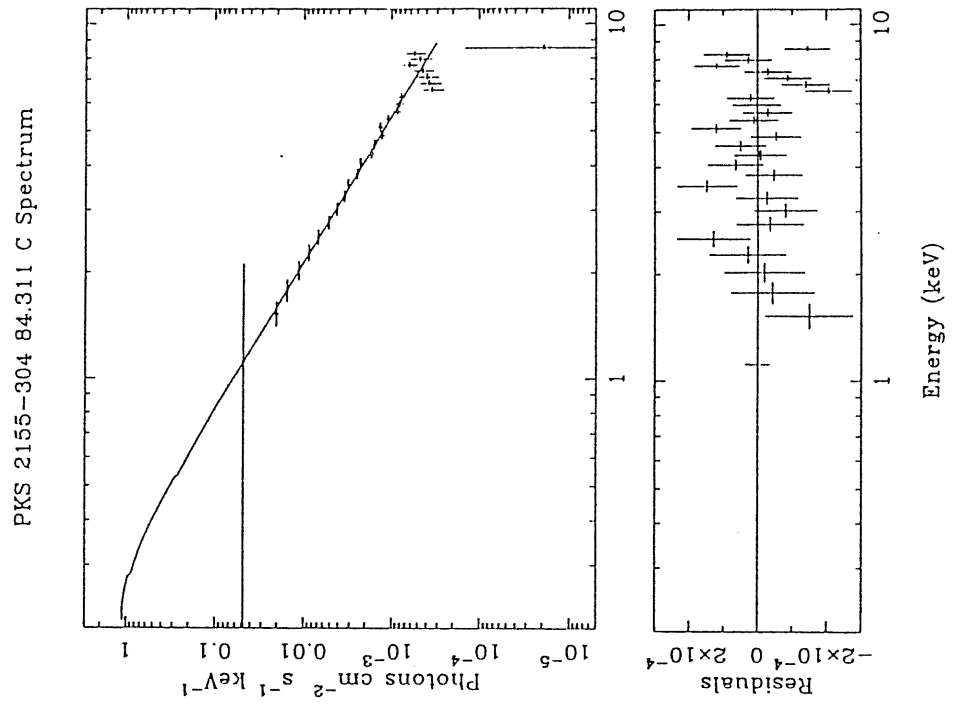
PKS 2155−304 84.311 C Spectrum
Photons cm^{-2} s^{-1} keV^{-1}
Residuals
Energy (keV)

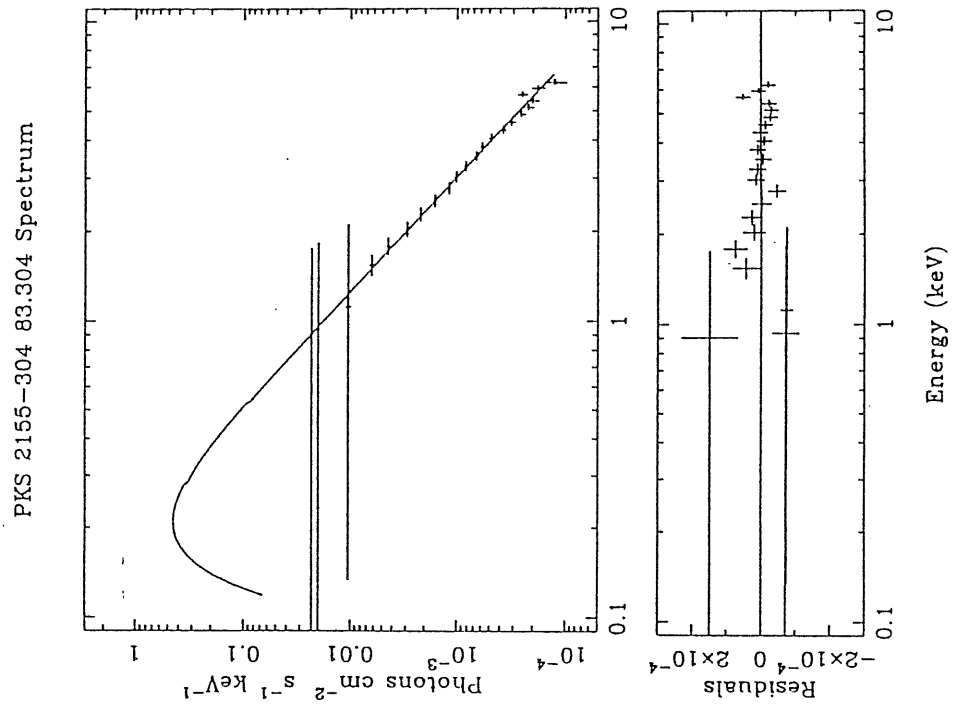
PKS 2155−304 83.304 Spectrum
Photons cm^{-2} s^{-1} keV^{-1}
Residuals
Energy (keV)

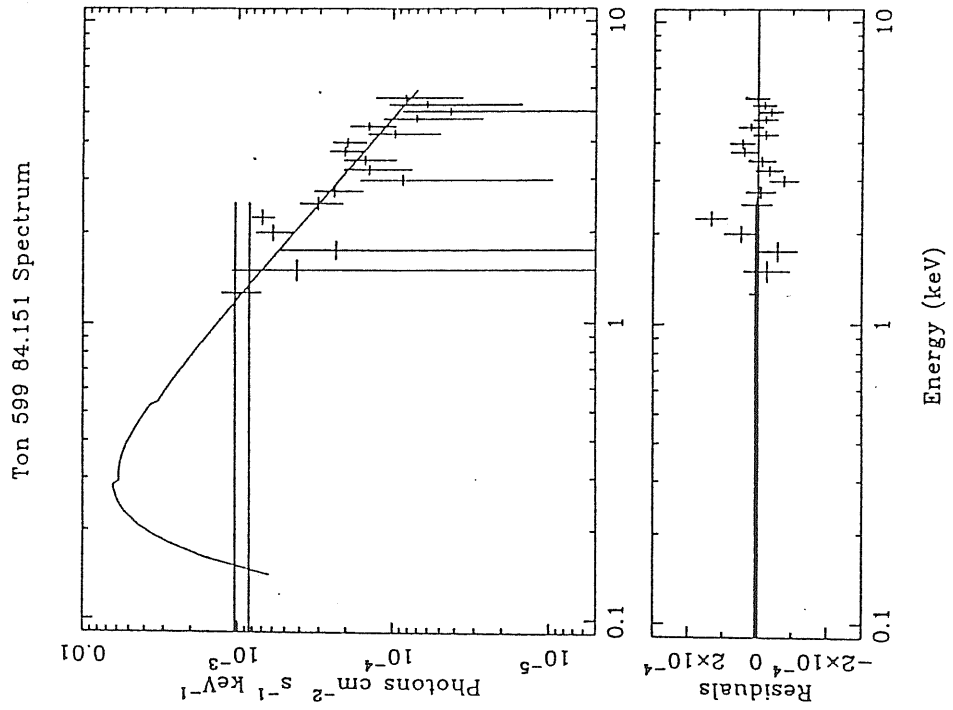
Ton 599 84.151 Spectrum
Photons cm^{-2} s^{-1} keV^{-1}
Residuals
Energy (keV)

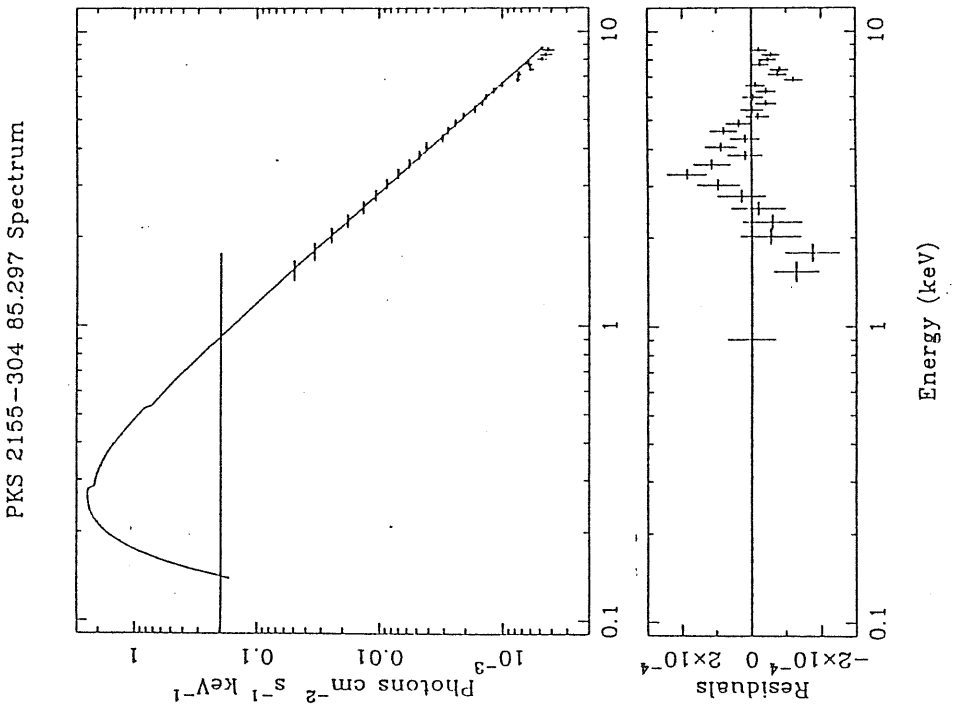
PKS 2155-304 85.297 Spectrum
Photons cm^{-2} s^{-1} keV^{-1}
Residuals
Energy (keV)

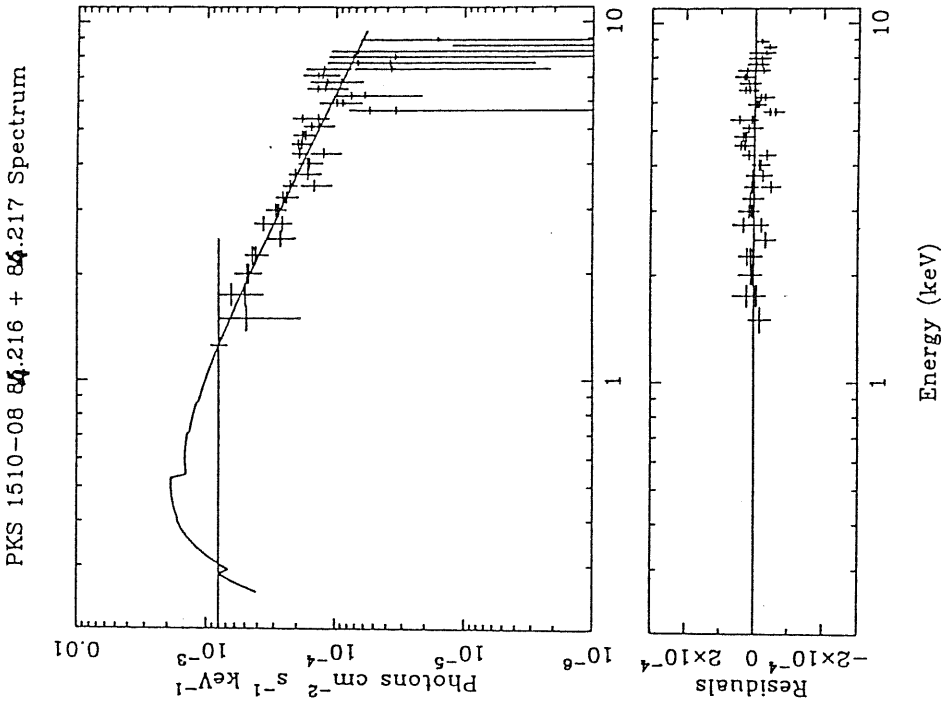
PKS 1510−08 84.216 + 84.217 Spectrum
Photons cm^{-2} s^{-1} keV^{-1}
Residuals
Energy (keV)

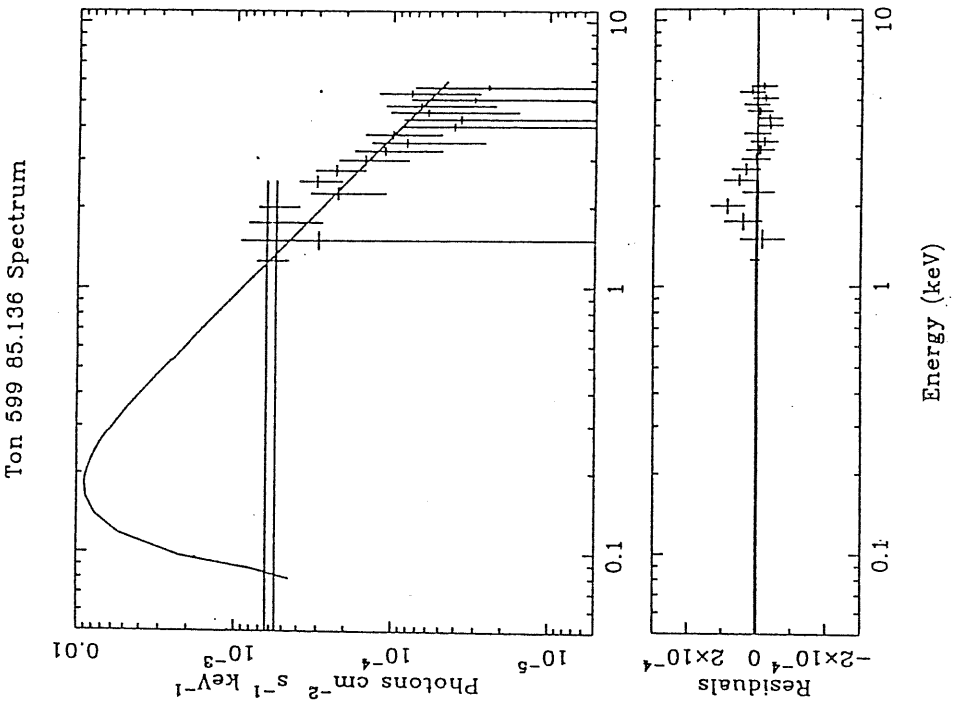
Ton 599 85.136 Spectrum
Photons cm^{-2} s^{-1} keV^{-1}
Residuals
Energy (keV)

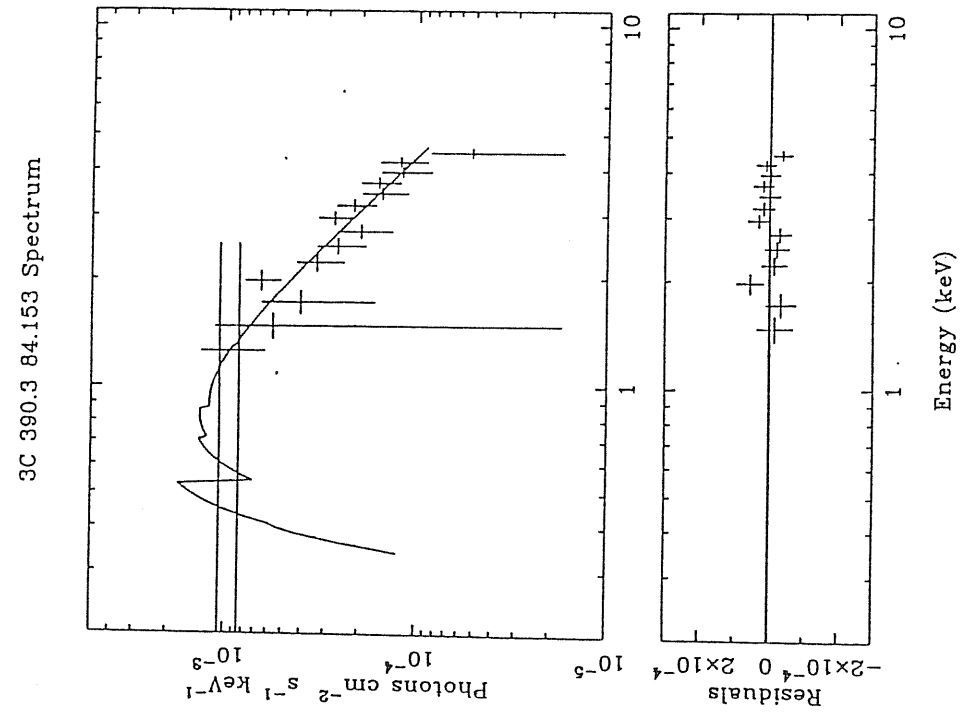
3C 390.3 84.153 Spectrum
Photons cm^{-2} s^{-1} keV^{-1}
Residuals
Energy (keV)

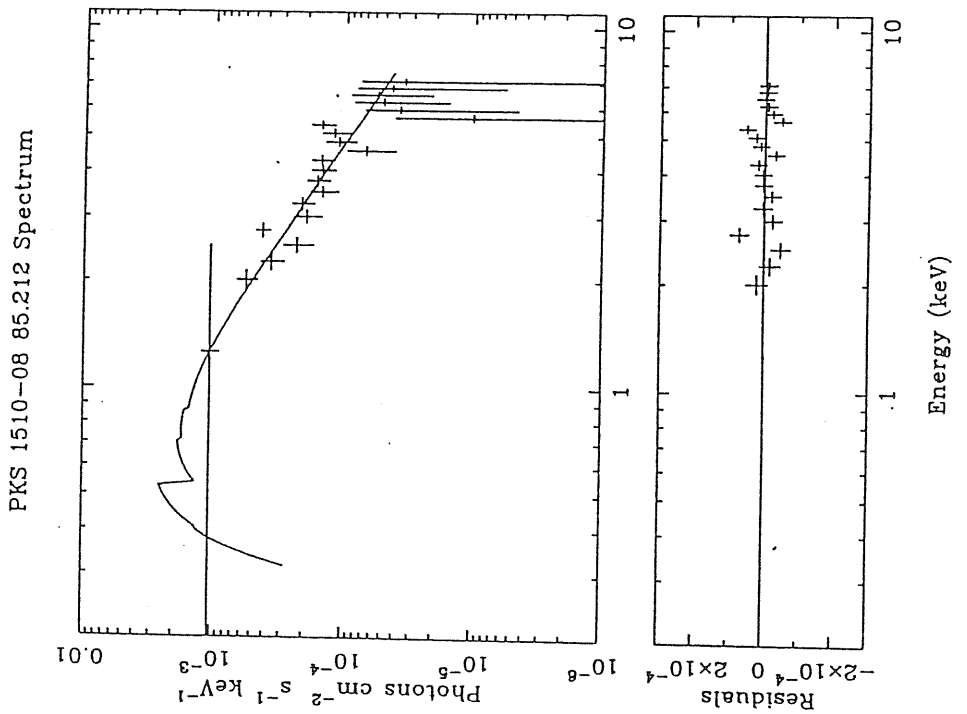
PKS 1510-08 85.212 Spectrum
Photons cm^{-2} s^{-1} keV^{-1}
Residuals
Energy (keV)

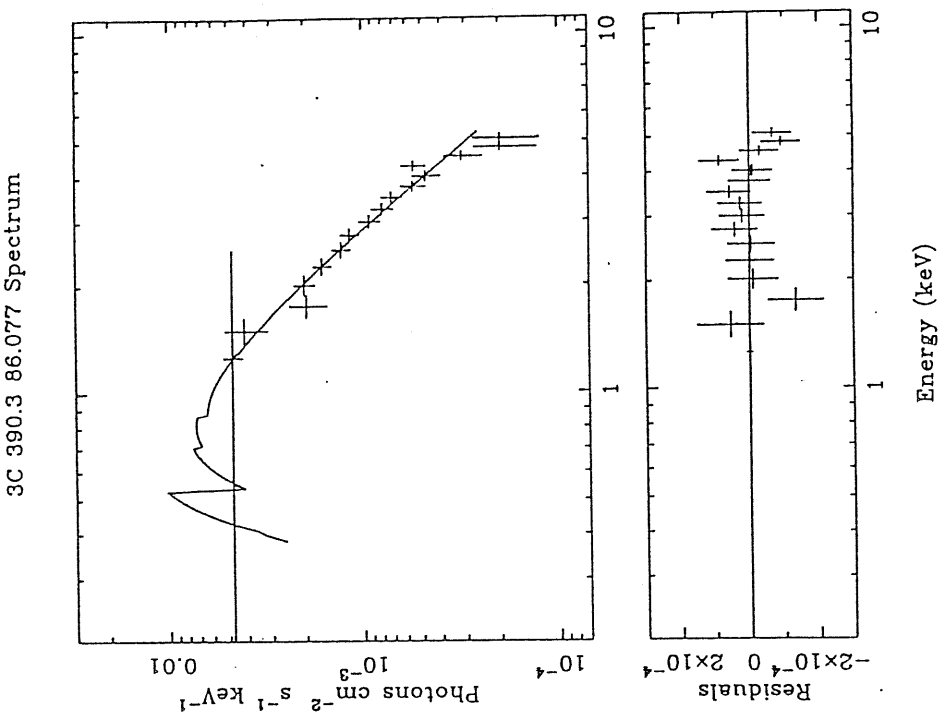
3C 390.3 86.077 Spectrum
Photons cm^{-2} s^{-1} keV^{-1}
0.01
10^{-3}
10^{-4}
1
10
Residuals
-2×10^{-4} 0 2×10^{-4}
Energy (keV)

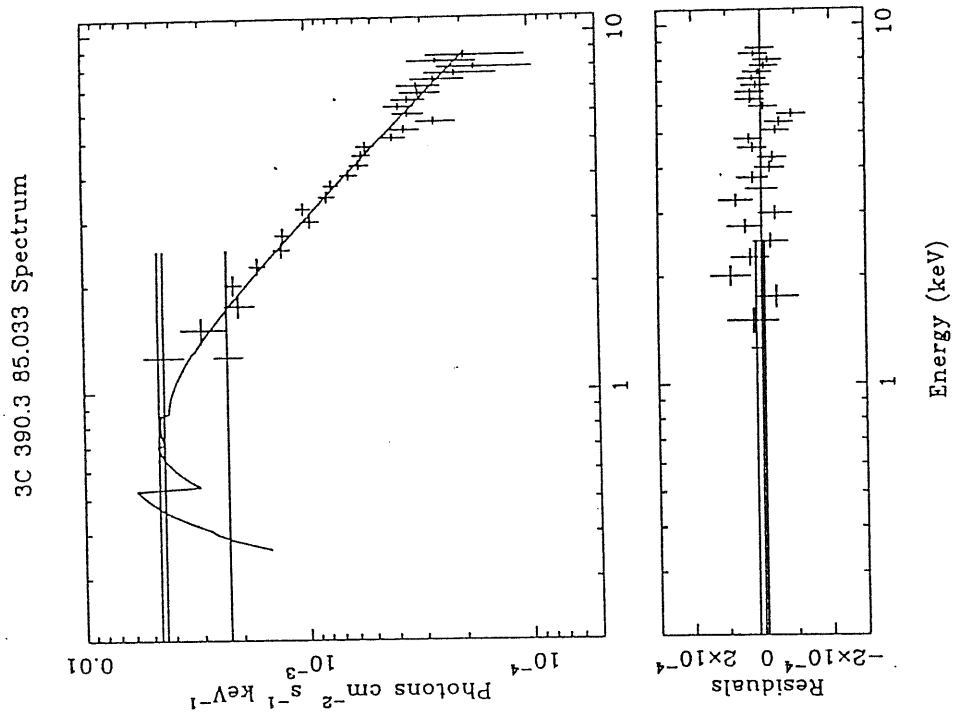
3C 390.3 85.033 Spectrum
Photons cm^{-2} s^{-1} keV^{-1}
0.01
10^{-3}
10^{-4}
1
10
Residuals
-2×10^{-4} 0 2×10^{-4}
Energy (keV)

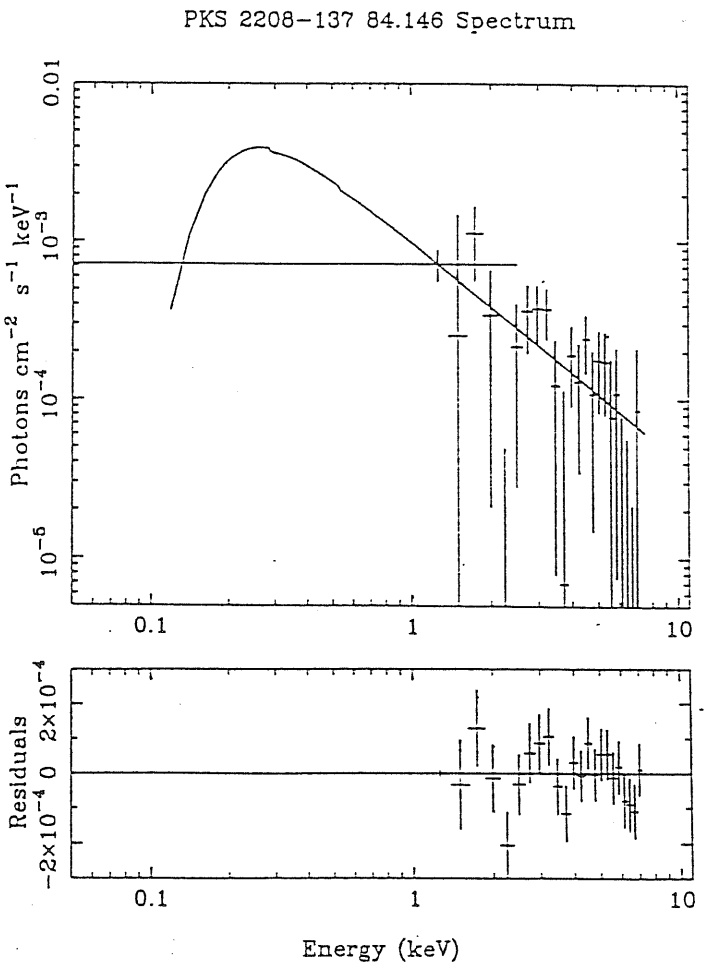
PKS 2208−137 84.146 Spectrum
Photons cm^{-2} s^{-1} keV^{-1}
0.01
10^{-3}
10^{-4}
10^{-5}
0.1
1
10
Residuals
2×10^{-4}
0
-2×10^{-4}
0.1
1
10
Energy (keV)

References

Altschuler, D.R. & Wardle, J.F.C. 1975, Nature 255, 306

Agrawal, P.C. & Riegler, G.R. 1979, ApJ Lett. 231, L25

Agrawal, P.C., Singh, K.P., & Riegler, G.R. 1983, in *Proc. 18th Internat. Cosmic Ray Conf.* (Bangalore), 1, 3

Angel, R. & Stockmann, H.S. 1980, A.R.A.A. 18, 321

Appenzeller, I. & Hiltner, W.A. 1967, ApJ Lett. 149, L17

Argue, A.N., Kenworthy, C.M., & Stewart, P.M. 1973 Ap. Lett.14, 99

Barr, P., Giommi, P., & Maccagni, D. 1988, ApJ Lett. 324, L11

Barr, P. *et al.* 1989, in *BL Lac Objects*, Eds. L. Maraschi, T. Maccacaro, M.-H. Ulrich, Springer – Verlag, 290

Bevington, P.R. 1969, Data Reduction and Error Analysis for the Physical Sciences (New York: McGraw – Hill), 200

Blake, G.M. 1970, Ap. Lett. 6, 201

Blisset, R.J. & Cruise, A.M. 1979, MNRAS 186, 45

Bolton, J.G. & Ekers, J. 1966, Aust.J.Phys. 19, 559

Bolton, J.G., Clarke, M.E., & Ekers, R.D. 1965, Aust. J. Physics 18, 627

Bowyer, S. *et al.* 1984, ApJ Lett. 278, L103

Brissenden, R.J.V. *et al.* 1990, ApJ 350, 578

Burbidge, E.M. & Kinman, T.D. 1966, ApJ 145, 654

Burbidge, E.M. 1968, ApJ Lett. 154, L109

Burbidge, E.M. & Burbidge, G.R. 1971, ApJ Lett. 163, L21

Burbidge, G.R., Crowne, A.H., & Smith, H.E. 1977, ApJ 33, 113

Burbidge, G. & Hewitt, A. 1987, ApJ 92, 1

Butcher, H.R. *et al.* 1976, ApJ Lett. 209, L11

Canizares, C.R. & Kruper, J. 1984, ApJ Lett. 278, L99

Canizares, C.R. & White, J.L. 1989, ApJ 339, 27

Colla, G. *et al.* 1972, A&AS 7, 1

Cooke, B.A. *et al.* 1978, MNRAS 182, 489

De Korte, P.A.J. *et al.* 1981, Spa.Sci.Rev. 30, 495

Doxsey, R. *et al.* 1983, ApJ 264, L43

Edge, A.C. & Stewart, G.C. 1991, MNRAS 252, 414

Elvis, M., Lochmann, F.J., & Wilkes, B. 1989, A.J. 97, 777

The EXOSAT Database System: Available Databases, Feb. 1991, ESA TM-13

Falomo, R. *et al.* 1987, ApJ 318, L39

Falomo, R., Tanzi, E.G., & Treves, A. 1989, in *BL Lac Objects*, eds. L. Maraschi, T. Maccacaro and M. -H. Ulrich, (Springer-Verlag), 73

Feigelson, E.D. *et al.* 1986, ApJ 302, 337

Filippenko, A.V. *et al.* 1986, AJ 91, 49

Fink, H.H. *et al.* 1992a, MPE Rep. 235, 181

Fink, H.H. *et al.* 1992b, MPE Rep. 235, 202

Fink, H.H. *et al.* 1991, A&A 246, L6

Fosbury, R.A.E. & Disney, M.J. 1976, ApJ 207, L75

Garilli, B. & Maccagni, D. 1990, A&A 229, 88

George, I.M. 1988, PhD Thesis, University of Leicester

George, I.M., Warwick, R.S., & McHardy, I.M. 1988a, MNRAS 235, 787

George, I.M., Warwick, R.S., & Bromage, G.E. 1988b, MNRAS 232, 793

Gioia, I. *et al.* 1984, ApJ 283, 495

Giommi, P. *et al.* 1987, ApJ 322, 662

Giommi, P. *et al.* 1989, MNRAS 236, 375

Giommi, P. *et al.* 1990, ApJ 356, 432

Giommi, P. *et al.* 1991, ApJ 378, 77

Giommi, P. & Tagliaferri, G. 1991, XIMAGE User's Guide, Ver. 1.8, EXOSAT Observatory, ESA, Noordwijk, The Netherlands

Ghisellini, G. Maraschi, L., & Treves, A. 1985, A&A 146, 204

Ghisellini, G. *et al.* 1986, ApJ 310, 317

Ghisellini, G. & Maraschi, L. 1989, ApJ 340, 181

Ghosh, K.K. & Soundararajaperumal, S. 1991, AJ 102, 1298

Griffiths, R.E. *et al.* 1979, ApJ 234, 810

Griffiths, R.E. *et al.* 1989, MNRAS 240, 33

Hall, R. *et al.* 1981, Spa.Sci.Rev. 30, 47

Halpern, J. *et al.* 1986, ApJ 302, 711

Halpern, J. *et al.* 1991, AJ 101, 818

Hewitt, A. & Burbidge, G. 1987, ApJS 63, 1

Hearn, D.R., Marshall, F.J., & Jernigan, J.G. 1979, ApJ Lett. 227, L63

Kahn, S.M. & Blisset, R.J. 1979, ApJ 238, 417

Kondo, Y. *et al.* 1981, ApJ 243, 690

Kühr, H. & Schmidt, G.D. 1990, AJ 99, 1

Kühr, H. *et al.* 1981a, A&AS 86, 854

Kühr, H. *et al.* 1981b, A&AS 45, 367

Impey, C.D. & Neuegebauer, G. 1988, AJ 95, 307

Impey, C.D. & Tapia, S. 1988, ApJ 333, 666

Impey, C.D., Lawrence, C.R., & Tapia, S. 1991, ApJ 375, 46

Lampton, M., Margon, B., & Bowyer, S. 1976, ApJ 208, 177

Landau, R. *et al.* 1986, ApJ 308, 78

Lawson, A.J. *et al.* 1992, MNRAS preprint

Ledden, J.E. & O'Dell, S.L. 1985, ApJ 298, 630

Liller, M.H. & Liller, W. 1975, ApJ Lett. 199, L133

Maccacaro, T. *et al.* 1982, ApJ 253, 504

Maccagni, D. *et al.* 1983a, ApJ 273, 75

Maccagni, D., Maccacaro, T., & Tarenghi, M. 1983b, ApJ 273, 70

Maccagni, D. *et al.* 1987, A&A 178, 21

Madejski, G.M. 1985, PhD thesis, Harvard University

Madejski, G.M. & Schwartz, D.A. 1989, in *BL Lac Objects*, Eds. L. Maraschi, T. Maccacaro, M.-H. Ulrich, Springer – Verlag, 267

Madejski, G.M. *et al.* 1992, preprint

Madejski, G.M. *et al.* 1991, ApJ 370, 198

Makino, F. *et al.* 1987, ApJ 313, 662

Maraschi, L. *et al.* 1985, ApJ 298, 630

Maraschi, L. *et al.* 1986, ApJ 310, 325

Maraschi, L. & Maccagni, D. 1988, Mem.S.A.It. 59, 277

Michelson P. F. *et al.* 1992, I.A.U. circ. 5470 .

Miller, J.S. 1975, ApJ Lett. 200, L55

Miller, J.S., French, H.B., & Hawley, S.A. 1978, in *Pittsburgh Conference on BL Lac Objects*, ed. A.M.Wolfe (Pittsburgh: University of Pittsburgh), 176

Miyoshi, S. *et al.* 1986, Astroph.&Spa.Sci. 119, 185

Moore, R.L. & Stockmann, H.S. 1981, ApJ 243, 60

Moore, R.L. & Stockmann, H.S. 1984, ApJ 279, 465

Morganti, R. *et al.* 1992, MNRAS 156, 1P

Morini, M., Anselmo, F., & Molteni, D. 1989, ApJ 347, 750

Morris, S.L. *et al.* 1991, ApJ 380, 49

Morrison,R. & McCammon, D. 1983, ApJ 270, 119

Mufson, S.L. *et al.* 1984, ApJ 285, 571

Mushotzky, R.F. *et al.* 1978, ApJ Lett. 226, L65

Mushotzky, R.F. *et al.* 1979, ApJ Lett. 232, L17

Northover, K.J.E. 1973, MNRAS 165, 369

Ohashi, T. 1989, in *BL Lac Objects*, Eds. L. Maraschi, T. Maccacaro, M.-H. Ulrich, Springer – Verlag, 296

Ohashi, T. *et al.* 1989, PASJ 41, 709

Oke, J.B. 1978, ApJ 219, L97

Padovani, P. & Urry, C.M. 1990, ApJ 356, 75

Penston, M.V. & Penston, M.J. 1973, MNRAS 162, 109

Peterson, B.A. & Bolton, J.G. 1972, ApJ Lett. 10, 105

Peterson, B.A. *et al.* 1976, ApJ Lett 207, L5

Piccinotti, G. *et al.* 1982, ApJ 253, 485

Raymond, J.C. & Smith, B.W. 1977, ApJS 35, 419

Remillard, R.A. *et al.* 1989, ApJ 345, 140

Riegler, G.R., Agrawal, P.C., & Mushotzky, R.F. 1979, ApJ Lett. 233, L47

Rieke, G.H. *et al.* 1976, Nature 260, 754

Sambruna, R.M. *et al.* 1992, ApJ, submitted

Sandage, A. 1973, ApJ 180, 687

Schwartz, D.A. *et al.* 1979, ApJ Lett. 229, L53

Schwartz, D.A. *et al.* 1989, in *BL Lac Objects*, Eds. L. Maraschi, T. Maccacaro, M.-H. Ulrich, Springer – Verlag, 209

Searle, L. & Bolton, J.G. 1968, ApJ Lett. 154, L101

Sembay, S. *et al.* 1992, ApJ, in press

Shafer, R.A., Haberl, F., Arnaud, K.A., & Tennant, A.F. 1991, XSPEC User's Guide, Ver. 2, ESA TM – 09

Shimmins, A.J. & Bolton, J. 1974, Aust.J.Phys.Astrophys.S. 32

Singh, K.P. & Garmire, G.P. 1985, ApJ 197, 199

Singh, K.P., Rao, A.R., & Vahia, M.N. 1990, ApJ 365, 455

Snijders, M.A.J. *et al.* 1979, MNRAS 189, 873

Spinrad, H. & Smith, H.E. 1975, ApJ 201, 275

Stark, A.A. *et al.* 1992, ApJS 79, 77

Staubert, R. *et al.* 1986a, A&A 162, 16

Staubert, R., Brunner, H., & Worrall, D.M. 1986b, ApJ 310, 694

Stein, W.A., O'Dell, S.L., & Strittmatter, P.A. 1976, ARAA 14, 173

Stickel, M. *et al.* 1991, ApJ 374, 431

Stocke, J.T. *et al.* 1985, ApJ 298, 619

Stocke, J.T. *et al.* 1990, ApJ 348, 141

Stocke, J.T. *et al.* 1991, ApJS 76, 813

Tagliaferri, G. *et al.* 1989, in *BL Lac Objects*, Eds. L. Maraschi, T. Maccacaro, M.-H. Ulrich, Springer – Verlag, 257

Tapia, S. *et al.* 1977, ApJ Lett. 215, L71

Treves, A. *et al.* 1989, ApJ 341, 733

Treves, A. *et al.* 1992, ApJ, in press

Turner, M.J.L., Smith, A., & Zimmermann, H.V. 1981, Spa.Sci.Rev. 30, 513

Turner, M.J.L. *et al.* 1990, MNRAS 244, 310

Turner, T.J. & Pounds, K.A. 1989, MNRAS 240, 833

Ulmer, M.P. *et al.* 1983, ApJ 270, L1

Ulrich, M.-H. *et al.* 1975, ApJ 198, 261

Ulrich, M.-H. 1978, ApJ Lett. 222, L3

Urry, C.M. 1984, PhD thesis, Johns Hopkins University

Urry, C.M. & Mushotzky, R.F. 1982, ApJ 253, 38

Urry, C.M. 1986, in *Continuum Emission in AGNs*, Ed. M.L. Sitko, 91

Urry, C.M., Mushotzky, R.F., & Holdt, S.S. 1986, ApJ 305, 369

Valtaoja, E. *et al.* 1990, AJ 99, 769

Veron, P. 1978, Nature 272, 430

Veron-Cetty, M.-P. & Veron, P. 1991, *A Catalogue of Quasars and Active Nuclei (5th Edition)*, ESO Scientific Report

Wall, J.V. *et al.* 1975, Aust.J.Phys.Astrophys.S. 34, 55

Wall, J.V. *et al.* 1986, MNRAS 219, 23P

Weistrop, D. *et al.* 1981, ApJ 249, 3

Williams, O.R. *et al.* 1992, ApJ 389, 157

Wills, B.J. & Wills, D. 1974 ApJ Lett. 190, L97

Wills, D. 1966, Observatory, 86, 245

Wilkes, B. & Elvis, M. 1987, ApJ 323, 243

Wilson, A.S. *et al.* 1979, MNRAS 187, 109

Wood, K.S. *et al.* 1984, ApJS 56, 507

Worrall, D.M. & Wilkes, B.J. 1990, ApJ 360, 396

Worrall, D.M. *et al.* 1981, ApJ 243, 53

Worrall, D.M. *et al.* 1984a, ApJ 286, 711

Worrall, D.M. *et al.* 1984b, ApJ 278, 521

Zwicky, F. 1966, ApJ 143, 192